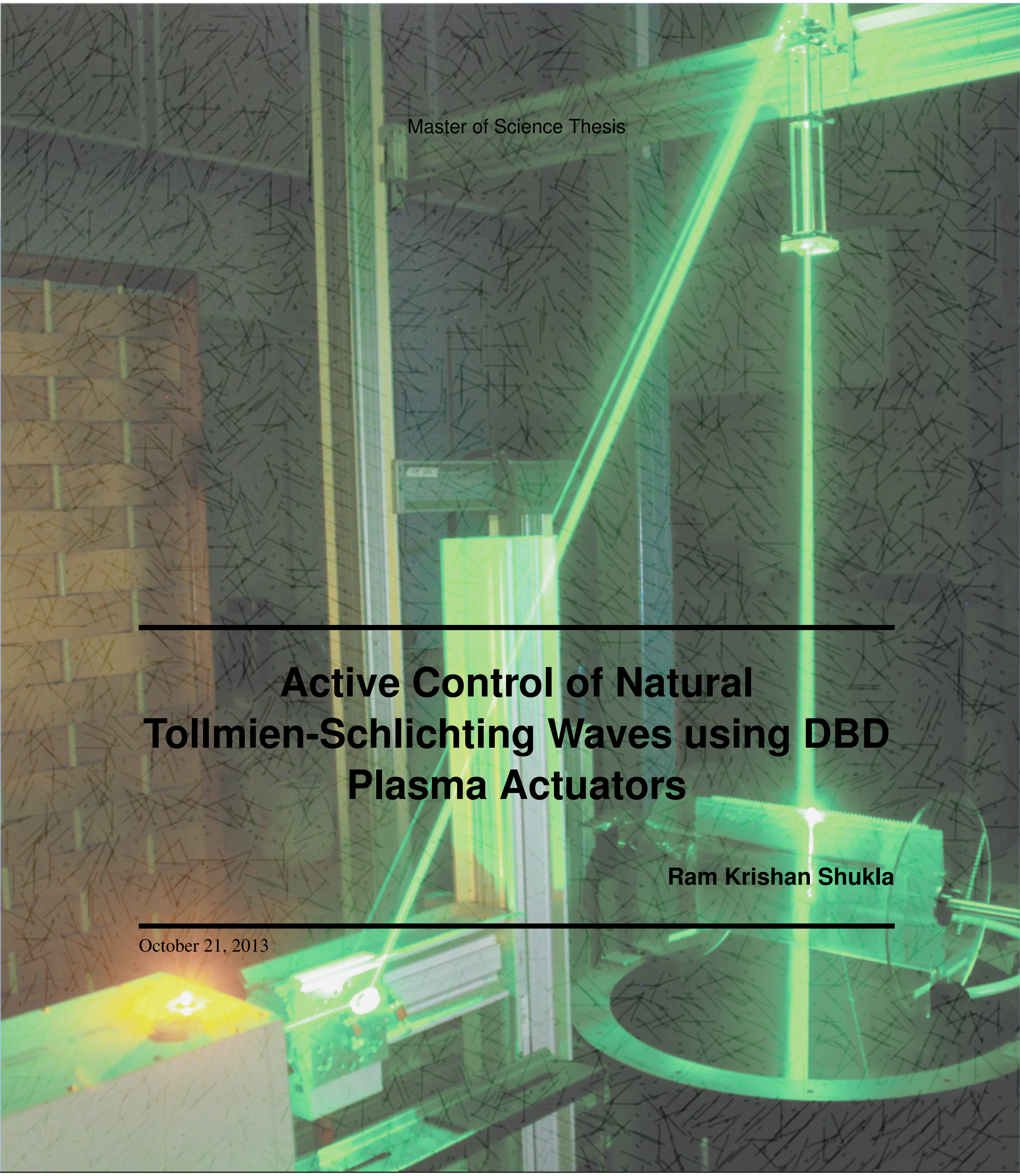

Master of Science Thesis

Active Control of Natural Tollmien-Schlichting Waves using DBD Plasma Actuators

Ram Krishan Shukla

October 21, 2013

Faculty of Aerospace Engineering

Delft University of Technology

Active Control of Natural Tollmien-Schlichting Waves using DBD Plasma Actuators

Master of Science Thesis

For obtaining the degree of Master of Science in Aerospace Engineering at
Delft University of Technology

Ram Krishan Shukla

October 21, 2013

Faculty of Aerospace Engineering · Delft University of Technology

Delft University of Technology

DELFT UNIVERSITY OF TECHNOLOGY
DEPARTMENT OF AERODYNAMICS

The undersigned hereby certify that they have read and recommend to the Faculty of Aerospace Engineering for acceptance the thesis entitled **"Active Control of Natural Tollmien-Schlichting Waves using DBD Plasma Actuators"** by **Ram Krishan Shukla** in fulfillment of the requirements for the degree of **Master of Science**.

Dated: October 21, 2013

Supervisors:

Dr.ir. Marios Kotsonis

Ir. Stefan Pröbsting

Prof. Dr. ir. L.L.M. (Leo) Veldhuis

Dr.ir. B.W. (Bas) van Oudheusden

Dr.ir.Daniele Ragni

Acknowledgements

This thesis is dedicated to the memory of my mother, Late Champa Shukla (1956-2011), who had the greatest influence on my life. The words are not enough to describe my mother's contribution to my life and career. I owe every bit of my existence to her.

To start with I would like to offer my sincerest gratitude to my supervisor, Asst Prof Marios Kotsonis, who has supported me throughout my thesis with his patience and knowledge, whilst allowing me the freedom to implement my ideas within the defined scope of my research topic. One simply could not wish for a better and friendlier supervisor. I would also like to thank Stefan Pröbsting for the support and confidence he has shown in me. His knowledge and work ethics have deeply inspired me and helped me in times when the end of this work seemed very far.

A special mention should go to my friends and batch mates especially Ankur, Tanmay, Anurag, Saurabh, Siddharth, Nitin, Abhineet, Darwin, Ashish, PKG, Varun, Gaurav, Nakul-Sujaya and Aritra without whom it would have been difficult to complete my studies within 2 years.

Finally, a very special thanks to my family who have always supported me in everything I did, and encouraged me to follow my dreams. Their support and encouragement has been instrumental in overcoming several hurdles in my life.

Nomenclature

0.1 Symbols

Symbol	Unit	Definition
U_∞	m/s	Freestream velocity
u_{rms}	m/s	Fluctuating streamwise velocity
v_{rms}	m/s	Fluctuating normal velocity
u_f	m/s	velocity fluctuations in the x direction
v_f	m/s	velocity fluctuations in the y direction
$\overline{uu}$	m^2/s^2	Normal Reynolds stress in x direction
$\overline{vv}$	m^2/s^2	Normal Reynolds stress in y direction
$\overline{uv}$	m^2/s^2	Shear Reynolds stress
α	deg	Angle of attack
δ^*	mm	Displacement thickness
θ	mm	Momentum thickness
H	-	Shape factor
c	mm	chord
f_r	Hz	Resonating frequency
V_{app}	kV	Applied voltages
l_l	cm	Lower electrode length
l_u	cm	Upper electrode length
l_{act}	cm	Actuation length
t_d	mm	Dielectric thickness
f_{ac}	Hz	Carrier frequency
Re	$-$	Reynolds number based on chord length
$f_\#$	-	Aperture number
Δt	μs	Pulse separation
N_{PIV}	-	Number of PIV samples
N_{mic}	-	Number of microphone samples
$f_{s_{PIV}}$	Hz	Sampling frequency of PIV
$f_{s_{mic}}$	Hz	Sampling frequency of microphone

0.2 Abbreviations

AWC	Active wave cancellation
DBD	Dielectric Barrier Discharge plasma actuator
FIR	Finite Impulse Response
IIR	Infinite Impulse Response
PIV	Particle Image Velocimetry
RMS	Root Mean Square
LPF	Low Pass Filter
FOV	Field of View
PSD	Power Spectral Density
T-S	Tollmien-Schlichting
LMS	Least Mean Square
FXLMS	filtered-x LMS algorithm

Summary

Understanding, predicting and controlling laminar to turbulent transition is of great interest due to the wide range of practical applications where transition is significant. Generally, turbulent flow has an order of magnitude higher skin friction. Fuel savings of up to 25% would be possible for a large commercial aircraft if laminar flow could be maintained over the wings. At low to moderate Reynolds number several types of airfoils show the development of Tollmien-Schlichting (T-S) instabilities. These T-S waves become the dominant cause of transition which is further amplified by an adverse pressure gradient.

Natural T-S instabilities occur randomly as wave packets. Effective damping can only be achieved by a closed loop feed-forward control algorithm. The current work presents an experimental study on active control of natural T-S waves developing on the suction side of an NACA 0012 airfoil. A closed-loop control system has been implemented using the filtered-x Least Mean Squares adaptive algorithm based on Finite Impulse Response filters. Surface mounted microphones are used as sensors. The controller drives a Dielectric Barrier Discharge plasma actuator placed along the span of the airfoil. In contrast to the conventional sinusoidal signal, the actuator is powered using a continuously adapted signal selected by the controller in order to damp the incoming wavetrain of T-S waves. High speed 2-component Particle Image Velocimetry is used to characterize the flow in the vicinity of the actuator. Several cases are tested using both open-loop and closed-loop actuation. Tested freestream velocities range from 17 to 25 m/s at chord Reynolds of 2.2×10^5 to 3.3×10^5 respectively.

Results indicate the suppression of the tonal component of unstable T-S waves with closed-loop actuation. In the case of closed loop control, spectral analysis of error microphones shows the reduction of natural T-S waves up to 7.65 dB, 3.7 dB and 2 dB for freestream velocities 17, 20 and 25 m/s respectively. The RMS reduction of error microphone signals indicates a reduction of approximately 50% for 17 m/s while a significant reduction of approximately 17% and 11% is maintained for freestream velocities 20 and 25 m/s. In the case of open-loop control, the actuation at naturally stable actuation frequencies results in a dampening of instabilities due to the dominant blowing effect of the actuator whereas amplification of instabilities occurs at unstable actuation frequencies. In the open loop, the actuator is operated using non-adapted single-frequency sinusoidal signal.

Table of Contents

List of Figures

List of Tables

Chapter 1

Introduction

1.1 Motivation

In the aviation industry huge effort and great sums of money are invested towards methods of drag and noise reduction. For an aircraft, reduced drag means reduced fuel cost, longer range and higher speed (Gad-el Hak, 2000). Therefore better understanding, predicting and controlling laminar to turbulent transition are of great interest because of the wide range of practical applications where transition is significant. Generally, turbulent flow has an order of magnitude higher skin friction and heat transfer than a laminar boundary layer due to increased mixing between the boundary layer and free-stream flow (Gad-el Hak, 2000). Due to turbulence and the increased momentum transfer towards the wall, resulting in a full velocity profile and therefore a steeper gradient close to the wall, the wall shear stress increases which results in increased viscous drag on aircraft wings. Saric (1994) estimated that fuel savings of up to 25% would be possible for a large commercial aircraft if laminar flow could be maintained over the wings.

For decades, many scientists all around the world are considering the importance of transition. The primary instability arises due to an inflection point in the velocity profile which can further break down into turbulence. At low to moderate Reynolds number several types of airfoils show the development of Tollmien-Schlichting (T-S) instabilities. These T-S waves become the dominant cause of transition which is further amplified by an adverse pressure gradient. Also, these instabilities induce pressure perturbations which propagate over the trailing edge of the airfoil, where acoustic waves are scattered. In the far field these waves are perceived as strong tones and at the same time it contributes to the development of new instabilities on the airfoil through a feedback mechanism. This is controversially discussed in literature. For detail information regarding tonal noise and aero-acoustic feedback loop refer to Paterson et al. (1973), Arbey and Bataille (1983), Desquesnes et al. (2007), Lowson et al. (1994); McAlpine (1997), Chong et al. (2012). It is important to mention that tonal noise mechanism is beyond the scope of this research. From literature Kotsonis et al. (2010), Gmelin et al. (1999), Sturzebecher and Nitsche (2003), the evolution and spatial amplification of T-S waves can be suppressed by using principle of linear superposition principle via means of an active skin consisting sensors, actuators and adaptive controllers. Therefore, the focal point of this research is to investigate active control of natural T-S waves developing on the suction side of the NACA 0012 airfoil.

1.2 Research objective

The aim of this research is to bring AWC using plasma actuators closer to application. This involves the cancellation of natural T-S waves over a NACA 0012 airfoil by a closed-loop control system using the filtered-x Least Mean Squares adaptive algorithm based on Finite Impulse Response (FIR) filters. Surface mounted microphones are used as sensors. The controller drives a Dielectric Barrier Discharge plasma actuator (DBD) placed along the span of the airfoil. In contrast to the conventional sinusoidal signal, the actuator is powered using a continuously adapted signal selected by the controller in order to damp the incoming wave train of T-S waves. In the case of open-loop control, the actuator is operated using non-adapted single-frequency sinusoidal signal. The concept of active T-S wave cancellation is depicted in Figure 1.1. The novel thing about this research is cancelling of natural occurring T-S waves over NACA 0012 airfoil. Natural T-S waves implies that it will have random phase, amplitude and frequencies which makes the control task more challenging and interesting. Most of the research in the past was focussed on cancelling artificially introduced T-S waves over flat plates or an airfoil.

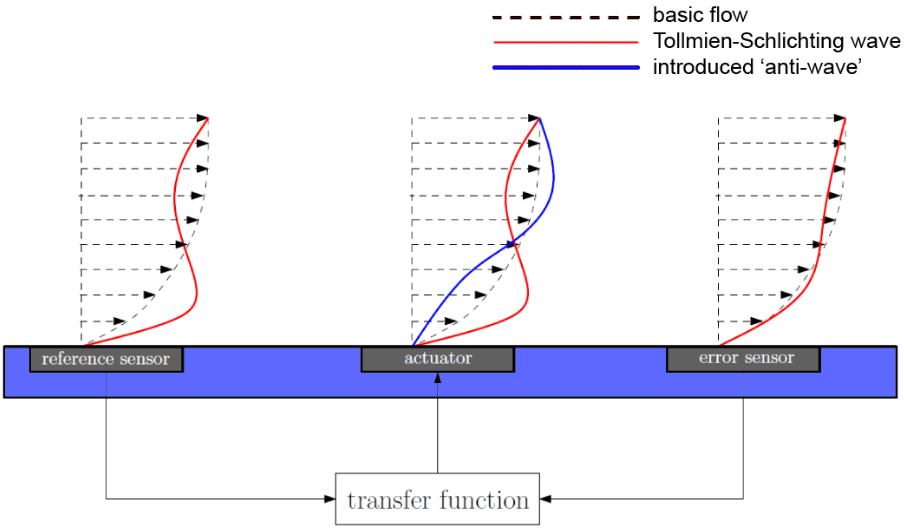

Figure 1.1: Concept of active T-S wave cancellation. Kotsonis et al. (2010)

It is realized that the information of surface pressure fluctuation on the surface of an airfoil will be highly beneficial for the effectiveness of the FXLMS adaptive controller. Therefore, an airfoil has been designed in two parts i.e. top and bottom. A detailed explanation of airfoil model is done under Chapter 4. The isometric view and drawing is depicted in Appendix A. The surface sensor embedded in the airfoil facilitate to use a close loop control in an effective way for attenuating T-S waves using DBD actuator. The controller is built using Labview FPGA. It is a fast real time digital signal processor and expected to reduce the boundary layer instabilities (T-S) on the suction side of an airfoil. It follows the principle of cancelling the T-S waves in their linear stage by superimposition of artificially generated counter waves. The measurement techniques such as high speed 2 component PIV and microphone measurements (surface measurements) are employed to investigate the effect of adaptive control. In addition, an open loop control system is also applied where the actuator is operated using a non-adapted single-frequency sinusoidal signal. Several cases are tested using both open-loop and closed-loop actuation. Tested freestream velocities range from 17 to 25 m/s at chord Reynolds of 2.2×10^5 to 3.3×10^5 respectively.

1.3 Thesis outline

The body of the work is divided in six chapters, summarized below:

Chapter 2 gives an overview of the description of the dynamics of the boundary layer phenomenon, transition roadmap, receptivity, instabilities associated with it and linear stability theory.

Chapter 3 presents the description of the working principles of DBD, its electrical, mechanical properties and its application over the airfoil. Furthermore, the theory of control systems is also presented along with a detailed description of the feed-forward controller.

Chapter 4 presents the description of experimental facility, actuator set up, NACA 0012 airfoil model along with side plates and matrices of experiments performed during the research.

Chapter 5 presents the description of statistical flow properties for the actuation conducted in quiescent flow condition, clean configuration, close loop and open loop case. Furthermore, the parametric study on control performance is also presented.

Chapter 6 summarizes the conclusions to the work performed and suggestions for further research.

Chapter 2

Boundary layer stability and transition

This chapter is dedicated to the establishment of a clear description and understanding of the boundary layer phenomenon, transition roadmap, receptivity, instabilities associated with it and linear stability theory.

2.1 The boundary layer

In 1904, Prandtl introduced the boundary layer concepts (Anderson, 2005). The concepts bring in some key points. A region near the surface, experienced a frictional effects in the boundary layer. In a region outside the boundary layer, the flow can be assumed to be inviscid. The flow velocity is a function of the normal distance to the surface, from zero velocity on the surface (no-slip condition) up to the full inviscid-flow value (U). The parameters like pressure distribution, free stream flow, surface roughness etc. are dependent for exact velocity profiles. A schematic of the concept is shown in Figure 2.1.

The boundary layer may be laminar or turbulent depending on the Reynolds number. Also, the boundary layer thickness grows as the flow moves over the body. This means more of the flow is affected by the friction as the distance along the surface increases. The presence of friction leads to shear stress at the surface τ_w which acts tangentially to the surface. As mentioned earlier, a shear stress is responsible for skin friction drag. In other words, as the boundary layer thickness δ increases in the downstream direction at which point the flow inside the boundary layer may become reversed. This causes the decelerated particles to move away from the wall and known as separation phenomenon. Therefore, the fluid (decelerated) particles do not always remain inside the boundary layer for all cases.

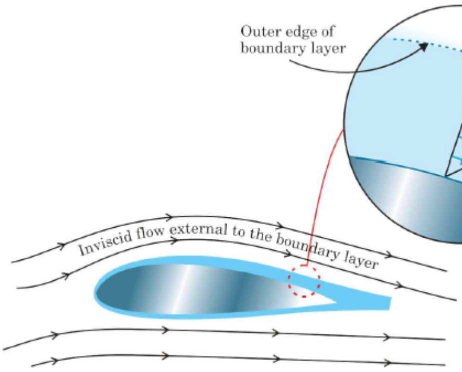

Figure 2.1: Boundary layer phenomenon. Michelis (2012)

The boundary layer parameters like displacement thickness, momentum thickness and shape factor are defined below. These parameters will be used for result analysis.

Displacement thickness:

The displacement thickness physically shows the distance through which the external inviscid flow is displaced by the presence of boundary layer. It is denoted by δ^*. The mathematical form is given by eq 2.1, where u is the flow velocity in the boundary layer and U_∞ is the freestream velocity.

$$\delta^* = \int_0^\infty \left(1 - \frac{u}{U_\infty}\right) dy \tag{2.1}$$

Momentum thickness:

The momentum thickness is referred as the distance the object should move parallel to itself in the inviscid fluid stream in order to get the same momentum as the one existing in the viscous fluid. The momentum thickness is directly related to the drag of an airfoil, since it is proportional to the decrement in momentum flow due to presence of boundary layer. It is denoted by θ. The mathematical form is given by eq 2.2, where u is the flow velocity in the boundary layer and U_∞ is the freestream velocity.

$$\theta = \int_0^\infty \frac{u}{U_\infty}\left(1 - \frac{u}{U_\infty}\right) dy \tag{2.2}$$

Shape factor:

The shape factor (H) defines the nature of the flow and is the ratio between displacement thickness and momentum thickness. It is given by eq 2.3, where δ^* is the displacement thickness and θ is the momentum thickness.

$$H = \frac{\delta^*}{\theta} \tag{2.3}$$

A higher the value of H, stronger the adverse pressure gradient and higher risk of separation. A high adverse pressure gradient can greatly reduce the Reynolds number at which transition into turbulence may occur. For H>2.59 the profile is considered laminar, for H<1.4, the profile is considered turbulent, and for values of H in between, the profile is considered transitional.

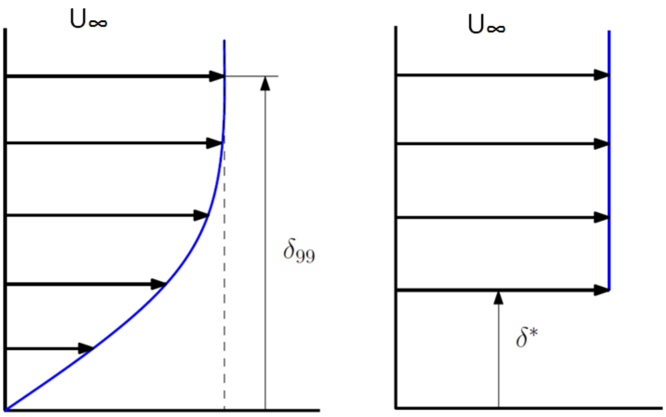

Figure 2.2: Displacement thickness

2.2 Boundary layer transition

The transition phenomenon from laminar to turbulent boundary layer is of fundamental and practical importance. As a result, it has been widely studied. The momentum loss and energy dissipation occurs due to high mixing in turbulent boundary layers results increased in drag. Generally, turbulent flow has an order of magnitude higher skin friction and heat transfer than the laminar boundary layer due to increased mixing between the boundary layer and free-stream flow by (Gad-el Hak, 2000). The viscous drag experienced by the body in a flow can be reduced by delaying the transition from laminar to turbulent. More important, Hefner et al. (1990) and Joslin (1998) estimated that 50 % of total drag is caused by the viscous drag. Additionally the drag caused by the laminar boundary layer is only the tenth part of the turbulent one. It is well known that the stability, transition, and turbulent characteristics of bounded shear layers are fundamentally different from those of free shear layer (Reshotko, 1976; Morkovin, 1969, 1978, 1983). Free-shear flows, such as jets, wakes, and mixing layers, are characterized by inflectional mean-velocity profiles and are therefore susceptible to inviscid instabilities (Gad-el Hak, 2000).

The type of transition occurs is strongly influenced by the amplitude and spectral characteristics of the disturbances inside the laminar viscous layer whereas in the external flows, the transition occurs because of an incipient instability of the basic flow field (Reshotko, 1976). Therefore, from aforementioned studies, it is quite evident that the transition from laminar to turbulent flow takes place due to the instability occurrence in the flow field. There are many parameters that may affect transition. The identification of these parameters provides insight for controlling the boundary layer. Transition from laminar to turbulent flow is influenced by Reynolds number, pressure gradient, sound (pressure fluctuations), surface vibrations, turbulence level of the flow, boundary layer suction, surface heating (cooling) and surface roughness. The Reynolds number at which transition begins is defined as the critical Reynolds number Re_{crit}. The predominant view of laminar-turbulent transition was centered around the slow linear amplification of exponentially growing disturbances (the familiar Tollmien-Schlichting (T-S waves), preceded by a receptivity process to the disturbance environment and followed by secondary instabilities, further non-linearity and finally a breakdown to a recognizable turbulent flow.

The flow development over an airfoil surface is quite complicated.

The demand of boundary layer control techniques depends on the properties of the specific boundary layer and its dispersion characteristics as well as nature of external disturbance and the receptivity of the boundary layer. The dispersion characteristics of boundary layer depends on various parameters like Reynolds number, wave number, span-wise and stream-wise pressure gradients. If the boundary layer is non-receptive then it will be impossible to control them. Moreover, Morkovin (1969) explained the receptivity phenomenon as the free-stream disturbances (such as sound or vorticity) unsteady fluctuation of the basic state enter into the boundary layer. These disturbances may transfer energy to the boundary layer and establish boundary-layer instability waves that may amplify and attain amplitudes far above those of the external disturbances resulting an ending with the transition of the boundary layer. Therefore, receptivity is also described as the coupling between the ambient disturbances and the boundary-layer instabilities.

Transition roadmap

A transition roadmap is portrayed in Figure 2.3. The initial amplitude increases schematically from left to right. For infinitesimal disturbances (path A) natural transition occurs, described by the (T-S waves). The next step in the transition process is the interaction between the different Λ vortices. In regions with a high amount of shear these vortices start to breakdown. In the flow state that is then produced, turbulent spots start to form at random locations and times. As visualized in Figure 2.3, turbulence spreads downstream from these turbulent spots and entrails the air that is still in transition from a laminar to turbulent state. The turbulent spots start to merge and the entire boundary layer becomes turbulent. In case of strong free-stream disturbances, it follows path E, where the growth of linear disturbances is bypassed and turbulent spots or secondary instabilities occur and the flow quickly becomes turbulent. The large amplitudes can also be achieved through transient growth when the boundary layer is provided with appropriate initial conditions. Therefore depending on amplitude, transient growth can lead to span-wise modulations of 2-D waves (path B), direct distortion of the basic state which leads to secondary instabilities (path C), or direct bypass (path D). But an important point to note is that Figure 2.3 narrows the definition of bypass to those mechanisms that resist successful modelling by linear or secondary instability theory. However, the research project focuses on the transition process of path A. Once T-S waves reach a sufficient amplitude, 3-D instability effects (secondary mode disturbances) started appearing in the flow and they are not predicted by linear stability theory. Klebanoff et al. (1962) investigated process thoroughly and referred these disturbances as Λ vortices. Λ vortices are of three types K-type, C-type and H-type. The K-type vortices are the strongest and can reach an amplitude of approximately 1 % of the free-stream velocity. They also have the same stream-wise frequency as the TS waves, whereas the other types of vortices are sub-harmonics of these waves. The fundamental definition of T-S wave and K-H instability wave is mentioned below:

Tollmien-Schlichting waves

The predominant view of laminar-turbulent transition was centered around the slow linear amplification of exponentially growing disturbances (the familiar Tollmien-Schlichting (T-S) waves), preceded by a receptivity process to the disturbance environment and followed by secondary instabilities, further non-linearity and finally a breakdown to a recognizable turbulent flow.

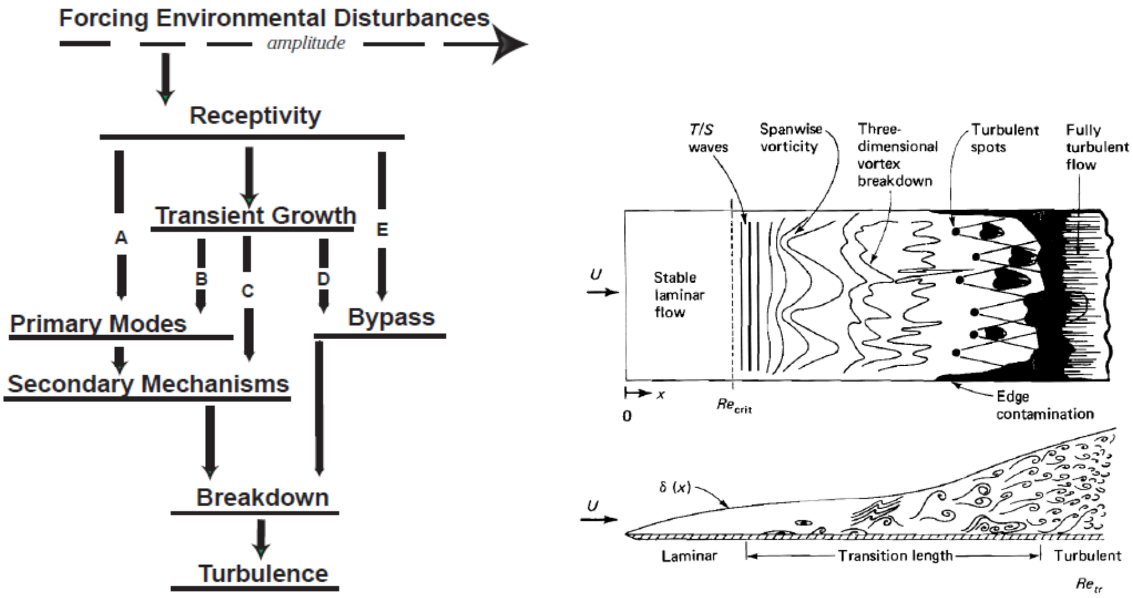

(a) (b)

Figure 2.3: Showing (a) roadmap of transition phenomenon. Morkovin et al. (1994),(b) transition process for path A. White (2006)

Historically, the ideas of Prandtl were extended by Heisenberg (1924), Tollmien (1929), and Schlichting (1933) by the use of asymptotic solutions to the Orr-Sommerfeld equation. The existence of the viscous instability waves was confirmed experimentally (Schubauer and Skramstad, 1948). Eventually the names of Tollmien and Schlichting were associated with the viscous instability mechanism and today this mechanism is called the Tollmien-Schlichting (T-S) instability. The historical development of this work is given by (Schubauer and Skramstad, 1948). It should be mentioned that not all the shear-layer instabilities are T-S instabilities. We reserve the T-S appellation for the viscous instability (Reshotko, 1976). These are stream-wise travelling structures of span-wise oriented vorticity. These waves exhibits periodic velocity fluctuations, whose amplitude grows in the downstream direction.

The instability (T-S waves) is called viscous because the boundary-layer velocity profile is stable in the inviscid limit and thus, an increase in viscosity (a decrease in Reynolds number) causes the instability to occur (Reshotko, 1976). Due to viscosity, it establishes no slip condition on the surface which in turn creates the Reynolds stress which may destabilize the flow. Therefore, flow which is stable to purely inviscid disturbances may be unstable to viscous disturbances. Therefore, it will be right to say that the actual distribution of Reynold stress throughout the boundary layer will determine whether a particular disturbance is stable or not.

The two-dimensional travelling waves (TollmienSchlichting waves) are the most dangerous for incompressible-flow instability and become unstable when the Reynolds number exceeds a critical value. However, as soon as the T-S waves are amplified, gain a certain amplitude, and non-linear effects take hold, three-dimensional disturbances can no longer be excluded (Gad-el Hak, 2000). These three dimensional disturbances start to form vortices, which subsequently break up and form single turbulent spots in the boundary layer. These spots then develop into a fully turbulent flow. Since, their defined structure and periodic behaviour (compared to later stages of boundary layer transition), T-S waves can be easily manipulated. If compressibility effects can be neglected, then they travel in a mean flow direction. Generally when the local Reynolds number based on boundary-layer quantities is sufficiently high, the natural transition of an attached boundary layer is caused by amplification of T-S wave and very quickly amplify to three dimensional effect (turbulent spots).

Grundmann (2008) shows a typical example of a T-S wave measured is depicted in Figure 2.4. The standard deviation of the velocity fluctuations, u_{rms}, is shown normalized with the free stream velocity at the downstream position, U_{be}, and this profile exhibits a typical footprint of T-S waves: the small maximum at a height of one boundary-layer thickness δ_{99}, a minimum just below it and a strong increase of the turbulence near the wall. Simple and clean TS waves of the fundamental frequency would cause just one single maximum near the wall at about y/δ_{99}=0.2.

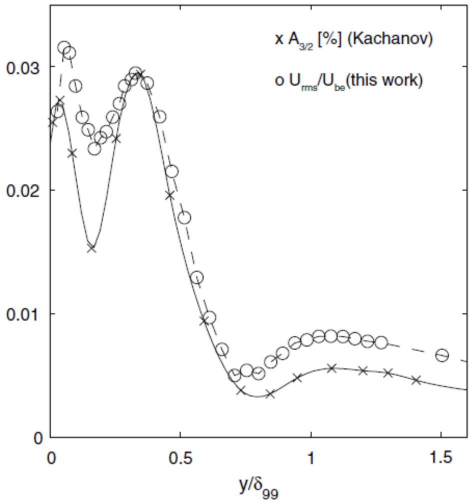

Figure 2.4: Turbulence level profile (U_{rms}) showing T-S wave. Grundmann (2008)

Kelvin-Helmholtz instability

It belongs to the category of inviscid-type instabilities. It is also known as K-H instability. These are formed when one fluid layer is on top of another fluid layer moving with a different velocity. It takes the form of small waves that can eventually grow into vortex rollers. If the boundary layer separates, it will develop as a result of the separated inflectional velocity profile. Since this instabilities causes the shear layer to roll up, it might be expected that the unsteadiness in the separation bubble will be dominated by large-scale vortex shedding and not small scale turbulence. In the low disturbance free stream environment, within separated flow region, small amplitude disturbances grow exponentially by means of K-H inviscid instability leading to roll up vortices in the separated shear layer by (Burgmann et al., 2006; Burgmann and Schröder, 2008),(, n.d.; Brendel and Mueller, 1988), (Yarusevych et al., 2006, 2009).

2.3 Acoustic effect on instability

At low to moderate Reynolds number several types of airfoils show the development of T-S waves. These instabilities induce pressure perturbation which propagates over the trailing edge of an airfoil and thus acoustic waves are scattered. In the far field these waves are perceived as strong tonal noise and at the same time it contributes to the development of new instabilities on the airfoil through a feedback mechanism. The phenomena are allied with noise spectrum to the laminar boundary layer instabilities that lead to the term laminar boundary layer instability noise. The particular features of boundary layer instability noise have been reported in literature, but remain controversial to date. For detail information regarding tonal noise and aero-acoustic feedback loop refers to Paterson et al. (1973), (Arbey and Bataille, 1983), Desquesnes et al. (2007), Lowson et al. (1994); McAlpine (1997), Chong et al. (2012).

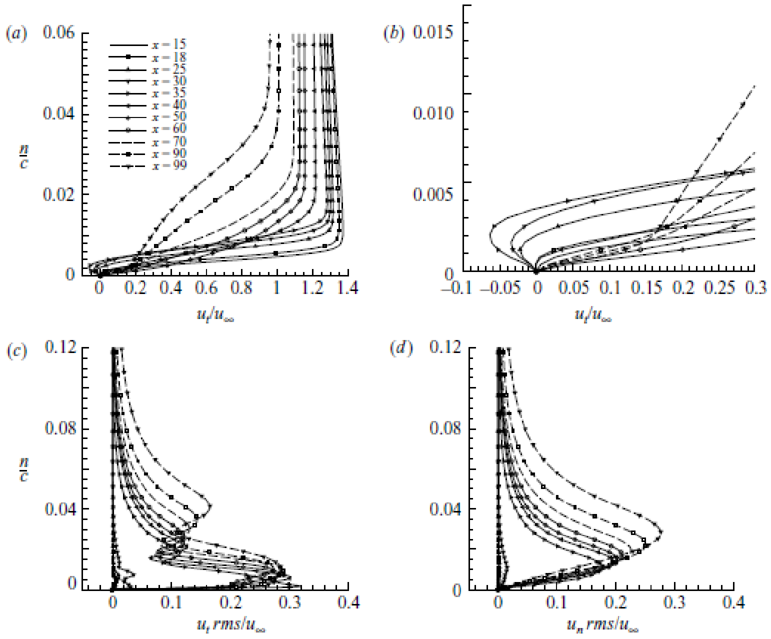

Figure 2.5: Mean and rms profiles of Case 2 suction side where n is the distance to the wall and x is percentage of chord. Desquesnes et al. (2007)

According to Desquesnes et al. (2007) double peak structure in the profile of velocity fluctuations interpreted as evidence for convecting instabilities of T-S waves. Also, the mean velocity profiles in the suction side depicts an inflection point at the most upstream stations but unlike the pressure side boundary layer close to the trailing edge reverse flow cannot be observed at the chosen stations as shown in Figure 2.5. Overall the tonal noise study is beyond the scope of research. But while carrying out the experiment, it is made sure that tonal noise is eliminated. As from the literature, the main feedback loop occurs between the boundary layer on the pressure side and the acoustic source owing to the interaction of the T-S waves with the trailing edge results tonal noise. Therefore, a zig-zag tape is applied on the pressure side of an airfoil, which basically breaks the feedback loop and results in elimination of tonal noise.

2.4 Linear stability theory

The perturbation enters into the boundary layer are being transformed into small amplitude waves. They are either linear damped or amplified while propagating downstream. A common way to investigate the hydrodynamic stability of a boundary layer is by means of the Orr-Sommerfeld equation. The idea behind the Orr-Sommerfeld equation is to add a disturbance in the basic flow state and then a disturbance equation is derived and a series of simplifications are performed. A parallel / incompressible base flow is assumed in combination with two dimensional T-S waves. It results fourth-order linear homogeneous equation, better known as the Orr-Sommerfeld equation:

$$(U-c)(\frac{\partial^2 v}{\partial y^2}-\alpha^2 v)-\frac{\partial^2 U}{\partial y^2}v+\frac{iv}{\alpha}\left(\frac{\partial^4 v}{\partial y^4}-2\alpha^2\frac{\partial^2 v}{\partial y^2}+\alpha^4 v\right)=0 \tag{2.4}$$

In eq 2.4 U is the velocity profile, c represents wave speed, α is the wave number and v is the T-S wave shape. So, this equation finally results into eigen value problem where α is eigen value and v is the eigen function. The Orr Sommerfeld equation is a linear homogeneous equation, so the linear superposition principle can be applied in this. It holds validity for the linear stage of amplification process. As the disturbance grows stronger, non-linear effects started to appear, that are not predicted by the Orr Sommerfeld equation. In the laminar boundary layer, the two dimensional disturbances are described by stream function

$$\psi(x,y,t)=\phi(y)e^{i(\alpha x-\omega t)} \tag{2.5}$$

The disturbance velocity components $u^{'}, v^{'}$ are calculated from the equation below:

$$u^{'}=\frac{\partial\psi}{\partial y}; v^{'}=-\frac{\partial\psi}{\partial x}. \tag{2.6}$$

In spatial mode of the stability analysis we take the circular frequency ω to be real and the wave number α to be complex.

$$\alpha=\alpha_r+i\alpha_i \tag{2.7}$$

Combining equation 2.5 and 2.7 results

$$\psi(x,y,t)=\phi(y)e^{-\alpha_i x}e^{i(\alpha_r x-\omega t)} \tag{2.8}$$

In equation 2.8, α_i determines the stability of the flow. The criterion is mentioned below:

- $\alpha_i < 0$: the disturbance grows and becomes unstable;
- $\alpha_i > 0$: the disturbance decreases and becomes stable;
- $\alpha_i = 0$: the disturbance stays constant and becomes neutral.

The stability of the flow is mainly dependent on the shape of the velocity profile (concave profile is less stable), the frequency of the disturbance (ω) and Reynolds number based on δ,θ and δ^*. The results from the Orr-Sommerfeld equation can be visualized by plotting contours of α_i for different

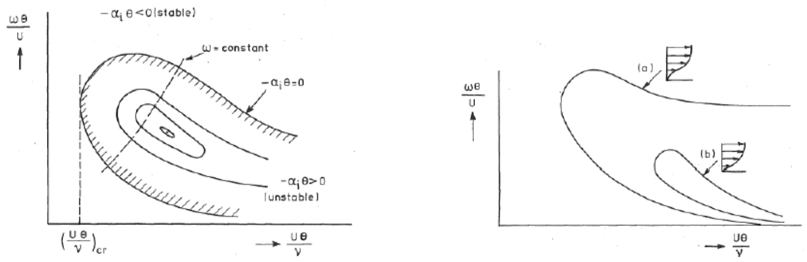

Figure 2.6: Stability diagram (left) and the influence of the velocity profile on the stability diagram. Veldhius (2012)

Reynolds number and different wave frequencies as depicted in Figure 2.6. The stability diagram depicted in Figure 2.6, acted as the input for the e^n method that was developed by Van Ingen and Smith. It calculates the growth of T-S waves in an incompressible two dimensional boundary layer and provides the estimation of the region where the transition occurs in less time. The amplitude a of a disturbance can be computed as function of x as soon as stability diagrams for various x-values are available. Using eq 2.8 it follows that the ratio of the amplitude $a + da$ at position $x + dx$ to the amplitude a at position x is given by

$$\frac{a + da}{a} = \frac{e^{-\alpha_i(x+dx)}}{e^{-\alpha_i x}} = e^{-\alpha i dx} \tag{2.9}$$

or can be written as

$$d(lna) = -\alpha_i dx \tag{2.10}$$

After integrating eq 2.10, we get

$$\sigma_a = ln(\frac{a}{a_0}) = \int_{x_0}^{x} -\alpha_i dx \tag{2.11}$$

where x_0 is the value of x at which the disturbance with frequency ω first becomes unstable and quantity σ_a represents an amplification factor.

Chapter 3

Flow control

In general, the demand of active wave cancellation techniques depends on the properties of the specific boundary layer and its dispersion characteristics as well as nature of external disturbances and the receptivity of the boundary layer to them. Therefore, this chapter concentrates on the description of the active flow control strategy, DBD plasma actuator, theory of control system and adaptive FXLMS feed forward controller.

3.1 Physical background

Flow control means manipulating of particular flow field to achieve a desired effect. The control strategies are classified in several ways depending on the character of flow instabilities, presence or lack of walls, Reynolds number and Mach numbers. Generally, the aim of control strategy is to reduce drag, enhancing the lift, augmenting the mixing of mass, momentum or energy, suppress the flow induced noise or combination thereof (Gad-el Hak, 2000). The engineering goals and scheme of flow control strategies are depicted in Figure 3.1. There are active control methods such as jet vectoring using piezoelectric actuator, oscillatory blowing etc requires energy expenditure and passive methods requires no auxiliary power. Passive techniques include geometric shaping to manipulate the pressure gradient, the use of fixed mechanical vortex generators for separation control, and placement of longitudinal grooves or riblets on a surface to reduce drag. In order to cancel the T-S waves over a NACA 0012 airfoil, an active flow control strategy using DBD plasma actuator is chosen because of the benefits of desired effect at less expenditure of power.

For the past years, the researchers around the world focused on cancelling laminar boundary layer instabilities at low to moderate Reynolds numbers. Milling (1981) performed experiment on a flat plate in a water channel. They used vibrating wire to excite the instabilities and applied second wire at the downstream position to cancel the instabilities and succeeded to delay the transition Reynolds number from 5.2×10^5 in the presence of disturbance to 6.7×10^5 using control but complete cancellation of instabilities was not accomplished due to the growth of 2D instability to 3D disturbances before reach-

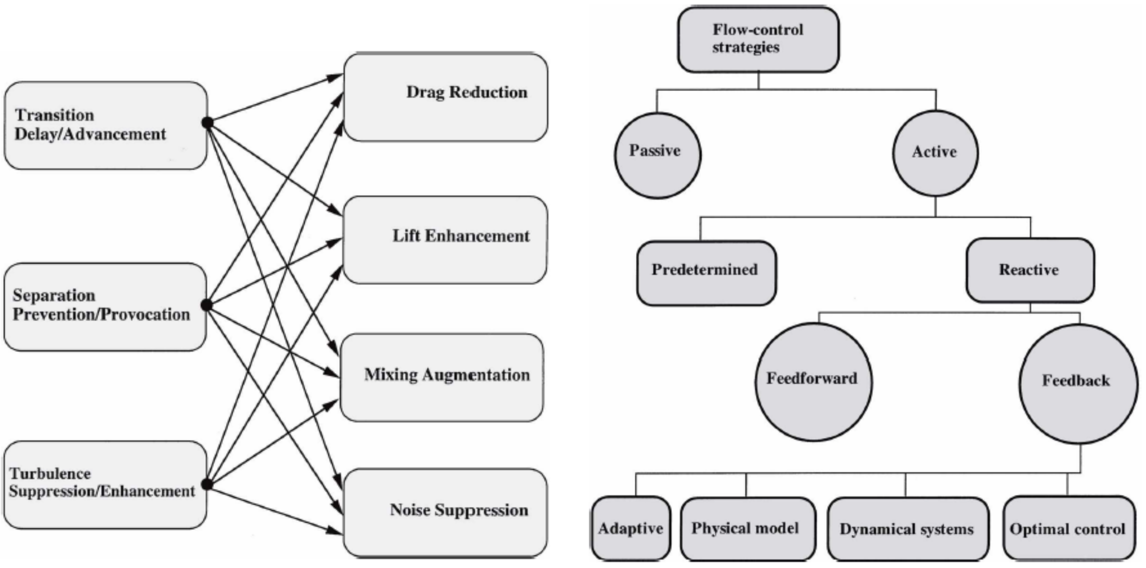

(a) (b)

Figure 3.1: Showing flow control (a) goals, (b) its classification of strategies. Gad-el Hak (2000)

ing control wave generator. Liepmann and Nosenchuck (1982) also performed experiment on a flat plate in the wind tunnel where they excite control waves using heating strips and showed reduction in amplitude of naturally occurring instability waves and also delayed transition from 8×10^5 to 1.1×10^6. Good thermal coupling with water and the strong temperature dependence with water viscosity make wave generation technique easier in water than in air. Thomas (1983) performed a wave cancellation on the flat plate using vibrating ribbons as the disturbance and control wave generator in the wind tunnel. They succeeded in attenuating T-S waves by varying phase and amplitude of the downstream ribbon. But they also observed that the complete cancellation of boundary layer instabilities did not occur due to the formation of three dimensional disturbances. Pupator and Saric (1994) used an active feedback control loop for the cancellation of broad band disturbances and calculated the appropriate counter disturbances with the help of transfer functions based on the fast Fourier transformation and demonstrated a reduction in the broad band instability wave and amplitude. Joslin et al. (1995) with direct numerical simulations using spectral control approach showed the attenuation of T-S waves with a sensor-actuator arrangement on a flat plate. Spectral control adapted amplification and phase shift by the direct conversion of sensor signal measured upstream into an actuating signal. Gmelin et al. (1999) investigated several control techniques and presented successful damping of linear instabilities by means of digital linear filters (FIR filters) and producing significant reductions of linear T-S instabilities and also described the concepts of the non-linear methods for reducing the resonant behaviour of 2-D and 3-D instability modes.

Sturzebecher and Nitsche (2003) demonstrated the successful cancellation of artificially excited T-S waves in a cascade of control actuators on NACA 0008 airfoil of chord 1.3 m at the freestream velocity of 17 m/s. The airfoil has an interchangeable segment $x/c = 0.39 - 0.78$, which allows the integration of different sensor actuator arrangements depending on the experimental application. A 3D source was installed at x/c = 0.3 to generate artificial 2D waves as well as 3D disturbances, such as oblique waves or point source induced instabilities in addition to the investigations on natural T-S instabilities. They use sensors downstream of the first control actuator to detect restarted wave growth. This signal is used to operate a second control actuator to cancel these oscillations. The arrangement is shown in Figure 3.2. For an active T-S wave cancellation, along with a choice of sensors and control algorithm, the choice of actuators is one of the important aspects. The actuator should be selected such that it should be able to generate waves corresponding to the characteristics wavelength and frequencies of T-S instabilities. The response of the actuator should be linear with a time delay that is smaller than the convection time of the T-S waves between reference sensor and actuator. A weak non-linear T-S development degrades the efficiency of the linear control approach. In case of adverse pressure gradient, the transition delay attained by the single-stage attenuation has a little effect. Therefore they performed stream-wise repeated control to yield a profitably extended delay of the turbulent transition on the unswept wing.

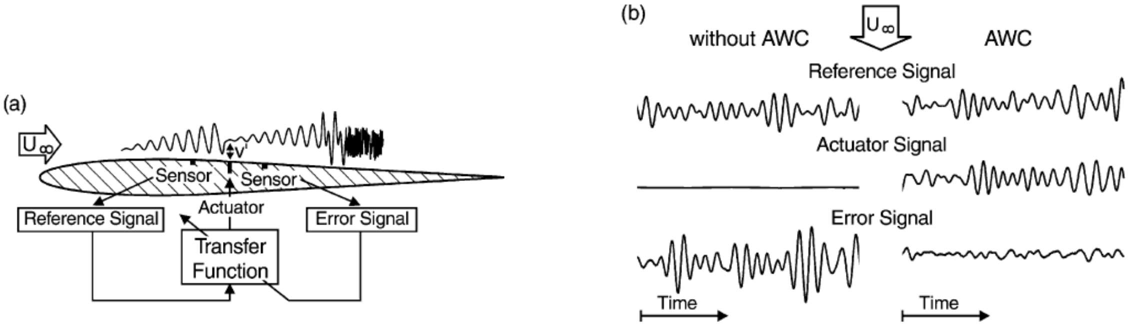

(a) (b)

Figure 3.2: Showing AWC method (a) principle of active T-S wave control, (b) typical sensor and actuator signals with and without control. Sturzebecher and Nitsche (2003)

Grundmann and Tropea (2008) demonstrated the attenuation of T-S waves (artificially introduced by excitation actuator) using one or two plasma actuators downstream of the excitation actuator by imparting steady and unsteady forces into the boundary layer. They concluded that the active wave control cannot be achieved successfully if no distinct frequency waves are present in the boundary layer or if the waves are not parallel to the electrodes. Kotsonis (2012) used filter x-LMS (FXLMS) adaptive algorithm for controlling T-S waves by DBD actuators on a flat plate. The system mainly comprises of the reference sensor (upstream of an actuator), error sensor (downstream of an actuator), actuator and adaptive control algorithms using FIR filters. The incoming instabilities are sensed by a reference sensor whereas error sensor placed downstream of the actuator in order to sense the instabilities after manipulation. The reference signal is directly calculated into an actuator signal by means of transfer function. The transfer function is continuously adapted to minimize the error signal. Therefore, the present research will be focus to cancel the T-S waves over NACA 0012 airfoil using DBD plasma actuator by means of closed loop feed-forward control(FXLMS) working in real time.

3.2 DBD plasma actuator

Dielectric Barrier Discharge Plasma Actuators (DBD) belong to the category of active flow control. They are cheap, easy to manufacture, do not require any mechanical or moving parts, have a very fast response, consume very little energy. Most importantly they do not affect the shape of the aerodynamic element on which they were applied for controlling the flow.

3.2.1 Working principles

The DBD flow control devices have been referred as plasma actuators by Cavalieri (1995), Post et al. (2001); Corke et al. (2002). It consists of two electrodes separated by a dielectric material. One of the electrodes is typically exposed to the air. The other electrode is fully covered by the dielectric material. When a high AC or DC voltage is passed, as a result of gaps between these two electrodes, electrons are formed by photo ionization. Electrons accelerated towards the anode under electric field and ionize the gas by collisions with neutral molecules. Discharge current results due to multiplication of electrons and drifting of cathode to the anode. The plasma in this case refers to the ionized air that forms over the electrode area covered by the dielectric as shown in Figure 3.3.

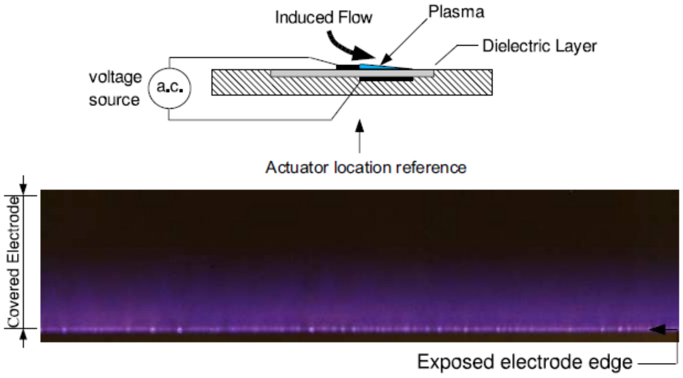

Figure 3.3: Schematic representation of SDBD plasma actuator (top) and photograph of ionized air at 1 atm pressure that forms over electrode covered by dielectric layer (bottom). Corke et al. (2007)

Langmuir (1926) denoted a plasma region of a gas discharge in which the number of electrons and ions are equal. Kunhardt (2000) defined plasma region to a system of particles whose collective behaviour is characterized by long range coulomb interactions. The definition from Kunhardt (2000) reflects the new property (as collisional) of plasma which has a profound effect on the momentum transfer process associated with the plasma actuation process. It refers that electron neutral collision frequency is of the order of or greater than the driving plasma frequency.

Another type is cold plasma discharges in which an electric field of sufficient amplitude is applied to a volume of gas to generate electron ion pairs through electron impact ionization of the neutral gas by

(Kunhardt and Luessen, 1981; Kunhardt, 1980; LLewellyn, 1966; Raizer et al., 1991). An alternating current or direct current is applied to the electrodes and the electric field is established. By increasing the amplitude of the field above the breakdown field, E_b (essential for sustaining electron-ion pairs in the gas in the absence of space charge fields) by (Kunhardt and Luessen, 1981; Kunhardt, 1980; LLewellyn, 1966; Raizer et al., 1991), resulting generation of plasma. The optimum AC frequency generally depends on the static pressure and the particular gas.

In the electrode gap, plasma is generated through a succession of micro-discharges which are randomly distributed in space and time. Streamer velocity ranges between $10^7 - 10^8$ m/sec and their width of 100 μ m with a duration of a few ns. Roth et al. (2000) used the following configurations as shown in Figure 3.4 i.e. Surface DBD where they demonstrated that the discharge induces a secondary airflow of several m/sec tangentially to the wall also measured velocity profiles above the surface discharges shown in Figure 3.6. Increasing applied voltage results increase in resulting force up to 11 mN. The secondary airflow can modify the free air stream and reduce the drag effectively.

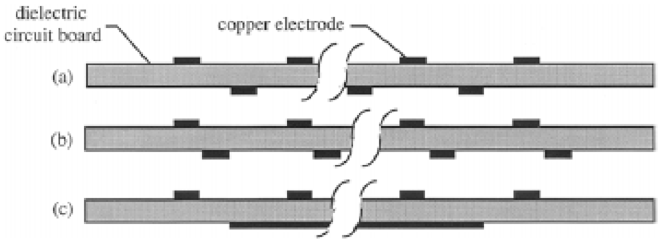

Figure 3.4: Plasma panel design concepts (a) symmetric staggered, (b) asymmetric staggered, (c) symmetric planar lower electrodes. Roth et al. (2000)

The most popular and used DBD actuator is shown in Figure 3.5 which consist of single actuator. It comprises of two plane electrodes flush mounted on both sides of a dielectric plate. One of the electrodes is grounded as shown above and another one is excited by an AC high voltage (usually a sine wave form). When the voltage surpasses the ignition voltage V_0, at the given conditions, a plasma sheet appears on both sides of dielectric. The generation of plasma sheet results in an electric wind on both sides of a dielectric as shown in Figure 3.5. Their mechanical and electrical properties strongly depend on following parameters such as electrode gap (g), the nature of dielectric, dielectric thickness (t) and electrode width (w_A and w_B) as depicted in Figure 3.6.

3.2.2 Electrical properties

Pons et al. (2004, 2005) demonstrated discharge current versus time for surface plasma actuator (in case of sine HV). They explained that discharge current comprises of short pulses appearing at the beginning of each inversion of polarity corresponds to plasma formation on both sides of the dielectric. Each pulse corresponds to a micro-discharge or streamers. In order to separate well the positive and negative half cycles, frequency is kept low. The electrode gap is g = 5 mm, the electrode length is equal to 20 cm, V = 20 kV and f = 300 Hz. The current pulses due to streamers are negative during positive voltage half period and positive during negative voltage half period by Enloe et al.

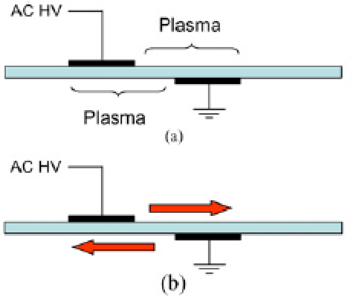

Figure 3.5: Schematic side view of a single DBD actuator, (a) area of plasma, (b) electric wind direction. Moreau (2007)

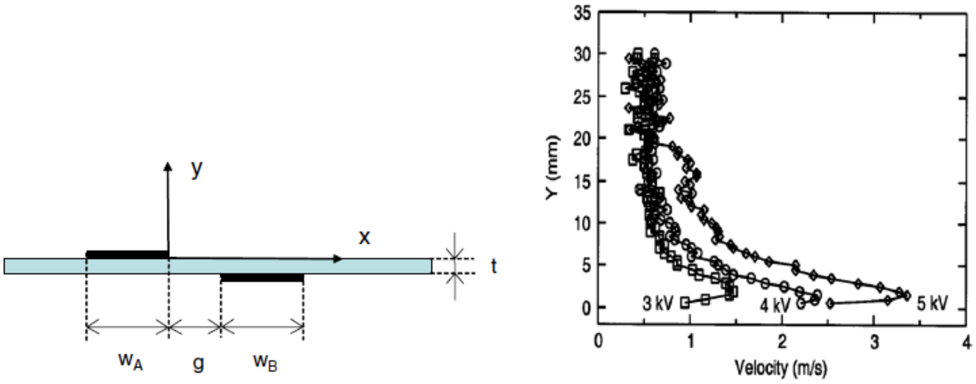

(a) (b)

Figure 3.6: Showing (a) geometrical electrode configuration of a single DBD actuator. Moreau (2007), (b) DBD plasma-induced velocity in still air. Roth et al. (2000)

(2006), Orlov et al. (2006). The grounded electrode must be encapsulated in a dielectric in order to prevent plasma formation below the dielectric. This configuration results plasma formation only on the upper side of the dielectric, near the air-exposed electrode. They also showed that during the positive half period, plasma is composed of a set of micro-discharges and plasma are more homogeneous during the negative half cycle. Therefore, the plasma is different during the negative and the positive half-cycles.

A few studies have been done in order to compute electrical power consumption. The electrical power is computed by multiplying the energy per period (area of the diagram corresponds to energy per period) with waveform frequency. For actuator configuration (5 mm-thick glass dielectric, electrode length 20 cm, f = 300 Hz), electrical power consumption versus applied voltage is shown Figure 3.7. It depicts that under this geometrical and electrical conditions, electrical power increases as a parabolic function $P_{el} = K \times (V - V_0)^2$. Roth and Dai (2006) confirmed the same trend of power in different geometrical and electrical condition. For thinner dielectric materials, Enloe, McLaughlin, VanDyken, Kachner, Jumper and Corke (2004); Enloe, McLaughlin, VanDyken, Kachner, Jumper,

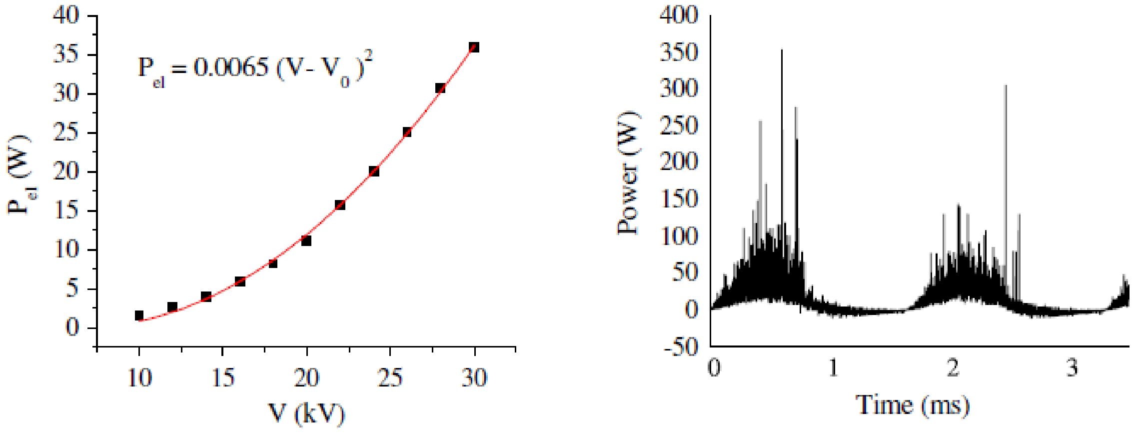

(a) (b)

Figure 3.7: Power consumption for surface DBD (a) time-averaged electrical power consumption,where V_0 is the minimum voltage to ignite the discharge, (b) instantaneous electrical power consumption versus time. Moreau (2007)

Corke, Post and Haddad (2004) found slightly different trend of power. Therefore, we can assume that the electrical power consumption of the surface DBD is in the same order of magnitude as the surface corona. However, the instantaneous power versus time is completely different. The power peaks up to 350 W, whereas the current peaks were strongly limited by the power supply as illustrated in Figure 3.7.

3.2.3 Mechanical effects

There are three different parameters which describe its effects over the mechanical behaviour of actuator i.e. electric wind velocity, mechanical power and electric force. DBD induced velocity is measured by the University of Tennessee as illustrated in Figure 3.8. Pons et al. (2004) by means of glass pitot tube along x and y axes and modifying several parameters such as the applied voltage, frequency, electrode gap, dielectric thickness and dielectric nature, measured velocity profiles in the absence of a free air stream. The following observations were made:

- The velocity induced by the HV electrode slightly greater than the induced by the grounded electrode (when it is not encapsulated).
- As for the surface corona, the momentum comes from the region placed above the air exposed electrode, meaning that the discharge induces a depression towards the wall.
- The maximum velocity is always reached at the limit of the plasma extension, usually placed at the downstream edge of the grounded electrode.

- The maximum velocity increases linearly with applied voltage which is usually at about 0.5 mm from the wall. This is obtained at low frequency (from 300 to 700 Hz) and up to 20 kV.

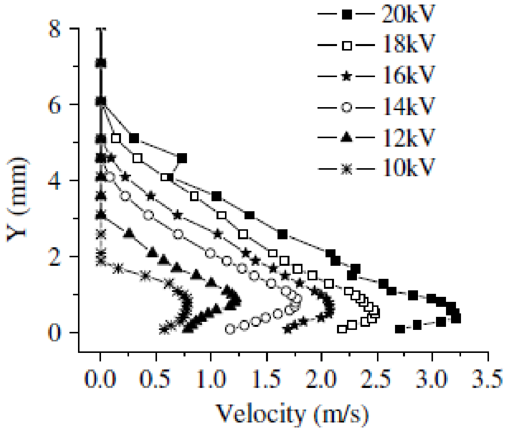

Figure 3.8: Typical velocity profiles measured with a glass Pitot tube for different voltages. Moreau (2007).

Forte et al. (2006) performed a study in order to increase the induced velocity. The induced velocity increases up to 8 m/sec present the maximum velocity at approximately y=0.5 mm. These induced velocities are a function of electrode gap g and the encapsulated electrode width w_B. From studies it can be concluded that the optimum electrode gap is 5 mm, because if g is bigger than the electric field may fall down and space charge cannot continue anymore to move towards the downstream electrode. It is depicted in Figure 3.9.

With the same actuator, keeping an electrode gap (g)=0 and increasing the width of the encapsulated electrode by a small amount. It is observed that the velocity increases with the electrode width and reaches a plateau. The wider the electrode is, the farther the plasma can expand. Thus ions are accelerated for a longer distance and resulting in a velocity increase. The dissipative phenomenon makes the plasma self-sustaining and it cannot expand more than about 20 mm. Enloe, McLaughlin, VanDyken, Kachner, Jumper, Corke, Post and Haddad (2004) presented that with the increase of voltage and frequency, induced velocity also increases, but their behaviour of the curves is completely different. It is depicted in Figure 3.9. The mechanical power is computed by the equation given below under the assumption of a stationary flow:

$$P_{mech} = \frac{1}{2}\rho L \int_0^{\infty} V_G^3(y)dy \tag{3.1}$$

where L is electrode length, V_G is the airflow flow velocity. The electro-mechanical efficiency in the absence of a free air stream may be computed by relation given below:

$$\eta = \frac{P_{mech}}{P_{elec}} \tag{3.2}$$

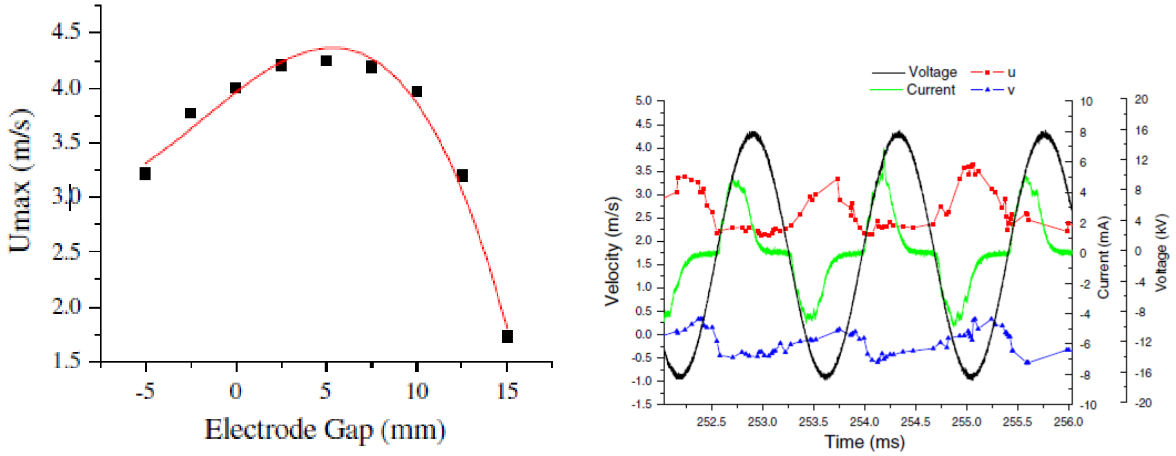

(a) (b)

Figure 3.9: Showing (a) maximum induced velocity versus electrode gap, (b) synchronized records of voltage, current, horizontal velocity (u) and vertical velocity (v) of the surface DBD-induced velocity versus time (current is here filtered by a 10 kHz low-pass filter). Moreau (2007)

Moreau and Touchard (2005), Van Dyken et al. (2004) demonstrated that the DBD efficiency is lower than the corona one even when the grounded electrode is encapsulated. One of the important characteristics of plasma operation is produced thrust. Roth et al. (2000) measured the electric force due to the space charge displacement inside the plasma. Recently Van Dyken et al. (2004) performed studies in order to demonstrate the net force produced by a single actuator. They investigated the influence of several parameters (signal waveform, signal frequency, electrode geometry electrical power consumption) on induced net force. The major conclusions from their studies are presented below:

- The waveform is of great importance in the net force. In fact, the positive saw tooth waveform produces the greatest net force for a given input power.
- The optimum frequency is 5 kHz (under their conditions).
- At 5 kHz, the maximum net force is about 0.9 g for an electrical power of 55W, i.e. about $16 mgW^{-1}$.
- Thicker dielectric configurations are generally able to produce higher maximum net forces because the dielectric is able to withstand higher currents.

Additionally from recent thrust measurements by Kotsonis (2012):

- The thrust is directly proportional to the carrier frequency.
- The relative frequency lies between 0.15 to 0.20 mN per electrical W.
- The force induced by a positive pulse is greater than the one induced by a negative pulse.

3.3 Theory of control system

Active control systems are generally applicable for low frequency range i.e. below 500 Hz. But it does not mean higher frequency range control systems are not built, they suffer from different problems like structural/acoustics (complex vibrations, radiated sound fields) and electronics (limited efficiency). Generally, there are two types of control system

- **Open loop control**: A open loop controller is a type of controller that does not use feedback to achieve desired output from the input. In the current research, the system comprises of microphone sensors located at various x/c positions over an airfoil surface. The sensor working principle and its location are described in Chapter 4. In short, the surface sensor detects the pressure fluctuations over the surface of an airfoil, which is read by the software Labview. Reading signals provide information about the frequency of the instabilities. Therefore, the actuator is operated using non-adapted single-frequency sinusoidal signal at constant amplitude of 10 kV and Duty (D) cycle of 100 % in order to demonstrate the behaviour of T-S waves and control of no feedback assistance.
- **Close loop control**: The close loop control system is defined as a type of control that automatically changes the output based on the difference between the feedback signal to the input signal. Under the active control system, there are two major types of active control systems i.e. adaptive filtering (feed-forward or feedback) and waveform synthesis. The focus is mainly on the adaptive filtering feed-forward types. This type of control strategy is used for this research. For detail information regarding waveform synthesis method refers to Hansen (2006). The controllers are mainly divided into two:

3.3.1 Feed-forward controller

The feed forward controller mainly comprises of reference sensor, the control source, error sensor, control algorithm, electronic controller. The simple diagram of feed forward control system is depicted in Figure 3.10 where control source is DBD actuator. The incoming signal is sampled by the reference sensor (microphone), which is then passed to electronic controller where it is filtered to generate the output signal from the control source. The error sensor measured the control effectiveness of the system since it provides a signal to the control algorithm and plays a role in adjusting control signal.

3.3.2 Feedback controller

The feedback controller is preferred over feed-forward controller where it is not possible to sample the incoming instabilities sufficiently to generate required cancelling signal. If it is applied in the case of high frequency noise, it will be difficult to prevent it to become unstable. At high frequency there is a phase shift taking place which is related to the delay and results in conversion of negative to positive feedback. That is why feedback is designed to provide a negative feedback (to reduce the

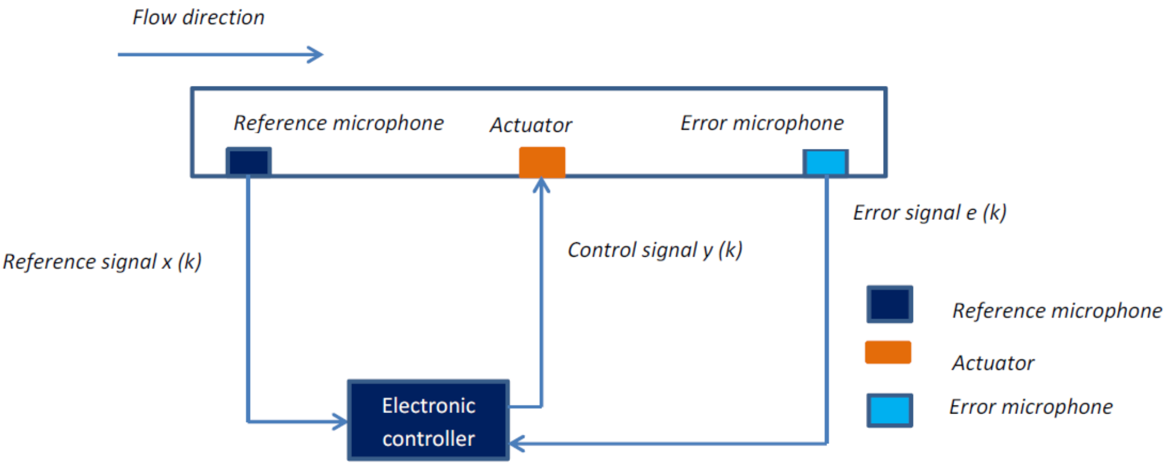

Figure 3.10: Simple diagram representing feed-forward control system

amplitude of the unwanted disturbances) rather than positive feedback. Bandwidth over which control will be effective is limited by the delay in the path between the controller output to loudspeaker and control input from sensors. Bandwidth of effective control is directly proportional to the reciprocal of delay by Hansen (2006). It is depicted in the Figure 3.11. The main difference between feedback and feed-forward controllers are as follows:

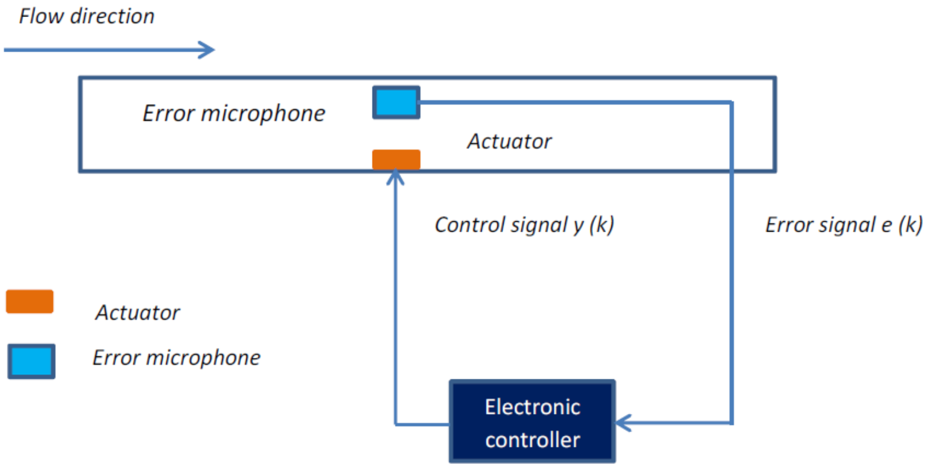

Figure 3.11: Simple diagram representing feedback control system

- In the feedback control, the error signal is processed to generate suitable control signal from control source whereas in feed-forward controller, the error signal is used to optimise the controller performance by minimising the error signal. In this case control signal is generated by processing the reference signal.

- In the feedback, physical system and controller can't be optimised separately and vice versa for feed-forward.
- Feedback systems are better at minimising transient response of the system whereas feed-forward for minimising steady state response.

Electronic control system

The electronic control system is backbone of both feed-forward and feedback control system. Since, FXLMS feed-forward controller is used for the application of cancelling T-S waves. Therefore, a feed-forward electronic controller is described in detailed. They are made up of three major components including two inputs and one output.

- Digital filter: It is also known as control filter and responsible for generating control signal output from the input reference signal. There are two major types of control filters i.e. finite impulse response (FIR) and infinite impulse response filters (IIR). Finite impulse response filters are used where the reference signal is few sinusoids and also where control signal does not corrupt reference signal in any way. These types of filters are suitable for tonal noise problems by (Hansen, 2006). FIR filter structure is an easy to implement and unconditionally stable filter. The output of a FIR filter can directly be calculated from several (previous) time values of the input, whereas in contrary an IIR filter also needs previous time values of the output signal. IIR filter is preferred over FIR filters where the noise to be controlled is broadband in nature, also if the system to be controlled has resonances in the control frequency range and where phase speed is independent of frequency and finally if there is an acoustic feedback from the control source to the reference sensor, leading to the corruption of the reference signal by (Hansen, 2006).
- Adaptation algorithms: It is a component of the controller which tune the digital filter weights in such a way that resulting control signal minimizes the error signal received by the controller. It is also responsible for obtaining the model for cancellation path impulse response (time domain equivalent to frequency domain transfer function). It is used to optimize the FIR or IIR filter weights on-line in active noise.
- Cancellation path transfer function: In order to update the control filter weights via adaptive algorithms, the transfer function between the electrical input to the control source and the electrical output from the error sensor is an input to adaptive algorithm.

3.4 FXLMS adaptive control system

A FXLMS adaptive feed forward controller is designed using Labview FPGA for the application of cancelling TS waves. The controller is inspired by the work Kotsonis (2012) who applied it for cancelling TS wave on the flat plate. The system mainly comprises of the reference sensor (upstream of an actuator), error sensor (downstream of an actuator), actuator and adaptive control algorithm using FIR filters.

3.4.1 Working principle

The incoming instabilities are sensed by a reference sensor whereas error sensor placed downstream of the actuator in order to sense the instabilities after manipulation. The reference signal is directly calculated into an actuator signal by means of transfer function. The transfer function is continuously adapted to minimize the error signal. The controller drives a DBD plasma actuator placed along the span of the airfoil. In contrast to the conventional sinusoidal signal, the actuator is powered using a continuously adapted signal selected by the controller in order to damp the incoming wave packets of T-S waves.

3.4.2 Least Mean Square (LMS) adaptive filter

An adaptive filter is a computational device that iteratively models the relationship between the input and output signals of a filter. A filter using adaptive algorithm self-adjusts the filter coefficients. In Figure 3.12, where $x(k)$ is the input signal to a linear filter, $y(k)$ is the corresponding output signal, $d(k)$ is an additional input signal to the adaptive filter, $e(k)$ is the error signal that denotes the difference between $d(k)$ and $y(k)$. The linear filter can be different filter types such as finite impulse response (FIR) or infinite impulse response (IIR). The FIR (Finite Impulse Response) filter is selected over IIR(Infinite impulse Response) mainly due to following reason:

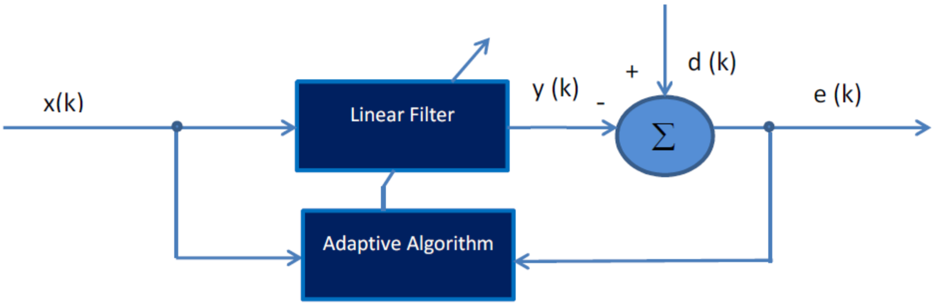

Figure 3.12: Schematic for LMS adaptive filter

- FIR is an easy to implement and unconditionally stable.
- The output of a FIR filters can directly be calculated from several (previous) time values of the input, whereas in contrary an IIR filters also needs previous time values of the output signal. An LMS adaptive algorithm adjusts the coefficients of the FIR filter iteratively to minimize the power of $e(n)$.

The steps involved for performing operations to update the coefficients of an adaptive filter is shown below: If $x(k)$ is the vector containing the L last samples of the reference signal.

$$x(k) = [x(k), x(k-1)....x(k-L+1)]^T \tag{3.3}$$

The primary finite impulse filter is given by:

$$w(k) = [w_1(k), w_2(k), ...w_{L-1}(k)]^T \tag{3.4}$$

where L is the length of the primary FIR filter w and k is the time instant of the last sample of reference signal. Then, the reference signal is passed through filter FIR, and output signal $y(k)$ is calculated as shown below:

$$y(k) = w(k)^T x(k) = \sum_{i=1}^{L-1} w_i(k)x(k-i) \tag{3.5}$$

The output signal is sent to the actuator and it drives the actuator. The weight w of the primary filter is continuously adapted by means of (Least Mean Square) LMS approach by comparing the filtered version of reference signal with the error signal at time instant k.

$$e(k) = d(k) - y(k) \tag{3.6}$$

The main objective of the LMS algorithm is to find the optimal weight vector where the mean square value of the error signal e(k) is minimized. The mean square error is defined as

$$\xi = E[e^2(k)] \tag{3.7}$$

This will provide the benefit of the desirable cancellation effect due to continuous adaptation of weight. The updating scheme for time instant k^+ is:

$$w(k+1) = w(k) - 2\mu e(k) f(k) \tag{3.8}$$

3.4.3 Leaky FXLMS algorithm

The adaptive filter is implemented in a signal processor with fixed word lengths, than round off signals is fed back to the filter weights. This results due to bias arising from the accumulation of quantization

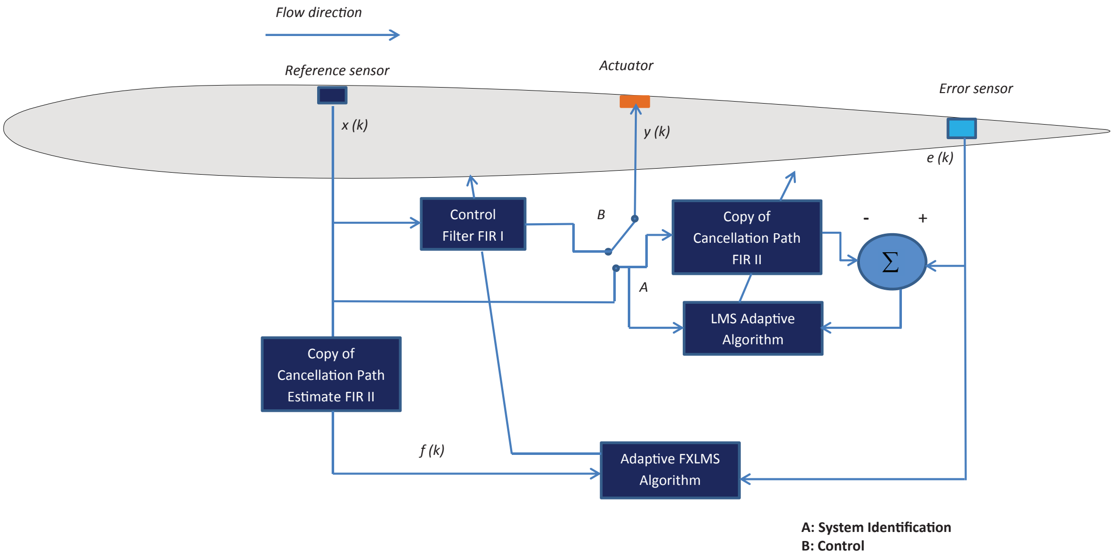

Figure 3.13: Schematic for the FXLMS control algorithm (not to scale).

errors. It can cause the coefficients to grow larger than the dynamic range of processor (overflow condition), results to inaccurate filter performance and system instability. Therefore, a Leaky FXLMS algorithm (also known as tap leakage) is applied to overcome the instability issue by removing a small portion of current weight values with each new weight calculation. After introducing this to the algorithm, the updating scheme for time instant k^+ will becomes:

$$w(k+1) = w(k)[1 - \mu\alpha] - 2\mu e(k)[c(k)x(k)] \tag{3.9}$$

where α is a small positive number referred to as leakage coefficient, μ is convergence coefficient constant. The selection of μ is important due to its usefulness in increasing and decreasing the convergence of the adaptation process. Larger μ renders the algorithm stable and smaller μ makes the convergence slower. Generally, the optimum convergence coefficient must be selected by trial and error on the basis of application. The factors affecting the choice of optimum convergence coefficient Hansen (2006) are mentioned below:

1. If number of control sources and error sensors are increasing then smaller convergence coefficient will be required.
2. Digital filter length (increasing the length requires reducing the convergence coefficient).
3. Time delay in the cancellation path(an increased time delay requires reduced convergence coefficient).
4. If comparing filter FIR versus IIR for the same application, a larger convergence coefficient may be used for an FIR filter.

The μ is normalized by the strength of the reference signal and have benefits of increased robustness of the convergence process and $f(k)$ is produced by filtering the reference signal with a secondary FIR filter (FIRII). The normalized equation is mentioned below:

$$\mu = \frac{\beta}{x(k)^T x(k)} \tag{3.10}$$

The digital representation of the natural cancellation path is shown by eq 3.11.

$$f(k-j) = \sum_{i=0}^{M-1} c_i(k)x(k-i-j) \tag{3.11}$$

$$c(k) = [c_1(k), c_2(k) ... c_{M-1}(k)]^T \tag{3.12}$$

where M is the length of c.

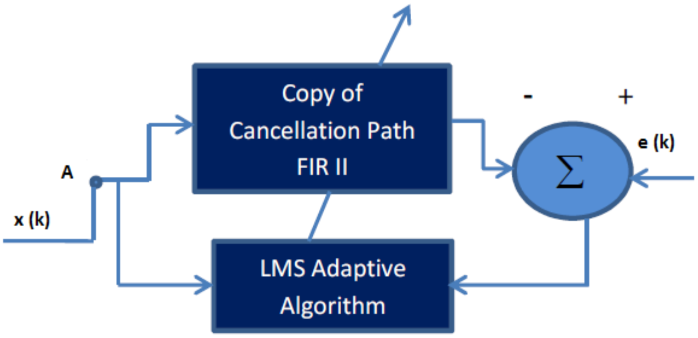

Figure 3.14: Schematic for system identification routine

3.4.4 System Identification

In general, an adaptive filter should handle the system identification task. The main task of system identification routine is to have a valid comparison between reference and error signals in order to update the process. Specifically, here it is used to obtain the cancellation path copy (FIRII) based on a modified version of the LMS adaptive algorithm as depicted in 3.13. In short the process works like, the actuator is driven by the reference signal $x(k)$ whereas at the same moment, the reference signal $x(k)$ is passed through the secondary filter. Then the signal is produced by the secondary filter. This signal is subtracted from error signal. The resulting signals obtained from the subtraction iteratively update the coefficients of FIRII by using an LMS adaptive algorithm. The criterion used for the final update of FIRII coefficients are such that $f(k)$=$e(k)$. It means FIRII is in converged state, and can model the natural cancellation path required initially by the primary control system. Therefore, in short, after running System Identification procedure (circuit A) as depicted in Figure 3.14, the control sequence starts and as soon as the system ID algorithm converges, FIRII are available and‘ the actual control will begin.

Chapter 4

Experimental techniques and setup

In this chapter, the experimental facility and equipment that was used to carry out the thesis work is explained. The experimental setup consists of an airfoil model, actuators and microphone sensors. In the latter part of this chapter, the experimental techniques such as high speed PIV and the data reduction process that was implemented, are explained in detail.

4.1 Experimental facility

The high speed PIV measurements with open and close loop adaptive control strategies are performed in the low-speed V-Tunnel facility, located at Delft University of Technology. The reason of choosing V-Tunnel facility was due to its relatively low background noise level at low velocities. It can go upto a maximum velocity of 45 m/sec. It is an open section low turbulence wind tunnel comprising of circular exit nozzle in the middle of the chamber. Air enters through nozzle to the circular test section of diameter 60 cm. The control area and test section are located on the third floor, with the free stream directed upwards towards the ceiling. In order to ensure a high flow quality, a large settling chamber is located under the test section to allow for a large contraction ratio. Therefore, for high flow quality the turbulence level should be smaller than $\frac{u_{rms}}{u_1} < 0.1\%$. The airfoil was mounted vertically at the center of the wind tunnel. The background noise level becomes dominated at higher velocities, due to structural vibrations inside the test chamber and at the ceiling. The experimental arrangement is presented in Figure 4.1.

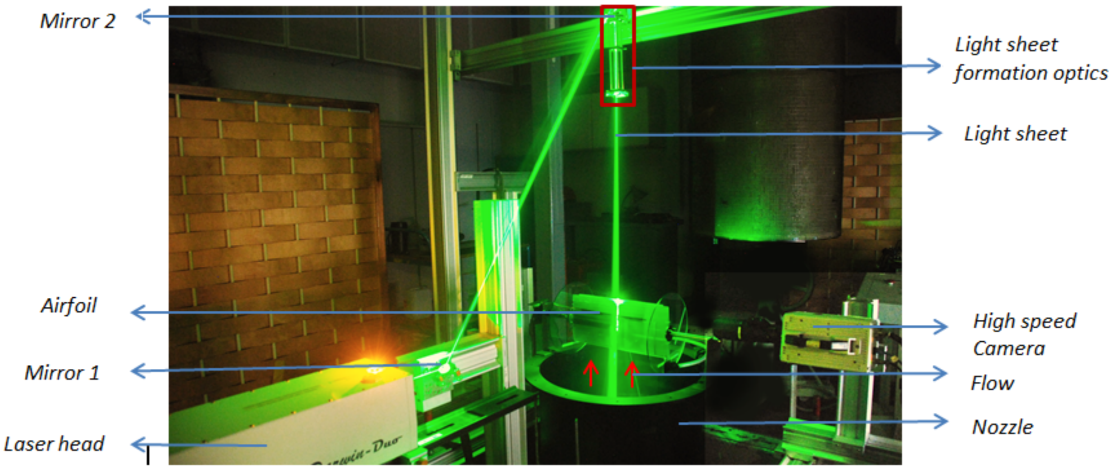

Figure 4.1: Experimental arrangement in V-Tunnel.

4.1.1 Airfoil model

The airfoil, NACA 0012, has been designed using Catia V5, with a chord and span of 20 and 40 cm respectively. The model is manufactured from polycarbonate to prevent electrical arcing generated due to DBD plasma actuators. The polycarbonate side plates of diameter 30 cm are placed on the sides of the airfoil in order to support the airfoil and to ensure 2D flow. The detailed drawing of the airfoil (see Appendix A). The airfoil is designed with two parts, top and bottom, so as to have sufficient space for accommodating seven microphones and its cable along the chord-wise position. The cable is shielded with conductive fabric in order to minimize the electromagnetic interference. Each microphone is of 2.56 mm diameter. The microphone is located from the leading edge along the chord in seven x/c position i.e. is depicted in Table 4.1, where x is the position of the microphone and c is the chord length of the airfoil.

In the experiment, the airfoil was mounted vertically at the center of the wind tunnel. The free stream velocity was varied at 17, 20, 25 m/sec with an incidence angle of α= 1.96, 1.66 and -0.60 deg respectively. The resulting Reynolds numbers (Re) are 2.27×10^5, 2.67×10^5 and 3.33×10^5 on the basis of chord number for above mentioned velocities. The zig-zag tape has been applied on the pressure side that is approximately 6 cm from the leading edge. The tape is also placed on the trailing edge of an airfoil. The 3-D roughness element (carborundum, 0.84 mm) has been applied on the suction side starting from the trailing edge as depicted in the Figure 4.3. The roughness elements are used to eliminate tones.

In the experiment, microphone 4,5,6 and 7 respectively are utilized to read the signals whereas 5 and 6 are mainly used as reference and error sensor for the Adaptive FXLMS controller. The perspective view of sensor, DBD plasma actuator and controller on an airfoil is depicted in Figure 4.3. The distance between the reference and error sensor is 20 mm. These two sensors are the backbone of the Adaptive FXLMS controller (see Chapter 3).

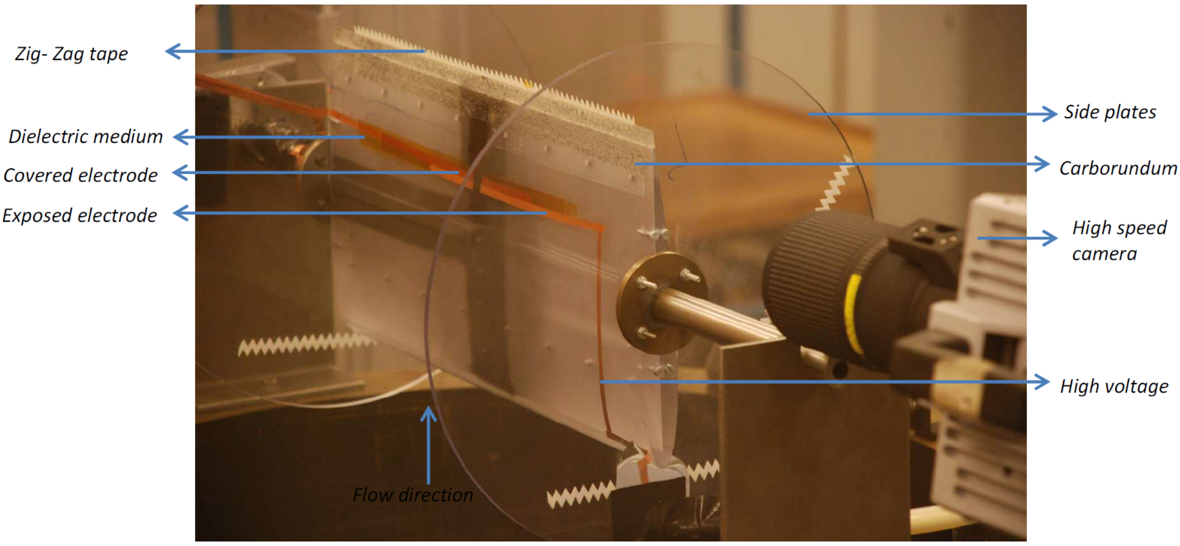

Figure 4.2: Experimental setup of airfoil model.

4.1.2 Microphone sensors

Microphone measurements are considered as an important tool for the experimental references and acoustical problems. There are various types of microphones available in the market depending on the types of transducer, directivity or working principles. The electret condenser Sonion 8010 T microphone is used to measure surface pressure fluctuation. It is Omni-directional and has a sensitivity of -33.5 dB at 1 kHz that is equivalent to 21 mV/Pa. The condenser microphone comprises of mobile diaphragm and a rigid back plate. When a constant polarisation voltage V_0 is applied over a large resistance $R(> 10G\Omega)$, it creates a constant charge on the condenser. A sound-induced modulation of the distance between the diaphragm and backplate results in a change in capacity with constant charge, and thus in a sound-induced AC voltage signal (V) added to the constant polarisation voltage. This voltage creates a constant charge on the condenser. An approximation of the linear relationship between sound pressure and voltage is quite accurate if the amplitudes are not too high. The reason for applying constant polarisation voltage V_0 was due to the non linear relation between the mechanical force and voltage on the condenser suggested by Müller and Möser (2009).

Surface pressure fluctuation measurements

Microphones are employed to measure the surface pressure fluctuation. Pressure fluctuations on the surface can also be measured by pressure transducer, but microphones are preferred over pressure transducers due to its application as a reference and error sensor for adaptive controller. The effect of placing microphones on the surface can affect the boundary layers on both sides of the profile. Therefore, these microphones are embedded in the airfoil surface. The detailed drawing of the airfoil is depicted in Appendix A.

As mentioned earlier, the role of microphone 5 and 6 is to act as a reference and error sensor respectively. The reference sensor samples the incoming signal. The incoming signal is passed to the

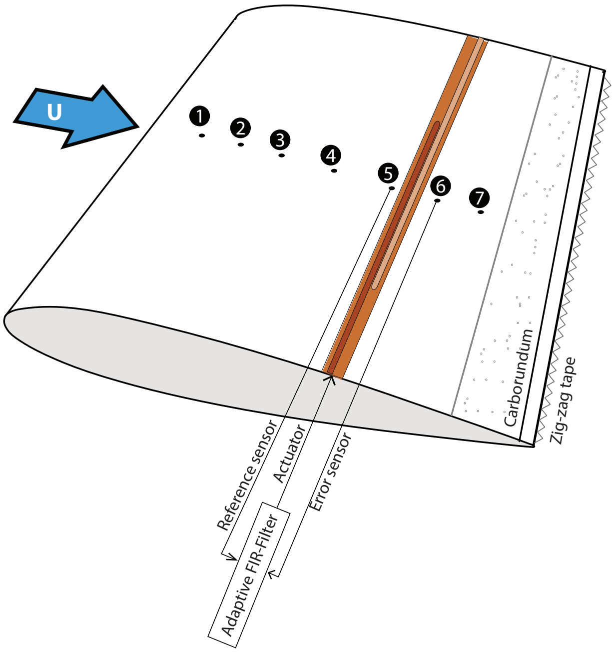

Figure 4.3: Schematic diagram of airfoil model with adaptive FIR filter.(not to scale)

electronic controller where it is filtered to generate the output signal from the control source i.e. DBD plasma actuator. The error sensor was used to measure the control effectiveness of the system. The detailed explanation is presented in Chapter 3.

Resonating frequency

The tendency of a system to oscillate at its maximum amplitude at certain frequencies than other frequencies is defined as resonance and the frequency is called as resonance frequency. At resonance frequency, even small periodic driving forces can produce large amplitude fluctuations. The mathematical form of resonance frequency for a pinhole microphone arrangement is shown in eq 4.1,where c is the speed of sound, A is the cross-section area of the pinhole, and V is the volume of the cavity between the microphone and the pinhole.

$$f_r = \frac{c}{2\pi}\sqrt{\frac{A}{Vl}} \tag{4.1}$$

The microphones are positioned behind a pinhole orifice of $d = 0.2$ mm diameter as depicted in Figure 4.4. According to Lueptow (1995),Tsuji et al. (2007), the smaller diameter of pinhole orifice prevents attenuation of high frequency fluctuations. As suggested by Shaw (1960), orifice aspect ratio (length/diameter) is $l/d = 2.5$ which satisfies the $l/d \geq 2$ limit. The pinhole orifice also shields the microphones from heating by the laser light during simultaneous microphone and PIV measurements suggested by (Ghaemi et al., 2012). The pinhole orifice induces a resonating frequency of $f_r \approx 14.7$ kHz. The advantage of using the smaller microphones is to have a higher resonating frequency.

Table 4.1: Microphone positioning on airfoil

No	Microphone	c (mm)	x(mm)	x/c
1	Microphone 1	200	30	0.15
2	Microphone 2	200	50	0.25
3	Microphone 3	200	75	0.375
4	Microphone 4	200	100	0.50
5	Microphone 5	200	120	0.60
6	Microphone 6	200	140	0.70
7	Microphone 7	200	170	0.85

Reduced cavity diameter results in smaller volume, which in turn gives higher resonating frequencies. In short, higher resonating frequency is beneficial.

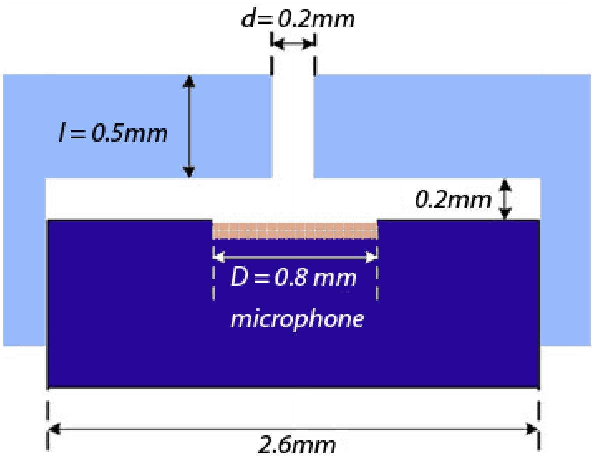

Figure 4.4: Schematic drawing of the microphone head in the pinhole orifice. Ghaemi et al. (2012)

Microphone data processing

The signals are sampled at 100 kHz using a National Instrument NI-9215 data acquisition system. The trigger signal (high speed camera) and Q switch (single cavity of the laser) is acquired for 1 sec and 5 second respectively using a NI-9263. The microphone 5 signals are passed through a low pass filter (LPF). The c-DAQ arrangement is shown in Figure 4.5. A low-pass filter (LPF) passes low-frequency signals and attenuates signals with frequencies higher than the cut off frequency. Since, each microphone has different amplification settings. A 2 kHz tonal noise from the speaker was recorded by microphone 4, 5, 6 and 7 respectively in still air. The RMS value of each microphone is calculated for 2 kHz tonal noise measured signals. All the microphones RMS values were divided by the microphone 4 RMS value. This results in amplification factor for the respective microphones. Finally, these amplification factors are multiplied to their respective microphone signals. This process has been applied in order to equalise the microphone signals. Initially, these microphone signals were recorded at different amplification settings. After equalizing the signals, the Power Spectral Density (PSD) has been estimated. PSD shows the strength of the variation of energy as a function

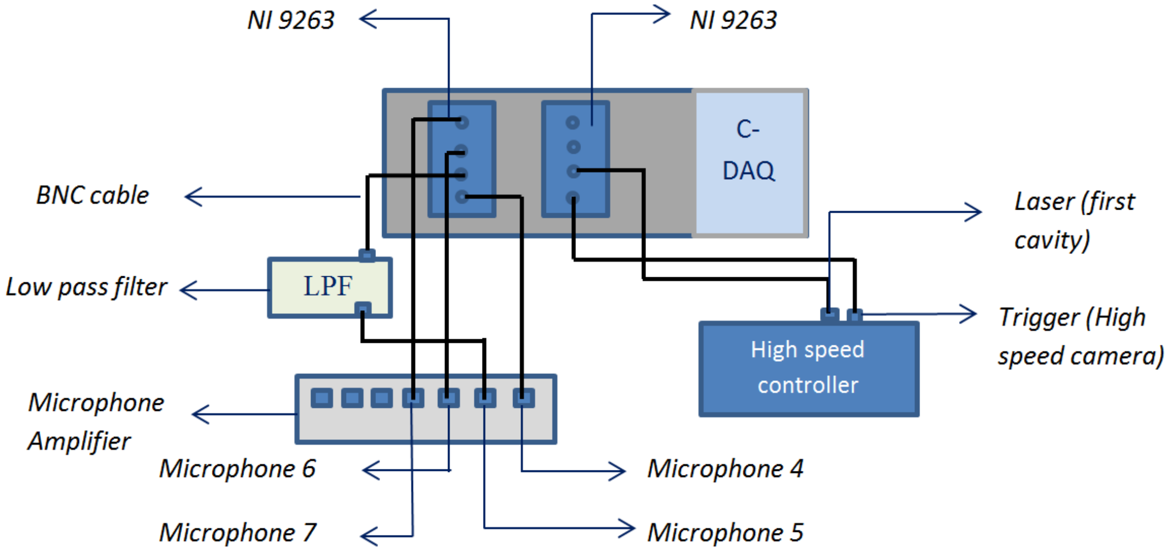

Figure 4.5: Experimental set up

of frequency. In simplified form, it provides information at which frequency variations are weak and strong. Average periodogram method is used for estimating the PSD (Welch,1967) of the signals. In this method, the input signal vector is divided into a number of overlapping segments. Each section is windowed with a Hamming windowing function. This is done in order to avoid windows effect of short time series. Accordingly, the periodograms are estimated for each segment independently by means of FFT and finally it is averaged to get an estimation of PSD of the signal. The basic concept of PSD is explained in Appendix B.

4.1.3 Actuator setup

In the experimental campaign, a conventional DBD actuator is placed between the reference sensor (microphone 5) and error sensor (microphone 6) as depicted in Figure 4.3. The actuator consists of two copper electrodes, separated by polyimide dielectric, directly attached on the surface of the airfoil. The thin rectangular copper electrodes are employed which are made out of self-adhesive copper tape. The thickness is 30 μm including adhesives. The electrodes are separated by two dielectric layers of polyimide Kapton tape. The thickness of each layer is 50.8 μm. The total thickness of dielectric including adhesive is approximately 110 μm. The geometrical layout of DBD plasma is depicted in Figure 4.6. According to Van Dyken et al. (2004), the thicker dielectric configurations are able to produce higher maximum net force because dielectric is able to withstand higher currents. Therefore, a double dielectric layer is used for the experiment. The upper electrode is kept grounded while the lower electrode is energized using a high voltage amplifier. The connector of the lower electrode is connected to the HV output cable of a TREK 20/20C HV amplifier. The gap between the electrodes must be as small as possible. This will lead to the smallest possible energy loss during discharge. In all the case studies, gap between the electrodes is kept to zero. If there is overlapping of electrodes, the actuator will act as a capacitor, storing energy rather than directing it to the flow. In all the cases, the DBD plasma actuator is actuated at constant applied voltage (V_{app})=10 kV and Duty cycle (D) of

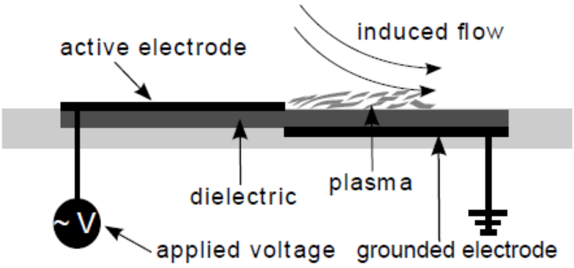

Figure 4.6: Geometrical lay-out of the DBD plasma actuator

100%.

In addition, the geometrical configuration and location of the actuator is kept the same for all the test cases in order to maintain a consistency in the results. The detailed geometrical configuration of the actuator is described in the Table 4.2.

Table 4.2: Actuator parameters

Parameters	Symbols	Values
Upper electrode length	l_u	26.5 cm
Lower electrode length	l_l	21.5 cm
Actuation length	l_{act}	13 cm
Dielectric thickness	t_d	2×0.06mm
Horizontal gap	g	0
Applied voltage	V_{app}	10 kV
Duty cycle	D	100%
Dielectric material	-	Kapton polymide
Electrode material	-	Copper

4.1.4 High speed Particle Image Velocimetry

Over the past decades, one of the fast emerging and successful measurement techniques is Particle Image Velocimetry (PIV). Raffel et al. (1998) along with many internationally recognized experts in the field of PIV demonstrated the development of PIV over decades, its working principle and its use in practice. It is a particle-based field measurement technique which measures the instantaneous velocity field within a plane. Recently, it is also extended to a three-dimensional volume within the flow domain making this technique more popular as a quantitative flow visualization tool.

Working principles

PIV measures the displacement of small tracer particles that are carried by the fluid during a short time interval. These tracer particles are illuminated within a thin light sheet generated from a pulsed light source (usually a double-head pulsed laser system). The light scattered by them is recorded onto two subsequent image frames by a digital imaging device, typically a CCD camera placed perpendicular to the measurement plane. Therefore, the technique requires an optical access for both the delivery of the light sheet and recording of the images. The local fluid velocity in location X is obtained indirectly as a displacement of the tracer particle within a frame time interval $\triangle t = t_2 - t_1$. This can be expressed as shown in eq 4.2.

$$D(X, \Delta t) = \int_{t_1}^{t_2} v(X(t), t))dt \tag{4.2}$$

where $v(X(t))$is the velocity of the tracer particles along the trajectory X within the time interval Δt. The basic theory of PIV such as flow seeding, mechanical properties and scattering properties of tracer particles, illumination etc are presented in Appendix B.

PIV setup

A Photron Fastcam SA1.1 high speed CMOS camera of 1024 × 1024 pixels is employed to capture the image of the field of view (FOV). The image acquisition has been performed at 5.4 kHz in double frame for all the cases (clean loop configuration, close loop and open loop control) whereas 10 kHz in a single frame for the Quiescent flow condition. The time separation (Δt) between successive images are chosen as an optimum trade-off allowing enough particles displacement between the two frames (in the order of 2-3 pixels) in the slower regions while keeping it within reasonable values in the faster regions (typically 16 pixels in the free-stream area). The camera was equipped with a Nikon objective with a focal length of 105 mm in order to capture the required field of view. The aperture number($f_\#$) was set to 4. The (FOV) field of view was set to be 32 mm × 16 mm with magnification of 0.64. In order to achieve the high sampling rate of 5.4 kHz, the sensor is cropped to a size of 1024×512 pixels. The synchronization between laser and camera was performed by means of a LaVision High-Speed controller and DAVIS 8.0.2 software package. Seeding particles based on non-toxic water glycol of approx 1mu m diameter were entrained in the flow through a SafeX Fog generator. The particles at the mid span are illuminated by a light sheet of 2 mm thickness generated by Quantronix Darwin-Duo laser system. The light-sheet optics (simple mirror, +200 mm spherical convergent, -100 mm spherical divergent, and 200 mm cylindrical lenses in this order) are positioned to achieve light sheet thickness of 2 mm as mentioned above.

Table 4.3: PIV parameters for statistical measurements(double frame mode) at U_∞=17 m/sec

Parameters	Symbols	Values
Field of View	FOV	32 mm×16 mm
Magnification	M	0.64
Focal length	f	105 mm
Aperture number	$f_\#$	4
Pulse separation	Δt	53 μs
Sampling frequency	$f_{s_{PIV}}$	5.4 kHz
Number of PIV samples	N_{PIV}	5400

The images are processed in order to extract and analyse the velocity vector fields. The basic idea is to find the shift of the tracer pattern between two frames recorded at a known time separation of Δt and then the cross-correlation operator is applied where correlation peak indicates the particle shift

Δx in unit of pixels. The minimum correlation window size is restricted by the minimum number of tracer particles required for the accurate cross correlation. Preprocessing helps to remove spurious light by subtraction of the minimum for each individual pixel. The images are analysed using Davis 8.0.2 by cross-correlating successive images. The final interrogation windows size of 16×16 pixels with 75% overlap are used for all cases except Quiescent flow case. For Quiescent flow condition, final interrogation window size of 6×6 pixels with 75% overlap is used. The field of view (FOV) and coordinate systems are presented in Figure 4.7. In the Figure 4.7 (a), number 5 and 6 designated as reference and error sensor. The section of the airfoil in the FOV was approximated by a straight line. The co-ordinates were transformed in the wall normal direction. The origin is placed at the start of actuator location as depicted in Figure 4.7. The wall tangential axis is denoted by x axis and the wall normal is denoted by y-axis.

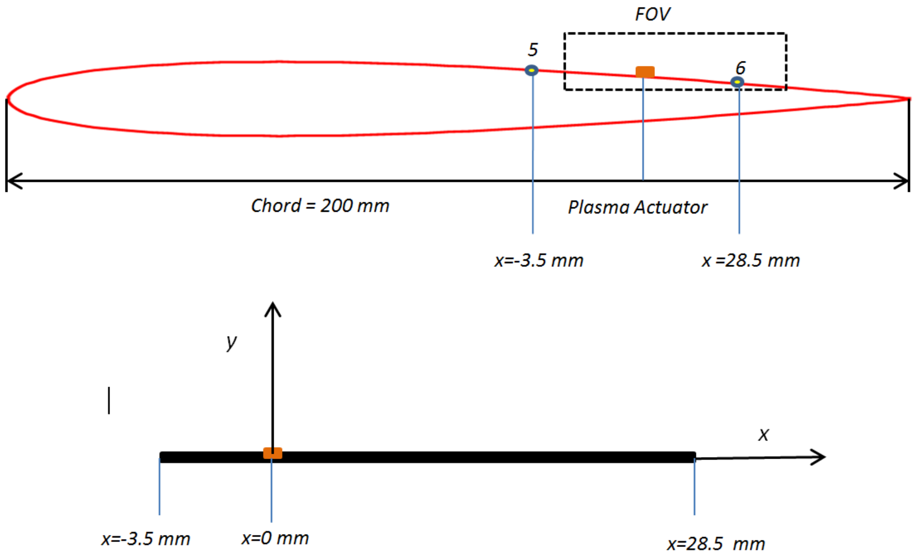

Figure 4.7: Coordinate system (All dimensions are in mm).(not to scale)

4.2 Test cases

The measurements are conducted into two major groups. In the first group, both PIV and microphone measurements were taken simultaneously whereas in the second group, the parametric studies are conducted by surface microphone measurements. The cases are explained in detail in further subsection.

4.2.1 PIV and microphone measurements

In the experiment, both PIV and microphone measurements were taken simultaneously. The test cases are further classified into four sub-cases described below:

Quiescent flow

The experiment are performed in still air in order to reduce the effect of any external disturbances on the measurements. The time resolved PIV have been applied in order to characterise the flow field produced by the DBD plasma actuator. The main reason of taking PIV (single frame) measurements in quiescent flow condition is to have more insight of the induced velocity field produced by the DBD plasma actuator. It is performed by varying carrier frequency (f_{ac}) at V_{app} of 10 kV. The surface microphone measurements are also performed simultaneously. The actuator configuration are kept same in all the cases as depicted in Table 4.2. The test case for quiescent flow condition is presented in Table 4.4.

Table 4.4: Parameters used for statistical measurements in Quiescent flow condition(Single frame).

Parameters	Symbols	Values
Applied voltage	V_{app}	10kV
Duty cycle	D	100 %
Carrier frequency	f_{ac}	750, 1000, 1500, 2000 Hz
Field of View	FOV	20 mm×10 mm
Focal length	f	105 mm
Aperture number	$f_{\#}$	4
Pulse separation	Δt	100 μs
Sampling frequency of microphone	$f_{s_{mic}}$	100 kHz
Number of microphone samples	N_{mic}	500,000
Sampling frequency of PIV	$f_{s_{PIV}}$	10 kHz
Number of PIV samples	N_{PIV}	5000

Clean configuration flow

The experiments are conducted for clean airfoil configuration at varying flow conditions i.e. (different velocities and angle of attack). Here, the clean configuration implies that an airfoil is tested without roughness element (zig-zag tape, carborundum) and DBD plasma actuator on its surface. The high speed PIV and surface microphone measurements were performed simultaneously. The main objective of taking PIV (double frame) and microphone measurements is to evaluate the effect of placing DBD plasma actuator and roughness element on the flow. It is conducted to ensure that the actuator is not tripping the boundary layer. The selection of angle of attack and velocities are done on the basis of observing T-S waves through online PIV and labview programme. The test case is depicted in Table 4.5.

Closed loop control

The Adaptive FXLMS control (close loop) study has been performed in order to cancel T-S waves. The concept deals with the cancellation of T-S instability waves by superimposing them with adaptive counter waves. The advantage of this technique is the much lower energy input compared with conventional methods of manipulating the mean velocity profile. The high speed PIV (double frame) and surface pressure measurement (microphone) were performed simultaneously in order to understand

Table 4.5: Parameters used for statistical measurements in Clean flow configuration.

Parameters	Symbols	Values
Free stream velocity	U_∞	10, 15, 20, 25 m/sec
Angle of attack	α	2.85, 0.98, -0.8, -1.96 deg
Applied voltage	V_{app}	10kV
Duty cycle	D	100 %
Carrier frequency	f_{ac}	750, 1000, 1500, 2000 Hz
Field of View	FOV	32 mm×16 mm
Magnification	M	0.64
Focal length	f	105 mm
Aperture number	$f_\#$	4
Pulse separation	Δt	90, 60, 45, 36 μs
Sampling frequency of microphone	$f_{s_{mic}}$	100 kHz
Number of microphone samples	N_{mic}	500,000
Sampling frequency of PIV	$f_{s_{PIV}}$	5.4 kHz
Number of PIV samples	N_{PIV}	5400

the evolution and cancellation of T-S waves spatially as well as temporally. The angle of attack is adjusted according to the free stream velocities U_∞=17, 20 and 25 m/sec in order to have natural TS waves. The test case for the close loop case are presented in the Table 4.6.

Table 4.6: Parameters used for statistical measurements in close loop control case.

Parameters	Symbols	Values
Free stream velocity	U_∞	17, 20, 25 m/sec
Angle of attack	α	1.96, 1.66, -0.60 deg
Control	-	on, off
Applied voltage	V_{app}	10kV
Duty cycle	D	100 %
Field of View	FOV	32 mm×16 mm
Magnification	M	0.64
Focal length	f	105 mm
Aperture number	$f_\#$	4
Pulse separation	Δt	53, 45, 36 μs
Sampling frequency of microphone	$f_{s_{mic}}$	100 kHz
Number of microphone samples	N_{mic}	500,000
Sampling frequency of PIV	$f_{s_{PIV}}$	5.4 kHz
Number of PIV samples	N_{PIV}	5400

Open loop control

The working principle of open loop control has been described in Chapter 3. The objective of using open loop control strategy is to demonstrate the behaviour of T-S waves and control of no feedback assistance. Furthermore, the results are compared with closed loop control cases. The surface sensor placed on airfoil surface detects the pressure fluctuations. The fluctuations are read by the program built in Labview software. These signals yield information about the frequency of the T-S wave. Therefore, the actuator is actuated at different carrier frequencies within the range of acquired T-S wave frequency. In short, the actuator is operated using non-adapted single-frequency sinusoidal signal. The high speed PIV (double frame) and surface pressure measurement (microphone) were performed simultaneously in order to understand the evolution and cancellation of TS waves spatially as well as temporally. The test case for open loop control are presented in the Table 4.7.

Table 4.7: Parameters used for statistical measurements in open loop control case.

Parameters	Symbols	Values
Free stream velocity	U_∞	17, 25 m/sec
Angle of attack	α	1.96, -0.60 deg
Applied voltage	V_{app}	10kV
Duty cycle	D	100 %
Carrier frequency	f_{ac}	0, 700, 850, 1000, 1500 Hz
Field of View	FOV	32 mm×16 mm
chal Magnification	M	0.64
Focal length	f	105 mm
Aperture number	$f_\#$	4
Pulse separation	Δt	53, 36 μs
Sampling frequency of microphone	$f_{s_{mic}}$	100 kHz
Number of microphone samples	N_{mic}	500,000
Sampling frequency of PIV	$f_{s_{PIV}}$	5.4 kHz
Number of PIV samples	N_{PIV}	5400

4.2.2 Microphone parametric study

The parametric study using surface microphone measurements is conducted. The studies are mainly divided into three sub-cases. The sampling rate of the sensor ($f_{sS_{ensor}}$) was taken same for all cases. The sampling frequency of 100 kHz was used to record 500,000 samples in 5 seconds. The microphone 5 signal is also passed through a low pass filter (LPF) as mentioned in the above section. The sub-cases are described below:

Ambient noise

The ambient noise measurements are conducted in no flow conditions in four scenarios. In the first scenario, the measurements were conducted only putting laser on, while the second scenario comprises only putting an amplifier on, thirdly putting both laser and amplifier on and at last measurements were performed by shutting off everything. The main objective of the experiment is to find out the major noise causing element among these four scenarios. The test case of ambient noise is presented in Table 4.8.

Table 4.8: Parameters used for surface microphone measurements for ambient noise case.

Scenario	Components	on/off
1	Laser only	on
2	Amplifier only	on
3	Laser and amplifier	on
4	Shut-off	off

Interference effect

The interference measurements were conducted in still air by switching off the laser. The main objective of performing this test is to investigate the electromagnetic interference while carrying out actuation. Therefore, the test was conducted by varying carrier frequency f_{ac} in order to have an insight of EM noise effects on the signals. The test case is tabulated in Table 4.9.

Table 4.9: Parameters used for surface microphone measurements for the interference test at U_{∞}=0 m/sec(No flow).

Parameters	Symbols	Values
Applied voltage	V_{app}	10 kV
Duty cycle	D	100 %
Carrier frequency	f_{ac}	700, 850, 1000, 1200, 1500, 2000 Hz.
Sampling frequency of microphone	$f_{s_{mic}}$	100 kHz
Number of samples	N_{mic}	500,000

Effect of variation of step size and filter length(number of taps)

Lastly, the measurements were performed with an objective to evaluate the performance of controller in two scenarios. In the first scenario, the step size was varied in constant filter length whereas in the second scenario, the filter length was varied at constant step size. The step size is a convergence factor that controls stability and the rate of descent. It is denoted as μ. According to Kuo and Morgan (1995), the step size affects important properties such as performance, stability and error as discussed in Chapter 3. Therefore, evaluation in this case will give a clear idea of the appropriate filter length and step size used for this specific controller. The parametric test case is tabulated in Table 4.10 and 4.11 respectively.

Table 4.10: Parameters used for surface microphone measurements for the variation of step size in Close loop control at U_∞=17 m/sec.

Parameters	Symbols	Values
Free stream velocity	U_∞	17 m/sec
Angle of attack	α	1.96 deg
Applied voltage	V_{app}	10 kV
Duty cycle	D	100 %
System ID	FIRII	0.3
Step size	μ	0.00001, 0.0005, .001, 0.005, 0.01 0.02, 0.05, 0.1, 0.2, 0.3, 0.5, 0.8
Filter length	l_{filter}	80
Sampling frequency of microphone	$f_{s_{mic}}$	100 kHz
Number of microphone samples	N_{mic}	500,000

Table 4.11: Parameters used for surface microphone measurements for the variation of filter length in Close loop control at U_∞=17 m/sec.

Parameters	Symbols	Values
Free stream velocity	U_∞	17 m/sec
Angle of attack	α	1.96 deg
Applied voltage	V_{app}	10 kV
Duty cycle	D	100 %
System ID	FIRII	0.3
Step size	μ	0.3
Filter length	l_{filter}	20, 40, 60, 80,100, 120
Sampling frequency of microphone	$f_{s_{mic}}$	100 kHz
Number of microphone samples	N_{mic}	500,000

Chapter 5

Results and discussions

The chapter makes an attempt to characterize the flow in the vicinity of the actuator for several cases. Section 5.1 gives the statistical flow properties of actuation conducted in quiescent flow condition. Section 5.2, 5.3 and 5.4 gives the description of statistical flow properties conducted for clean flow configuration, closed loop control and an open loop control respectively. Under the statistical flow properties the mean velocity profiles, Reynolds stresses profiles and contours, time evolution of velocity fluctuations and PSD of the microphone signals will be discussed. Section 5.5 gives the description of autocorrelation of microphone signals and cross correlation of microphone and velocity signals for a open and closed loop. Finally, in the last section, the parametric study on control performance will be discussed.

5.1 Actuation in Quiescent flow condition

The experimental investigation is performed in no flow condition is also known as quiescent flow. In this case, the actuator is operated using non-adapted single-frequency sinusoidal signal. The main objective of this test is to have an insight of the DBD plasma actuator effect of different carrier frequency f_{ac}= 750 Hz, 1000 Hz, 1500 Hz and 2000 Hz at fixed applied voltage f_{app}=10 kV. The still air test helps to understand the actuator effect without any external disturbances. It gives a clear estimation of induced velocity information during actuation. Therefore, the measurement in the still air makes it more accurate. On the other hand, the disadvantage of this method is the lack of information into the interaction process of the actuator and a given external flow. The time resolved PIV technique is used for two main purposes. Firstly, to have an insight about induced velocity produced by an actuator and secondly, to characterize the flow field in the proximity of the DBD plasma actuator.

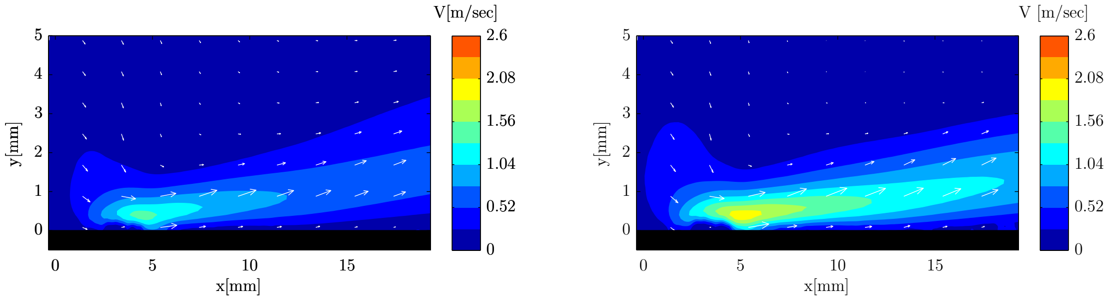

(a) f_{ac}=750 Hz (b) f_{ac}=1000 Hz

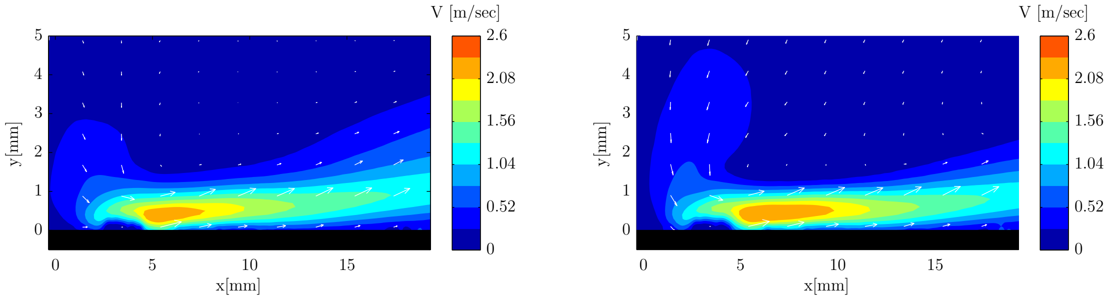

(c) f_{ac}=1500 Hz (d) f_{ac}=2000 Hz

Figure 5.1: Comparison of average total velocity fields for different carrier frequency (a) 750 Hz, (b) 1000 Hz, (c) 1500 Hz (d) 2000 Hz.

The averaged velocity field for the different tested carrier frequencies are depicted in Figure 5.1. The jet velocity increases with increasing carrier frequency. This is apprehended as an increase in the actuator produced body force. The rate of momentum transfer to the flow increases in increasing carrier frequency at fixed applied voltage. This is because of more HV (high voltage) cycles occurs with a given time span. Furthermore from 5.2 (a), it also reflects that velocity is not a linear function of frequency which is consistent with the observations made by (Kotsonis, 2012). According to Kotsonis (2012), the thrust does not change in magnitude of fixed applied voltage , but still the rate of momentum transfer to the flow increases with an increase in the carrier frequency.

5.1.1 Mean velocity profiles

Figure 5.2 (b) shows the mean velocity profile (u) at position x=5.5 mm, y=0.5 mm for varying carrier frequency in quiescent flow conditions. Most prominent features in mean velocity profiles is acceleration in the vicinity of the actuator surface. This increase is due to the ionic wind which was induced close to the wall by DBD. The velocity acceleration is significantly higher for f_{ac}=1500 and 2000 Hz as compared to f_{ac}= 750 and 1000 Hz. This is again because of the rate of momentum transfer to the flow increases with increasing carrier frequency. Another interesting observation is for f_{ac}= 1500 and 2000 Hz, the mean velocity profiles are negative but in very small magnitude. This is because of the fact that air is entrained towards the wall in order to restore the mass flow.

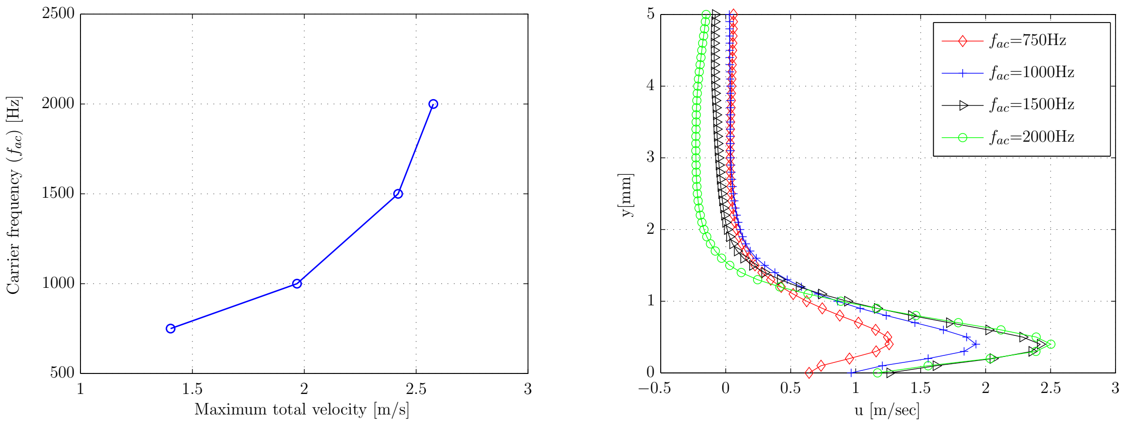

(a) Maximum total velocity

(b) Mean velocity profile (u) at x=5.5 mm, y=0.5 mm.

Figure 5.2: Maximum total velocity and mean velocity profile for varying carrier frequency in Quiescent flow conditions.

5.1.2 Time evolution

This section provides an overview of the true control authority of the actuator over the fluid. In order to analyse the effect from the operation of the actuator, it will be interesting to see the downstream development of the velocity. Therefore, the measurement is taken in still air, ensuring that the only momentum input is provided by the actuator at downstream position. Figure 5.3 shows the time evolution of the velocity (u) at x=10 mm, x=15 mm (measured at y=0.5 mm) for the sequence of carrier frequency. It should be noted that the effect of the actuator is more pronounced by increasing the carrier frequency. For instance, in the Figure 5.3, the velocity (u) values for f_{ac}=2000 Hz are higher as compared to other carrier frequencies. It is evident that the coherent structures associated with the impulsive start of the actuation and also velocity fluctuations appear in the vicinity of the actuator. This is attributed to the electrostatic oscillation of the body force as reported by (Kotsonis, 2012). In addition, the effect of the actuator is strong at x=10 mm. On moving further downstream

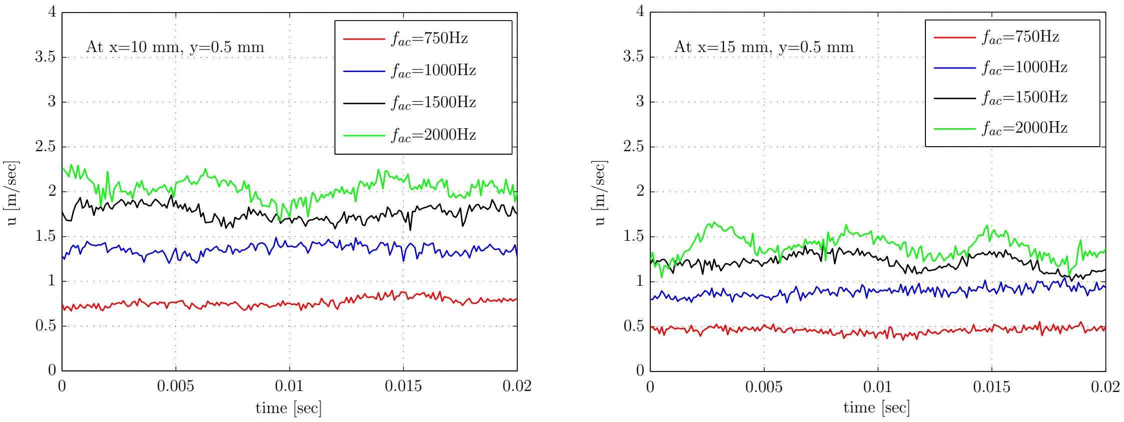

(a) At x=10 mm, y= 0.5 mm

(b) At x=15 mm, y= 0.5 mm

Figure 5.3: Time evolution of velocity component (u) in quiescent flow condition at x=5.5 mm, y=0.5 mm for varying carrier frequency.

position (x=15 mm), the velocity component (u) for the sequence of frequencies shows a significant decrease as compared to the position x=10 mm.

5.2 Clean configuration

The main objective of conducting clean configuration experiment is order to ensure that the actuator is not tripping the boundary layer. Here, the clean configuration implies that an airfoil is tested without roughness element (zig-zag tape, carborundum) and DBD plasma actuator on its surface. The selection of angle of attack and velocities are done by observing T-S waves through online PIV and Labview program. The test case of clean configuration is described in Chapter 4.

This section gives a statistical description of the mean velocity field and the Reynolds stresses. Data used in this section has been recorded using the high speed 2-component PIV set-up described in Chapter 4. Statistics of the velocity field in this section have been obtained by averaging 5381 statistically independent vector fields recorded at a sampling rate of 5.4 kHz. Furthermore, PSD of reference and error microphone signals are discussed. The microphone data are recorded at a sampling rate of 100 kHz.

5.2.1 Mean velocity profiles

Figure 5.4 shows the streamwise evolution of the mean velocity profiles on the suction side. Tested freestream velocities range from 10 to 25 m/s at chord Reynolds of 1.3×10^5 to 3.3×10^5 respectively.

The location at which the mean velocity profiles were plotted at several stations with streamwise coordinates is x= 0, 7.5, 15, 22.5 and 30 mm. This represents 62 %, 65 %, 69 %, 73 % and 77 % of the chord respectively.

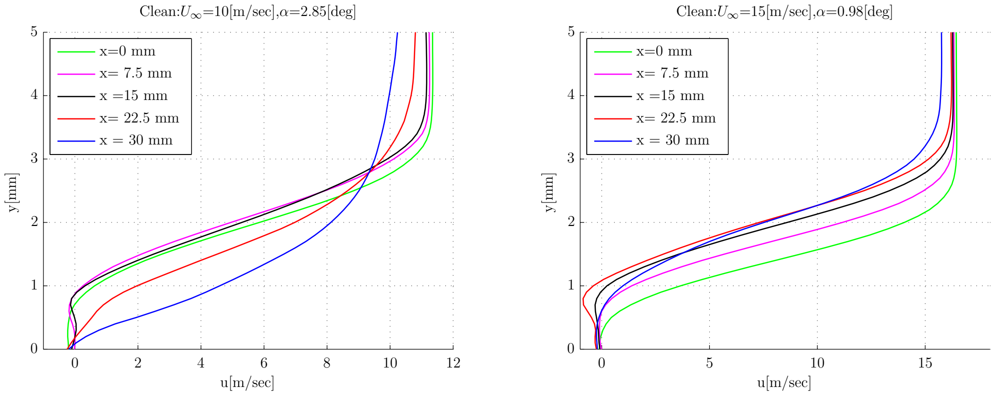

(a) U_∞=10 m/sec (b) U_∞=15 m/s

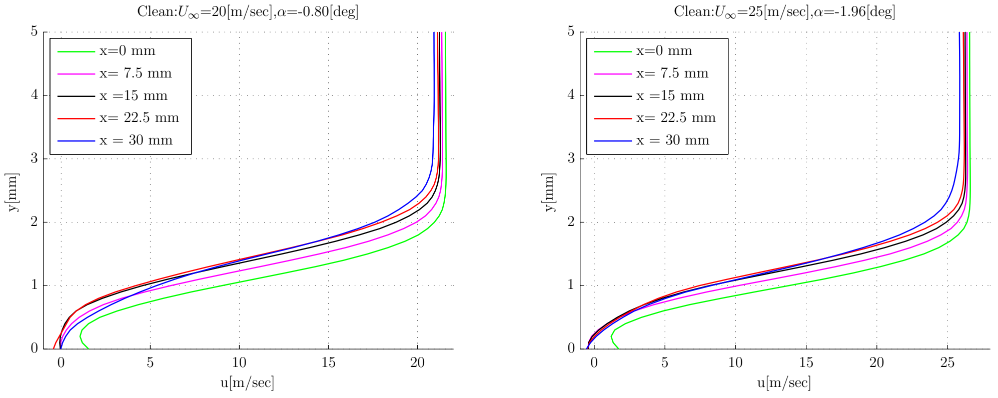

(c) U_∞=20 m/s (d) U_∞=25 m/s

Figure 5.4: Comparison of mean velocity profiles for clean configuration at U_∞=10, 15, 20 and 25 m/s.

Figure 5.4 shows the profiles for all cases exhibits an inflection point. The velocity profile exhibits an inflection point, to appear provided that this inflection point is far enough away from the wall, a necessary condition for the occurrence of inviscid type instabilities (Lowson et al., 1994). For U_∞=10 m/s, at x>22.5 mm, the point of inflection of the velocity profile moves away from the wall. The mean flow passes from a region of reversed flow back to streamwise direction before approaching zero near the surface for U_∞=15 m/s at location x=15 and 22.5 mm. In the case, U_∞=20 and 25 m/s, the velocity profiles exhibit an inflection point are closer to the wall and their profile are fuller as compared to U_∞=10 and 15 m/s. Therefore, the presence of inflection point ensures that the instabilities are present in the flow conditions. These instabilities are found to be T-S waves. This will

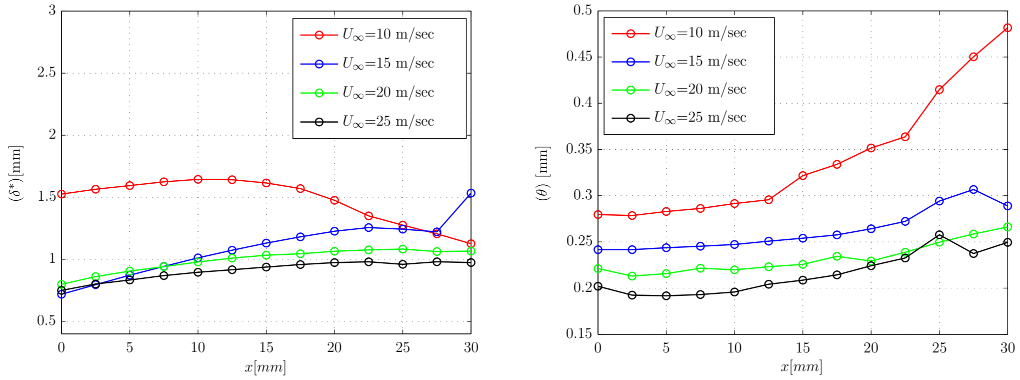

(a) Displacement thickness

(b) Momentum thickness

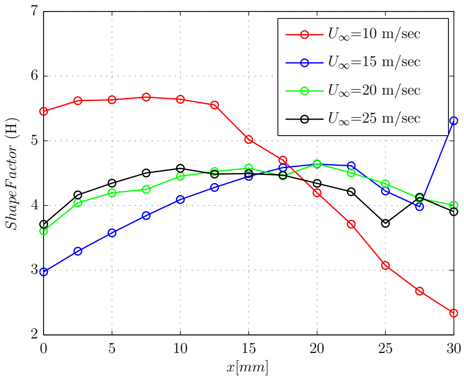

(c) Shape factor

Figure 5.5: Comparison of boundary layer parameters for clean configuration at U_∞=10, 15, 20 and 25 m/s.

be confirmed by observing the typical characteristics of T-S waves in u_{rms} profile and time traces of velocity fluctuations.

Figure 5.5 shows the plot of displacement thickness, momentum thickness and shape factor against x which is the distance along the chord. It should be noted that momentum thickness profile increases for all velocities on proceeding downstream. In the case for U_∞=10 m/s, in a region of x>12 mm, it shows a significant increment which is attributed to the momentum loss due to presence of boundary layer. In other words, momentum thickness is directly related to the drag of the airfoil. Therefore, it can also be inferred that U_∞=10 and 15 m/s has the higher momentum loss as compared to U_∞=20 and 25 m/s. The shape factor (H) provides an indication of the resistance of a boundary layer to flow separation with a decreasing (H) being a favourable for resisting separation. In Figure 5.5 (c), for U_∞= 20 and 25 m/s shows that their shape factor is increased on proceeding downstream. In addition, their following shape factor is staying above the separation value of 3.85. The shape factor for U_∞=10 m/s is approaching a value of below 3.85 for x>22.5 mm. This is a typical value for the profile to be considered as transitional. For the region x<22.5 mm, the shape factor is staying above the separation value of 3.85. Overall, in the region of x>17.5 mm, the freestream velocity U_∞=15, 20 and 25 m/s shows higher shape factor values as compared to U_∞=10 m/s. Furthermore, the analysis of the Reynolds stress profile will ensure the presence of T-S waves.

5.2.2 Reynolds stress profiles

The viscous mechanism of instability proposed by Tollmien and Schlichting. Viscous forces modify the phases of the velocity perturbations which lead to positive Reynolds stresses, enabling the transfer of energy from the mean flow to the disturbance (McAlpine, 1997).

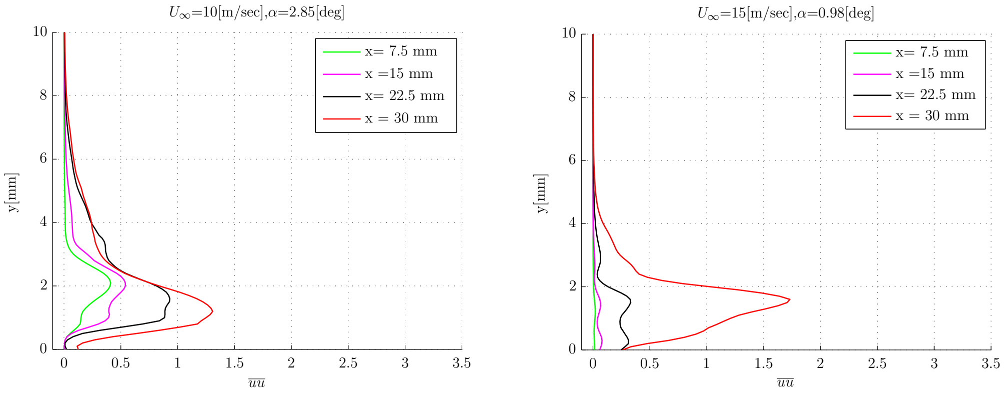

(a) U_∞=10 m/s.

(b) U_∞=15 m/s.

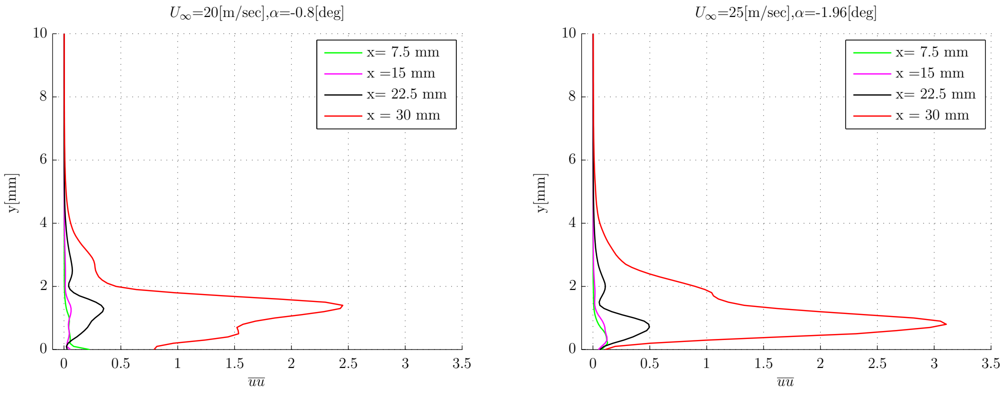

(c) U_∞=20 m/s.

(d) U_∞=25 m/s.

Figure 5.6: Reynolds stress $\overline{uu}$ profiles for clean configuration case at U_∞ (a) 10 m/s; (b) 15 m/s; (c) 20 m/s; (d) 25 m/s.

The Reynolds stress profiles ($\overline{uu}$) at locations x= 7.5, 15, 22.5 and 30 mm is shown in Figure 5.6 for freestream velocities U_∞=10, 15, 20 and 25 m/s. In the case of U_∞=10 m/s, all the profiles are characterised by a two peak distribution with the highest one located away from the wall and the lower one approximately at the point of inflection. The presence of two peak distribution of fluctuations corresponds to that of T-S waves. The maxima values of normal stress $\overline{uu}$ obtained is 1.31 m^2/s^2. In the case of U_∞=15 to 25 m/s for x=7.5 mm, the profiles are characterised by a single peak distribution. Simple and clean T-S waves of the fundamental frequency would cause just one single peak distribution (Grundmann, 2008). After x>7.5 mm, the instability increases more rapidly moving downstream leading to the maximum values of normal stress. At x=30 mm, the maximum values of normal stress $\overline{uu}$ obtained is 1.73, 2.45 and 3.12 m^2/s^2. The profiles ($\overline{uu}$) show that these instabilities are amplified as they move downstream until they may eventually grow large enough. This is a typical characteristic of T-S waves. Figure 5.7, 5.8, shows the Reynolds normal stress ($\overline{vv}$) and shear stress ($\overline{uv}$) for U_∞=10 to 25 m/s at x =7.5, 15, 22.5 and 30 mm. At x= 7.5 mm, the profiles ($\overline{vv}$) are insignificant for U_∞=10 to 25 m/s. They, however, become significant at x >7.5 mm. The maximum values of normal stress ($\overline{vv}$) remain much lower than those of the normal stress ($\overline{uu}$). The Reynolds shear stress profiles is depicted in Figure 5.8.

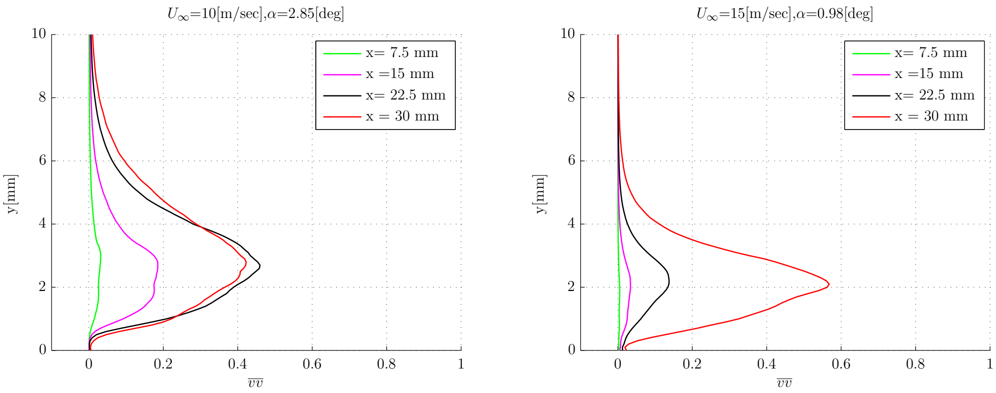

(a) U_∞=10 m/s.

(b) U_∞=15 m/s.

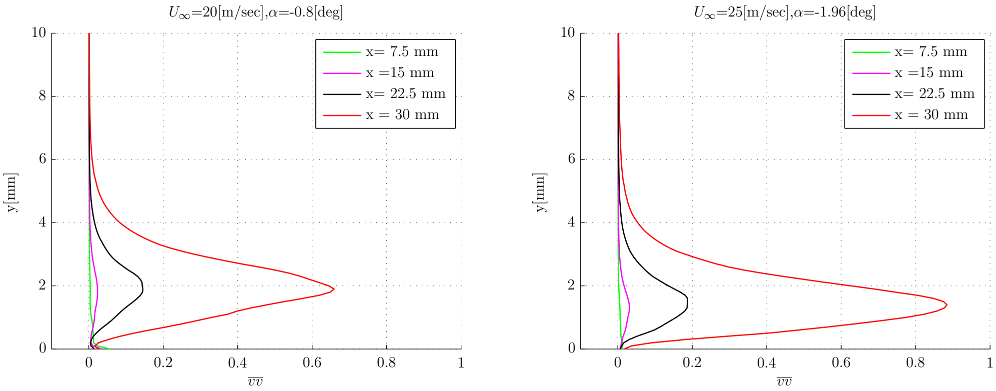

(c) U_∞=20 m/s.

(d) U_∞=25 m/s.

Figure 5.7: Reynolds stress $\overline{vv}$ profiles for clean configuration case at U_∞ (a) 10 m/s; (b) 15 m/s; (c) 20 m/s; (d) 25 m/s.

It should be noted that for U_∞=10 m/s, at x< 30 mm, shear stresses are having higher values as compared to the respective locations for higher velocities whereas vice versa for x> 30 mm. This is explained by the fact as the flow moves over the body which means more of the flow is affected by the viscous forces. These viscous forces modify the phases of the velocity perturbations which lead to positive Reynolds stresses, enabling the transfer of energy from the mean flow to the disturbance. The amplitude of shear stress remains lower than the normal stress ($\overline{uu}$). At location x=30 mm, the magnitude of maximum values of shear stress $\overline{uv}$ obtained is approximately 0.12, 0.41, 0.55 and 0.63 m^2/s^2.

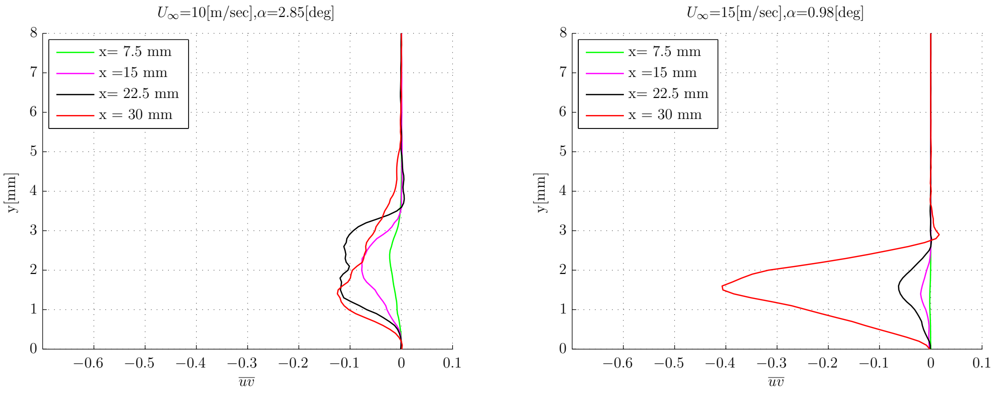

(a) U_∞=10 m/s.

(b) U_∞=15 m/s.

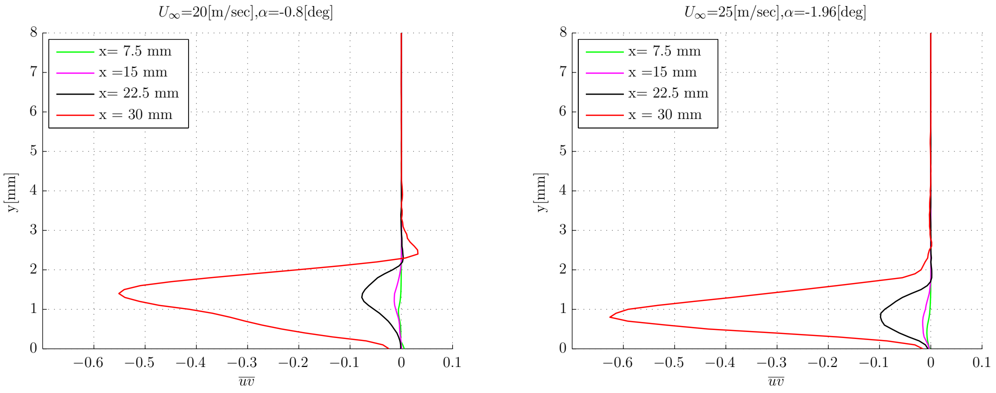

(c) U_∞=20 m/s.

(d) U_∞=25 m/s.

Figure 5.8: Reynolds stress $\overline{uv}$ profiles for clean configuration case at U_∞ (a) 10 m/s; (b) 15 m/s; (c) 20 m/s; (d) 25 m/s.

5.2.3 Time evolution

The time traces of velocity fluctuations u_f (in the x direction) and v_f (in the y direction) for U_∞=10 to 25 m/s is plotted. Data used in this section has been recorded using the high speed 2-component PIV set-up described in Chapter 4. Statistics of the velocity field in this section have been obtained by averaging 5381 statistically independent vector fields recorded at a sampling rate of 5.4 kHz. The three positions are selected such that one position is at the upstream of error sensor , second on the error sensor and last at the downstream of error sensor. The positions are depicted in Figure 5.9 for their respective velocities. For all the freestream velocity the time traces of velocity fluctuations for the upstream position are shown in Appendix D. These positions will allow us to understand the evolution of natural developing T-S waves over an airfoil for different flow conditions.

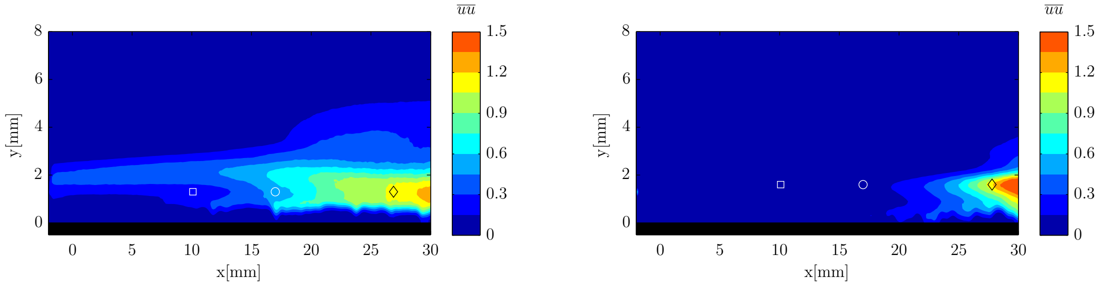

(a) U_∞=10 m/s

(b) U_∞=15 m/s

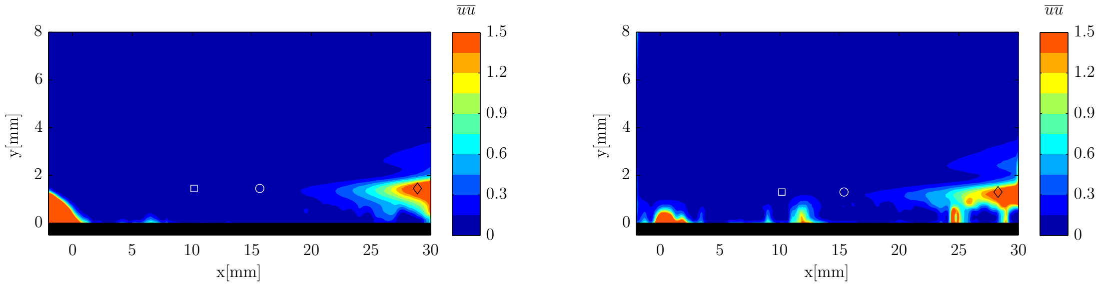

(c) U_∞=20 m/s

(d) U_∞=25 m/s

Figure 5.9: Showing points at which velocity fluctuations are plotted versus time U_∞=10, 15, 20 and 25 m/s.

Figure 5.10 shows the time traces of velocity fluctuations (u_f and v_f) for U_∞=10 m/s at positions x=17 mm and 26.90 mm (for y=1.3 mm). The time traces of velocity fluctuations (u_f,v_f) shows that they become amplified on proceeding downstream. For instance, at x=17 mm (error microphone), the fluctuations are stronger as compared to fluctuations at x=10.10 mm. At x= 26.90 mm, the amplitude of fluctuations (u_f) is significantly higher. The similar behaviour is observed for (v_f) fluctuations. This is evident from the 5.10 (a)-(d). The deviation of the fluctuations from zero (u_f) observed in Figure 5.10 (a) at x=10.10 and 17 mm for time instance 0.3 to 0.5 seconds is unexplainable.

Figure E.1 shows the time evolution of velocity fluctuations (u_f and v_f) for U_∞=15 m/s at positions x=10.10, 17 and 27.80 mm (at y=1.6 mm) respectively. At x=10.10 mm, the fluctuations shows the footprint of the development of T-S waves in its early stage in which amplitudes of these fluctuations are very small. On moving downstream position (x=17 mm), there is a small rise in the amplitudes of the fluctuations which results in the development of typical T-S wave packets. On moving further downstream position (x=27.80 mm), there is a significant rise in the amplitudes of the fluctuations. This results the T-S wave packets which are in intermittent stage.

Figure E.2 shows the time evolution of velocity fluctuations (u_f and v_f) for U_∞=20 m/s. The time traces of velocity fluctuations are plotted for positions x=10.20, 15.70 and 28.90 mm (at y=1.45 mm)respectively. The time traces fluctuations shows the similar behaviour as it is observed for U_∞=10 and 15 m/s. At x=10.20 mm, the fluctuations shows the development of T-S waves in its early stage. The amplitudes of these fluctuations are very small. On moving further downstream (x=15.70 mm), these are developing into T-S waves packets. At x= 28.90 mm, the typical T-S wave packets are apparent. These wave packets are well defined as compared to wave packets formed at the downstream position for U_∞=15 m/s.

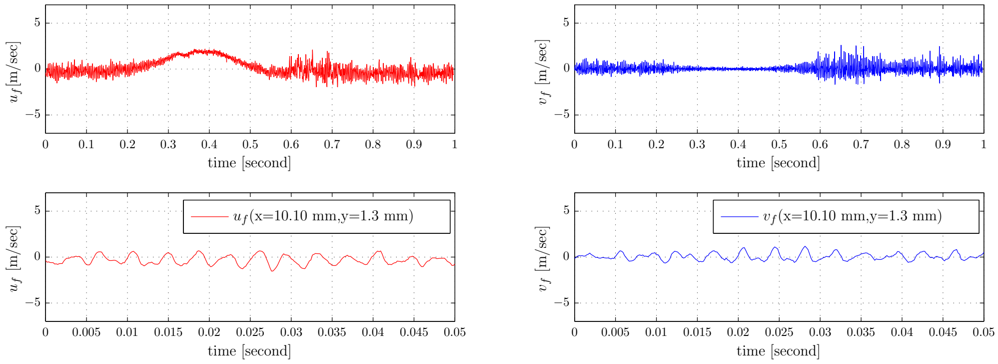

(a) u_f at x=10.10 mm, y =1.3 mm

(b) v_f at x=10.10 mm, y =1.3 mm

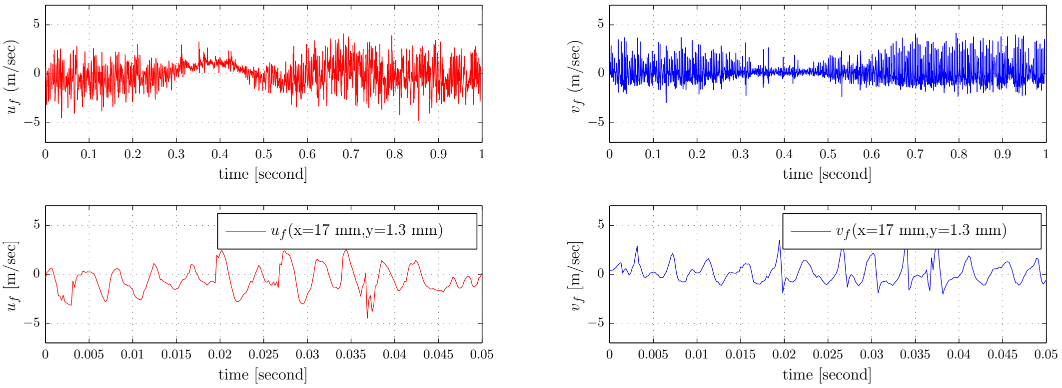

(c) u_f at x=17 mm, y =1.3 mm (Error microphone)

(d) v_f at x=17 mm, y =1.3 mm (Error microphone)

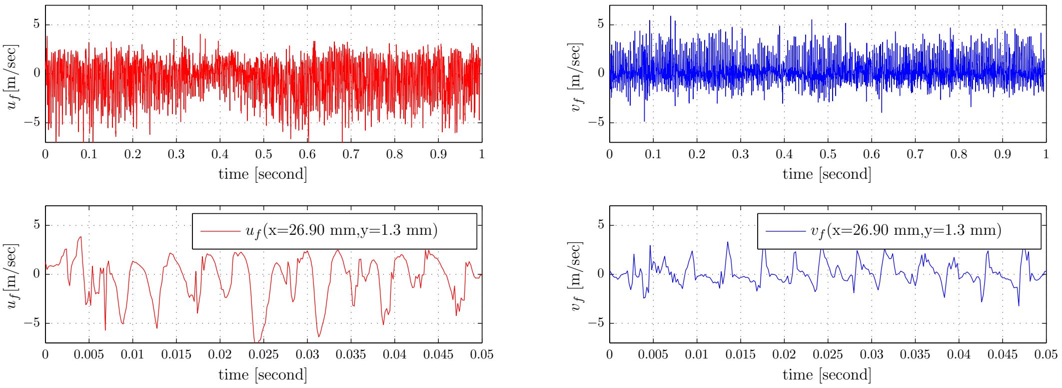

(e) u_f at x=26.90 mm, y =1.3 mm

(f) v_f at x=26.90 mm, y =1.3 mm

Figure 5.10: Time evolution of velocity fluctuations (u_f, v_f) at U_∞=10 m/s.

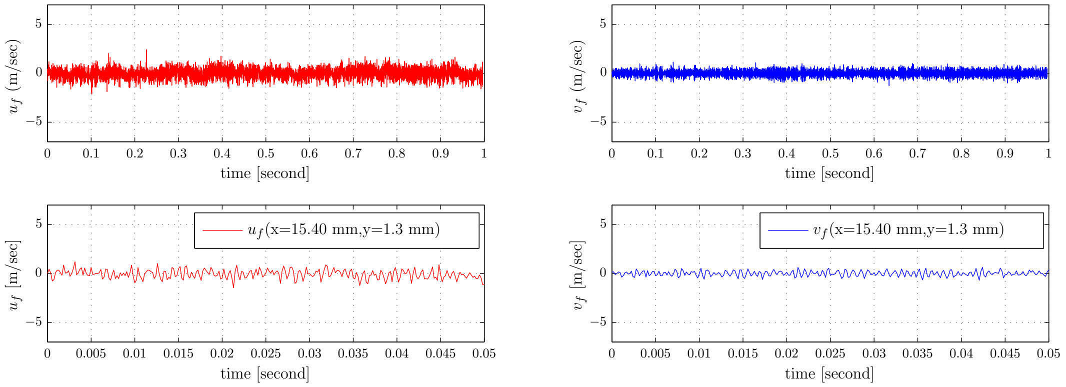

(a) u_f at x=15.40 mm, y=1.3 mm (Error microphone)

(b) v_f at x=15.40 mm, y=1.3 mm (Error microphone)

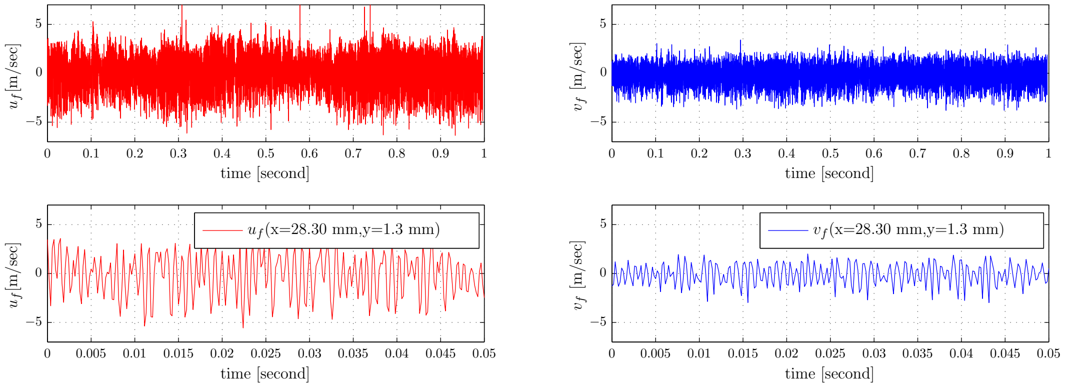

(c) u_f at x=28.30 mm, y=1.3 mm

(d) v_f at x=28.30 mm, y=1.3 mm

Figure 5.11: Time evolution of velocity fluctuations (u_f, v_f) at U_∞= 25 m/s.

Figure 5.11 shows the time evolution of velocity fluctuations (u_f and v_f) for U_∞=25 m/s. The time traces of velocity fluctuations are plotted for positions x=10.20, 15.40 and 28.30 mm (at y=1.3 mm) respectively. Similar behaviour is observed as explained above for U_∞=15 and 20 m/s cases. Therefore on the basis of time traces of velocity fluctuations, overall it can be concluded that the T-S waves continue to grow stronger as we move further downstream. The typical appearance of T-S waves is in the form of wave packets which can be clearly visible for U_∞=15, 20 and 25 m/s respectively. Furthermore, the power spectra of velocity fluctuations are plotted which will provide the information about the frequency and energy content of T-S waves.

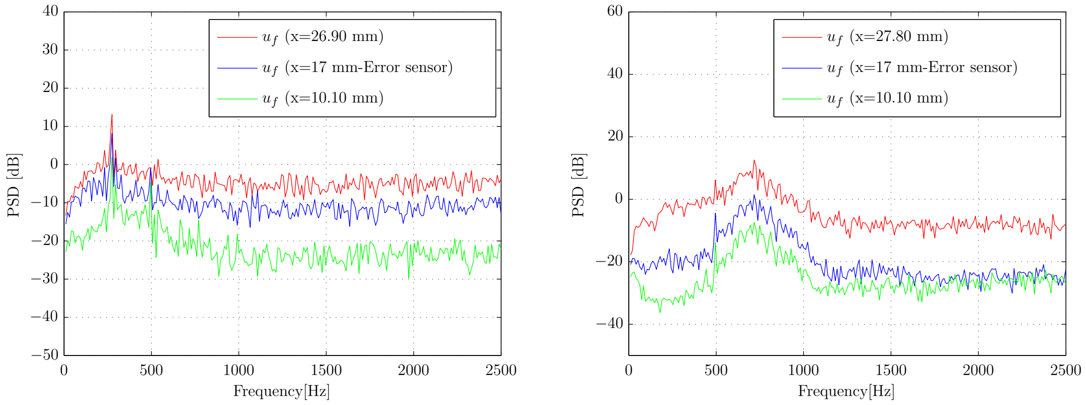

(a) U_∞=10 m/s

(b) U_∞=15 m/s

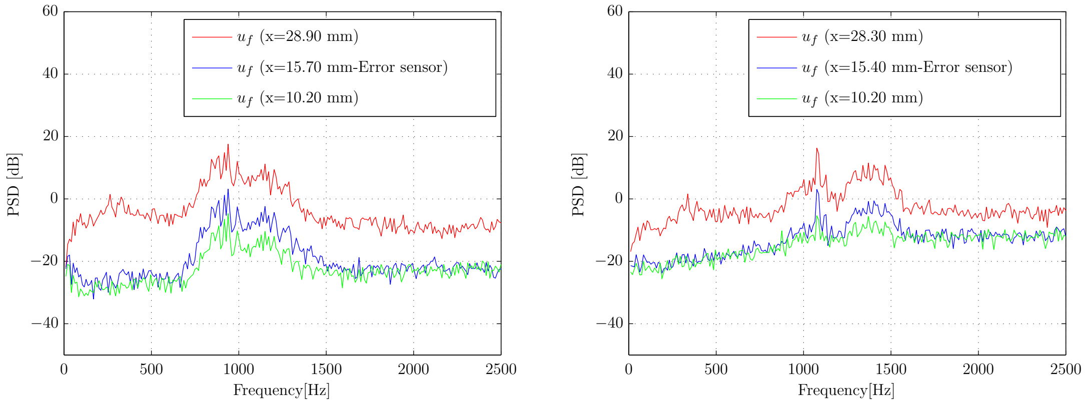

(c) U_∞=20 m/s

(d) U_∞=25 m/s

Figure 5.12: PSD of velocity fluctuations (u_f) for clean configuration at U_∞=10, 15, 20 and 25 m/s.

PSD of velocity fluctuations (u_f) is depicted in Figure 5.12 for freestream velocity 10, 15, 20 and 25 m/s. These are plotted at three different streamwise positions for there respective velocities. Welch's algorithm is used to compute the spectra with a window size of 512 and an overlap of 50%. The power spectral density is plotted on the y-axis against frequency on the x-axis. The selection of window size is done on the basis of convergence criterion which is given by eq 5.1, where N_{PIV} is number of PIV samples and WS is the window size. This criterion is used throughout the thesis for selecting window size to compute the spectra.

$$\frac{N_{PIV}}{WS} > 10 \tag{5.1}$$

For U_∞=10, 15, 20 and 25 m/s, the spectra of the velocity fluctuations shows that T-S waves have the form of a multi frequency wave train. In addition, the energy content of the naturally occurring

T-S waves spread over the whole frequency range is significantly higher for the downstream position as compared to upstream position. As can be seen, the T-S waves domain shifts to higher frequencies with increasing freestream velocity as reported by (Engert and Nitsche, 2008). The spectra for freestream velocity U_∞=10, 15, 20 and 25 m/s plotted for three measured positions shows the dominant T-S wave appears at a frequency of 274, 717, 938.7 and 1076 Hz respectively. On comparing with frequency at which the dominant T-S waves occurs compared U_∞=10 m/s, it gives a shift of frequency=443, 665 and 802 Hz.

With the convection velocity of the T-S waves and the corresponding T-S frequencies, the T-S wavelength can be calculated using $\lambda_{TS} = c_{conv}/f_{TS}$. The c_{conv} is approximated using $0.5U_\infty$ (Dovgal et al., 1989). The λ_{TS} values is depicted in Table 5.4. It can be inferred from the Table 5.4 that as the flow velocity increases, the dominating frequency f_{TS} of T-S waves increases.

Table 5.1: Properties of dominating T-S wave frequency from PIV.

U_∞	c_{conv}	f_{TS} [PIV]	λ_{TS} [PIV]
[m/s]	[m/s]	[Hz]	[m]
10	5	274.2	0.0182
15	7.5	717.2	0.0105
20	10	938.7	0.0106
25	12.5	1076	0.0116

5.2.4 Spectral analysis of surface pressure fluctuations

Figure 5.13 shows the power spectra of reference and error sensor for U_∞=10 to 25 m/s. The unfiltered signals are calculated using the average periodogram method for estimating the PSD (Welch,1967). The resulting spectra are firstly normalized with V_{ref}=1 volts to make them non dimensional and then converted to the decibel scale. The number of points taken for Fast Fourier Transform (FFT) is 4096. The power spectral density is plotted on the y-axis against frequency on the x-axis. Figure 5.13 shows that for both the reference and error sensor, the unstable domain shifts to higher frequency with increasing flow velocity. The strong single frequency components visible in the spectra for U_∞=10 to 25 m/s, are the dominating T-S wave frequency for their respective velocities. With the convection velocity of the T-S waves and the corresponding T-S frequencies, the T-S wavelength can be calculated using $\lambda_{TS} = c_{conv}/f_{TS}$. The c_{conv} is approximated using $0.5U_\infty$ (Dovgal et al., 1989). The λ_{TS} values is depicted in Table 5.2. It can be inferred from the Table 5.2 that as the flow velocity increases, the dominating frequency f_{TS} of T-S waves increases. The peak of power spectra shows the frequency

Table 5.2: Properties of dominating T-S wave frequency from microphone.

U_∞	c_{conv}	f_{TS} [Ref]	λ_{TS} [Ref]	f_{TS} [Error]	λ_{TS} [Error]
[m/s]	[m/s]	[Hz]	[m]	[Hz]	[m]
10	5	293	0.0171	269	0.0186
15	7.5	488	0.0154	732	0.0102
20	10	952	0.0105	928	0.0108
25	12.5	1074	0.012	1074	0.012

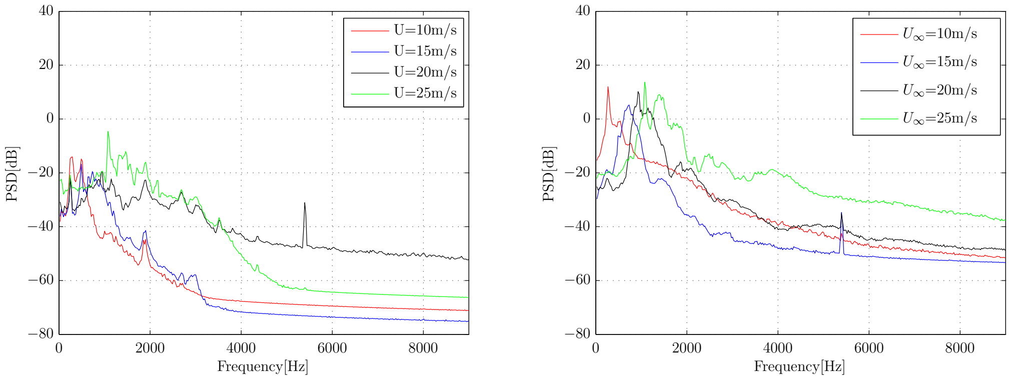

(a) Microphone-5(Reference Sensor)

(b) Microphone-6(Error Sensor)

Figure 5.13: Power spectral density of microphone signals for clean configuration at different velocities

at which natural T-S waves occur. PSD of the reference sensor shows that T-S waves have a multiple frequency for particular velocities. For instance, for U_∞=10 m/s(reference sensor spectra), shows that the natural T-S waves occur at two frequencies of 293 and 488 Hz. In the PSD of error sensor, peak at 269, 732, 928 and 1074 Hz can be identified as the dominating part of the T-S waves for particular velocities. This first peak is followed by a second one. In addition, PSD for error sensor also shows that the energy content of the naturally occurring T-S waves becomes significantly higher for one of the frequencies and other dampens out. This is explained by the fact, the T-S waves are amplified on proceeding downstream. The peak occurrence at a frequency of 5.4 kHz for U_∞=20 m/s (reference sensor) and 15 m/s (error sensor) may be due to the laser and should be ignored.

5.3 Closed loop control

The Adaptive FXLMS control (close loop) study is performed with an objective of cancelling natural T-S waves using a DBD plasma actuator. The concept deals with the cancellation of T-S waves by superimposing them with adaptive counter waves. A detailed explanation is given in Chapter 3. The angle of attack is adjusted according to the free stream velocity U_∞=17, 20 and 25 m/s in order to have natural TS waves. The 3-D roughness element (carborundum, 0.84 mm) has been applied on the suction side starting from the trailing edge. The roughness elements are used to promote transition to turbulence and thereby eliminate tones. The test case for the close loop case are presented in the Table 4.6.

This section gives a statistical description of the mean velocity field and the Reynolds stresses for U_∞=17, 20 and 25 m/s respectively. Data used in this section has been recorded using the high speed PIV set-up described in Chapter 4. Statistics of the velocity field in this section have been obtained by averaging 5381 statistically independent vector fields recorded at a sampling rate of 5.4 kHz. Furthermore, PSD of reference and error microphone signals are discussed. The microphone data are recorded at a sampling rate of 100 kHz.

5.3.1 Mean velocity profiles

Figure 5.14 shows the streamwise evolution of the mean velocity profiles on the suction side for no control and control case. Tested freestream velocities range from 17 to 25 m/s at chord Reynolds of 2.3×10^5 to 3.3×10^5 respectively. The location at which the mean velocity profiles were plotted at several stations with streamwise coordinates is x= -2, 5.5, 13, 20.5 and 28 mm. This represents 64 %, 68 %, 72 %, 75 % and 79 % of the chord respectively. Rayleigh's first theorem states that the existence of an inflection point is a necessary condition for the shear layer to be unstable. The profiles depicted in Figure 5.14 exhibits an inflection point which confirms that there are instabilities present in the flow for their respective velocities which are found to be T-S waves. This will be later confirmed by observing the typical characteristics of T-S waves in u_{rms} profile and time traces of velocity fluctuations.

For U_∞=17 m/s, the mean profiles at position x=5.5 and 13 mm exhibits an inflection point for no control whereas with control the inflection point is suppressed. Similar behaviour is also observed for U_∞=20 m/s for the similar streamwise positions. This shows that the close loop control using DBD plasma actuator attenuates the instabilities. The velocity profiles for U_∞=25 m/s exhibits an inflection point but these profiles looks fuller as compared to other two velocities. In addition, for U_∞=20 and 25 m/s, the inflection point for streamwise position x<5.5 are closer to the wall whereas for another three positions are further away. As mentioned above, that pressure gradients along the chord strongly affect the amplification of T-S waves (Boik and Klingmannlt, 1994). Therefore, at U_∞=20 m/s (α=1.66 deg) shows higher amplitudes as compared to U_∞=25 m/s (α=-0.60 deg) m/s. According to Kendall (1991) that T-S waves are more effectively excited when an adverse pressure gradient favours the amplification of T-S waves. Overall on the basis of the mean velocity profile it is evident that there is a significant effect in reduction of amplifying T-S waves.

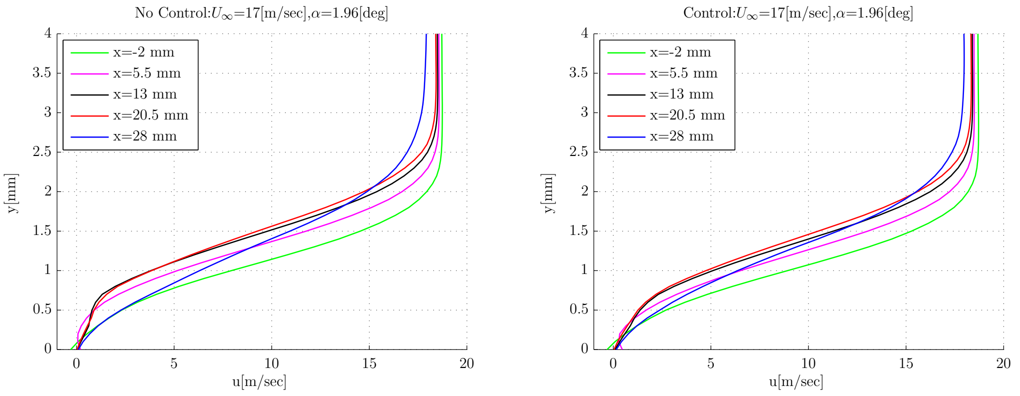

(a) U_∞=17 m/s (No control) (b) U_∞=17 m/s (Control)

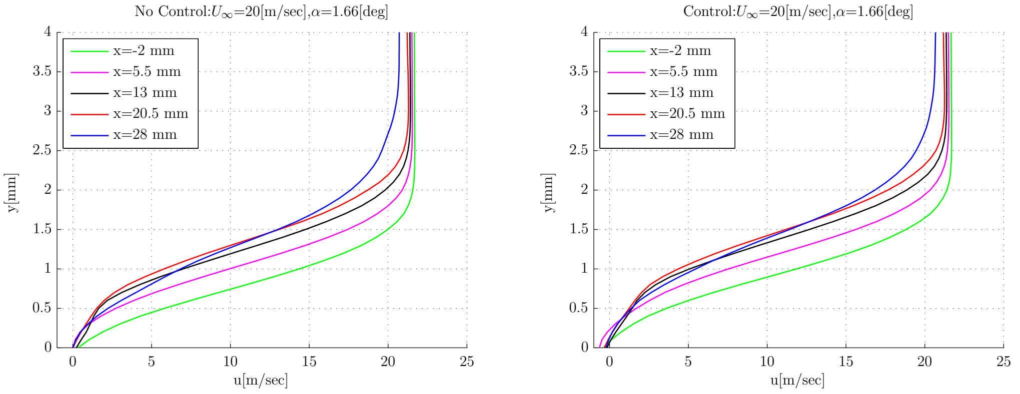

(c) U_∞=20 m/s (No control) (d) U_∞=20 m/s (Control)

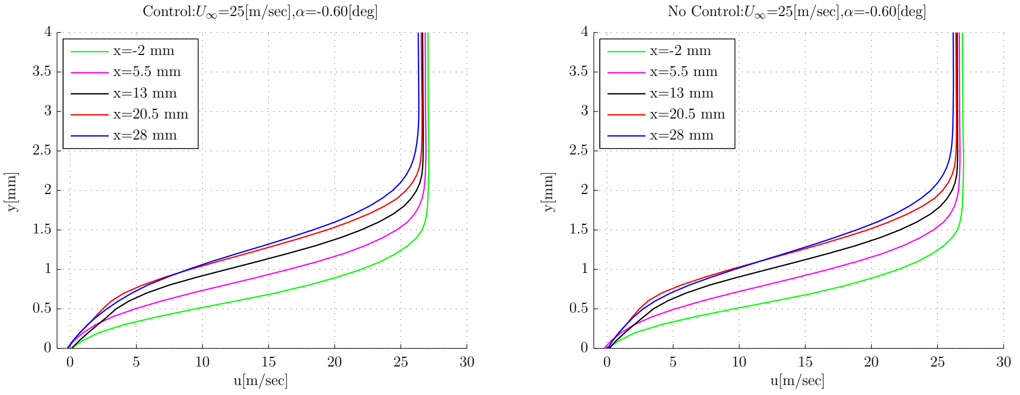

(e) U_∞=25 m/s (No control) (f) U_∞=25 m/s (Control)

Figure 5.14: Comparison of mean velocity profiles for close control loop at U_∞=17, 20 and 25 m/s.

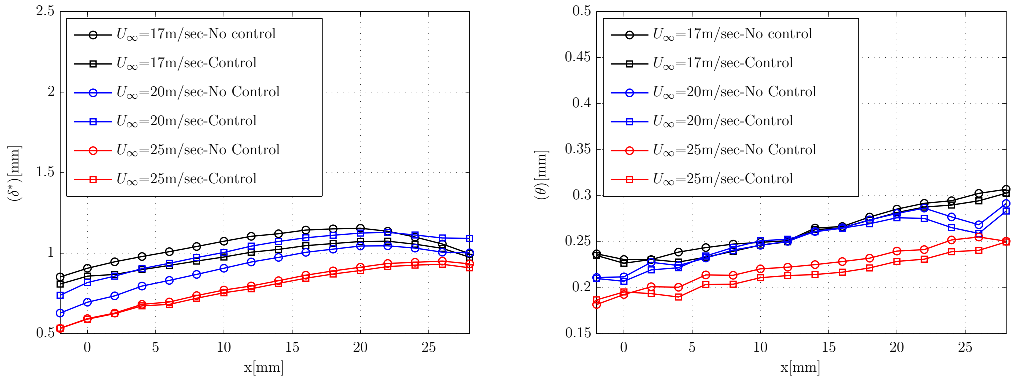

(a) Displacement thickness

(b) Momentum thickness

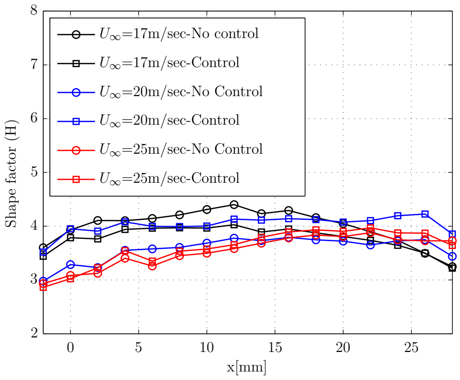

(c) Shape factor

Figure 5.15: Comparison of boundary layer parameters for close loop control at U_∞=17, 20 and 25 m/s.

The displacement thickness, momentum thickness and shape factor which will be given further, supports the reasoning of the mean velocity profile as mentioned above for no control and control cases. The line with circle and square marker respectively represents a no control and control case. Figure 5.15 shows the plot of displacement thickness, momentum thickness and shape factor against x (which is the distance along the chord).

In general, at U_∞=17, 20 and 25 m/s, the momentum thickness plot for both the cases increases on proceeding downstream. This is obvious since the boundary layer thickness grows as the flow moves over the airfoil surface which means more of the flow is affected by the friction as the distance along the surface increases. This results in the decrement of momentum in the flow due to the presence of boundary layer.

On comparing control and no control case, for U_∞=17 and 25 m/s the prior shows a significant reduction of momentum thickness on proceeding downstream whereas there is a lesser effect for U_∞=20 m/s. The shape factor (H) provides an indication of the resistance of a boundary layer to flow separation with a decreasing (H) being a favourable for resisting separation. In Figure 5.15(c) we can see for U_∞= 17 m/s, for the region (-2 mm<x>27 mm), there is a higher reduction in shape factor. In the same region for U_∞=25 m/s , there is a significant reduction whereas there is a lesser effect for U_∞=20 m/s. This supports the reasoning mentioned above for a mean velocity profile. This is explained by the fact that the adaptive FXLMS controller is effectively attenuates the growing T-S waves by superimposing them with adaptive counter waves.

5.3.2 Turbulence level and Reynolds stress profiles

Figure 5.17 shows the qualitative investigation of Reynolds stress contours ($\overline{uu}$, $\overline{vv}$, $\overline{uv}$) for freestream velocities U_∞=17 m/s (no control and control cases). The contours for other velocities U_∞=20 and 25 m/s are depicted in Appendix D. Furthermore, the quantitative effect of control will be discussed in detail by observing the Reynolds stress and u_{rms} profile as shown in Figure 5.18, 5.19, 5.20 for freestream velocities U_∞=17, 20 and 25 m/s respectively.

The $\overline{uu}$,$\overline{vv}$ are the normal stress where $\overline{uv}$ represents shear stress. The contours with no control cases shows a significant amount of Reynolds stresses in the downstream position. This is explained by the fact that as we move further downstream the T-S waves continues to grow stronger (the flow moves over the airfoil surface which means more of the flow is affected by the friction as the distance along the surface increases). Therefore, these instabilities modify the phases of velocity perturbations leading to higher Reynolds stresses in the downstream position. With the control case, there is a significant amount of reduction in normal and shear stresses as shown in Figure 5.17 (b),(d) and (f) respectively. This is due to the adaptive cancellation of instabilities (T-S waves) using DBD plasma actuator by close loop control. The actuator is powered using a continuously adapted signal selected by the controller.

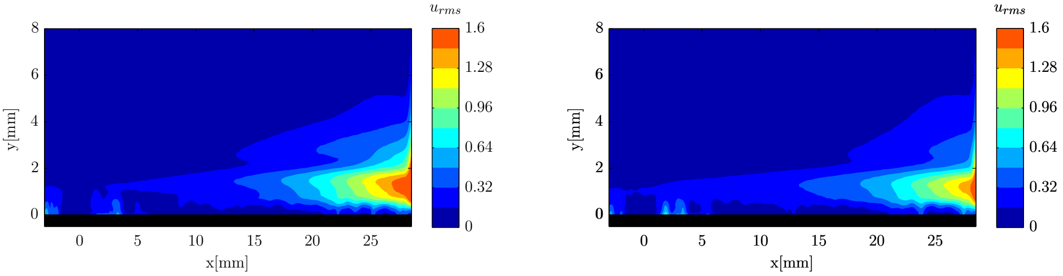

(a) u_{rms}-No control

(b) u_{rms}-Control

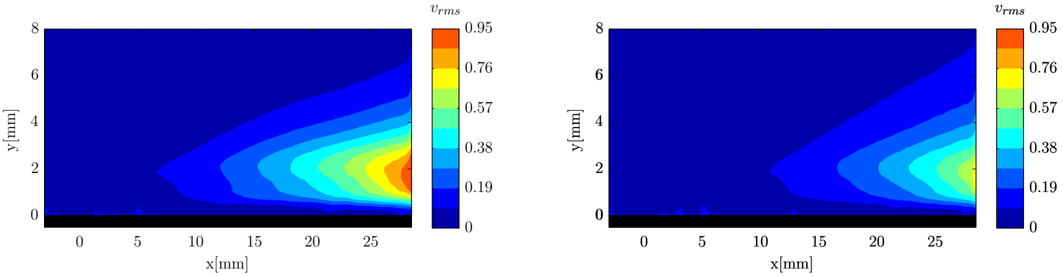

(c) v_{rms}-No control

(d) v_{rms}-Control

Figure 5.16: RMS contours for close loop control at U_∞=17 m/s.

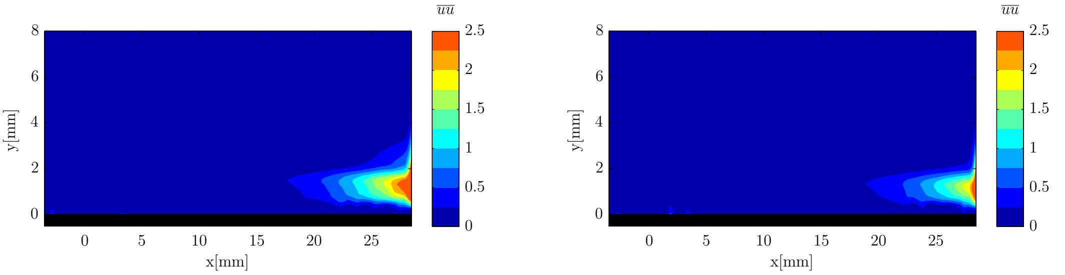

(a) $\overline{uu}$-No control (b) $\overline{uu}$-Control

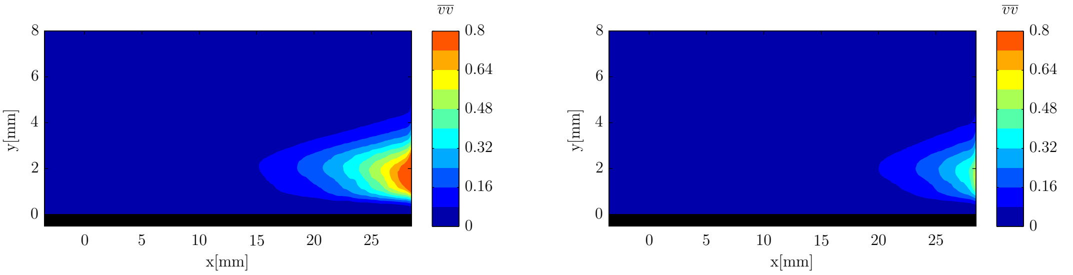

(c) $\overline{vv}$-No control (d) $\overline{vv}$-Control

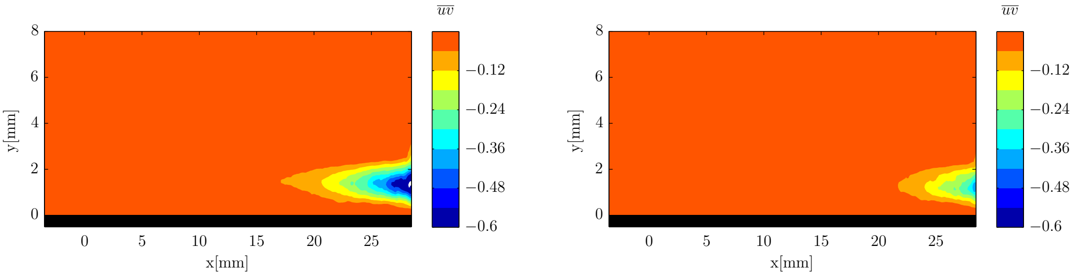

(e) $\overline{uv}$-No control (f) $\overline{uv}$-Control

Figure 5.17: Reynolds stress contours for close loop control at U_∞=17 m/s.

The Reynolds stresses and velocity fluctuation profile (u_{rms}) for U_{∞}=17 m/s (α=1.96 deg) are shown in Figure 5.18 with solid and dotted line representing the no control and control cases respectively. The u_{rms} and $\overline{uu}$ profile exhibits a typical footprint of T-S waves: the small maximum, a minimum just below it and a strong increase of the turbulence near the wall (Grundmann, 2008). The natural T-S waves are cancelled for streamwise positions x=13, 20.5 and 28 mm considerably with close loop control. The $\overline{uu}$ maximum values at x=28 mm is 2.59 m^2/s^2 (no control) whereas with control it is reduced to 2.04 m^2/s^2 which is significant. The reduction of normal stress $\overline{vv}$ and shear stress $\overline{uv}$ is also significant. Overall the maximum values of average Reynolds stress component ($\overline{uu}$) are damped by 18-22 % and ($\overline{vv}$) by 54-60 % of the uncontrolled boundary layer. The maximum values of Reynolds stress profiles of $\overline{uu}$ and $\overline{vv}$ will be plotted and discussed in detail under the section (Comparison of maximum peak reduction).

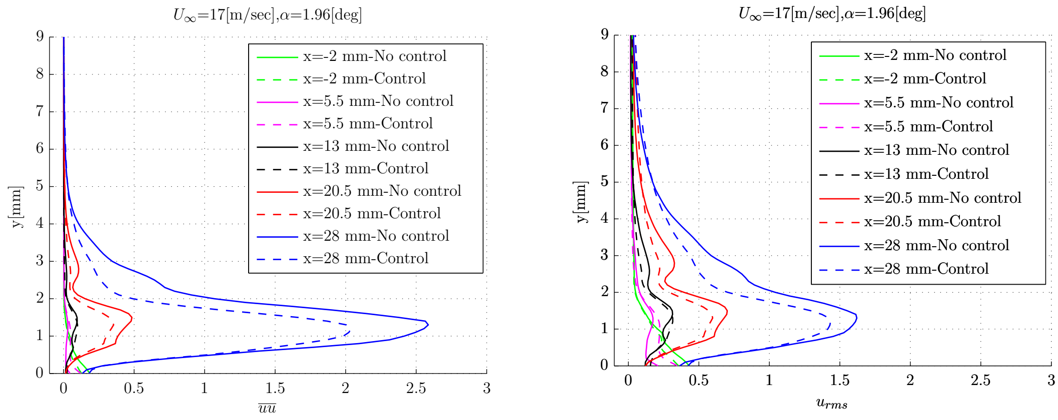

(a) $\overline{uu}$ (b) u_{rms}

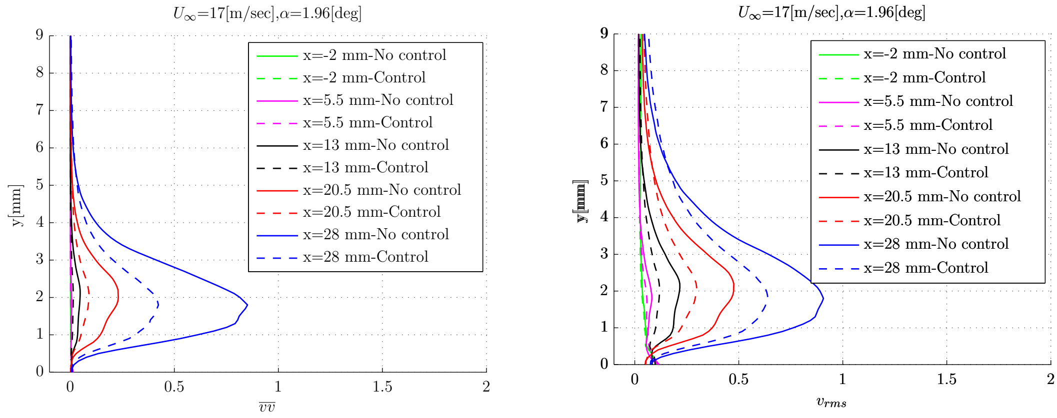

(c) $\overline{vv}$ (d) v_{rms}

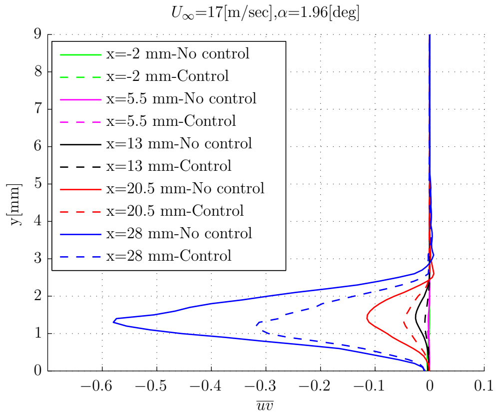

(e) $\overline{uv}$

Figure 5.18: Reynolds stress and u_{rms} profile for close loop control at U_∞=17 m/s.

The Reynolds stresses and velocity fluctuation profile (u_{rms}) for U_∞=20 m/s (α=1.66 deg) is shown in Figure 5.19 with solid and dotted line representing the no control and control cases respectively. Similar to the case of U_∞=17 m/s, the u_{rms} and $\overline{uu}$ profile of U_∞=20 m/s exhibits a T-S waves highlighted by a two peak distribution: the small maximum, a minimum just below it and a strong increase of the turbulence near the wall (Grundmann, 2008). The striking difference from earlier case is the a strong increase of amplitude of $\overline{uu}$. This is due to the combination of increase in free stream velocity and angle of attack (α=1.66 deg) which results in amplification of sensitive viscous instabilities (T-S waves). It shows maximum values of 5.78 m^2/s^2 for no control case at x=28 mm whereas with control case it is reduced to 4.84 m^2/s^2 which is significant. The T-S waves are effectively cancelled for streamwise positions x=13, 20.5 and 28 mm while show a significant suppression for their other respective positions. The reduction of normal stress $\overline{vv}$ and shear stress $\overline{uv}$ is also significant. Overall the amplitudes of the fluctuations ($\overline{uu}$) are damped by 8-16 % and ($\overline{vv}$) by 24-28% of the uncontrolled boundary layer.

The Reynolds stresses and velocity fluctuation profile (u_{rms}) for U_∞=25 m/s (α=-0.60 deg) is shown in Figure 5.19 with solid and dotted line representing the no control and control cases respectively. It should be noted that there is a strong increase of normal stress ($\overline{uu}$,$\overline{uv}$) holding the maximum value of 4.6 m^2/s^2 and 0.76 m^2/s^2 respectively at x=28 mm. These values are smaller for the same streamwise position as compared to U_∞=20 m/s. This is explained by the fact the for U_∞=25 m/s (α=-0.60 deg) the angle of attack is very small as compared to U_∞=20 m/s (α=1.66 deg). Although, the freestream velocity is high but due to very small angle of attack (combination of both velocity and angle of attack), there is less adverse pressure gradient, therefore instabilities development will be less stronger as compared to later case. Furthermore, substantial effect is observed in cancelling the instabilities developed along the streamwise position using close loop control. For position x=28 mm, it shows enhancement of normal stresses ($\overline{uu}$) with control which is unusual. The reason for this behaviour is unclear to the author. The close loop control effect ($\overline{vv}$,$\overline{uv}$) seems to have pronounced effect for the positions x=13, 20.5 and 28 mm. Overall the maximum peak of normal Reynolds stress ($\overline{uu}$) are damped to a values by 8-12 % and ($\overline{vv}$) by 16-22 % of the uncontrolled boundary layer.

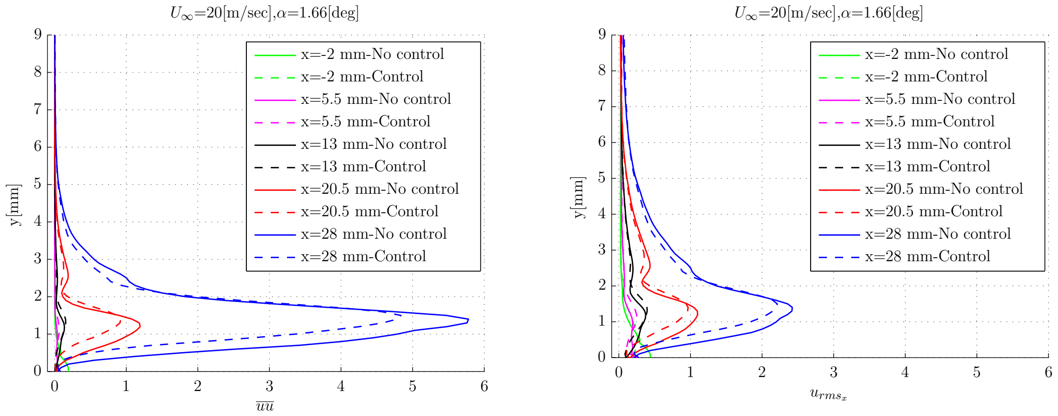

(a) $\overline{uu}$

(b) u_{rms}

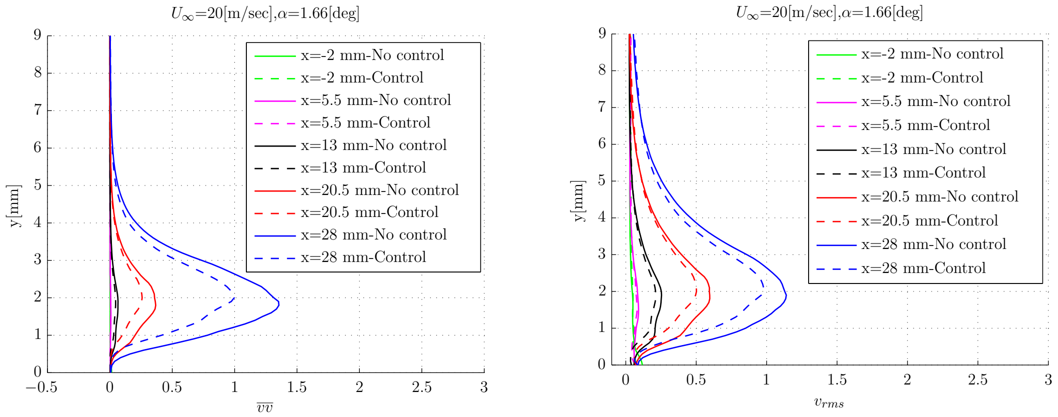

(c) $\overline{vv}$

(d) v_{rms}

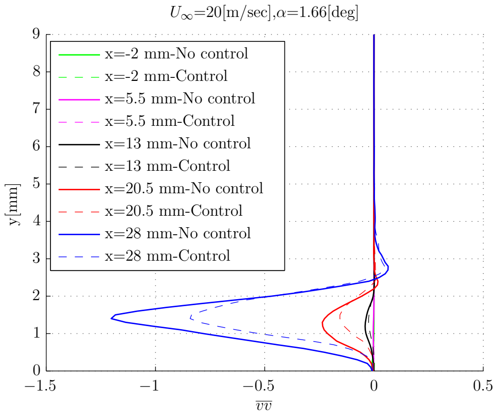

(e) $\overline{uv}$

Figure 5.19: Reynolds stress and u_{rms} profile for close loop control at U_∞=20 m/s.

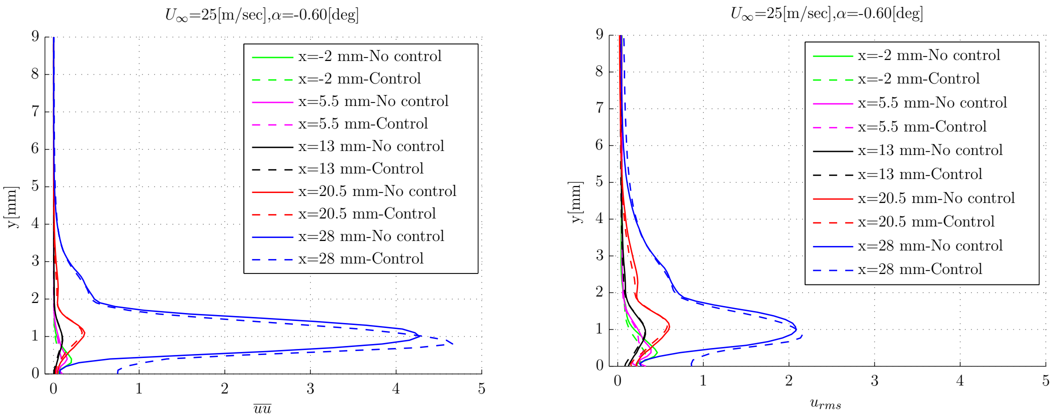

(a) $\overline{uu}$ (b) u_{rms}

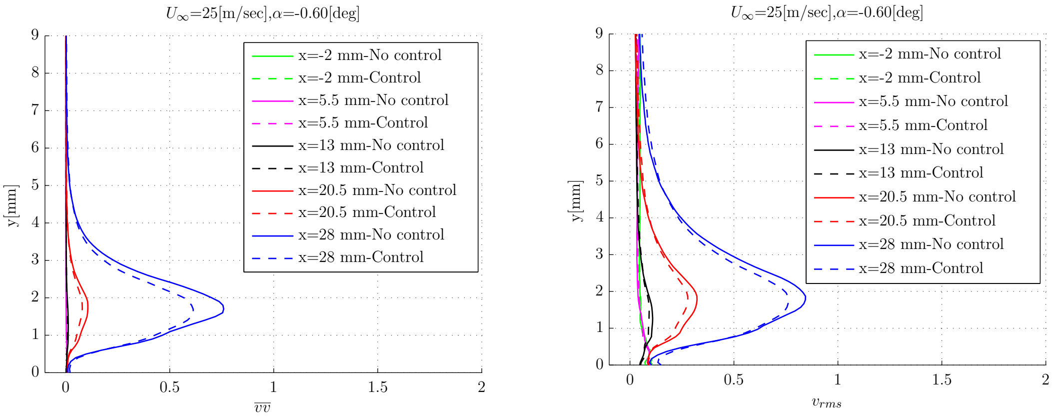

(c) $\overline{vv}$ (d) v_{rms}

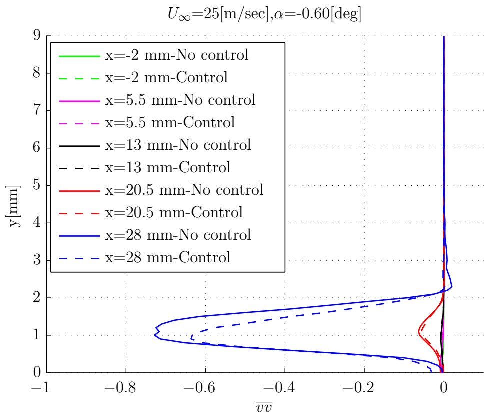

(e) $\overline{uv}$

Figure 5.20: Reynolds stress profile for close loop control at U_∞=25 m/s.

5.3.3 Comparison of maximum peak reduction

The maximum peak of Reynolds stress profiles of $\overline{uu}$ and $\overline{vv}$ along the suction side is shown in Figure 5.21 (a)-(f) for both control and no control case. For all the velocities, before x=5 mm, the maximum amplitude of $\overline{uu}$ and $\overline{vv}$ remains very small whereas after x=10 mm, a strong increase in the amplitude is observed. This is explained by the fact as the flow moves over the body which means more flow is affected by the viscous forces. These viscous forces modify the phases of the velocity perturbations which lead to positive Reynolds stresses, enabling the transfer of energy from the mean flow to the disturbance. The time traces of velocity fluctuations given further will support this fact.

The maximum peak of Reynolds stress profiles of ($\overline{uu}$ and $\overline{vv}$) with control case has shown a higher reduction in the freestream velocity U_∞=17 m/s. For U_∞=20 and 25 m/s, it also shows a significant reduction of maximum amplitude. The reduction is due to the cancellation of T-S waves by superimposition with continuously generated counter waves using DBD plasma actuator by means of close loop control (Adaptive FXLMS control). Therefore, from this observation it can be concluded that the cancellation of T-S waves is higher for 17 m/s while significant suppression is maintained for higher velocities. This is explained by the fact that the relative body force generated by the plasma remains same whereas instabilities grows stronger as the velocity increases, therefore, effectiveness is reduced at higher velocities. The Table 5.3 shows the closed loop control effectiveness of maximum normal Reynolds stresses at the downstream position x=28 mm for U_∞=17, 20 and 25 m/s.

Table 5.3: Control effectiveness of maximum normal Reynolds stresses at x=28 mm.

U_∞	$\overline{uu}$ (No control)	$\overline{uu}$ (Control)	$\overline{vv}$ (No control)	$\overline{vv}$ (Control)
[m/s]	$[m^2/s^2]$	$[m^2/s^2]$	$[m^2/s^2]$	$[m^2/s^2]$
17	2.59	2.04	0.85	0.42
20	5.78	4.84	1.36	0.99
25	4.34	4.6	0.76	0.61

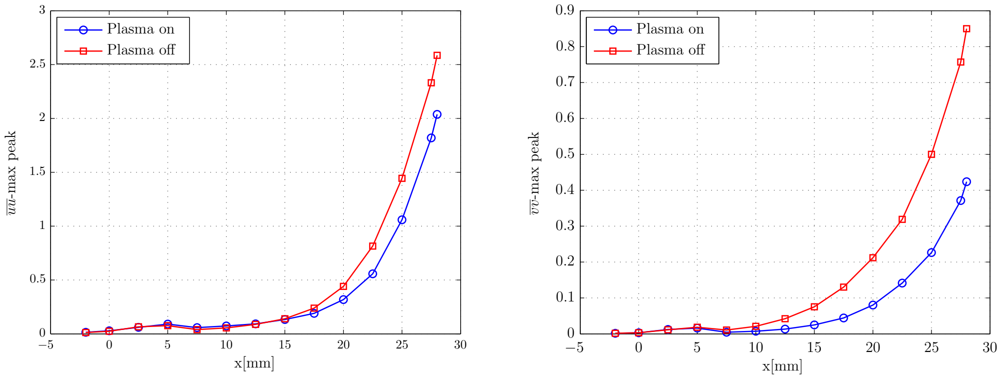

(a) $\overline{uu}$ max peak at U_∞=17 m/s.

(b) $\overline{vv}$ max peak at U_∞=17 m/s.

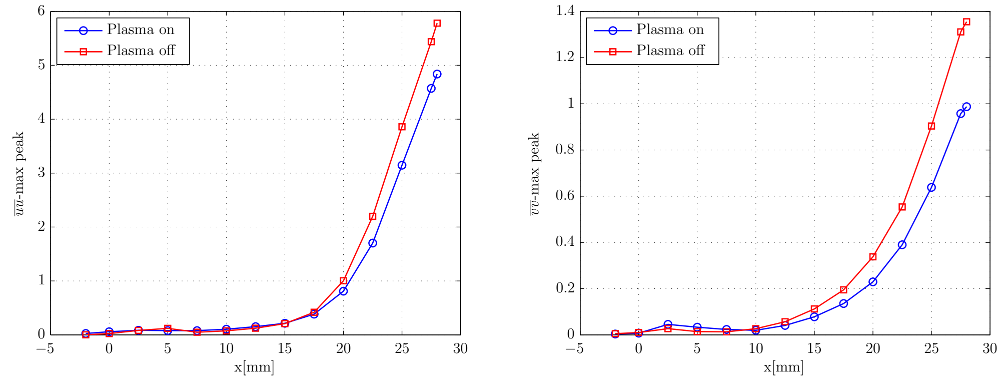

(c) $\overline{uu}$ max peak at U_∞=20 m/s.

(d) $\overline{vv}$ max peak at U_∞=20 m/s.

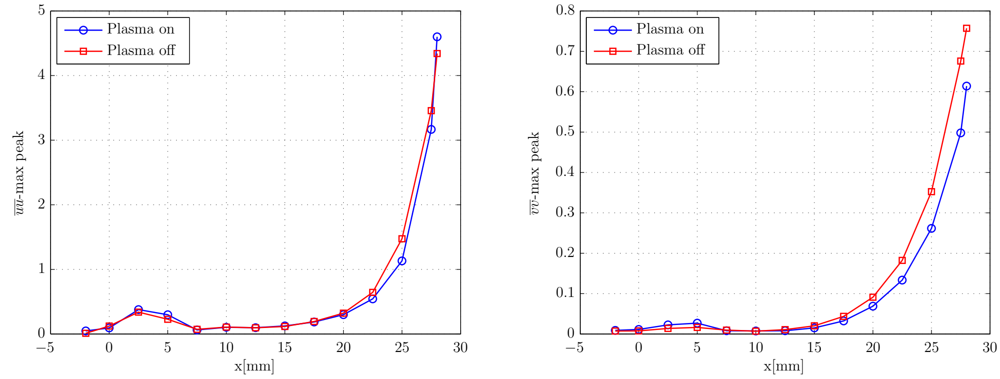

(e) $\overline{uu}$ max peak at U_∞=25 m/s.

(f) $\overline{vv}$ max peak at U_∞=25 m/s.

Figure 5.21: Comparison of the evolution of maximum $\overline{uu}$,$\overline{vv}$ for close loop control at U_∞= 17, 20 and 25 m/s respectively

5.3.4 Time evolution

The time traces of velocity fluctuations u_f (in x-direction) and v_f (in y-direction) for U_∞=17, 20 and 25 m/s is plotted for three streamwise positions. The time traces is shown here for U_∞=17 m/s whereas other two cases are depicted in Appendix E. Data used in this section has been recorded using the high speed 2-component PIV set-up described in Chapter 4. Statistics of the velocity field in this section have been obtained by averaging 5381 statistically independent vector fields recorded at a sampling rate of 5.4 kHz. The position is selected at the uppermost downstream position. Additionally, this type of study will help to demonstrate the T-S wave cancellation effect.

Figure 5.22 shows the time traces of velocity fluctuations (u_f and v_f) for U_∞=17 m/s at positions x=10, 14.71 and 27.70 mm (for y=1.3 mm). The fluctuations shows the footprint of the development of T-S waves in its early stage in which amplitudes of these fluctuations are small. These occurs in the form of wave packets which can be visualised in Figure 5.22(a)-(d). Secondly, these T-S waves become amplified on proceeding downstream. This is explained by the fact as the flow moves over the body which means more of the flow is affected by the viscous forces. These viscous forces modify the phases of the velocity perturbations which lead to positive Reynolds stresses, enabling the transfer of energy from the mean flow to the disturbance. Therefore, as we move further downstream, the T-S waves grow stronger.

With the control actuator working, the amplitude of the velocity fluctuations reduced significantly for upstream positions especially in v_f fluctuations which can be visualised in Figure 5.22(a)&(d). In addition, only small changes between control and no control case can be observed at (x=27.70 mm) downstream positions. This is explained by the fact that, at the downstream position, the T-S waves grows stronger. It can be visualised in Figure 5.22(e)-(f). In addition, their wave packets seems to get distorted which indicates that these instabilities are in intermittent stage. For higher velocities, the similar trend is observed. Furthermore, PSD of the velocity fluctuation (u_f) which will be given further, supports the reasoning of the time traces for no control and control cases.

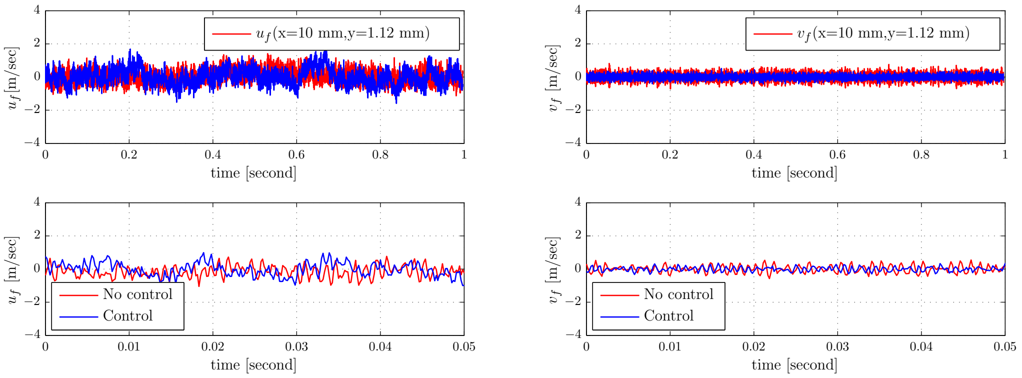

(a) u_f at x=10 mm

(b) v_f at x=10 mm

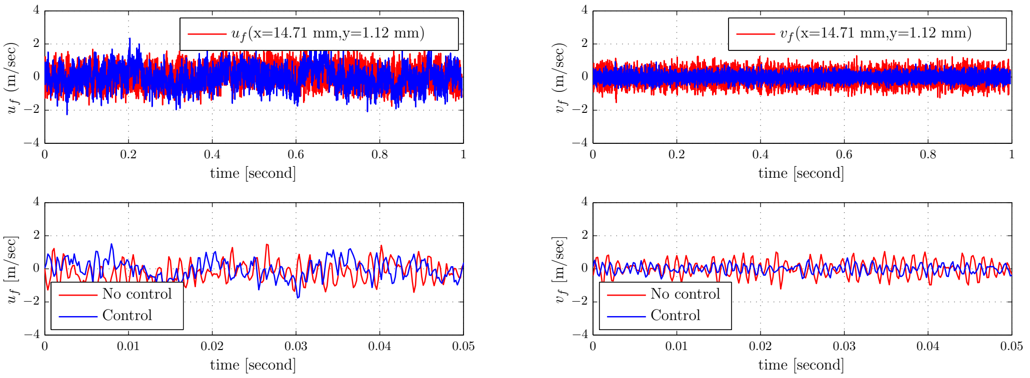

(c) u_f at x=14.71 mm

(d) v_f at x=14.71 mm

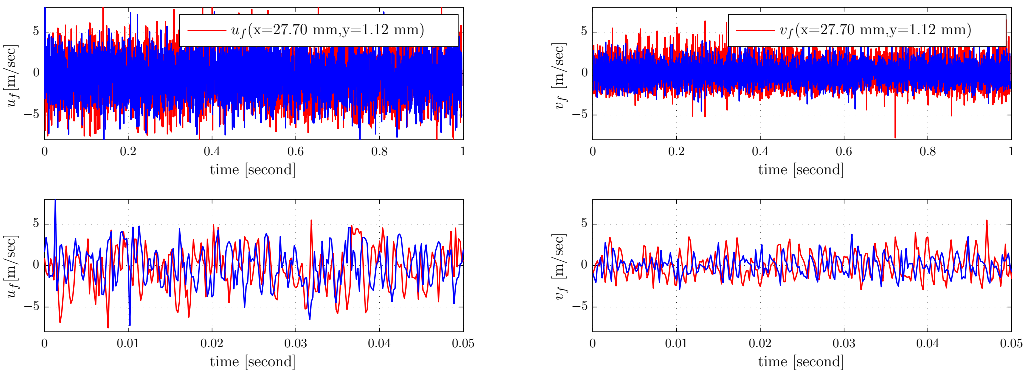

(e) u_f at x=27.70 mm

(f) v_f at x=27.70 mm

Figure 5.22: Time evolution of velocity fluctuations (u_f,v_f) for close loop control at U_∞= 17 m/s .

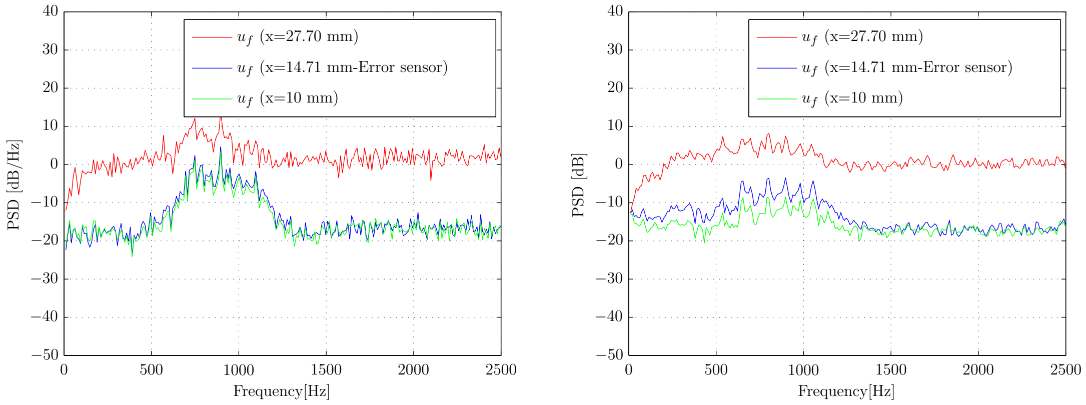

(a) U_∞=17 (No control)

(b) U_∞=17 m/s(Control)

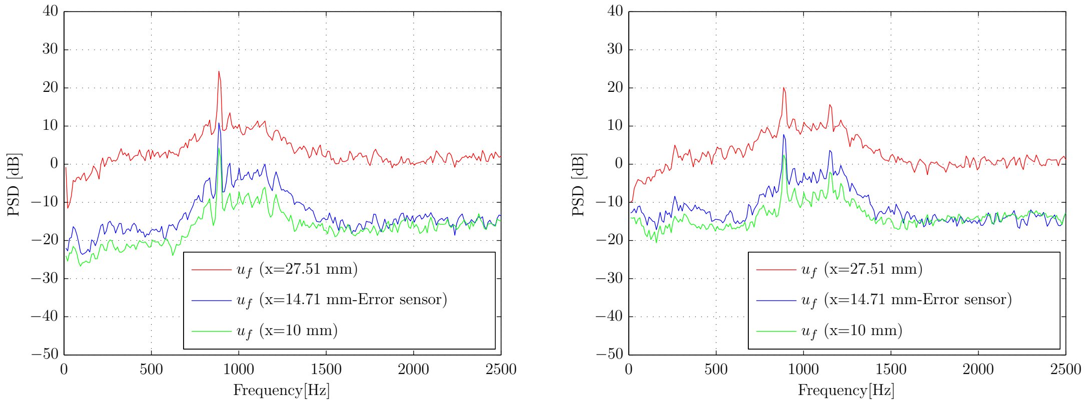

(c) U_∞=20 m/s (No control)

(d) U_∞=20 m/s (Control)

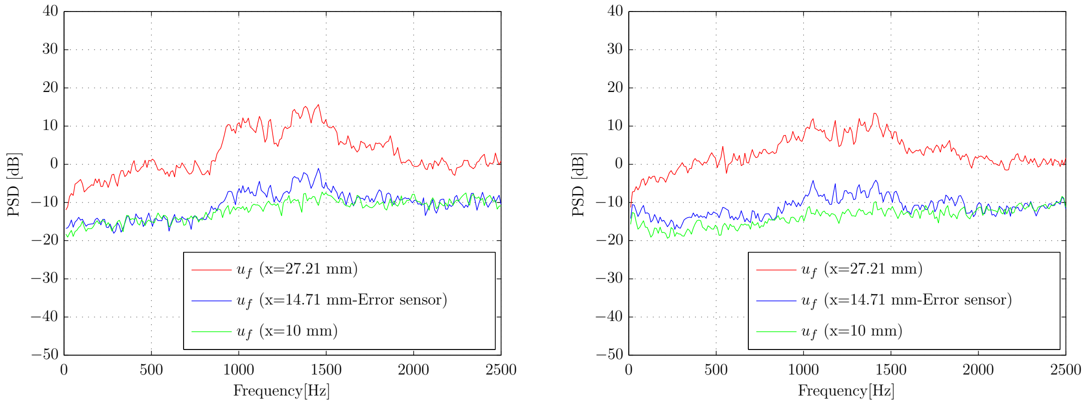

(e) U_∞=25 m/s (No control)

(f) U_∞=25 m/s (Control)

Figure 5.23: PSD of velocity fluctuations (u_f) for close loop at U_∞=17, 20 and 25 m/s.

Figure 5.23 shows the PSD of velocity fluctuations u_f plotted for U_∞=17, 20 and 25 m/s with no control and control case for three streamwise cordinates. The three positions are selected such that one position is at the upstream of error sensor, second on the error sensor and last at the downstream of error sensor. Average periodogram method for estimating the PSD (Welch,1967) with a window size of 512 and an overlap of 50%. The selection of window size is done on the basis of convergence criterion which is given by eq 5.1.

In general, PSD of the fluctuation for all the cases shows that the that the T-S waves have the form of a multi frequency wave train. Secondly, the unstable domain shifts to higher frequency with increasing flow velocity. In addition, there is a remarkable difference in terms of energy content of the spectra for uttermost downstream position as compared to other two upstream position. This is explained by the fact that on proceeding downstream the amplitude of instabilities shows significant rise as explained in u_{rms} and a stress profile section which lead to higher energy content of the spectra for the downstream position.

It should be noted that the spectra with control case indicate a higher reduction over the whole frequency range of the T-S waves for their respective streamwise position. In specific, a higher reduction for upstream position while significant suppression is maintained for downstream positions. For instance from Figure 5.23 (a) & (b) at U_∞=17 m/s, the dominant T-S wave appears at a frequency of 897 Hz (both no control and control)for all the three respective positions. The energy content of the spectra reduces to a significant amount for control cases especially for upstream positions. Similar trend is observed for other two freestream velocities U_∞=20 and 25 m/s respectively. The spectra for U_∞=20 m/s shows higher energy content for the uppermost downstream position which is also supported in terms of higher stresses as seen in Figure 5.18 (a), 5.19 (a) and 5.20 (a).

5.3.5 Spectral analysis of surface pressure fluctuations

Figure 5.24 shows the power spectra of microphone 5 (reference sensor) and microphone 6 (error sensor) for U_∞=17, 20 and 25 m/s control and no control case. Average periodogram methods for estimating the PSD (Welch,1967) of the unfiltered signals. The resulting spectra are firstly normalized with V_{ref}=1 volts to make them non dimensional and then converted to the decibel scale. The number of points taken for Fast Fourier Transform (FFT) is 4096. The power spectral density is plotted on the y-axis against frequency on the x-axis. It is important to mention once again that the reference and error sensor are placed upstream and downstream of the DBD plasma actuator as mentioned under the section Aifoil model in Chapter 4. In addition, the reference sensor is passed through a low pass filter (LPF). A low-pass filter (LPF) passes low-frequency signals and attenuates signals with frequencies higher than the cut off frequency. The experimental setup arrangement is shown in Figure 4.5 in Chapter 4.

The spectra of reference and error sensor are shown in both cases in Figure 5.24 (a) & (b). One can distinguish the spectra for the no control and control case. The spectra of error sensor for U_∞=17 m/s indicate a higher reduction. The reason for being that the instability effects caused by the T-S waves is reduced at the streamwise position of the actuator by starting close loop control. This indicates the suppression of the tonal component of T-S waves with closed-loop actuation. The reduction up to 7.65 dB is achieved over the whole(660 Hz to 1270 Hz) frequency range of natural T-S waves. The spectra of the reference sensor also show reduction upto 3 dB over the whole(708 Hz to 1100 Hz) frequency range of natural TS waves. This shows that the actuator has an upstream influence for U_∞=17 m/s. Although, this effect is absent for other two freestream velocities U_∞=20 and 25 m/s.

With the convection velocity of the T-S waves and the corresponding T-S frequencies, the T-S wavelength can be calculated using $\lambda_{TS} = c_{conv}/f_{TS}$. The c_{conv} is approximated using $0.5U_\infty$ (Dovgal et al., 1989). The λ_{TS} values for error sensor is depicted in Table 5.4. It can be inferred from the Table 5.4 that as the flow velocity increases, the dominating frequency f_{TS} of T-S waves increases. The table gives an idea about the frequency of dominating T-S waves at a particular velocity.

Table 5.4: Properties of dominating T-S wave frequency for Error microphone (No control).

U_∞	c_{conv}	f_{TS}	λ_{TS}
[m/s]	[m/s]	[Hz]	[m]
17	8.5	781.3	0.0109
20	10	879	0.0114
25	12.5	1416	0.0083

From Figure 5.24 (d) & (f), the spectra of error sensor for U_∞=20 and 25 m/s indicate a significant suppression. The suppression is considerably less as compared to the case of U_∞=17 m/s. In specific, the error spectra for U_∞=20 m/s shows a suppression of (approximately 3.7 dB) for a dominating frequency of T-S waves whereas for U_∞=25 m/s shows a suppression of (approximately 2 dB).

The RMS value of the reference and error signals for both the cases 'Plasma off'(no control) and 'Plasma on'(control) is calculated. The high RMS value of no control case represents the T-S wave amplification. RMS reduction of approximately 50 % is achieved for error sensor with 'Plasma on'whereas on the other hand there is no effect on reference sensor. The % reduction of RMS values of error microphone is depicted in Table 5.5 for control and no control case at U_∞=17, 20 and 25 m/s. Overall, the RMS reduction of approximately 50 % is achieved for a freestream velocity of 17 m/s while significant suppression of approximately 17 and 11 % is maintained for a freestream velocity=20 and 25 m/s respectively.

Table 5.5: RMS reduction of error microphone for closed loop control.

U_∞[m/s]	RMS (No control)	RMS (Control)	Reduction (%)
17	1.1969	0.7187	47.82
20	1.5728	1.3071	16.89
25	0.8515	0.7553	11.29

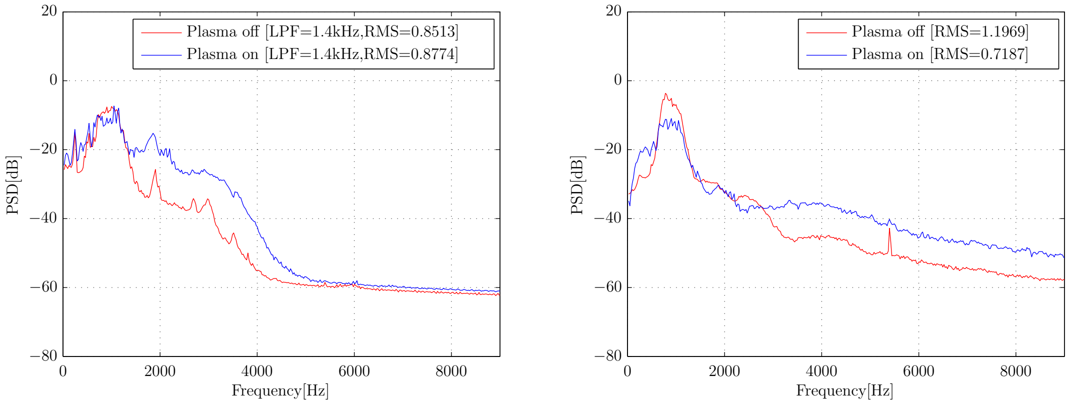

(a) U_∞=17 m/s, Microphone 5 (Reference sensor)

(b) U_∞=17 m/s, Microphone 6 (Error sensor)

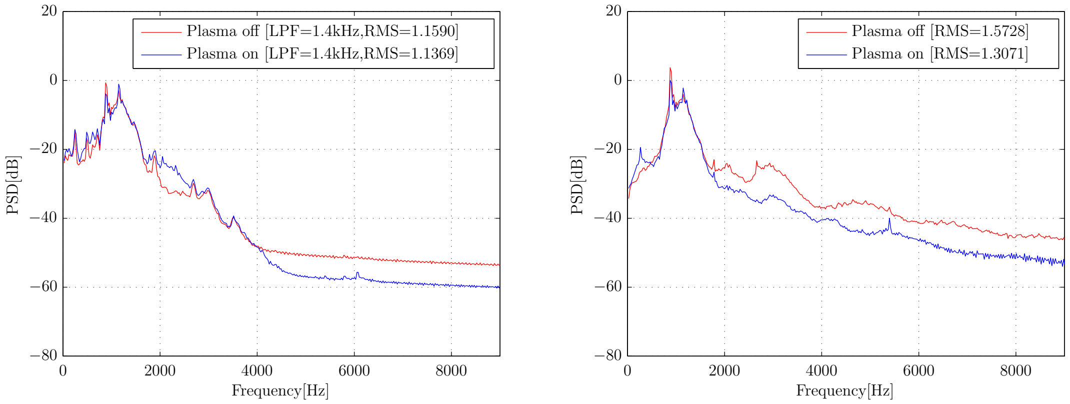

(c) U_∞=20 m/s, Microphone 5 (Reference sensor)

(d) U_∞=20 m/s, Microphone 6 (Error sensor)

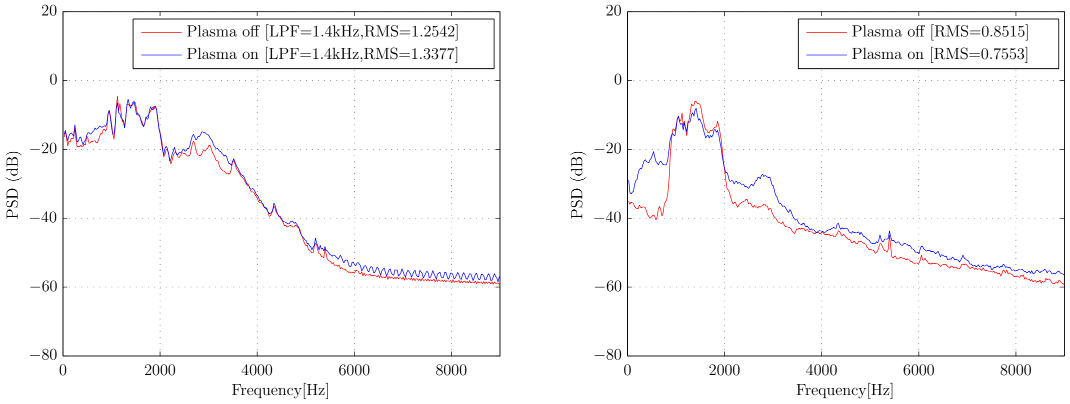

(e) U_∞=25 m/s, Microphone 5 (Reference sensor)

(f) U_∞=25 m/s, Microphone 6 (Error sensor)

Figure 5.24: PSD of microphone signals for close loop case at U_∞=17, 20 and 25 m/s.

5.4 Open loop control

In the open loop, the surface sensor placed on the airfoil surface detects the pressure fluctuations. These fluctuations are read by the program built in Labview software which yield information about the frequency of the T-S waves. The actuator is actuated at different carrier frequencies within the same and higher range of acquired T-S waves frequency. Here, the actuator is operated using non-adapted single-frequency sinusoidal signal. Later, the results are compared with closed loop case. The test case for open loop are presented in the Table 4.7.

This section gives a statistical description of the mean velocity field and the Reynolds stresses for U_∞=17 and 25 m/s respectively. Data used in this section has been recorded using the high speed PIV set-up described in Chapter 4. Statistics of the velocity field in this section have been obtained by averaging 5381 statistically independent vector fields recorded at a sampling rate of 5.4 kHz. Furthermore, PSD of reference and error microphone signals are discussed. The microphone data are recorded at a sampling rate of 100 kHz.

5.4.1 Mean velocity profiles

Figure 5.25 shows the streamwise evolution of the mean velocity profiles on the suction side of the open loop control case. Tested freestream velocities range from 17 and 25 m/s at chord Reynolds of 2.3×10^5 and 3.3×10^5 respectively. The location at which the mean velocity profiles were plotted at several stations with streamwise coordinates is x= -2, 5.5, 13, 20.5 and 28 mm. This represents 64 %, 68 %, 72 %, 75 % and 79 % of the chord respectively.

Figure 5.25 (a) shows that the inflection point (no control case) for streamwise position x=13, 20.5 and 28 mm are closer to the wall whereas for the position x=-2 mm are further away. It should be noted that the inflection point is suppressed for f_{ac}= 1000 and 1500 Hz. In addition, especially for f_{ac}=1500 Hz, there is a significant suppression of the inflection point and their profiles are fuller as compared to the other carrier frequencies. This is due to the fact that the carrier frequencies of f_{ac}=1000 and 1500 Hz which lies in a stable region, dampens the T-S waves by the dominant blowing effect of the DBD plasma actuator. On the other hand, actuation at the carrier frequencies of f_{ac}=700 and 850 Hz which lies in the unstable region (within the frequency range of T-S waves), results in amplification of T-S waves in the boundary layer.

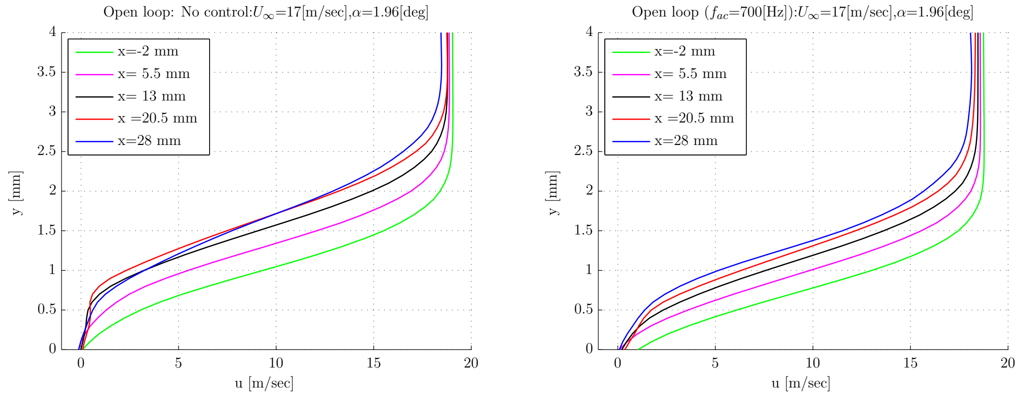

(a) No control

(b) 700 Hz

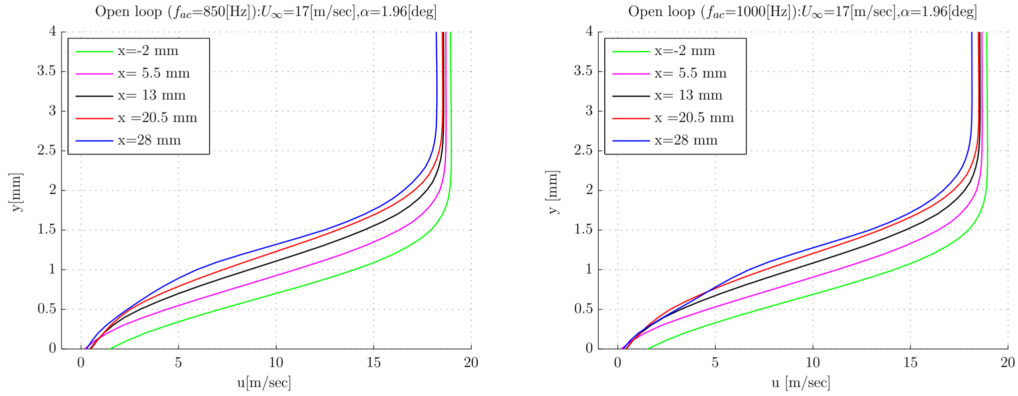

(c) 850 Hz

(d) 1000 Hz

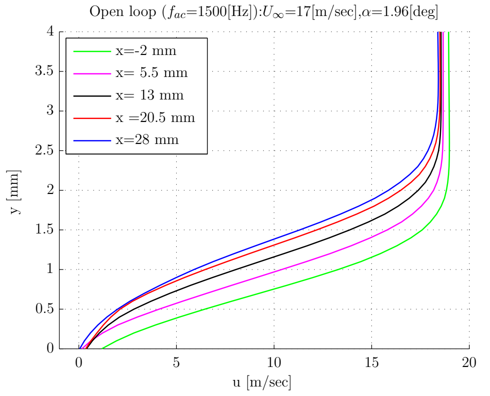

(e) 1500 Hz

Figure 5.25: Comparison of mean velocity profiles for open-loop at U_∞=17 m/s.

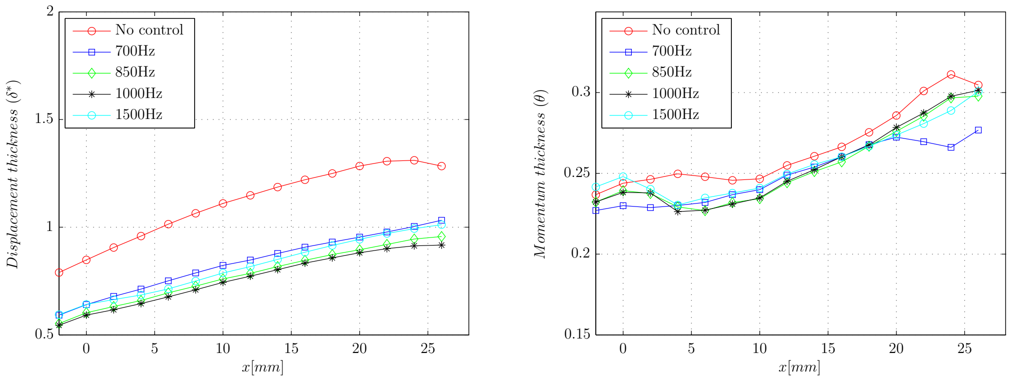

(a) Displacement thickness

(b) Momentum thickness

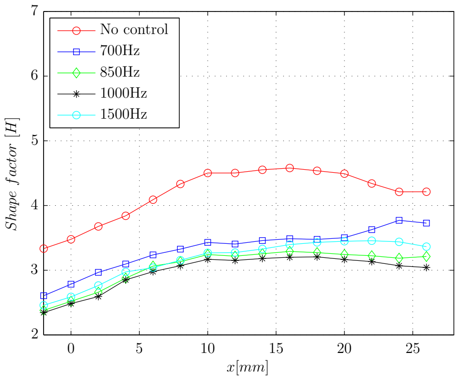

(c) Shape parameter

Figure 5.26: Comparison of boundary layer parameters for open-loop case at U_∞=17 m/s.

The profile of momentum thickness and shape factor shown in Figure 5.26. The momentum thickness profile increases on proceeding downstream for all the cases. For no control case, the momentum thickness shows a small increase for x<10 mm whereas a significant increase is observed for x>10 mm. The momentum thickness is reduced significantly for f_{ac}=1000 and 1500 Hz. With an increase in carrier frequency there is reduction of shape factor along the streamwise position. For f_{ac}=1000 and 1500 Hz, a significant amount of reduction is observed as compared to the other carrier frequencies. The shape factor for no control and f_{ac}=700 Hz case shows the degree of separation. This is well supported by observing the mean profiles in Figure 5.25 (a) & (b). This is explained by unstable carrier frequencies of f_{ac}=700 & 850 Hz results in amplification of the T-S waves which are reflected in the mean velocity profiles as shown in Figure 5.25 (b) & (c). As mentioned above, actuation at the stable carrier frequency of f_{ac}=1500 Hz, results in a dampening of T-S waves by the dominant blowing effect of the DBD plasma actuator. The blowing effect of the actuator becomes dominant with increasing frequency.

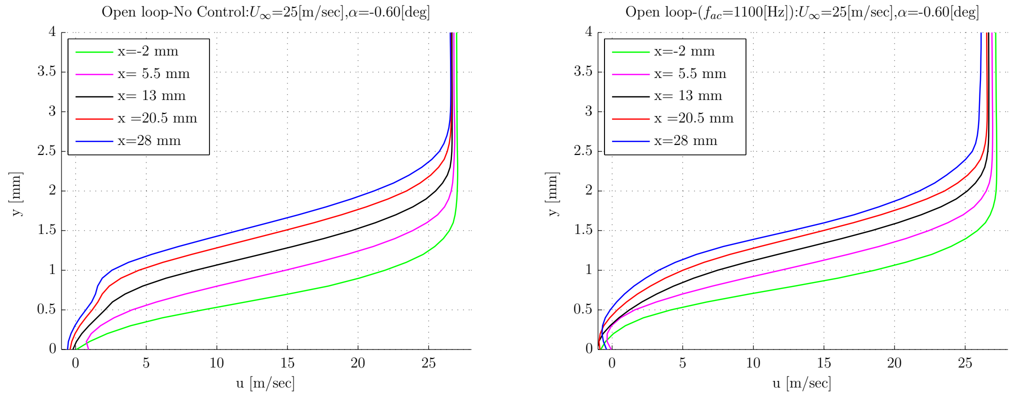

(a) No control (b) 1100 Hz

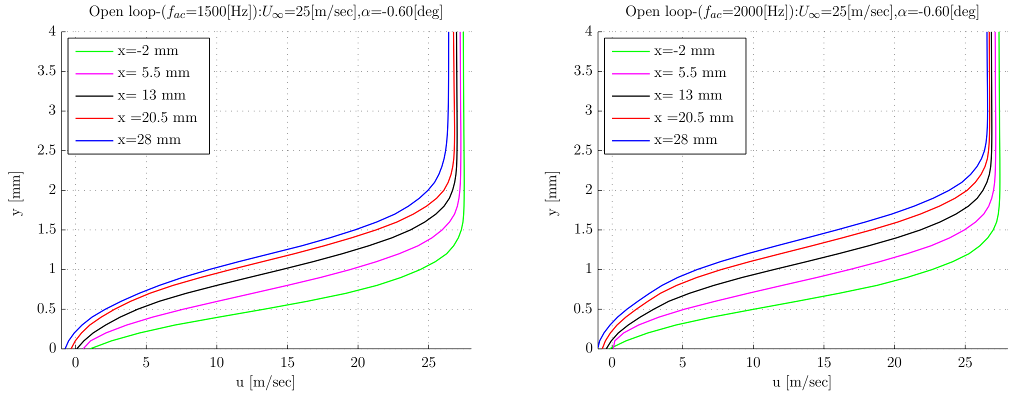

(c) 1500 Hz (d) 2000 Hz

Figure 5.27: Comparison of mean velocity profiles for open-loop at U_∞=25 m/s.

The mean profiles for no control case shown in Figure 5.27 (a) is different in comparison to no control case for closed loop as shown in the Figure 5.14 (e). In the ideal condition, the profiles should be same since prior case are acquired for the same freestream velocity and angle of attack. The difference may be explained by the fact that the prior case was performed on different days. Although, the angle of attack was fixed to the same value as it was set in closed loop case but it might have changed during the experiment run. In addition, the effects of temperature change may also have its role. Therefore, a considerable difference is observed in the mean profiles of open loop (no control case) to the closed loop (no control case) at U_∞=25 m/sec. Furthermore, studying and analyzing this case will be interesting to have a relative comparison between closed and open loop case.

Figure 5.27 shows that the inflection point for no control case at streamwise positions x= 13, 20.5 and 28 mm are closer to the wall whereas for the position x<13 mm are further away. The mean profiles at f_{ac}=1100 Hz exhibits an inflection. In addition, it also shows the degree of separation for the position x>-2 mm. This is due to the actuation at the unstable carrier frequency of f_{ac}=1100 Hz, enhanced the T-S waves which are reflected in mean velocity profiles. On the other hand, actuation at the stable carrier frequency of f_{ac}=2000 Hz, results in dampening of T-S waves in the boundary layer. The mean profiles at f_{ac}=2000 Hz are much fuller as compared to the cases. The displacement thickness, momentum thickness and shape factor against x which is the distance along the chord is shown in Figure 5.28. This will also support the reasoning given for the mean velocity profile.

It should be noted that momentum thickness profile increases on proceeding downstream for all the cases. For f_{ac}=1500 Hz, the momentum thickness shows the significant higher value whereas f_{ac}=1100 Hz exhibits lower values among all. The shape factor shows an interesting observation for no control and f_{ac}=1100 Hz case. They show a degree of separation as their values are above the separation value of 3.85 for downstream positions whereas for f_{ac}=2000 Hz the shape factor shows a significantly lower value as compared to other cases. This supports the fact that for f_{ac}=1100 Hz and no control case, the instabilities were amplified whereas for f_{ac}=2000 Hz there is a considerable reduction of T-S waves. The reason is same as explained for mean velocity profiles.

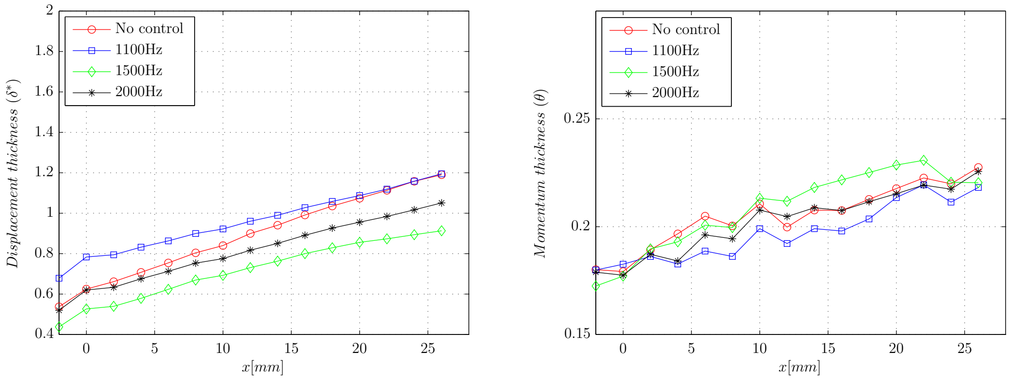

(a) Displacement thickness

(b) Momentum thickness

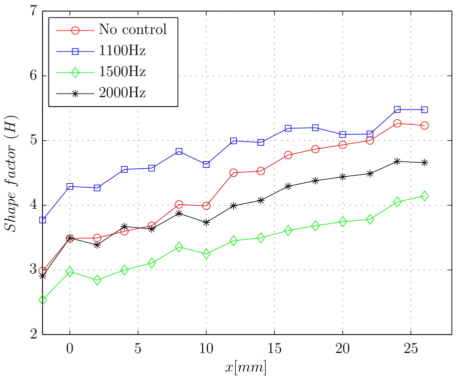

(c) Shape parameter

Figure 5.28: Comparison of boundary layer parameters for open-loop case at U_∞= 25 m/s.

5.4.2 Turbulence level and Reynolds stress profiles

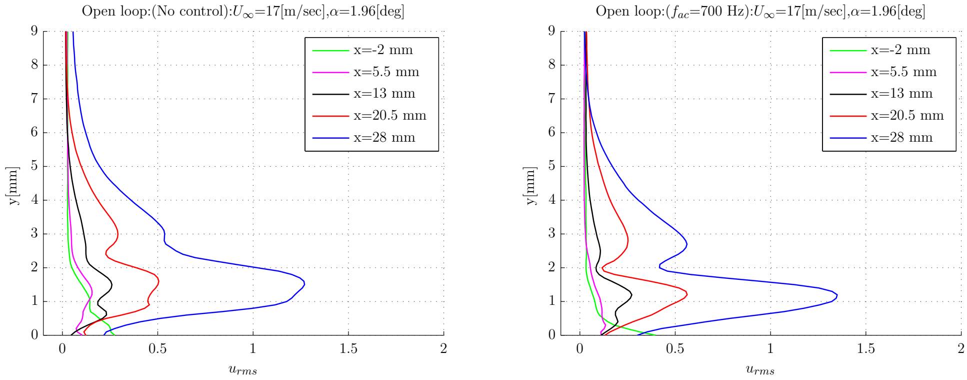

(a) No control (b) f_{ac}=700 Hz

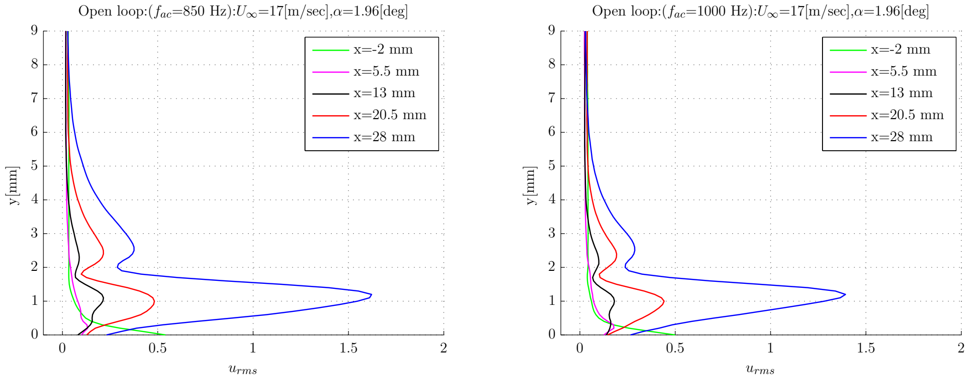

(c) f_{ac}=850 Hz (d) f_{ac}=1000 Hz

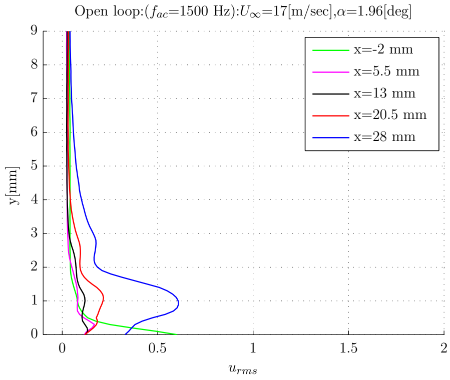

(e) f_{ac}=1500 Hz

Figure 5.29: Comparison of (u_{rms}) profiles for open loop control by varying carrier frequency f_{ac} (a) No control; (b) 700 Hz; (c) 850 Hz; (d) 1000 Hz; (e) 1500 Hz at U_∞=17 m/s.

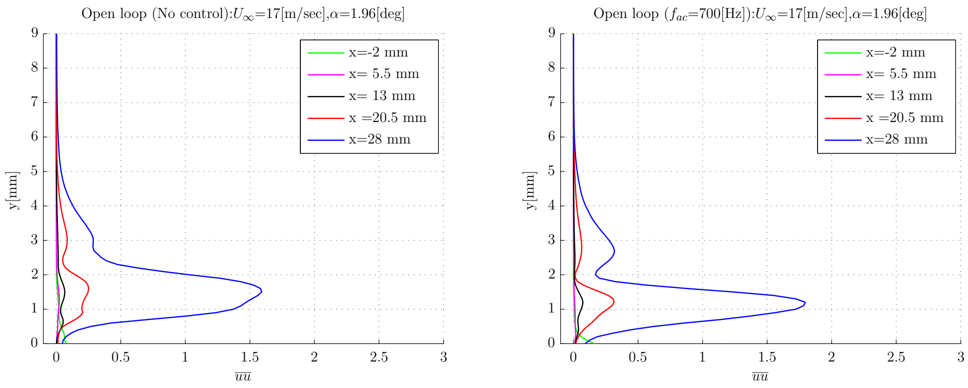

(a) No control

(b) f_{ac}=700 Hz

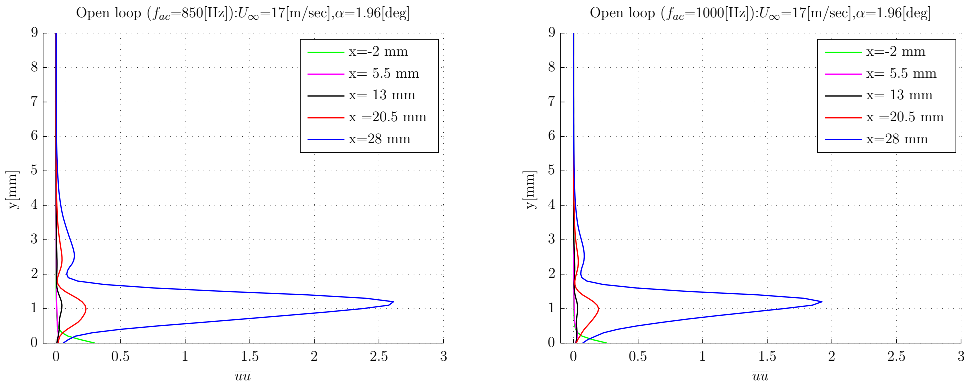

(c) f_{ac}=850 Hz

(d) f_{ac}=1000 Hz

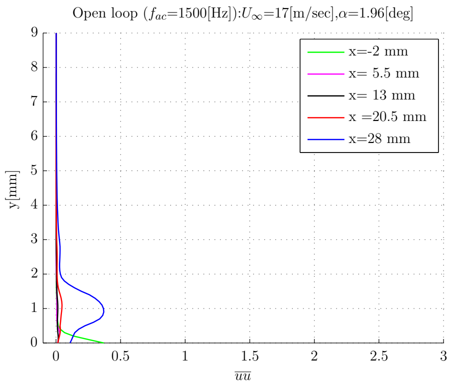

(e) f_{ac}=1500 Hz

Figure 5.30: Comparison of Reynolds stress $\overline{uu}$ profiles for open loop control by varying carrier frequency f_{ac} (a) No control; (b) 700 Hz; (c) 850 Hz; (d) 1000 Hz; (e) 1500 Hz at U_∞=17 m/s.

The contours of normal and shear Reynolds stress is depicted in Appendix D under section open loop control. The contours show that there is a significant reduction of fluctuations for f_{ac}=1500 Hz at U_∞=17 m/s and for f_{ac}=2000 Hz at U_∞=25 m/s respectively. Figure 5.29 and 5.30 show the turbulence level and normal Reynolds stress profile ($\overline{uu}$) respectively at U_∞=17 m/s for the sequence of carrier frequencies. From the profiles , it should be noted that u_{rms} for no control and f_{ac}=700 Hz case exhibits a two peak distribution whereas single peak for x<13 mm. The two peak distribution corresponds to that of typical T-S waves whereas single peak corresponds to simple and clean T-S waves of the fundamental frequency (Grundmann, 2008). The fluctuations are higher for f_{ac}=700 and 850 Hz as compared to other cases. This is explained by the fact that these frequencies lie in unstable region i.e. close to the T-S wave frequency. Therefore, actuating at these frequencies will amplify the instabilities which can be observed in both u_{rms} and $\overline{uu}$ profiles. At f_{ac}=1000 and 1500 Hz, the maximum of both u_{rms} and $\overline{uu}$ profiles reduces significantly. This is explained by the fact that 1000 and 1500 Hz lies in a stable region which results in dampening of T-S waves by the dominant blowing effect of the DBD plasma actuator. The reduction is higher for stable frequency of f_{ac}=1500 Hz due to the blowing effect becomes stronger than f_{ac}=1000 Hz. Therefore, f_{ac}=1500 Hz has a more stabilizing effect than 1000 Hz. The major disadvantage of operating at high carrier frequencies results in an increase in the power consumption(Kotsonis, 2012).

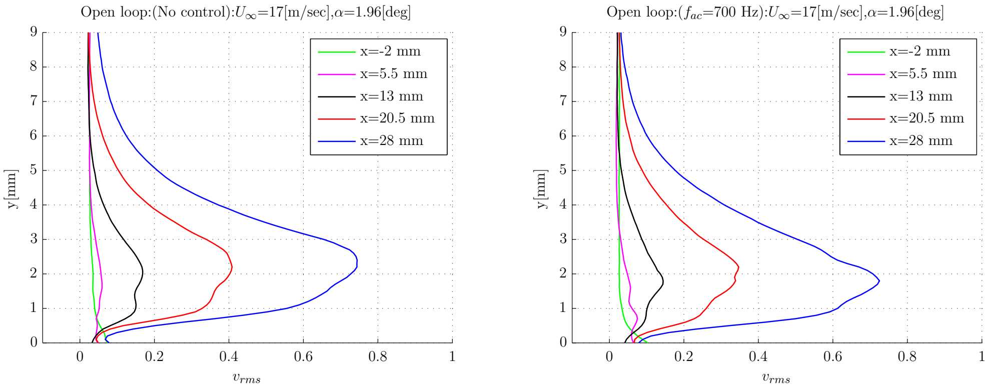

(a) No control

(b) f_{ac}=700 Hz

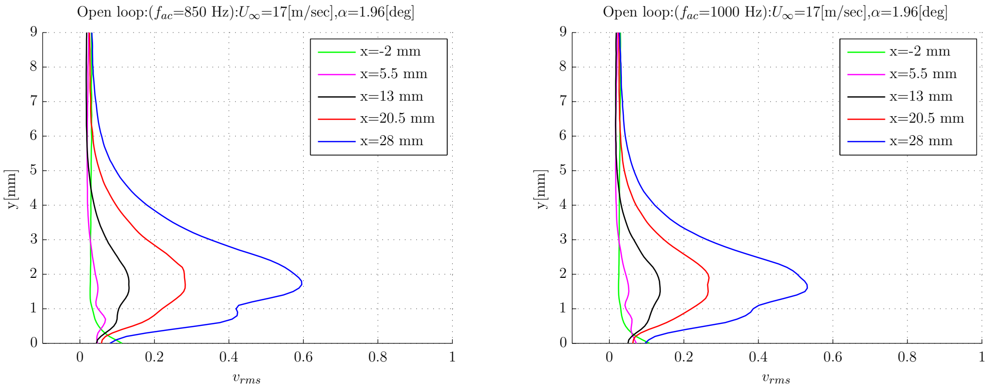

(c) f_{ac}=850 Hz

(d) f_{ac}=1000 Hz

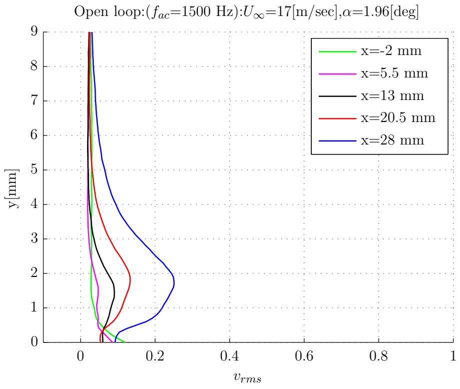

(e) f_{ac}=1500 Hz

Figure 5.31: Comparison of Reynolds stress v_{rms} profiles for open loop control by varying carrier frequency f_{ac} (a) No control; (b) 700 Hz; (c) 850 Hz; (d) 1000 Hz; (e) 1500 Hz at U_∞=17 m/s.

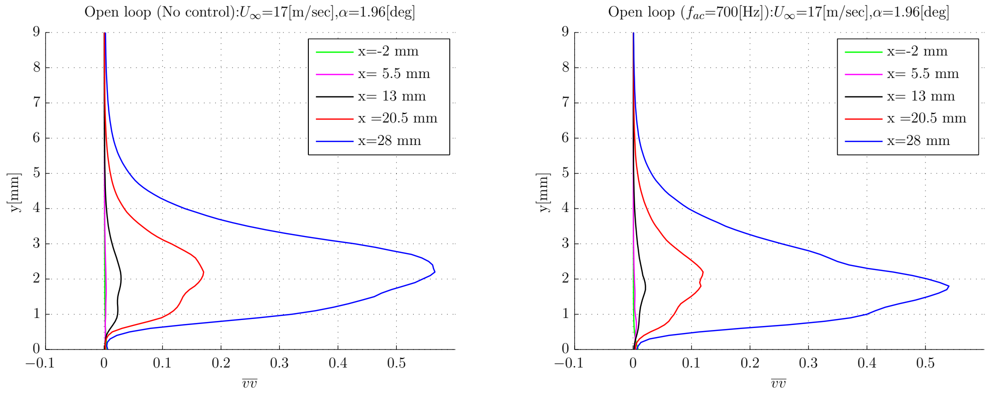

(a) No control (b) f_{ac}=700Hz

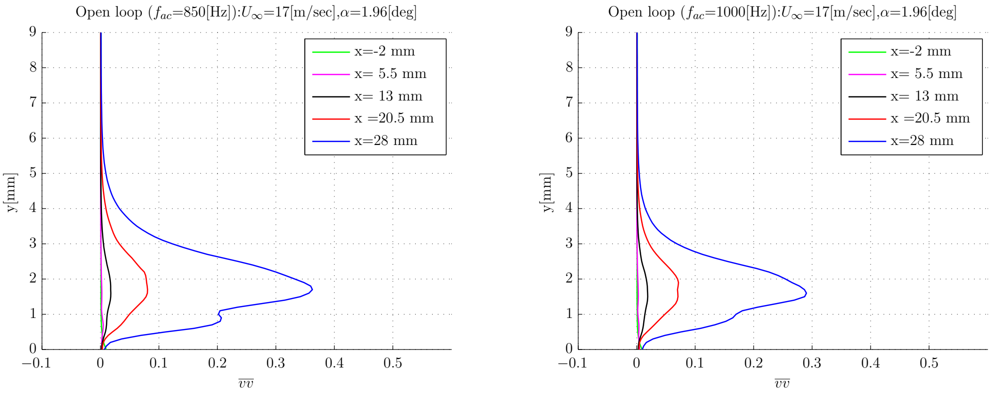

(c) f_{ac}=850Hz (d) f_{ac}=1000Hz

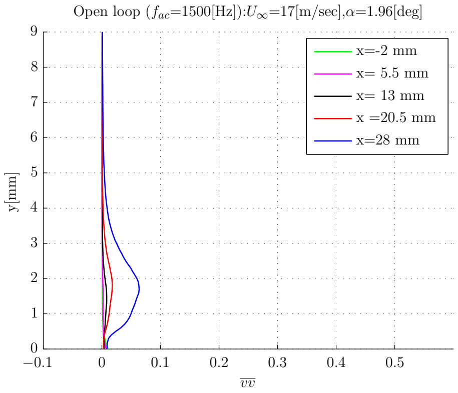

(e) f_{ac}=1500Hz

Figure 5.32: Comparison of Reynolds stress $\overline{vv}$ profiles for open loop control by varying carrier frequency f_{ac} (a) No control; (b) 700 Hz; (c) 850 Hz; (d) 1000 Hz; (e) 1500 Hz at U_∞=17 m/s.

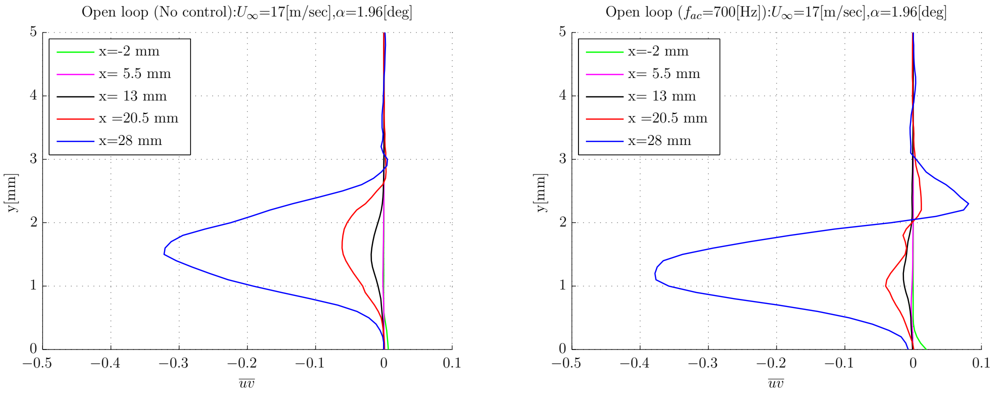

(a) No control

(b) f_{ac}=700Hz

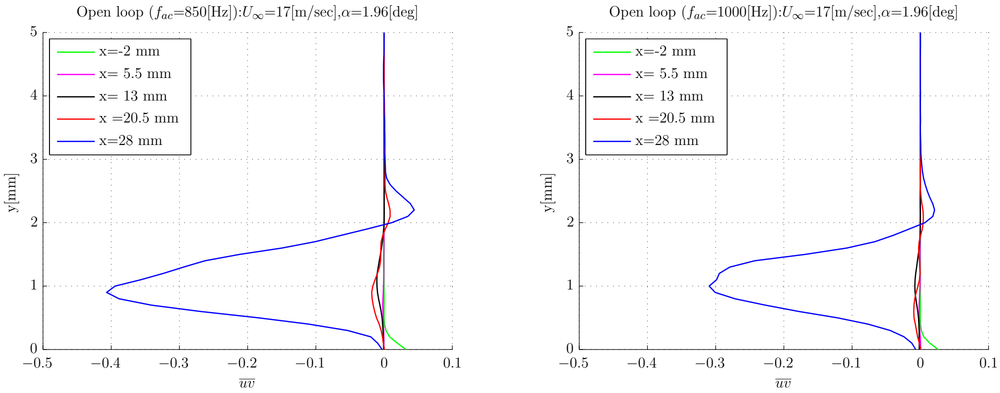

(c) f_{ac}=850Hz

(d) f_{ac}=1000Hz

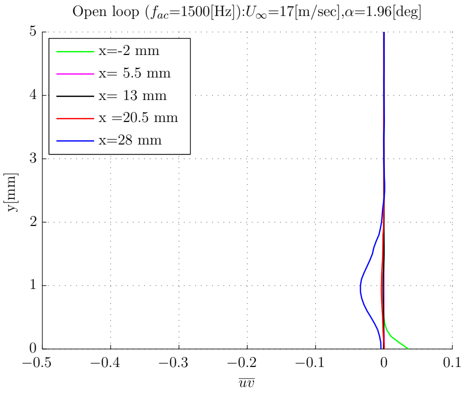

(e) f_{ac}=1500Hz

Figure 5.33: Comparison of Reynolds stress ($\overline{uv}$) profiles for open loop control by varying carrier frequency f_{ac} (a) No control; (b) 700 Hz; (c) 850 Hz; (d) 1000 Hz; (e) 1500 Hz at U_∞=17 m/s.

Figure 5.31 and 5.32 shows the turbulence level (v_{rms}) and Reynolds stress ($\overline{vv}$) profile respectively for the sequence of carrier frequencies at U_∞=17 m/s. The v_{rms} profile for no control and f_{ac}=700 Hz case exhibits a higher fluctuations for the positions x=20.5 and 28 mm as compared to other cases. This also supports the observation explained for the turbulence level (u_{rms}) and Reynolds stress ($\overline{uu}$) profile. As explained above, the turbulence level (v_{rms}) and Reynolds stress profile ($\overline{vv}$) for f_{ac}=700 Hz are significantly higher as compared to other cases. At f_{ac}=1500 Hz, the turbulence level (v_{rms}) and normal Reynolds stress profile ($\overline{vv}$) reduces significantly as compared to no control cases. This is due to the fact that for stable carrier frequencies f_{ac}= 1000 and 1500 Hz, results in dampening of T-S waves. The reduction is higher for f_{ac}=1500 Hz because the blowing effect becomes more dominant on increasing carrier frequency. Therefore, the stabilising effect is more pronounced for f_{ac}=1500 Hz as compared to f_{ac}=1000 Hz. Figure 5.33 shows the shear Reynolds stress ($\overline{uv}$) profile for the sequence of carrier frequencies at U_∞=17 m/s. Similar behaviour is observed for the shear Reynolds stress $\overline{uv}$ and the normal Reynolds stress profiles $\overline{uu}$ and $\overline{vv}$.

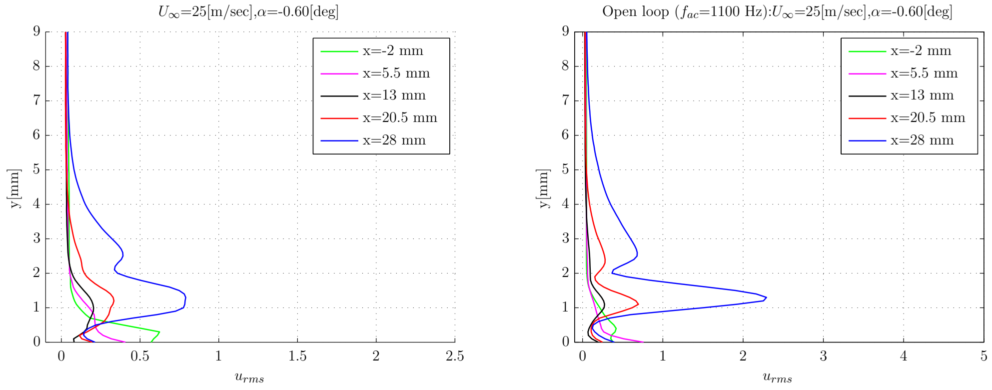

(a) No control

(b) f_{ac}=1100 Hz

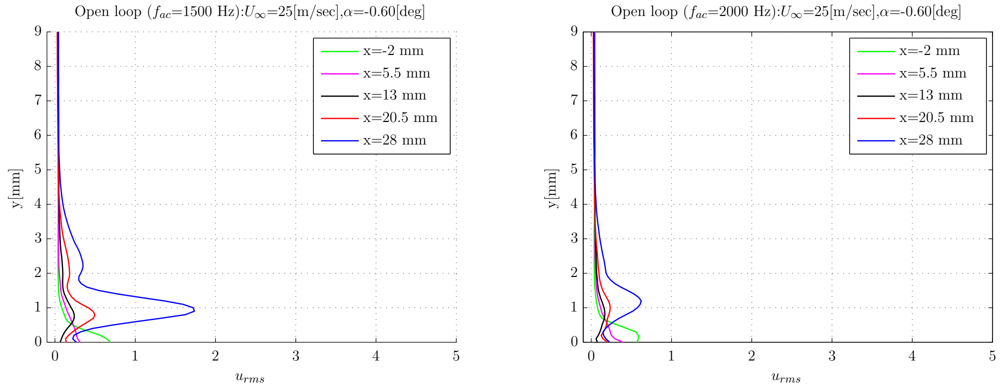

(c) f_{ac}=1500 Hz

(d) f_{ac}=2000 Hz

Figure 5.34: Comparison of turbulence level profiles u_{rms} for open loop control by varying carrier frequency f_{ac} (a)No control; (b) 1100 Hz; (c) 1500 Hz; (d) 2000 Hz at U_∞=25 m/s.

Figure 5.34 and 5.35 shows the turbulence level (u_{rms}) and Reynolds stress ($\overline{uu}$) profile respectively for the sequence of carrier frequencies at U_∞=25 m/s. The contours for the mentioned case is depicted in Appendix D under section open loop control. The contours shows that there is a significant reduction of fluctuations for f_{ac}=2000 Hz whereas amplification of fluctuations for f_{ac}=1100 Hz at U_∞=25 m/s. Furthermore, the profiles will support this fact as well.

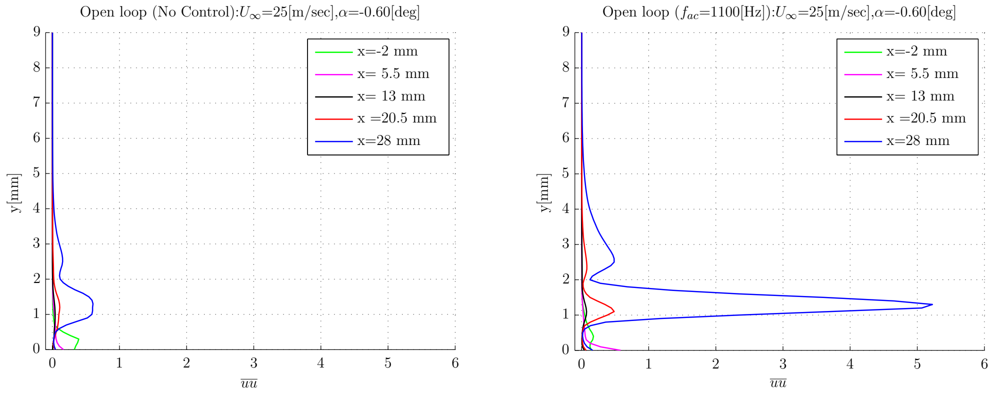

(a) No control

(b) f_{ac}=1100Hz

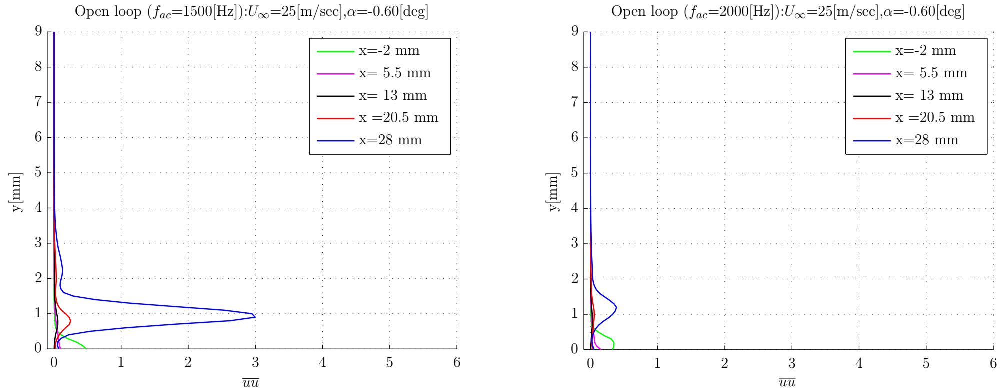

(c) f_{ac}=1500Hz

(d) f_{ac}=2000Hz

Figure 5.35: Comparison of Reynolds stress ($\overline{uu}$) profiles for open loop control by varying carrier frequency f_{ac} (a)No control; (b) 1100 Hz; (c) 1500 Hz; (d) 2000 Hz at U_∞=25 m/s.

In Figure 5.34 (a), the u_{rms} profile for no control and f_{ac}=1100 Hz case exhibits a two peak distribution of fluctuations for x=20.5 and 28 mm whereas single peak for x<20.5 mm. The two peak distribution corresponds to that of typical T-S waves and whereas single peak corresponds to simple and clean T-S waves of the fundamental frequency (Grundmann, 2008). The turbulence levels profile for f_{ac}=1100 Hz are significantly higher as compared to other cases. At f_{ac}=2000 Hz, the maximum of turbulence level profile reduces significantly. As explained earlier, the carrier frequency f_{ac}=2000 Hz lies in a stable region which result in dampening of T-S waves by the dominant blowing effect of the DBD plasma actuator. It is important to mention that turbulence level and Reynolds stress physically represents the same thing but differs only in magnitude. Therefore, a similar behaviour is observed for Reynolds stress profile ($\overline{uu}$) as depicted in Figure 5.35.

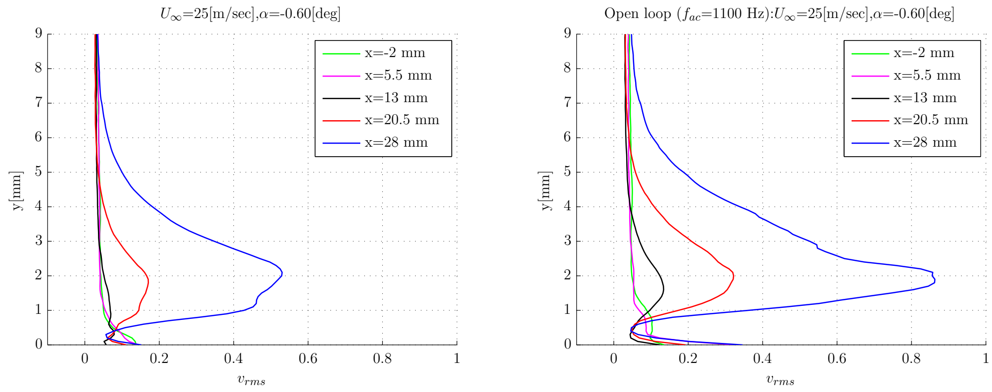

(a) No control

(b) f_{ac}=1100 Hz

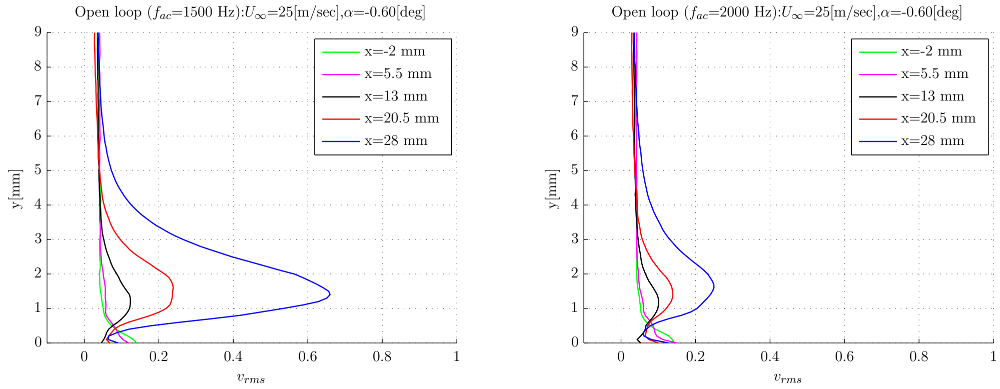

(c) f_{ac}=1500 Hz

(d) f_{ac}=2000 Hz

Figure 5.36: Comparison of turbulence level profiles v_{rms} for open loop control by varying carrier frequency f_{ac} (a)No control; (b) 1100 Hz; (c) 1500 Hz; (d) 2000 Hz at U_∞=25 m/s.

Figure 5.36 and 5.37 shows the turbulence level (v_{rms}) and Reynolds stress ($\overline{vv}$) profile respectively for the sequence of carrier frequencies at U_∞=25 m/s. The v_{rms} profile for no control and f_{ac}=1100 Hz case exhibits a higher fluctuation for the positions x=20.5 and 28 mm as compared to other cases. This also supports the observation explained for the turbulence level (u_{rms}) and Reynolds stress ($\overline{uu}$) profile. As explained above, the turbulence level (v_{rms}) and Reynolds stress profile ($\overline{vv}$) for f_{ac}=1100 Hz are significantly higher as compared to other cases. For f_{ac}=2000 Hz, the turbulence level profile reduces significantly as compared to no control cases. In addition, the carrier frequency f_{ac}=2000 Hz lies in a stable region which results in dampening of T-S waves by the dominant blowing effect of the DBD plasma actuator. Figure 5.38 shows the shear Reynolds stress ($\overline{uv}$) profile respectively for the

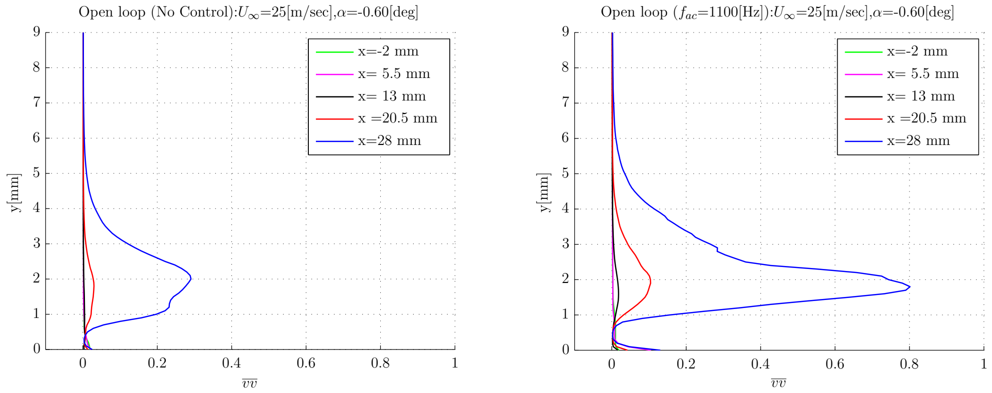

(a) No control

(b) f_{ac}=1100Hz

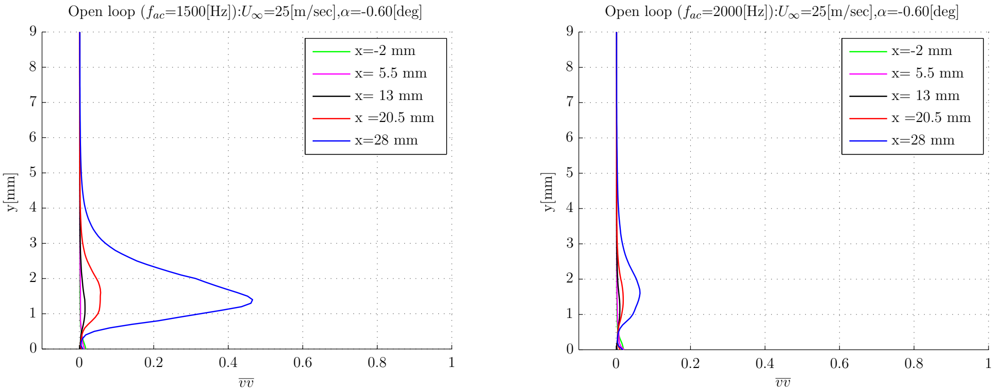

(c) f_{ac}=1500Hz

(d) f_{ac}=2000Hz

Figure 5.37: Comparison of Reynolds stress $\overline{vv}$ profiles for open loop control by varying carrier frequency f_{ac} (a)No control; (b) 1100 Hz; (c) 1500 Hz; (d) 2000 Hz at U_∞=25 m/s.

sequence of carrier frequencies at U_∞=25 m/s. Similar behaviour is observed for the shear Reynolds stress $\overline{uv}$ as in case of the normal Reynolds stress profiles $\overline{uu}$ and $\overline{vv}$ in terms of amplification and dampening of T-S waves.

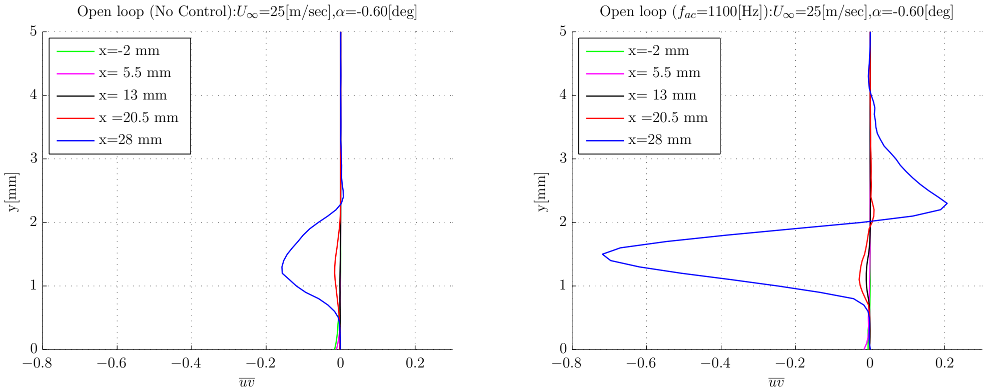

(a) No control (b) f_{ac}=1100Hz

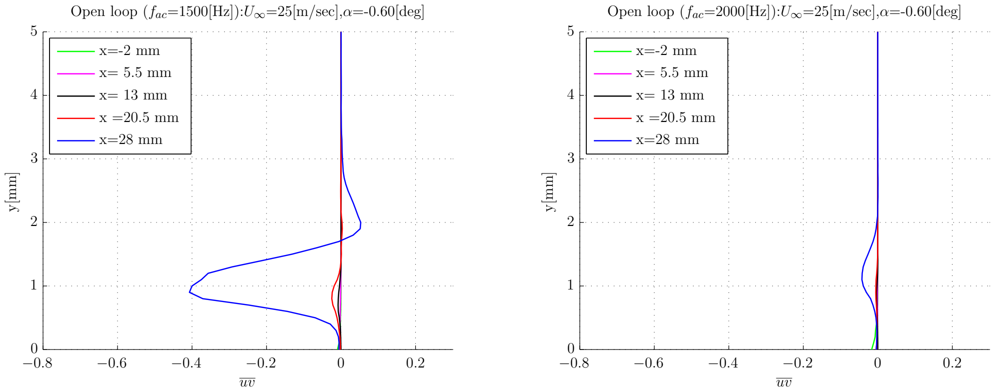

(c) f_{ac}=1500Hz (d) f_{ac}=2000Hz

Figure 5.38: Comparison of Reynolds stress $\overline{uu}$ profiles for open loop control by varying carrier frequency f_{ac} (a)No control; (b) 1100 Hz; (c) 1500 Hz; (d) 2000 Hz at U_∞=25 m/s.

5.4.3 Comparison of maximum peak reduction

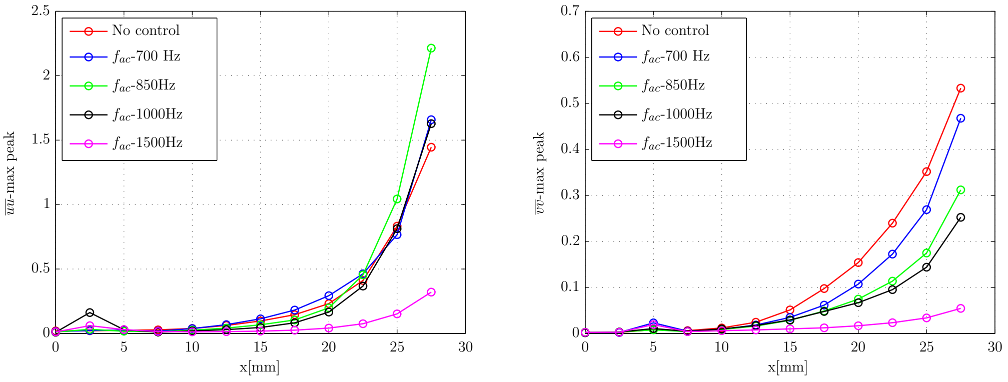

(a) $\overline{uu}$ maximum peak at U_∞=17 m/s.

(b) $\overline{vv}$ maximum peak at U_∞=17 m/s.

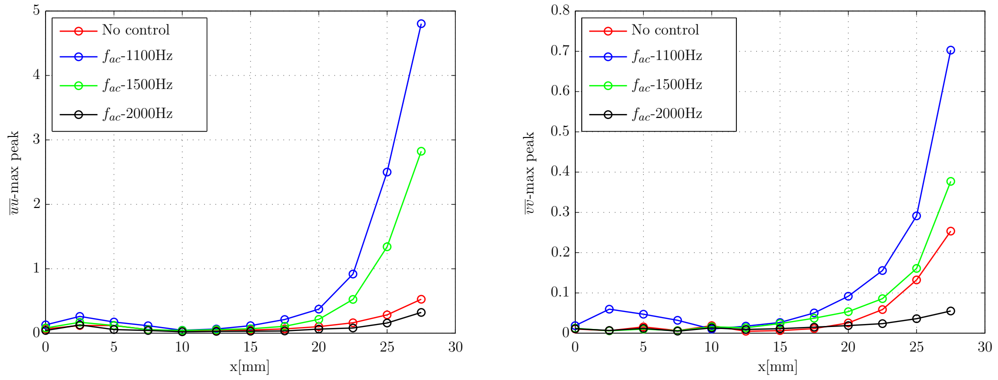

(c) $\overline{uu}$ maximum peak at U_∞=25 m/s.

(d) $\overline{vv}$ maximum peak at U_∞=25 m/s.

Figure 5.39: Comparison of maximum peak of normal Reynolds stress ($\overline{uu}$),($\overline{vv}$) for open loop control at U_∞=17 and 25 m/s respectively.

The maximum peak of normal Reynolds stress profiles of $\overline{uu}$ and $\overline{vv}$ along the suction side is shown in Figure 5.39 for the sequence of carrier frequencies at U_∞=17 and 25 m/s respectively. In general for all cases at U_∞=17 m/sec, before x=10 mm, the maximum values of average Reynolds stress components ($\overline{uu}$,$\overline{vv}$) remains very small whereas after x=10 mm, a strong increase in the maximum value is observed. This strong increase is due to the amplification of T-S waves on proceeding downstream. With f_{ac}=1000 and 1500 Hz, the maximum values of the average Reynolds stress component ($\overline{vv}$) are reduced significantly as compared to no control case. At higher frequency of f_{ac}=1000 and 1500 Hz, the plasma actuator imparts a higher momentum to the flow by the dominant blowing effect of the DBD plasma actuator.

Similar behaviour is also observed for the maximum values of the average Reynolds stress component

($\overline{uu}$) at f_{ac}=1500 Hz. In addition, a small reduction is observed for 10 mm<x<25 mm at f_{ac}=850 and 1000 Hz whereas for the positions x>25 mm it shows an increment in comparison with no control case. The T-S waves are significantly suppressed for f_{ac}=1500 Hz at U_{∞}=17 m/s. This is due to the fact that actuation at unstable carrier frequencies of f_{ac}=700 and 850 Hz, results in amplification of T-S waves. On the other hand, actuation at stable carrier frequencies of f_{ac}=1000 and 1500 Hz, results in dampening of T-S waves. Furthermore, a stabilizing effect for f_{ac}=2000 Hz whereas amplification of T-S waves for f_{ac}=1100 and 1500 Hz is observed at U_{∞}=25 m/s. In addition, the maximum peak for f_{ac}=1100 Hz is considerably higher as compared to other cases.

5.4.4 Time evolution

The time traces of velocity fluctuations u_f (in x-direction) for the open loop case at U_{∞}=17 and 25 m/s are shown in Figure 5.40 and 5.41. These are plotted approximately at the location of error microphone. Data used in this section has been recorded using the high speed 2-component PIV set-up described in Chapter 4. Statistics of the velocity field in this section have been obtained by averaging 5381 statistically independent vector fields recorded at a sampling rate of 5.4 kHz. This study will help to demonstrate the effect of varied frequency actuation on the T-S wave behaviour.

Figure 5.40 (b) shows that the velocity fluctuations (u_f) for f_{ac}=700 and 850 Hz are higher as compared to other cases. This is explained by the fact that the actuation at unstable carrier frequencies results in amplification of T-S waves. For f_{ac}=700 Hz, the wave packets seems to have stronger amplitude of fluctuations which indicates that these instabilities are in intermittent stage. The fluctuations are dampened for stable carrier frequency f_{ac}=1000 and 1500 Hz. The dampening effect is more pronounced for f_{ac}=1500 Hz.

Similarly, for U_{∞}=25 m/s, the fluctuations are dampened for stable carrier frequencies f_{ac}= 1500 and 2000 Hz. The dampening effect is predominant for f_{ac}=2000 Hz which is reflected in Figure 5.41 (d). Actuation at unstable carrier frequency f_{ac}=1100 Hz results in amplification of T-S waves. The explanation given for the both U_{∞}=17 and 25 m/s supports the reasoning given for the mean velocity, turbulence level and Reynolds stress profiles. The deviation of the fluctuations from zero (u_f) in no control case as shown in Figure 5.40 (a) and Figure 5.41 (a). The reason is unclear to the author. In general, the velocity fluctuations at U_{∞}=25 m/s are lower than U_{∞}=17 m/s cases. Furthermore, PSD of the velocity fluctuations (u_f) is given below which will supports the above mentioned facts.

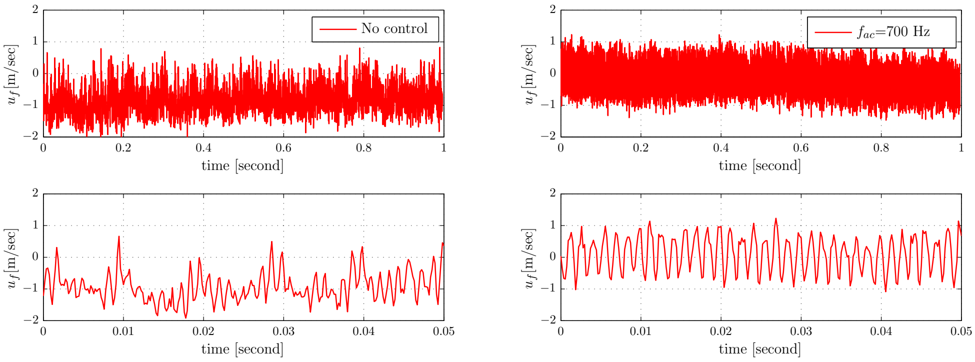

(a) No control

(b) f_{ac}=700 Hz

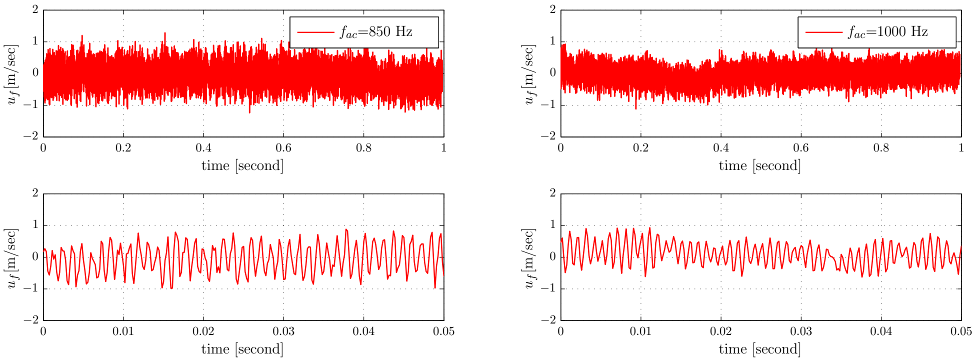

(c) f_{ac}=850 Hz

(d) f_{ac}=1000 Hz

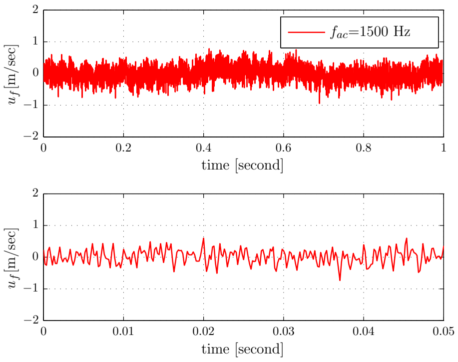

(e) f_{ac}=1500 Hz

Figure 5.40: Time evolution of velocity fluctuations (u_f) for open loop case at U_∞=17 m/s at x= 14.71 mm, y=1.12 mm.

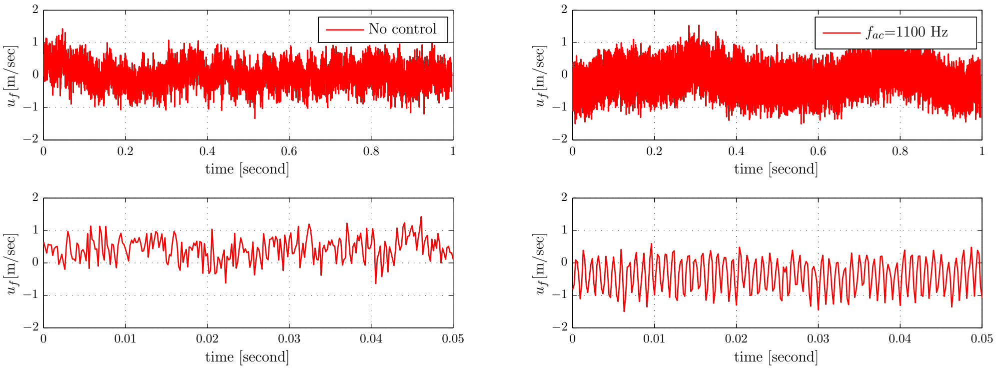

(a) No control

(b) f_{ac}=1100 Hz

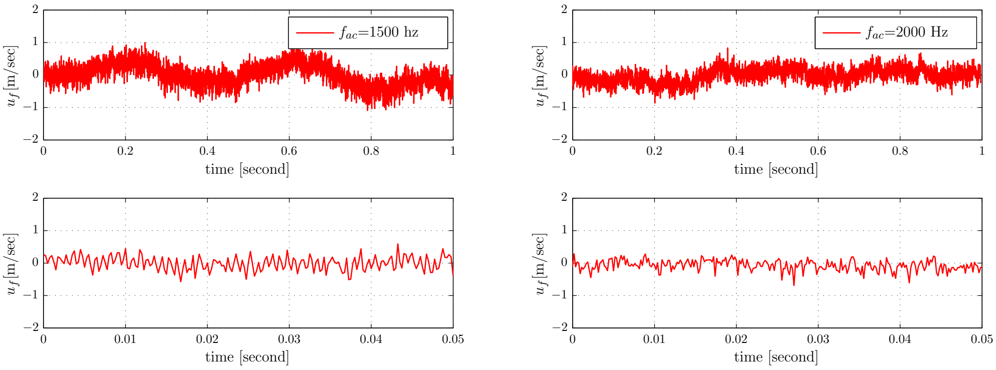

(c) f_{ac}=1500 Hz

(d) f_{ac}=2000 Hz

Figure 5.41: Time evolution of velocity fluctuations (u) for open loop case at U_∞=25 m/s at x= 14.71 mm, y=1.09 mm.

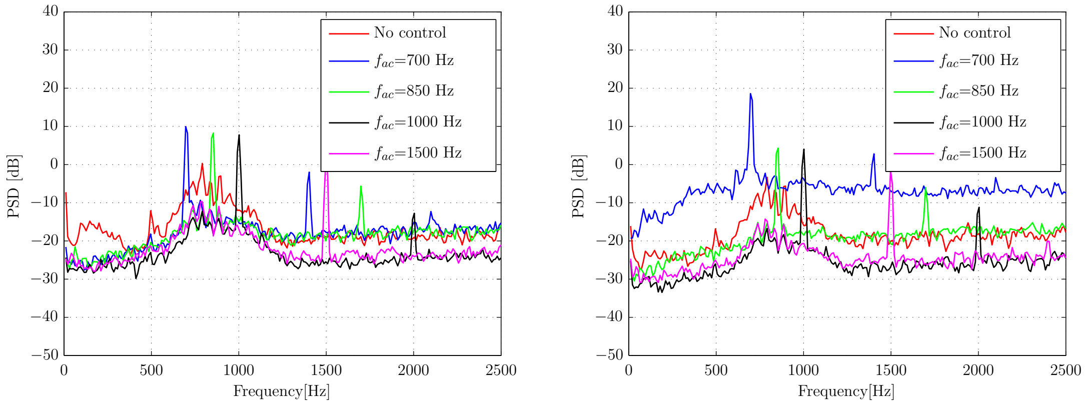

(a) U_∞=17 m/s at x=14.71 mm (Error microphone)

(b) U_∞=17 m/s at x=27.70 mm

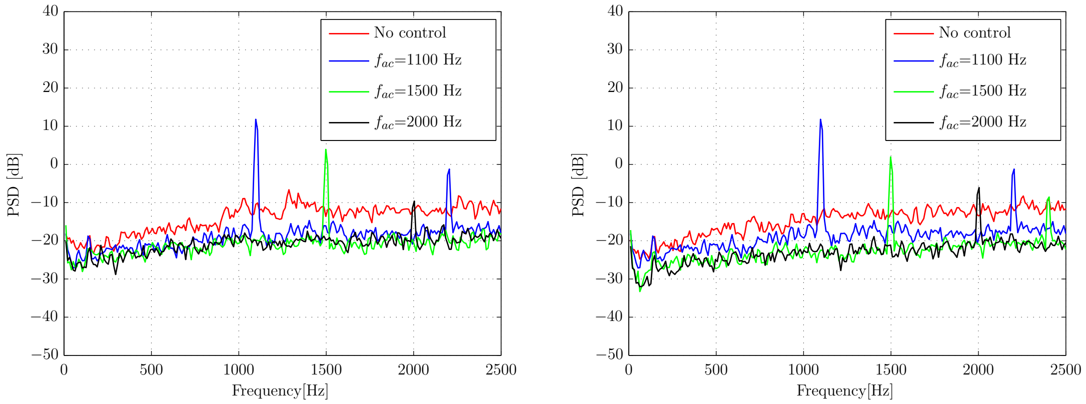

(c) U_∞=25 m/s at x=14.71 mm (Error microphone)

(d) U_∞=25 m/s at x=27.21 mm

Figure 5.42: PSD of velocity fluctuations (u_f) for open loop at U_∞=17 and 25 m/s.

Figure 5.42 shows the PSD of velocity fluctuations u_f plotted for U_∞=17 and 25 m/s in open loop case. These are done for the sequence of carrier frequencies at two streamwise co-ordinates. The two positions are selected such that one position is on the error sensor and other at the downstream of error sensor. Average periodogram method for estimating the PSD (Welch,1967) with a window size of 512 and an overlap of 50%. The selection of window size is done on the basis of convergence criterion which is given by eq 5.1.

For U_∞=17 m/s, at x=14.71 mm, PSD of the fluctuation (u_f) shows that the natural T-S waves have the form of a multi frequency wave train. There is a peak occurrence at its carrier frequency which is due to the EM noise and should be ignored. The spectra shows the higher values for no control and f_{ac}=700 Hz over the whole frequency range whereas a significant lower values for f_{ac}=1000 and 1500 Hz. At the downstream position of x=27.71 mm, the energy content of the spectra is higher as compared to x=14.71 for their respective carrier frequencies. This is due to the amplification of T-S waves on proceeding downstream. For U_∞=25 m/s, the unstable domain shifts to higher frequency as compared to U_∞=17 m/sec. The spectra of no control and f_{ac}=1100 Hz case are significantly higher as compared to f_{ac}=1500 and 2000 Hz.

5.4.5 Spectral analysis of surface pressure fluctuations

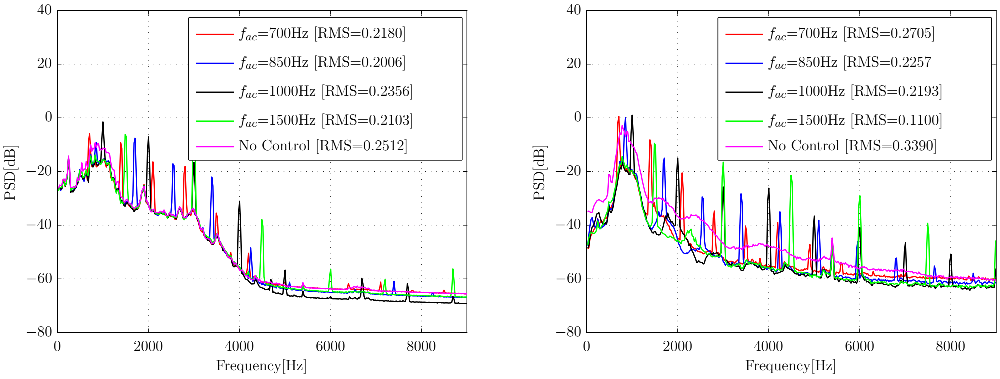

(a) U_∞=17 m/s, Microphone-5 (Reference Sensor)

(b) U_∞=17 m/s, Microphone-6 (Error sensor)

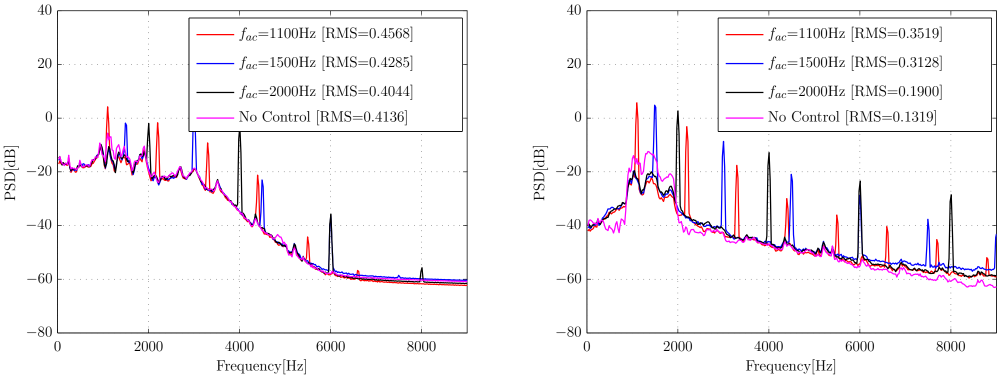

(c) U_∞=25 m/s, Microphone-5 (Reference Sensor)

(d) U_∞=25 m/s, Microphone-6 (Error sensor)

Figure 5.43: PSD of microphone signals for open case at U_∞=17 and 25 m/s with the sequence of carrier frequency.

Figure 5.43 shows the power spectra of microphone 5 (reference sensor) and microphone 6 (error sensor) for U_∞=17 and 25 m/s in an open loop case. The unfiltered signals are calculated using the average periodogram method for estimating the PSD (Welch,1967) of the spectra. The resulting spectra are firstly normalized with V_{ref}=1 volts to make them non dimensional and then converted to the decibel scale. The number of points taken for Fast Fourier Transform (FFT) is 4096. The power spectral density is plotted on the y-axis against frequency on the x-axis.

The carrier frequencies for both the velocities contains the harmonics of its carrier frequency whereas this behaviour is not observed for no control case. For instance the carrier frequency of f_{ac}=700 Hz has a harmonic peaks at 1400, 2100, 2800 Hz and so on. Similar behaviour is also found in other carrier frequencies. These harmonic peak occurrences are due to the EM noise which results in aliasing error and should be ignored. It is also important to mention that these are not due to physical effects such as the plasma flow interaction.

The peak of power spectra for no control case shows the frequency range at which natural T-S waves occur for their respective velocities. In the error sensor spectra, the frequency range of natural T-S waves is (732-1100 Hz) and (1025-1831 Hz) for U_∞=17 and 25 m/s respectively. The dominating peak occurs at the frequency of 781.3 Hz and 1367 Hz for U_∞= 17 and 25 m/s respectively. The unstable domain shifts to higher frequency with the increasing freestream velocity as explained earlier in the section of clean and closed loop. For U_∞=17 m/s, the carrier frequencies shows a significant reduction as compared to no control case over the whole frequency domain whereas highest is achieved for f_{ac}=1000 Hz. Similar behaviour is observed for the sequence of carrier frequencies at U_∞=25 m/s. In addition, the carrier frequency f_{ac}=1100 Hz shows the highest reduction as compared to other cases.

Table 5.6: RMS reduction of error microphone for open loop control at U_∞=17 m/s.

f_{ac}[Hz]	RMS	Reduction (%)
0	0.3390	-
700	0.2705	+20.20
850	0.2257	+33.42
1000	0.2193	+35.31
1500	0.1100	+67.56

The RMS value of the reference and error signals for all the cases is calculated and shown in Figure 5.6 and 5.7. The high RMS value of no control case represents the T-S wave amplification whereas a lower RMS value indicates a reduction. For U_∞=17 m/s, f_{ac}=1500 Hz shows a approximately 68% reduction. For U_∞=17 m/s and 25 m/s, the RMS reduction in comparison to no control case is depicted in the Table 5.6 and 5.7 respectively. Similarly, for U_∞=25 m/s, f_{ac}=2000 Hz shows a approximately 18% reduction as compared to no control case. The positive and negative percentage depicted in the table represents reduction and amplification respectively. The percentage of RMS reduction is significantly higher for stable carrier frequencies for their respective velocities. The two major disadvantage of using open loop is the problem of scaling up with increasing velocities and secondly for open loop the amount of energy required to manipulate the flow to induce the desired behaviour is higher as compared to close loop.

Table 5.7: RMS reduction of error microphone for open loop control at U_∞=25 m/s.

f_{ac}[Hz]	RMS	Reduction (%)
0	0.2319	-
1100	0.3519	-51.75
1500	0.3128	-34.89
2000	0.1900	+18.07

5.5 Auto-correlation and cross-correlation of fluctuating velocity and surface pressure

5.5.1 Auto-correlation

Autocorrelation is the cross-correlation of a signal with itself. It will give insight of the repeating patterns and intrinsic time scales, such as the presence of periodic signals of the surface pressure signals. The sampling frequency of 100 kHz was used to record 500,000 samples in 5 seconds. The method of equalizing the signal is mentioned in section 4.1 under Microphone data processing.

Figure 5.44 shows the auto-correlation coefficient of the equalize microphone 6 (error sensor) surface pressure signals in the closed loop case at U_{∞}=17, 20 and 25 m/s respectively. A marking feature in Figure 5.44 depicts a strong correlation of a signal with itself at a time lag of zero for all cases. Additionally, one should note the time separation between the highest and the second highest peaks which corresponds to a dominating frequency of T-S waves. The dominating frequencies are 862, 1053 and 1334 Hz for U_{∞}=17, 20 and 25 m/s respectively.

Figure 5.45 and 5.46 show the auto-correlation coefficient of the equalize microphone 6 (error sensor) surface pressure signals for the open loop case at U_{∞}=17 and 25 m/s respectively. It should be noted that an auto-correlation coefficient function maximum occurs at a time lag of zero. This implies that there is a strong correlation of a signal with itself. Figure 5.45 (b), (c) and (d) shows the locking of signals for the carrier frequencies of f_{ac}=700, 850 and 1000 Hz at U_{∞}=17 m/s. Similar behaviour is also observed for the carrier frequencies of f_{ac}=1500 and 2000 Hz at U_{∞}=25 m/s. The frequency of dominating T-S waves for open loop no control case on the basis of auto correlation are 772 and 1351 Hz at U_{∞}=17 and 25 m/s respectively.

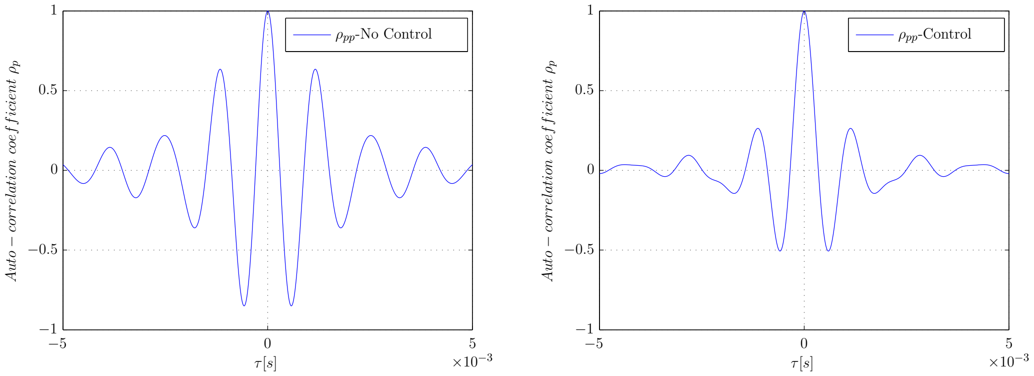

(a) 17 m/s (No Control)

(b) 17 m/s (Control)

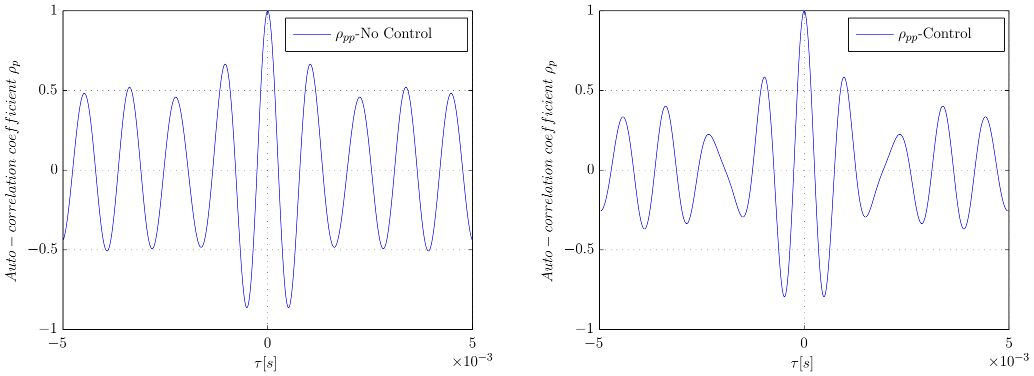

(c) 20 m/s (No Control)

(d) 20 m/s (No Control)

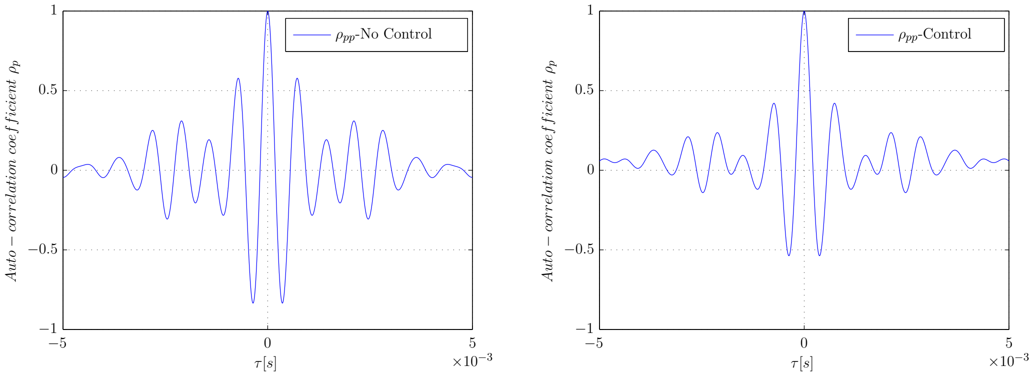

(e) 25 m/s (No Control)

(f) 25 m/s (Control)

Figure 5.44: Autocorrelation of microphone signals for close loop at U_∞=17, 20 and 25 m/s.

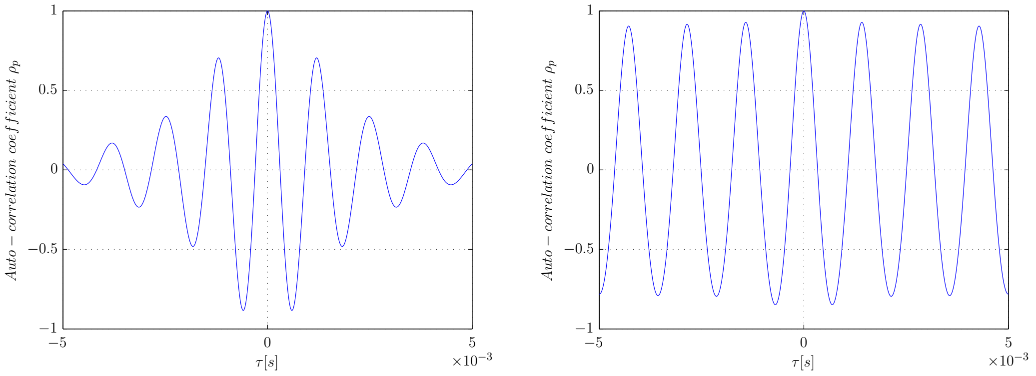

(a) No Control

(b) 700 Hz

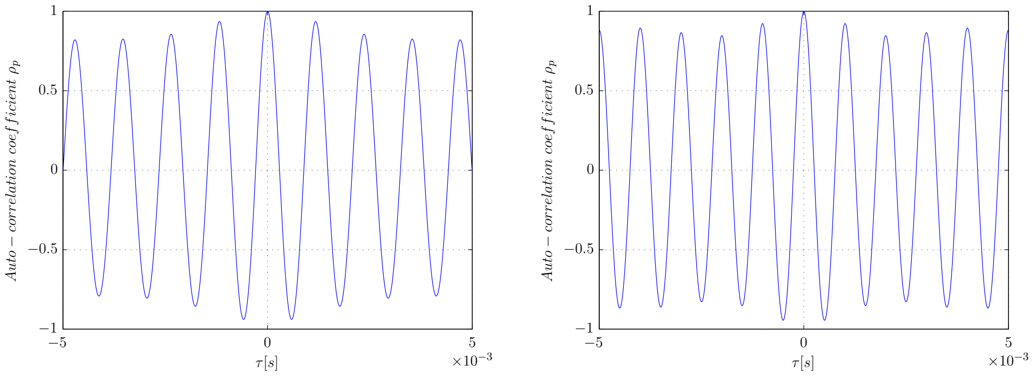

(c) 850 Hz

(d) 1000 Hz

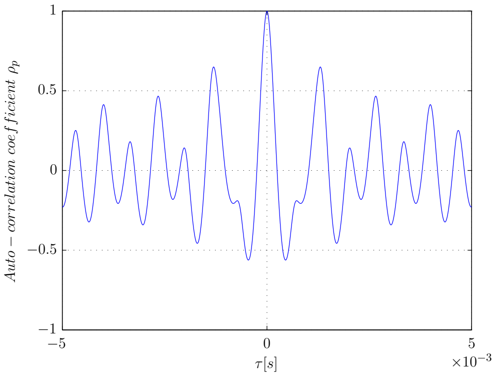

(e) 1500 Hz

Figure 5.45: Autocorrelation of microphone signals for open loop at U_∞=17 m/s.

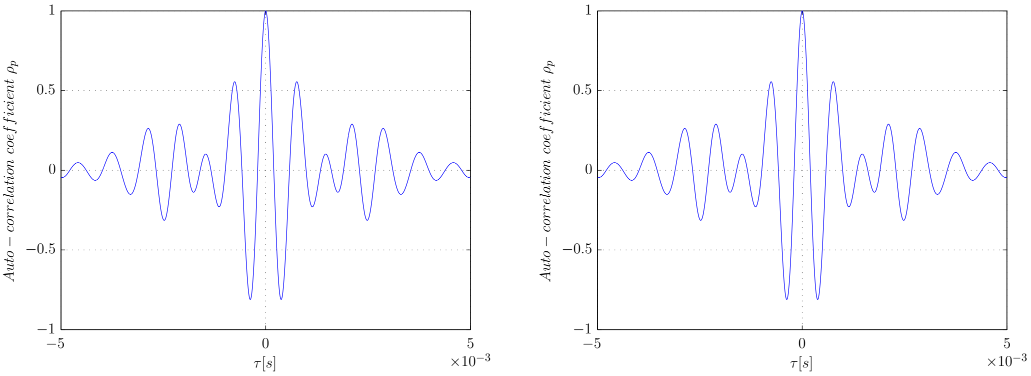

(a) No Control

(b) f_{ac}=1100 Hz

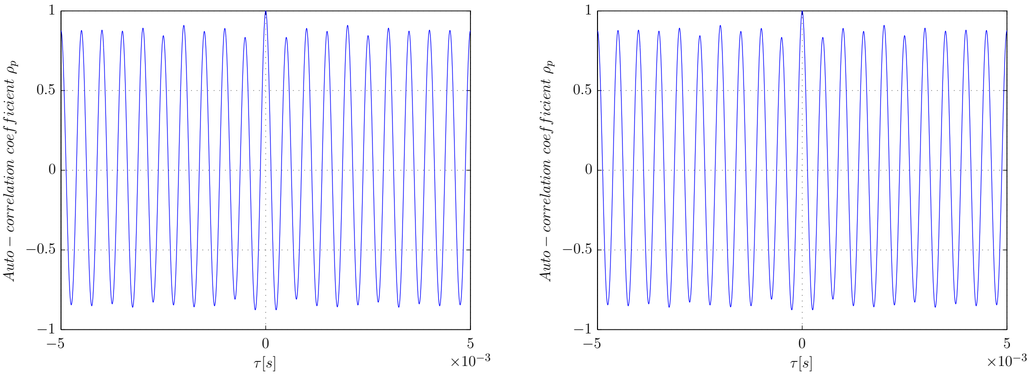

(c) f_{ac}=1500 Hz

(d) f_{ac}=2000 Hz

Figure 5.46: Autocorrelation of microphone signals for open loop at U_∞=25 m/s.

5.5.2 Cross-correlation

After having examined the occurrence of T-S waves in the previous sections and with the knowledge about the surface pressure of error microphone, it is of interest to investigate correlations between velocity fluctuations and the surface pressure. A simple method yielding first indications is to correlate the PIV measured velocity fluctuations at the locations of error microphone. The vector fields recorded at a sampling rate of 5.4 kHz from high speed PIV systems whereas microphone signals recorded at a sampling rate of 100 kHz. Therefore, in order to correlate the pressure and velocity fluctuations, the pressure time-series acquired at 100 kHz with the surface microphones is down-sampled to the PIV sampling frequency of 5.4 kHz. The cross-correlation between simultaneously acquired signals of stream-wise velocity and surface pressure at the location of error microphone was computed to quantify the degree of similarity between these signals.

As mentioned in the Appendix F, the correlation coefficient has two important properties. These are

- $\left|\rho_{up}\right| \leq 1$
- $\left|\rho_{up}\right| = 1$

These properties imply that of and only if two time series are linearly dependent, the correlation coefficient will be equal to unity. Near zero $\left|\rho_{up}\right|$ means that the two time series u and p are not linearly related whereas values between 0 and 1 indicate partial linear coupling. The correlation coefficient can be negative, which indicates linear, but out-of-phase, coupling. In addition, there can be a phase opposition (negative sign), and also a phase shift between velocity and pressure, which would displace the maximum from the origin. The greatest degree of similarity between pressure and velocity signals occurs when the cross-correlation coefficient function is the maximum which occurs at a time lag of zero. Interpretation of the cross-correlation coefficient (ρ_{up}) computed for velocity fluctuations and surface pressure signals measured at the location of the error microphone over an airfoil surface can be inferred from the preceding discussion for the closed and open loop case. In an irrotational field one would expect to find high pressures at locations of low velocity in accordance with Bernoulli, which should yield a clear correlation between the stream wise velocity fluctuation and the pressure fluctuations measured by the microphone.

Figure 5.47 shows the cross-correlation coefficients for close loop control at U_∞=17, 20 and 25 m/s respectively. These figures contain information on the timing of events in the flow as well as information on the relationship between velocity and pressure fluctuations. For no control cases, the periodicity in the cross-correlation coefficient function indicates that the instabilities observed in the velocity and surface pressure signals. The typical appearance of T-S waves is in the form of wave packets which is clearly visible for both closed and open loop control. Additionally, for control case, the wave packets are distorted as it is observed in Figure 5.47 (b), (d) and (f). The trend of cross correlation plot for control case at U_∞=25 m/s is not clear to the author.

In an open loop case, focussing at the correlation of pressure and u_f, one should note the time separation between the highest and the second highest peaks which corresponds to a dominating frequency of T-S waves. The frequency of dominating T-S waves for open loop (no control) case are 784 and 1349 Hz at U_∞=17 and 25 m/s respectively. These frequency values are identical to the frequency obtained from an autocorrelation plot. The cross correlation depicted in Figure 5.48 (b), (c), (d) and Figure 5.49 (b) shows the locking of signals for the carrier frequencies of f_{ac}=700, 850, 1000 Hz at U_∞=17 m/s whereas for f_{ac}=1100 and 2000 Hz at U_∞=25 m/s. The mentioned frequencies for their respective velocities depicts the relatively high correlation coefficient at a time-shift of approximately τ=0 s. In addition, in the cross-correlation plots for U_∞= 17 and 25 m/s, the peak is not at the origin as observed earlier in an autocorrelation plot; there is now a time lag τ, between the two signals.

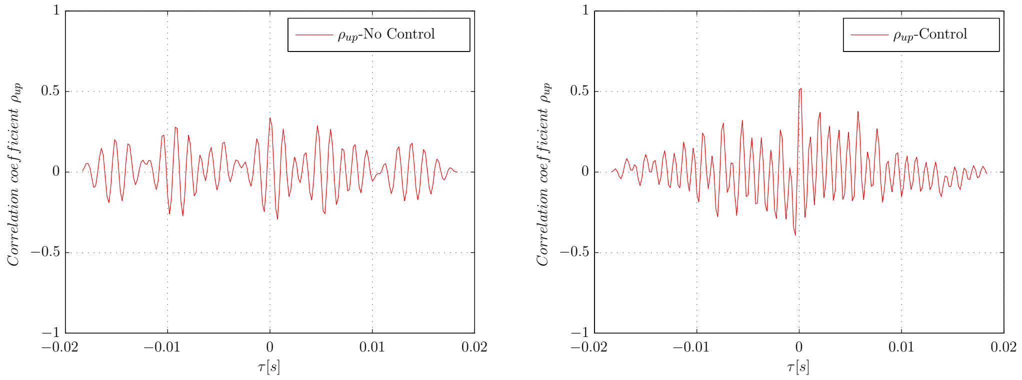

(a) No control (b) Control

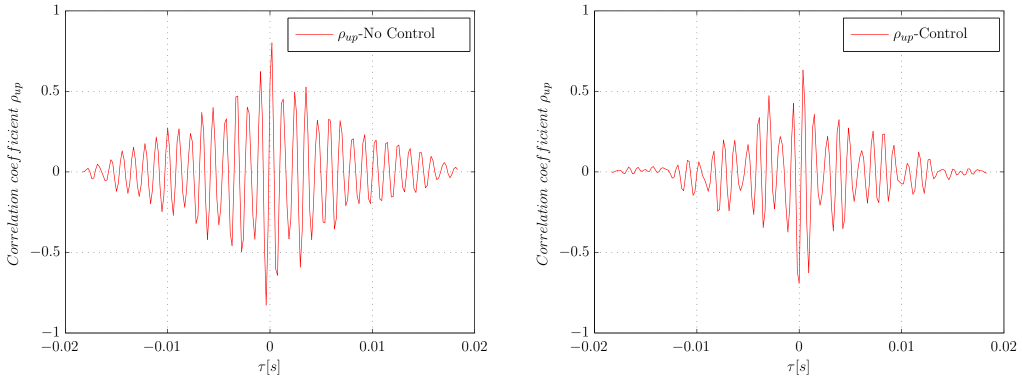

(c) No Control (d) Control

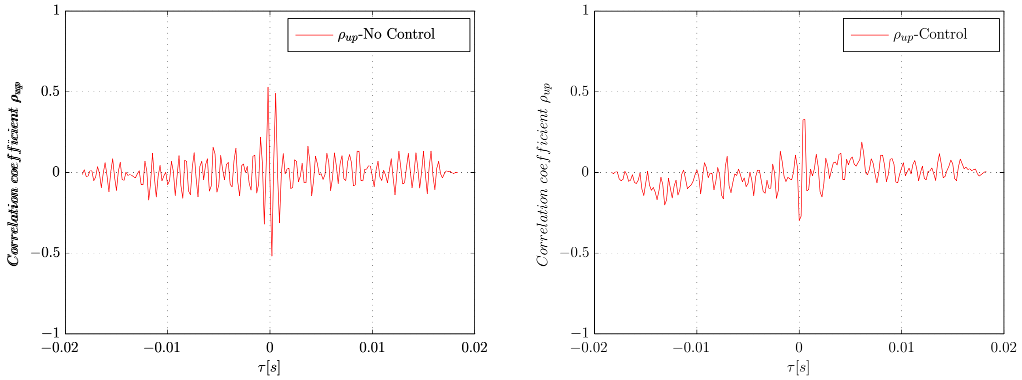

(e) No Control (f) Control

Figure 5.47: Cross-correlation of pressure and streamwise velocity (u_f) signals at U_∞=17, 20 and 25 m/s.

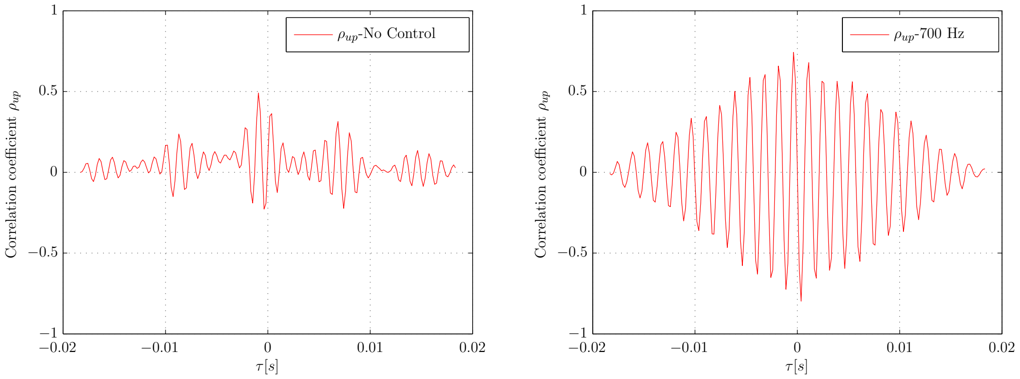

(a) No control

(b) f_{ac}=700 Hz

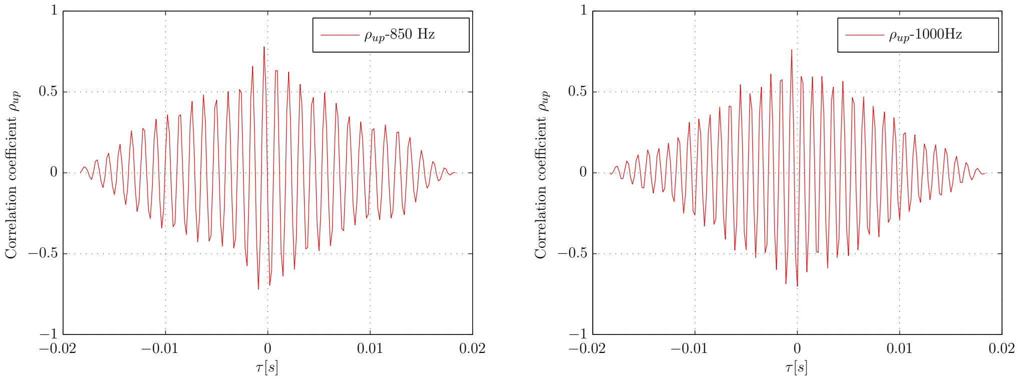

(c) f_{ac}=850 Hz

(d) f_{ac}=1000 Hz

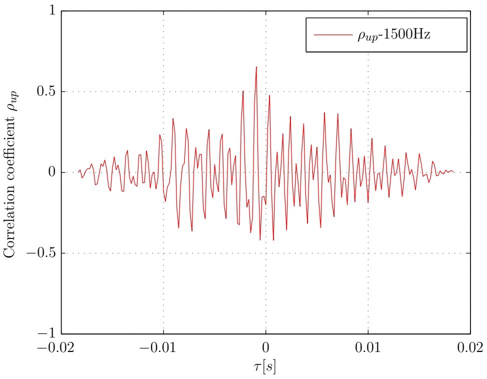

(e) f_{ac}=1500 Hz

Figure 5.48: Cross-correlation of pressure and streamwise velocity(u_f) signals for open loop case at U_∞=17 m/s.

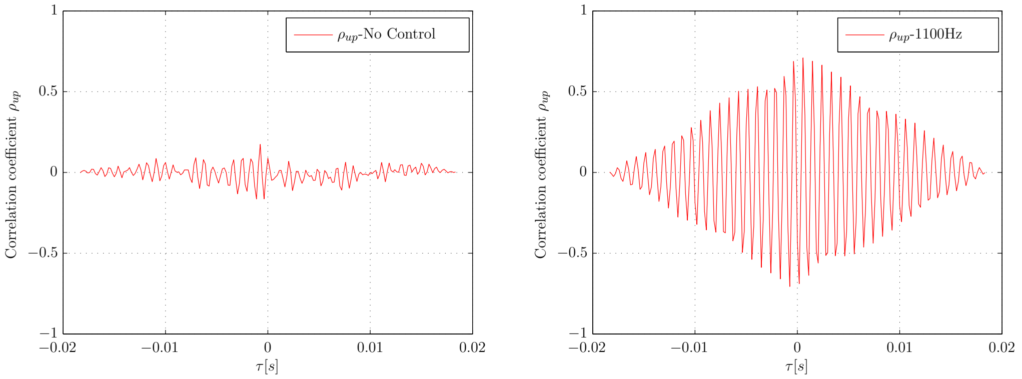

(a) No control

(b) f_{ac}=1100 Hz

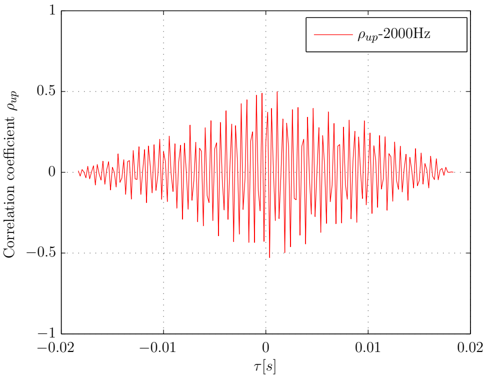

(c) f_{ac}=2000 Hz

Figure 5.49: Cross correlation of pressure and streamwise velocity (u_f)signals for open loop case at U_∞=25 m/s.

5.6 Parametric study on control performance

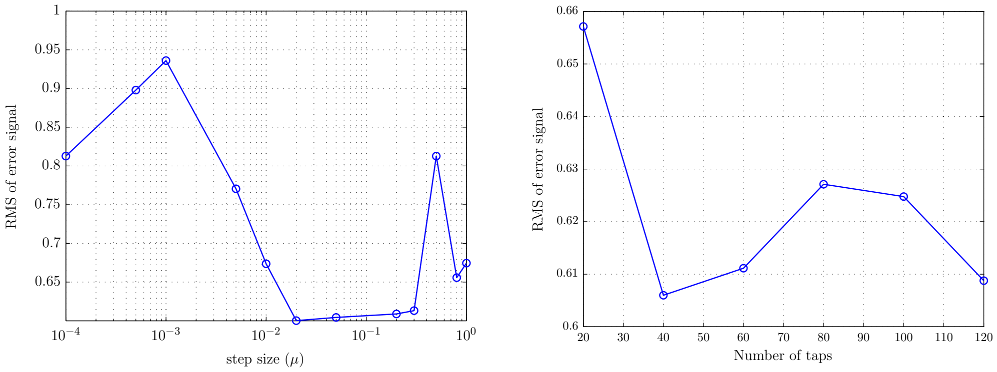

(a) RMS of the error signal for different step size at number of taps=80.

(b) RMS of the error signal for different number of taps at step size of 0.3.

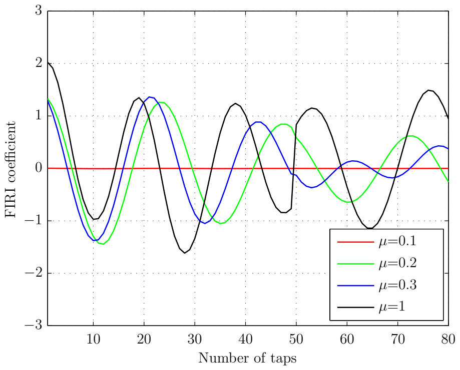

(c) controller behaviour for the variation of step size

Figure 5.50: RMS of the error signal for different (a) step size (μ); (b) number of taps and (c) behaviour of the controller for the variation of step size.

Prior to the actual control cases, a parametric investigation on the operation of the controller is performed. Two separate studies are conducted involving variation of the step size (μ) and the number of taps (length). In both the cases all other parameters are kept constant. Figure 5.50 (a) depicts a RMS of error signal for different step size (μ) at number of taps=80 in semilogx scale. Two effects are evident here which are typical for FXLMS algorithm. Firstly, if the step size is too low (μ=0.0005, 0.0001 and 0.001) the algorithm is unstable, which is justified by the higher RMS values of the error signal. From the step size of (μ=0.005 to 0.05) the algorithm is converging to the optimum solution drastically. The step size (0.05, 0.2 and 0.3) is the best options for the stable algorithm. Although μ=0.05 provides best algorithmic solution but μ=0.3 is preferred as the optimum step size due to its effectiveness in all the cases. This is selected by trial and error. On the other hand, if the step size

(μ=0.5, 0.8 and 1) is too large then the algorithm becomes unstable which is also justified by the sudden increase of RMS values of the error signal.

The second parameter is investigated is the variation of the number of taps at a constant step size of 0.3. Figure 5.50 (b) shows the RMS of the error signal for different number of taps at a step size of 0.3. It should be noted that the RMS error signal magnitude varies within 0.62 to 0.66 for different number of taps. Although the number of taps of 40 provides best algorithm solutions but for number of taps 80 is preferred as the optimum number of taps due to its effectiveness for all the cases. In addition, the behaviour of the controller is depicted in Figure 5.50 (c) for the variation of step size. Therefore, step size of 0.3 and the number of steps of 80 is selected for the effective use of the FXLMS controller in order to cancel T-S waves.

Chapter 6

Conclusions and outlook

This final chapter aims at presenting a summary of the major conclusions this work has arrived at. Additionally, based on the findings, presents a recommendations for possible pathways towards future research in the area of active cancellation of T-S waves using DBD plasma actuator.

6.1 Conclusions

The first part of the research presented in this thesis is to have an insight of the DBD plasma actuator effect of different carrier frequency f_{ac}= 750 Hz, 1000 Hz, 1500 Hz and 2000 Hz at fixed applied voltage f_{app}=10 kV in Quiescent flow conditions. The major conclusions for this part is listed below:

- The jet velocity is not a linear function of carrier frequency. In addition, it increases with the increasing carrier frequencies.
- The mean velocity profiles show that the velocity acceleration is significantly higher for f_{ac}=1500 and 2000 Hz as compared to f_{ac}= 750 and 1000 Hz. Additionally, for f_{ac}= 1500 and 2000 Hz, the mean velocity profiles are negative but very small magnitude. This is due to the fact that air is entrained towards the wall in order to restore the mass flow.
- The time evolution of the velocity component (u) reveals that on moving further downstream position (x=15 mm), the velocity component (u) for the sequence of frequencies shows a significant decrease as compared to the position x=10 mm. The velocity (u) values for f_{ac}=2000 Hz are higher as compared to other carrier frequencies. It is evident that the coherent structures associated with the impulsive start of the actuation and also velocity fluctuations appear in the vicinity of the actuator. This is attributed to the electrostatic oscillation of the body force as reported by Kotsonis (2012).

The second part of this work involves the statistical flow properties conducted for clean flow configuration. The major conclusions are mentioned below:

- The mean velocity profiles exhibits an inflection point which confirms the presence of instabilities present in the boundary layer for the freestream velocities U_∞=10, 15, 20 and 25 m/s.
- The instabilities are natural T-S waves which are confirmed by the normal Reynolds stress profiles exhibiting ($\overline{uu}$) typical footprint of T-S waves as reported by Grundmann (2008). In addition, the natural T-S waves increases more rapidly on moving downstream which is confirmed by the Table 6.1. This shows the maximum value of normal Reynolds stresses at the downstream location (x=30 mm).

Table 6.1: Maximum normal Reynolds stress values at x= 30 mm.

U_∞[m/s]	$\overline{uu}$ $[m^2/s^2]$	$\overline{vv}$ $[m^2/s^2]$
10	1.31	0.12
15	1.73	0.41
20	2.45	0.55
25	3.12	0.63

- The time evolution of velocity fluctuations also confirms the growing of T-S waves stronger on proceeding downstream. The typical appearance of T-S waves is in the form of wave packets which is clearly visible for U_∞=15, 20 and 25 m/s. Furthermore, PSD of velocity fluctuations also shows that the unstable domain shifts to a higher frequency with increasing flow velocity. The Table 5.4 depicts the dominating frequency (f_{TS}) and their wavelength of T-S waves.
- PSD of error sensor also shows that the unstable domain shifts to a higher frequency with increasing flow velocity. The dominating frequency of T-S waves obtained from error sensor matches well with PSD of velocity fluctuations from PIV.

The third part of this work involves the statistical flow properties conducted for closed loop case. The main objective of this case is to cancel the T-S waves by superimposing them with adaptive counter waves. The major conclusions of this case are presented below:

- The mean velocity profiles exhibits an inflection point for no control cases confirms the presence of instabilities present in the boundary layer for the freestream velocities U_∞=17, 20 and 25 m/s respectively. The inflection point is significantly suppressed for all the cases. The suppressive effect is higher for U_∞=17 m/s.
- The turbulence level and Reynolds stress profiles shows typical characteristics of natural T-S waves for no control cases for U_∞=17, 20 and 25 m/s respectively. With control case, the cancellation of T-S waves is higher for 17 m/s while significant suppression is maintained for higher velocities. The reduction is due to the cancellation of T-S waves by superimposition with continuously generated counter waves using DBD plasma actuator by means of close loop control (Adaptive FXLMS control). More specifically, the cancellation effectiveness is reduced for higher velocities due to the fact that the relative body force generated by the plasma remains same whereas instabilities grows stronger as the velocity increases.

- The time evolution of velocity fluctuations for no control cases reveals the occurrence of T-S waves in the form of wave packets. Secondly, these T-S waves become amplified on proceeding downstream. With control on, there is a significance attenuation of the velocity fluctuations for upstream positions whereas only small attenuation for the downstream position. Furthermore, PSD of velocity fluctuations (u_f) for closed loop control case indicate a significant reduction over the whole frequency range of the T-S waves for their respective streamwise position. In terms of positions, the upstream position shows higher reduction as compared to downstream positions. In addition, reduction is higher for U_∞=17 m/s whereas significant suppression is achieved for U_∞=20 and 25 m/s.
- Finally, PSD of error microphone shows the reduction of a natural T-S waves up to 7.65 dB, 3.7 dB and 2 dB for U_∞=17, 20 and 25 m/s respectively. In addition, RMS of error microphone shows a reduction of approximately 50 % is achieved for a U_∞=17 m/s while significant suppression of approximately 17 % and 11 % is maintained for U_∞=20 and 25 m/s respectively.

The fourth part of this work involves the statistical flow properties conducted for open loop case. The objective of using open loop control strategy is to demonstrate the behaviour of natural T-S waves and control of no feedback assistance. The major conclusions of this case are presented below:

- The mean velocity profiles for U_∞=17 m/s exhibiting inflection point confirms the presence of instabilities. These instabilities are amplified while actuating at an unstable carrier frequency of f_{ac}=700 and 850 Hz whereas attenuates at stable carrier frequency f_{ac}=1500 Hz. Similar behaviour is observed in unstable (f_{ac}=1100 Hz) and stable (f_{ac}=2000 Hz) carrier frequency at U_∞=25 m/s.
- The turbulence level and Reynolds stress profiles confirm the presence of natural T-S waves for no control cases at 17 and 25 m/s respectively. The natural T-S waves are amplified, actuating at unstable carrier frequencies while dampening of natural T-S waves actuating at stable carrier frequencies. This behaviour is also confirmed by the PSD of the velocity fluctuation (u_f).
- Finally, PSD of error microphone shows the natural T-S waves of the frequency range is (732-1100 Hz) and (1025-1831 Hz) for U_∞=17 and 25 m/s respectively. The dominating peak occurs at the frequency of 781.3 Hz and 1367 Hz for U_∞= 17 and 25 m/s respectively. Additionally, RMS of error microphone shows a reduction of approximately 35 % and 68 % is achieved for stable carrier frequency of f_{ac}=1000 and 1500 Hz at U_∞=17 m/s whereas significant suppression of approximately 18 % is maintained for stable carrier frequency of f_{ac}=2000 Hz at U_∞=25 m/s respectively.

6.2 Outlook

The present work successfully demonstrates a cancellation of natural occurring T-S waves over a NACA 0012 airfoil by a closed-loop control system using the filtered-x Least Mean Squares adaptive algorithm based on Finite Impulse Response (FIR) filters. This is considered to be an important step towards natural T-S wave cancellation with plasma actuators. In the future, it might be of interest to focus research on the improvement of performance and an adaptation of the actuator will be necessary for further improvement of the cancellation of natural T-S waves at higher freestream velocities. At higher velocities using thicker dielectric configuration and varying applied voltage (12 kV, 14 kV and 16 kV) could lead to significant step changes in the ability of the DBD to provide significant forcing. The proper optimization of the controller with the significant forcing could lead to increase in an effectiveness of cancelling natural T-S waves by closed loop control especially at higher velocities. The reason behind this suggestion is supported by the fact that the thicker dielectric configurations are generally able to produce higher maximum net forces as the dielectric is able to withstand higher currents. The implementation of such concept could lead to a higher cancellation T-S waves at higher velocities.

Bibliography

(n.d.).

Anderson, J. (2005), 'Ludwig prandtl boundary layer.', *Physics Today* **38**, 42–47.

Arbey, H. and Bataille, J. (1983), 'Noise generated by airfoil profiles placed in a uniform laminar flow.', *Journal of Fluid Mechanics* **134**, 33–47.

Boik, A. and Klingmannlt, B. (1994), 'Experiments in a boundary layer subjected to free stream turbulence. part 2. the role of ts-waves in the transition process', *J. Fluid Mech* **1**(281), 219–245.

Brendel, M. and Mueller, T. (1988), 'Boundary-layer measurements on an airfoil at low reynolds numbers', *Journal of aircraft* **25**(7), 612–617.

Burgmann, S., Brücker, C. and Schröder, W. (2006), 'Scanning piv measurements of a laminar separation bubble', *Experiments in Fluids* **41**(2), 319–326.

Burgmann, S. and Schröder, W. (2008), 'Investigation of the vortex induced unsteadiness of a separation bubble via time-resolved and scanning piv measurements', *Experiments in Fluids* **45**(4), 675–691.

Cavalieri, D. (1995), On the experimental design for instability analysis on a cone at mach 3.5 and 6.0 using a corona discharge perturbation method, Master's thesis, Illinois Institute of Technology, Illinois, USA.

Chong, T., Joseph, P. and Kingan, M. (2012), 'An investigation of airfoil tonal noise at different reynolds numbers and angles of attack', *Applied Acoustics* **74**, 38–48.

Corke, T., Cavalieri, D. and Matlis, E. (2002), 'Boundary-layer instability on sharp cone at mach 3.5 with controlled input', *AIAA journal* **40**(5), 1015–1018.

Corke, T., Martiqua, L. and Dmitry, M. (2007), 'Sdbd plasma enhanced aerodynamics: concepts, optimization and applications', *Progress in Aerospace Sciences* **43**.

Desquesnes, G., Terracol, M. and Sagaut, P. (2007), 'Numerical investigation of the tone noise mechanism over laminar airfoils.', *Journal of Fluid Mechanics* **591**.

Dovgal, A., Kozlov, V. and Michalke, A. (1989), 'Laminar boundary layer separation:instability and associated phenomena', *Progress in Aerospace Sciences* **30**, 61–94.

Engert, M. and Nitsche, W. (2008), Active cancellation of tollmien-schlichting instabilities up to m= 0.40., *in* ‘International Congress of the Aeronautical Sciences, Paper’, Vol. 3.

Enloe, C., McLaughlin, T. E., VanDyken, R., Kachner, K. D., Jumper, E. and Corke, T. (2004), ‘Mechanisms and responses of a single dielectric barrier plasma actuator: plasma morphology’, *AIAA J* **42**(58994).

Enloe, C., McLaughlin, T., Font, G. and Baughn, J. (2006), ‘Frequency effect on the efficiency of the aerodynamic plasma actuator’, *AIAA Meeting* (166).

Enloe, C., McLaughlin, T., VanDyken, R. D., Kachner, K., Jumper, E. J., Corke, T., Post, M. and Haddad, O. (2004), ‘Mechanisms and responses of a single dielectric barrier plasma actuator: geometric effect’, *AIAA J* **42**(595-604).

Forte, M., Jolibois, J., Moreau, E., Touchard, G. and Cazalens, M. (2006), ‘Optimization of a dielectric barrier discharge actuator by stationary and instationary measurements of the induced flow velocity, application to airflow control’, *AIAA* (2863).

Gad-el Hak, M. (2000), *Flow Control; Passive, Active, and Reactive Flow Management*, Cambridge University Press.

Ghaemi, S., Ragni, D. and Scarano, F. (2012), ‘Piv-based pressure fluctuations in the turbulent boundary layer’, *Experiments in Fluids* **53**(6), 1823–1840.

Gmelin, C., Rist, U. and Wagner, S. (1999), ‘Dns of active control of disturbances in a blasius boundary layer.’, *IUTAM Symposium Sedona AZ,Springer-Verlag* pp. 149–154.

Grundmann, S. and Tropea, C. (2008), ‘Delay of boundary-layer transition using plasma actuators.’, *46th AIAA Aerospace Sciences Meeting and Exhibit* (1369).

Grundmann, S.and Tropea, C. (2008), ‘Active cancellation of artificially introduced tollmien–schlichting waves using plasma actuators’, *Experiments in Fluids* **44**(5), 795–806.

Hansen, H. (2006), *Understanding Active Noise Cancellatio*, Taylor and Francis.

Hefner, J., Bushnell, Dennis, M. and Hefner, J. (1990), *Viscous drag reduction in boundary layers*, Vol. 123, AIAA.

Joslin, R. D. (1998), ‘Aircraft laminar fow control’, *Ann. Rev. Fluid Mech* **30**, 1–29.

Joslin, R., Nicolaides, R., Erlebacher, G., Hussaini, M. and Gunzburger, M. (1995), ‘Active control of boundary layer instabilities: use of sensors and spectral controller.’, *AIAA J.* **33(8)**.

Kendall, J. M. (1991), Studies on laminar boundary-layer receptivity to freestream turbulence near a leading edge, *in* ‘Boundary layer stability and transition to turbulence’, Vol. 1, pp. 23–30.

Klebanoff, P., Tidstrom, K. and Sargent, L. (1962), ‘Three-dimensional nature of boundary layer instability’, *Journal of Fluid Mechanics* **12**, 1–24.

Kotsonis, M. (2012), Dielectric barrier discharge actuators for flow control, PhD thesis, Delft Univeristy of Technology, The Netherlands.

Kotsonis, M., Veldhuis, L. and Bijl, H. (2010), Plasma assisted aerodynamics for transition delay., *in* 'Seventh IUTAM Symposium on Laminar-Turbulent Transition', Springer, pp. 219–224.

Kunhardt, E. (1980), 'Electrical breakdown of gases: The prebreakdown stage', *Plasma Science, IEEE Transactions on* **8**(3), 130–138.

Kunhardt, E. (2000), 'Generation of large-volume, atmospheric-pressure, nonequilibrium plasmas', *Plasma Science, IEEE Transactions on* **28**(1), 189–200.

Kunhardt, E. and Luessen, L. (1981), 'Electrical breakdown and discharges', *New York, USA: Plenum* **28(1)**(189-99).

Kuo, S. and Morgan, D. (1995), *Active noise control systems: algorithms and DSP implementations*, John Wiley and Sons, Inc.

Langmuir, I. (1926), *Proc Natl Acad Sci* **14**(627).

Liepmann, H. and Nosenchuck, D. (1982), 'Active control of laminar-turbulent transition.', *Journal of Fluid Mechanics* **118**(1), 201–204.

LLewellyn, J. (1966), 'The glow discharge and an introduction to plasma physics', *New York, USA: Methuen* .

Lowson, M. V., Fiddes and Nash, S. P. (1994), 'Laminar boundary layer aeroacoustic instabilities.', *AIAA Paper* **94**(0358).

Lueptow, R. (1995), 'Transducer resolution and the turbulent wall pressure spectrum', *The Journal of the Acoustical Society of America* **97**, 370.

McAlpine, A. (1997), Generation of discrete frequency tones by the flow around an aerofoil., PhD thesis, University of Bristol.

Michelis, T. (2012), On the interaction of ns-dbd plasma actuation with flat plate boundary layers, Master's thesis, Delft University of Technology.

Milling, R. (1981), 'Tollmien-schlichting wave cancellation.', *Physics of Fluids* **24**, 979.

Moreau, E. (2007), 'Airflow control by non-thermal plasma actuators', *J. Phys. D: Appl. Phys* **40**, 605–636.

Moreau, E. and Touchard, G. (2005), About the kinetic power induced by ac and dc discharges, *in* 'Electrical Insulation and Dielectric Phenomena, 2005. CEIDP'05. 2005 Annual Report Conference on', IEEE, pp. 469–473.

Morkovin, M. (1969), 'On the many faces of transition', *Viscous Drag Reduction* pp. 1–31.

Morkovin, M. (1978), 'Instability, transition to turbulence and predictability', *NASA STI/Recon Technical Report N* **78**, 31–40.

Morkovin, M. (1983), 'Understanding transition to turbulence in shear layers', *Final Report, 1 Oct. 1976-31 Dec. 1982 Illinois Inst. of Tech., Chicago. Dept. of Mechanics, Mechanical, and Aerospace Engineering.* **1**.

Morkovin, M., Reshotko, E. and Herbert, T. (1994), 'Transition in open flow systems-a reassessment', *Bull. Am. Phys. Soc* **39**(9), 1–31.

Müller, G. and Möser, M. (2009), *Handbook of engineering acoustics*, Springer.

Orlov, D., Corke, T. and Patel, M. (2006), 'Electric circuit model for aerodynamic plasma actuator', *AIAA paper* **1206**, 2006.

Paterson, R., Vogt, P., Fink, M. and Munch, C. (1973), 'Vortex noise of isolated airfoils.', *Journal of Aircraft* **10**(5), 296–302.

Pons, J., Moreau, E. and Touchard, G. (2004), 'Electrical and aerodynamic characteristics of atmospheric pressure barrier discharges in ambient air', - pp. 307–310.

Pons, J., Moreau, E. and Touchard, G. (2005), 'Asymmetric surface dielectric barrier discharge in air at atmospheric pressure: electrical properties and induced airflow characteristics', *Journal of physics D: applied physics* **38**(19), 3635.

Post, M., Erturk, E. and Corke, T. (2001), Phased plasma arrays for unsteady flow control, *in* 'APS Division of Fluid Dynamics Meeting Abstracts', Vol. 1.

Pröbsting, S. (2011), 'Coherent structures at the serrated trailing-edge of a naca 0012'.

Pupator, P. and Saric, W. (1994), 'Control of random disturbances in a laminar boundary layer.', *AIAA* **89**(1007).

Raffel, M., Willert, C. and Kompenhans, J. (1998), *Particle Image Velocimetry: A Practical Guide; with 24 Tables.*, Springer.

Raizer, Y., Kisin, V. and Allen, J. (1991), *Gas discharge physics*, Vol. 1, Springer-Verlag Berlin.

Reshotko, E. (1976), 'Boundary-layer stability and transition', *Annual Review of Fluid Mechanics* **8**(1), 311–349.

Roth, J. R. and Dai, X. (2006), 'Optimization of the aerodynamic plasma actuator as an electrohydrodynamic (ehd) electrical device', *AIAA paper* **1203**.

Roth, J., Sherman, D. and Wilkinson, S. (2000), 'Electrohydrodynamic flow control with a glow-discharge surface plasma', *AIAA journal* **38**(7), 1166–1172.

Saric, S. (1994), Physical description of boundary-layer transition: Experimental evidence, *in* 'In AGARD, Special Course on Progress in Transition Modelling', Vol. 1.

Schubauer, G. and Skramstad, H. K. (1948), 'Laminar-boundary-layer oscillations and transition on a flat plate'.

Shaw, R. (1960), 'The influence of hole dimensions on static pressure measurements', *Journal of Fluid Mechanics* **7**(4), 550–564.

Sturzebecher, D. and Nitsche, W. (2003), 'Active cancellation of tollmien–schlichting instabilities on a wing using multi-channel sensor actuator systems.', *International Journal of Heat and Fluid Flow* **24**(4), 572–583.

Thomas, A. (1983), 'The control of boundary-layer transition using a wave-superposition principle.', *Journal of Fluid Mechanics* **137**, 233–250.

Tsuji, Y., Fransson, J., Alfredsson, P. and Johansson, A. (2007), 'Pressure statistics and their scaling in high-reynolds-number turbulent boundary layers', *Journal of Fluid Mechanics* **585**, 1–40.

Van Dyken, R., McLaughlin, T. and Enloe, C. (2004), 'Parametric investigations of a single dielectric barrier plasma actuator', *AIAA paper* **846**, 5–8.

Veldhius, L. (2012), *Aircraft Aerodynamics reader*, Delft University of Technology.

White, F. (2006), *Viscous Fluid Flow*, Third Edition. McGraw Hill.

Yarusevych, S., Sullivan, P. and Kawall, J. (2006), 'Coherent structures in an airfoil boundary layer and wake at low reynolds numbers', *Physics of Fluids* **18**.

Yarusevych, S., Sullivan, P. and Kawall, J. (2009), 'On vortex shedding from an airfoil in low-reynolds-number flows', *Journal of Fluid Mechanics* **632**, 245.

Appendix A

Airfoil drawing [NACA 0012]

All dimensions are in mm

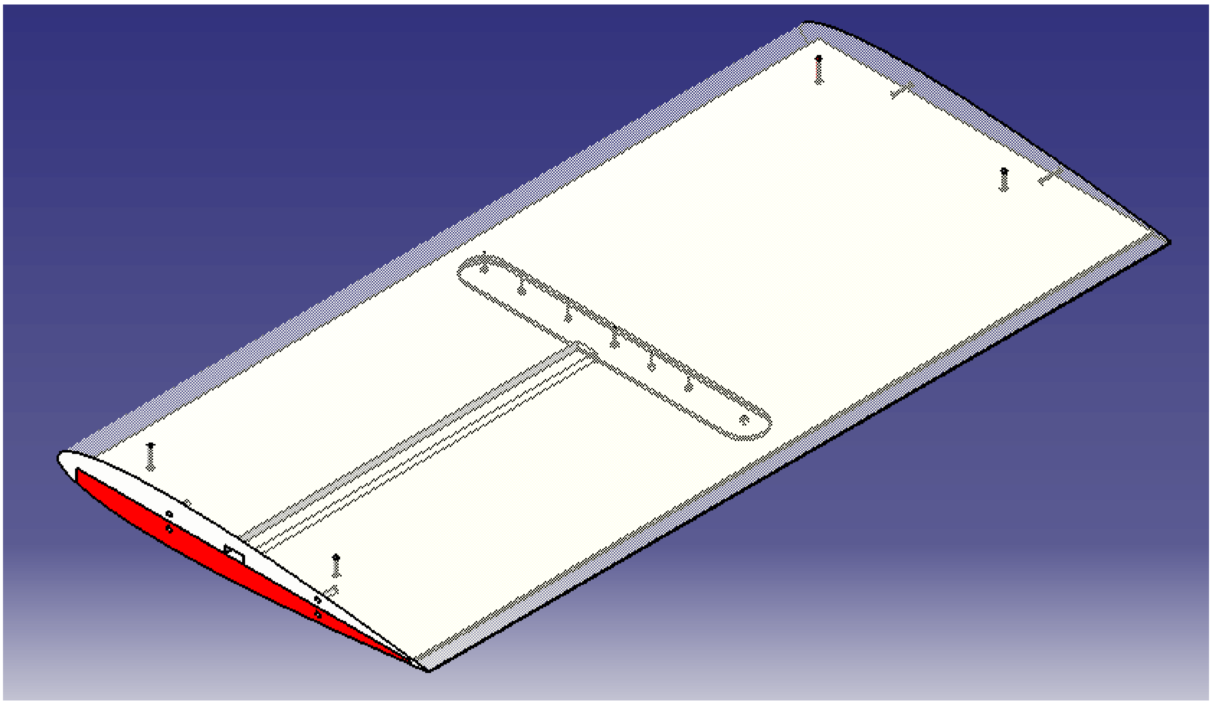

Figure A.1: Isometric View

A.1 Airfoil top part

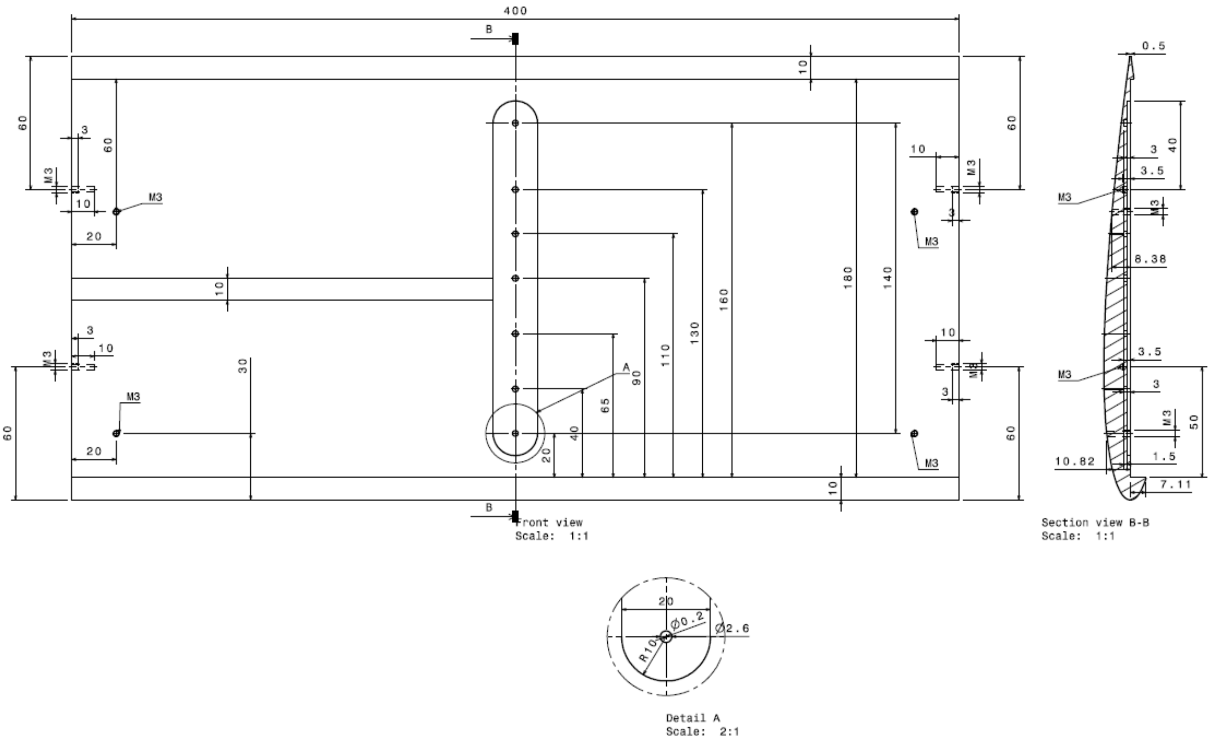

Figure A.2: Front and Section view

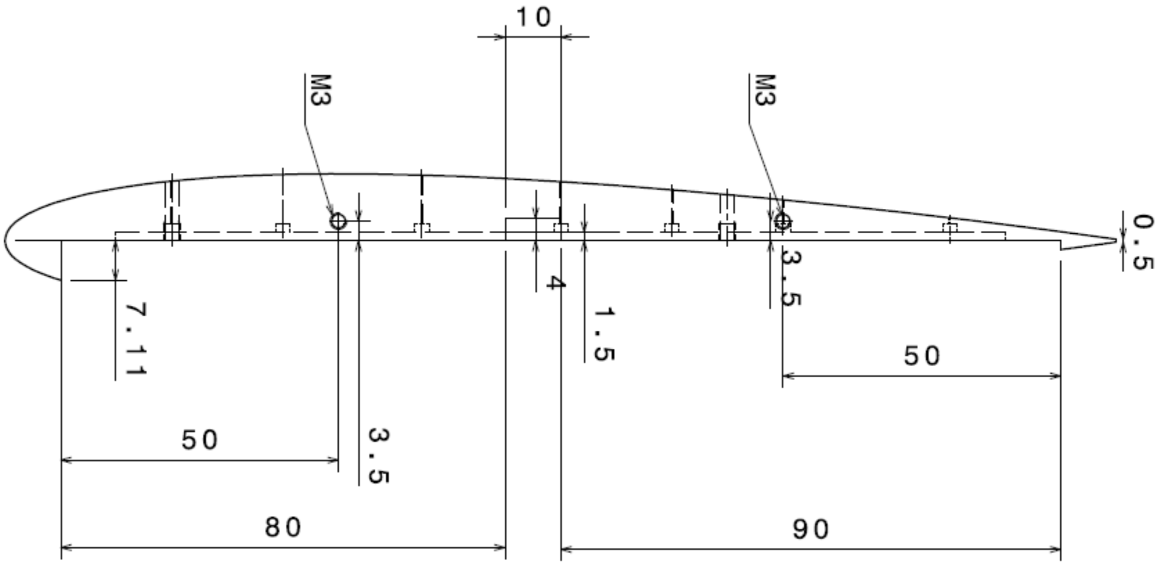

Figure A.3: Left view (Scale 1:1)

A.2 Airfoil bottom part

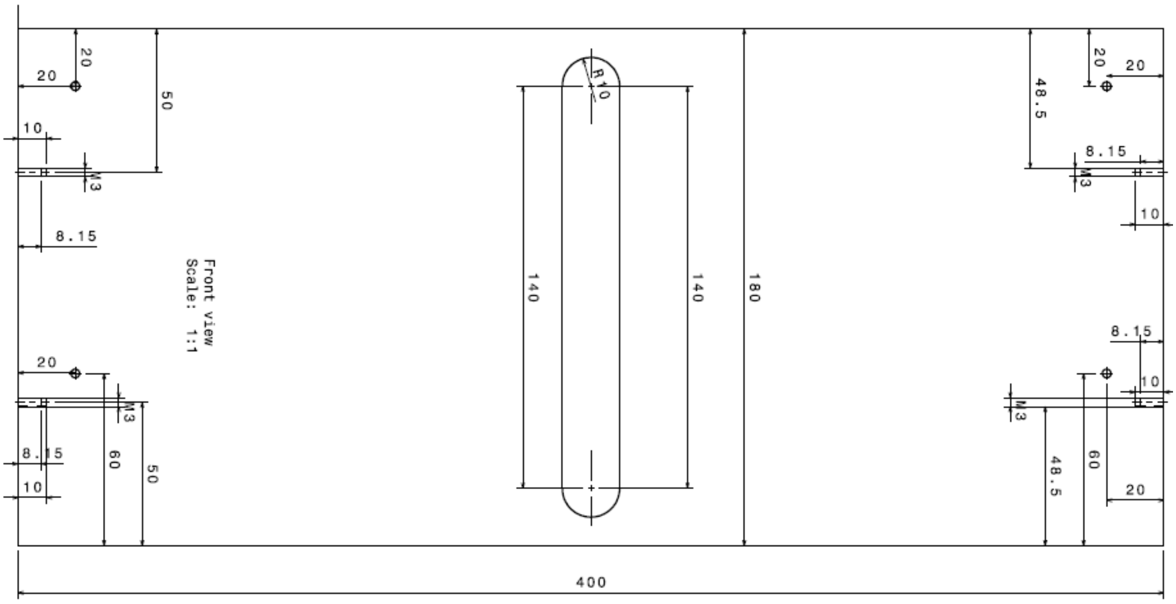

Figure A.4: Front and Left view (Scale 1:1)

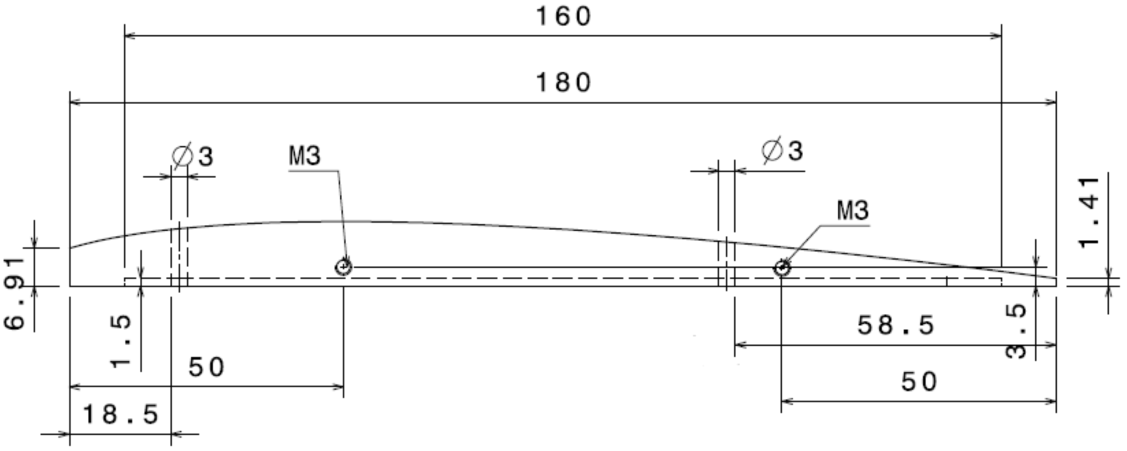

Figure A.5: Top view (Scale 1:1)

Appendix B

Basics of experimental techniques

B.1 Flow seeding

In PIV measurement techniques, a microscopic particles are introduced to track the fluid flow. The concentration of tracer particle plays a vital role. It should be introduced in an appropriate amount so that it doesn't alter the fluid flow. The concentration of seeding tracer particle ranges about 10^9 and 10^{12} $particles/m^3$. Above this range it will start affecting the flows (which is also known as multiphase flows effects). The process is governed by the mass ratio $m_{fluid}/m_{particles}$, which for micron size droplets in air flows should not exceed the order of 10^{-3}. The three important properties of tracer particles need to be considered. Firstly, the tracer particles exactly follow the motion of fluid. Secondly, the tracer particles do not alter the motion of fluid. Thirdly, the tracer particles should have sufficient light scattering properties. In the flow medium, the tracer particles are randomly distributed and they are convected along the local flow trajectory without altering their properties Raffel et al. (1998). The knowledge of mechanical principles for small particles immersed in fluid flows is critical in order to have accurate flow tracing.

B.1.1 Mechanical properties

In low speed motions the Stoke drag dominates the motion of the particles with respect to the difference between the particle velocity (V) and that of the surrounding fluid (U). It is given by eq B.1:

$$V - U = \frac{2}{9}a^2\frac{\rho_p - \rho_f}{\mu}\frac{dV}{dt} \tag{B.1}$$

where V-U is referred as settling velocity or slip velocity, d_p is the particle diameter, ρ_p density of the particles, ρ_f the density of the fluid, μ the dynamic viscosity and a the local acceleration of a fluid parcel. The condition of buoyancy neutral particles $\frac{\rho_p - \rho_f}{\mu}$ allows to obtain particles tracers accurately following the flow. For liquid flows it is easy to achieved as compared to gas flows. Typical values of density ratios $\frac{\rho_p}{\rho_f} = 0(10^3)$ and particles with a smaller diameter ($0.5\mu m < d_p < 5\mu m$) are employed. It is given by eq B.2:

$$\tau_p = d_p^2 \frac{\rho_p}{18\mu} \tag{B.2}$$

From the eq B.3, τ_p is a characteristics time and it is related to particle Stoke number S_k as given below:

$$S_k = \frac{\tau_p}{\tau_f} \tag{B.3}$$

Stoke number is a good indication for the ability of the tracers to follow the fluid given that $St << 1$. But due to practical limitations $St < 0.1$ is used.

B.1.2 Scattering properties of tracer particles

The requirements of accurate flow tracking and sufficient light scattering conflict with each other. Therefore, it requires a trade-off solution to obtain an optimum. The scattering efficiency of the particles depends on the ratio of refractive index n/n_f, wavelength of light λ^{-4} and particle diameter d_p. The micro-metric particles scattered light in the Mie regime. In this regime, the particle diameter is comparable or larger than the light wavelength λ. The scattering efficiency is maximum at 180 degrees and 0 deg and lower on the sides. Unfortunately most of the PIV technique is applied with a view oriented at 90 deg where the scattered light intensity attains a minimum Raffel et al. (1998).

B.2 Illumination

For PIV measurement techniques, lasers are used as an illumination sources. As a light source different kind of monochromatic lasers are used. These monochromatic lasers are differ in the laser material, power consumption, geometrical dimensions, resulting pulse energy, pulse repetition rate and wavelength of the emitted light. They can produce a pulsed, collimated and monochromatic light beam that can be easily shaped into a thin light sheet. Some lasers can be used in continuous wave mode(CW) while others emit light only in the form of short pulses with a duration from a few nanoseconds up to a hundred microseconds. Pulsed light sources are most used because of the high temporal definition of the illumination pulse (in order of nanoseconds) whereas CW lasers can be used when the flow velocity is limited and the duration of illumination can be controlled by the camera exposure time shutter (nowadays electronic). CW lasers are relatively less expensive and simpler than pulsed ones. Moreover no signal losses due to partial light sheet overlap can occur since a single light beam is used.

B.3 Imaging

The images of the tracer particles are formed by the lens on the surface of an image sensor. The imaging of the particle is limited by diffraction due to the small particles diameters. This implies that the wavelength of the light has an influence on the aperture of the camera and as well as on the size of the particle image. The characteristics of imaging system is depended on focal length (f),aperture number ($f_{\#}$) which is defined as the ratio of focal length to the aperture diameter (D) and image magnification (M) which is defined as the ratio of the image distance d_i and object distance d_o. And its mathematical representation by eq B.4:

$$\frac{1}{f} = \frac{1}{d_i} + \frac{1}{d_0}; M = \frac{d_i}{d_0} \tag{B.4}$$

The effective particle diameter in combination of the geometric optics effect is given by eq B.5:

$$d_{geom} = d_p M \tag{B.5}$$

where d_p is the effective particle diameter and then diffraction effect is given by eq B.6:

$$d_{diff} = 2.44\lambda(1 + M)f_{\#} \tag{B.6}$$

where λ is the wavelength of light source.

$$d_\tau = \sqrt{(Md_p)^2 + (d_{diff})^2} \tag{B.7}$$

An approximation of the resulting particle diameter using Euclidean sum of the above terms is given by eq B.7. Also, the geometric image of the particle Md_p is often neglected as compared to the diffraction limited image diameter.

$$\delta z = 4.88\lambda(f_{\#})^2(\frac{M}{M+1})^2 \tag{B.8}$$

From eq B.8 is applicable for particle image diameter only for the particle images in focus. That is when the light sheet thickness Δz_0 is smaller than the focal depth δz of the optical system. A large value of the numerical aperture is desired to obtain a higher depth of field while a small value has a positive effect on the light intensity collected by the sensor, posing another trade-off which is especially critical for recordings at high repetition-rates where the power per light pulse decreases.

Image processing

The next step is image processing that need to be done after gathering images. These images are processed to extract and analyse the velocity vector fields. The basic idea is to find the shift of tracer pattern between two frames recorded at a known time separation of Δt and then the cross-correlation operator is applied where correlation peak indicates the particle shift Δx in unit of pixels. The minimum correlation window size is restricted by the minimum number of tracer particles required for the accurate cross correlation. The average velocity of a fluid in the correlation volume is given by eq B.9, where Δx is the particle shift, Δt time separation, M magnification factor, l_{px} physical pixel size (property of the sensor).

$$U = \frac{\Delta x M l_{px}}{\Delta t} + \frac{\epsilon M l_{px}}{\Delta t} \tag{B.9}$$

In order to have higher vector resolution and statistically independent velocity vectors, a small correlation windows are required without large overlap. But this requirement creates an issue that tracer particles might travel further than the linear dimension of the correlation window during defined time separation. This makes cross-correlation between the correlation windows impossible as long as the windows are centred on identical pixels in both frames. As a result there is an decrease in signal to noise ratio. This problem can be overcome by using multi-pass iteration procedure. In Multi-pass iteration procedure, a correlation process is repeated for windows of different sizes. During first iteration step, relatively large window size is used to have an initial idea for the velocity vectors which is used to apply a shift between correlation windows in the second iteration step. It also facilitates to reduce the correlation window size in the second iteration without losing correlation peak. The particle displacement must not be too small since this decreases the accuracy due to the constant error ϵ. There are certain pre-processing techniques are often applied in order to improve the image and cross-correlation quality. Preprocessing helps to remove spurious light by subtraction of the minimum for each individual pixel. Furthermore, in order to increase the reliability of vectors close to the reflecting surfaces, a normalisations such as multiplication by a constant and division by the average are used suggested by Pröbsting (2011).

Optimization rules

The cross relation operator is applied in order to find the shift of the tracer pattern between two frames recorded at time separation of Δt. The correlation peak indicates the particle shift Δx in units of pixels. There are important conditions need to follow for an optimal experiment. Firstly, The maximum in-plane displacement should be smaller than $\frac{1}{4}$of the window size. Secondly, The maximum out-of-plane displacement should be less that $\frac{1}{4}$ of the light sheet thickness. Thirdly, The maximum in-plane variation of particle image displacement for particles inside the same window should not exceed the particle image diameter.

B.4 Power spectral density

The processing of surface microphone and PIV velocity data, the power spectral density function is used. It shows the strength of the variation of energy as a function of frequency. In simplified form, it provides information at which frequencies variations are weak and strong. The autocorrelation of a single variable u(t) at two times t_1 and t_2 is defined by eq B.10

$$R(t_1, t_2) = \overline{u(t_1)u(t_2)} \tag{B.10}$$

The statistics are independent of the origin of time in case of stationary process, therefore the auto-correlation function is given by eq B.11

$$R(\tau) = \overline{u(\tau)u(\tau + t)} \tag{B.11}$$

The Fourier transform of R(τ) is called the Power Spectral Density (PSD).

$$S(\omega) = \frac{1}{2\pi} \int_{-\infty}^{+\infty} R(\tau) e^{-i\omega\tau}\, d\tau \tag{B.12}$$

In the eq B.12, substituting $\tau = 0$ and taking inverse Fourier transform will give eq B.13

$$\overline{u^2} = \int_{-\infty}^{+\infty} S(\omega)\, d\omega \tag{B.13}$$

The term $S(\omega)d\omega$ shows that the energy (more precisely, variance) in a frequency band $d\omega$ centred at ω. Therefore, the function $S(\omega)$ represents the way energy is distributed as a function of frequency ω. We say that $S(\omega)$ is the energy spectrum, and equation shows that it is simply the Fourier transform of the autocorrelation function.

Appendix C

Acoustic and interference study

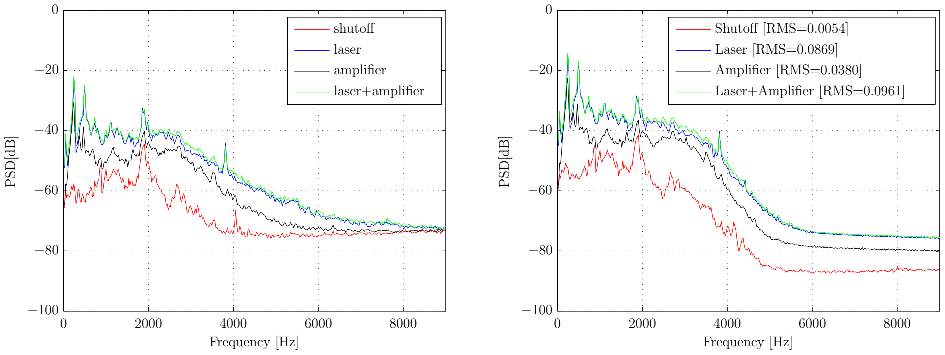

(a) Microphone-4

(b) Microphone-5 (Reference Sensor)

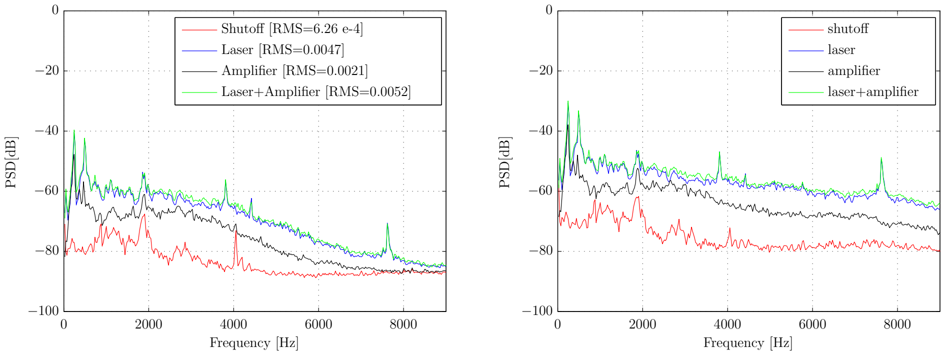

(c) Microphone-6 (Error Sensor)

(d) Microphone-7

Figure C.1: Power spectral density of microphone signals in ambient condition.

In the experimental environment, ambient noise level (sometimes called background noise level) to find out the major noise causing element among four different scenarios. In the first scenario, the measurements were conducted only putting laser on, while second scenario comprises only putting amplifier on, thirdly putting both laser and amplifier on and at last measurements were performed by shutting off everything. The test case is tabulated in Table 4.8 in Chapter 4. As observed in Figure C.1 which shows the PSD plots for the ambient condition it can be concluded that laser and amplifier combination shows higher energy content as compared to other scenarios. On comparing with the cases of shut-off, laser, amplifier, laser stands out to be the dominating one. The interference measurements were also conducted in still air by switching off laser. The main objective of performing this test to investigate the electromagnetic interference while carrying actuation. The test was conducted by varying carrier frequency f_{ac} in order to have an insight of EM noise effects on the signals. The test case is tabulated in Table C.2. The frequencies contains the harmonics of its own frequency observed for all the microphone. For instance the carrier frequency of f_{ac}=700 Hz has a harmonic peaks at 1400, 2100, 2800 Hz and so on. Similar behaviour is also found in other carrier frequencies. These harmonic peak occurrences are due to the EM noise which results in aliasing error and should

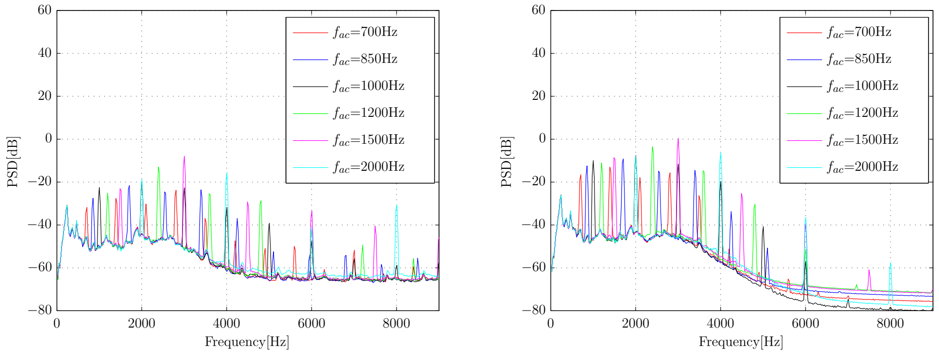

(a) Microphone-4

(b) Microphone-5 (Reference Sensor)

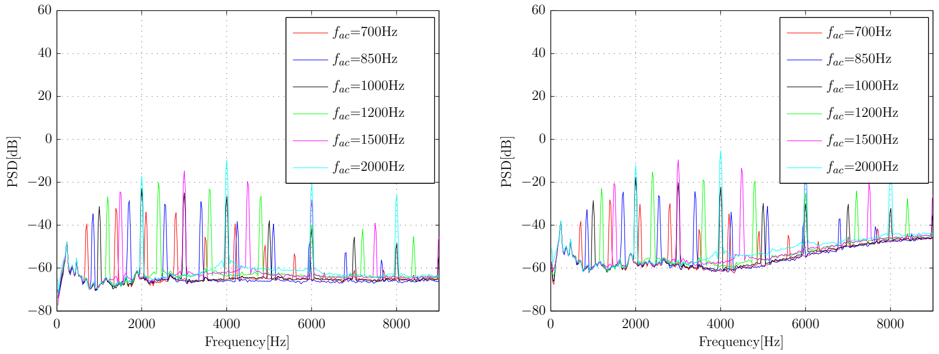

(c) Microphone-6 (Error Sensor)

(d) Microphone-7

Figure C.2: Power spectral density of microphone signals for interference case.

be ignored. It is also important to mention that these are not due to physical effects such as the plasma flow interaction.

Appendix D

Reynolds stress contours

The viscous mechanism of instability proposed by Tollmien and Schlichting. Viscous forces modify the phases of the velocity perturbations which lead to positive Reynolds stresses, enabling the transfer of energy from the mean flow to the disturbance (McAlpine, 1997). The Reynolds stress contours $\overline{uu}$,$\overline{vv}$ and $\overline{uv}$ are presented in the this section for clean configuration, close loop and open loop control cases.

D.1 Clean configuration

This section gives a description of the normal ($\overline{uu}$, $\overline{vv}$) and shear ($\overline{uv}$) Reynolds stresses contours for U_∞=10, 15, 20 and 25 m/s respectively. Data used in this section has been recorded using the high speed PIV set-up described in Chapter 4. The normal and shear Reynolds stresses contours are plotted from the statistics of the velocity field which has been obtained by averaging 5381 statistically independent vector fields recorded at a sampling rate of 5.4 kHz.

Figure D.1, D.2 and D.3 shows the contours of normal ($\overline{uu}$, $\overline{vv}$) and shear Reynolds stress($\overline{uv}$) respectively. As observed in ($\overline{uu}$) contours, for U_∞=20 m/s (x<1 mm) and 25 m/s (-1 mm <x<3 mm) shows a orange patches which is due to the bad illumination and should be ignored. In addition, for U_∞=10 m/s, the Reynolds normal stress seems to have higher values at the upstream positions as compared to other velocities. For the downstream positions, the normal Reynolds stress values are higher as the velocity increases. At x=30 mm, the maximum values of normal stress $\overline{uu}$ obtained is 1.31, 1.73, 2.45 and 3.12 m^2/s^2 for velocities 10 to 25 m/s respectively. The profiles ($\overline{uu}$) show that these instabilities are amplified as they move downstream until they may eventually grow large enough. This is a typical characteristic of T-S waves. Similar behaviour is also observed for normal ($\overline{vv}$) and shear Reynolds stress ($\overline{uv}$) as shown in contours. The detailed explanation in terms of Reynolds stress profiles is given Chapter 5 under subsection 5.2.2.

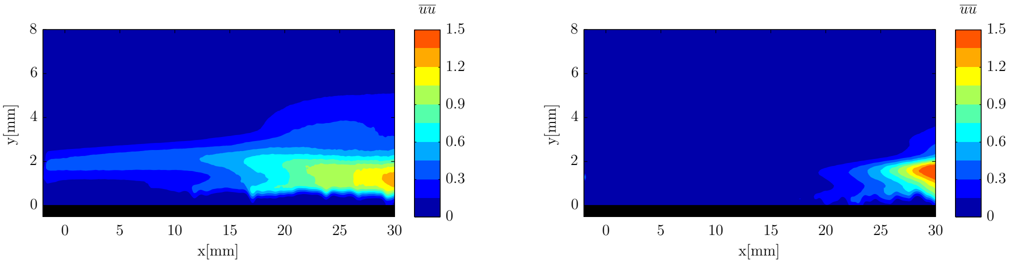

(a) U_∞=10 m/sec.

(b) U_∞=15 m/sec.

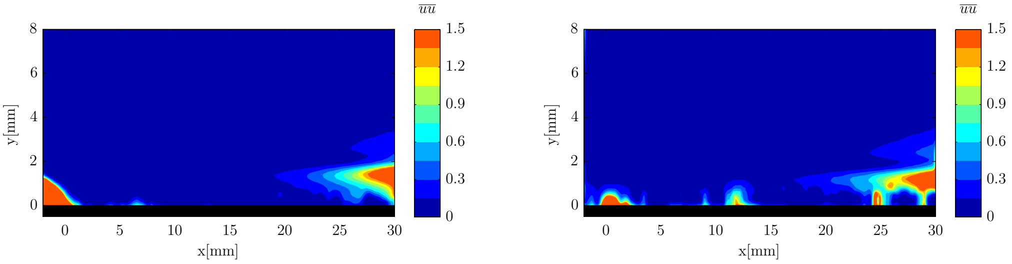

(c) U_∞=20 m/sec.

(d) U_∞=25 m/sec.

Figure D.1: Reynolds stress $\overline{uu}$ contours for clean configuration case at U_∞ (a) 10 m/sec; (b) 15 m/sec; (c) 20 m/sec; (d) 25 m/sec.

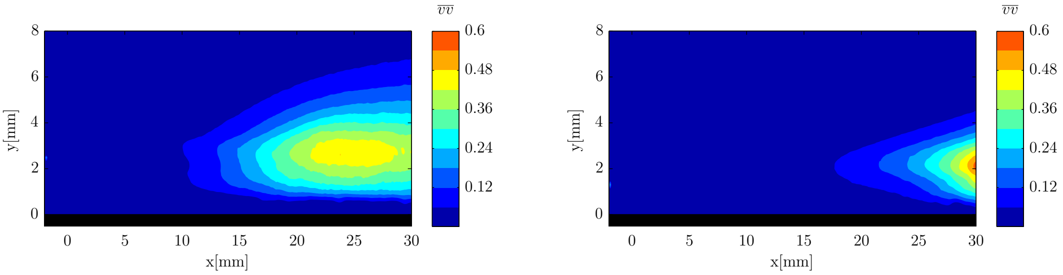

(a) U_∞=10 m/s.

(b) U_∞=15 m/s.

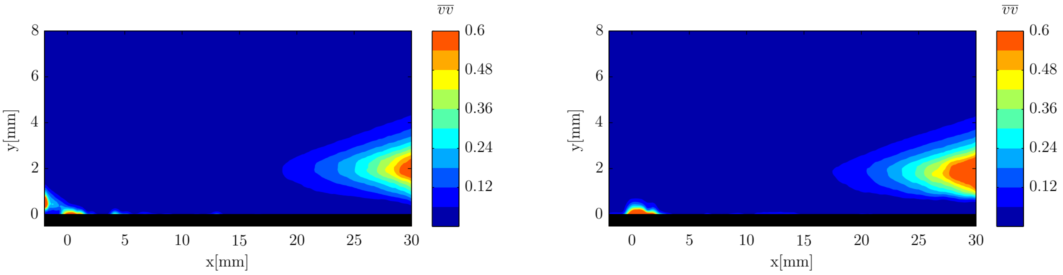

(c) U_∞=20 m/s.

(d) U_∞=25 m/s.

Figure D.2: Reynolds stress $\overline{vv}$ contours for clean configuration case at U_∞ (a) 10 m/s; (b) 15 m/s; (c) 20 m/s; (d) 25 m/s.

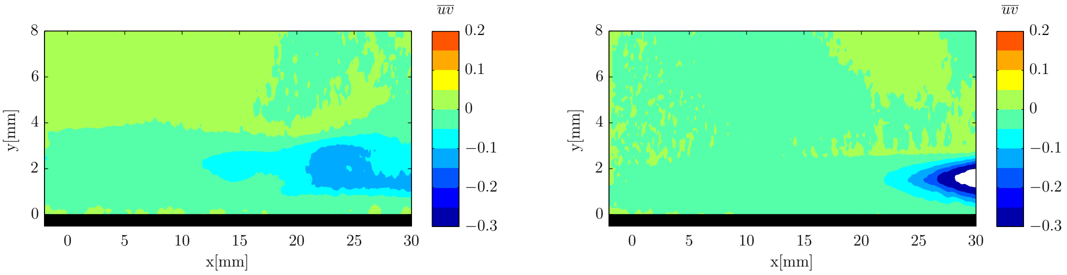

(a) U_∞=10 m/s.

(b) U_∞=15 m/s.

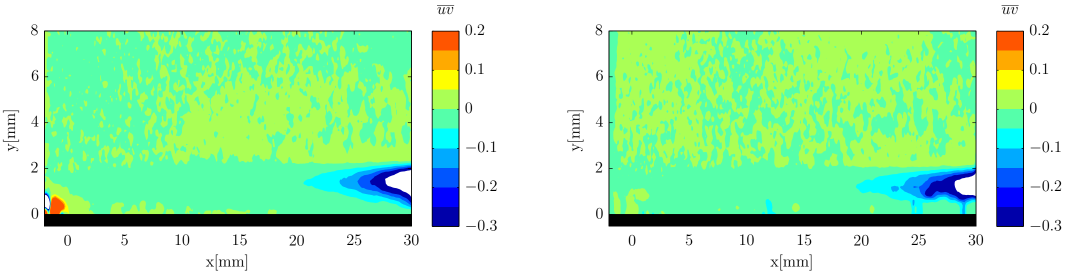

(c) U_∞=20 m/s.

(d) U_∞=25 m/s.

Figure D.3: Reynolds stress $\overline{uv}$ contours for clean configuration case at U_∞ (a) 10 m/s; (b) 15 m/s; (c) 20 m/s; (d) 25 m/s.

D.2 Closed loop control

This section gives a description of the normal ($\overline{uu}$, $\overline{vv}$) and shear ($\overline{uv}$) Reynolds stresses contours for closed loop case at U_∞=17, 20 and 25 m/s respectively. Data used in this section has been recorded using the high speed PIV set-up described in Chapter 4. The normal and shear Reynolds stresses contours are plotted from the statistics of the velocity field which has been obtained by averaging 5381 statistically independent vector fields recorded at a sampling rate of 5.4 kHz.

At U_∞=17, 20 and 25 m/s will show the qualitative investigation of Reynolds stress contours. The contours for U_∞=17 m/s is depicted in Chapter 5 under subsection 5.3.2 whereas for other two velocities are depicted here. In general, the contours with no control case shows considerable amount of Reynolds stresses especially in the downstream positions. This is explained by the fact that as we move further downstream the T-S waves continues to grow stronger (the flow moves over the airfoil surface which means more flow is affected by the friction as the distance along the surface increases). The presence of these instabilities modify the phases of the velocity perturbations leading to higher Reynolds stresses in the downstream positions.

For control case there is significant amount of reduction in normal and shear stresses as compared to no control cases. This is due to the adaptive cancellation of instabilities (T-S waves) using DBD plasma actuator. The reduction is higher for U_∞=17 m/s whereas there is a significant suppression is maintained for higher velocities U_∞= 20 and 25 m/s. This is explained by the fact that the relative body force generated by the plasma remains same whereas instabilities grows stronger as the velocity increases. Therefore, effectiveness is reduced at higher velocities. Furthermore, the Reynolds stress profiles in closed loop case shown in section 5.3.2 will support the fact explained here.

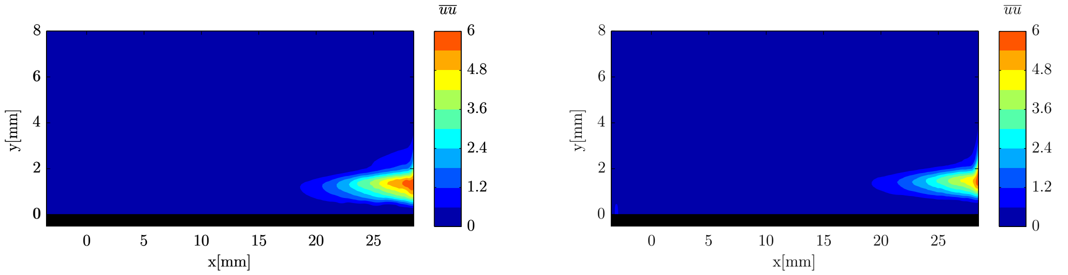

(a) $\overline{uu}$-No control

(b) $\overline{uu}$-Control

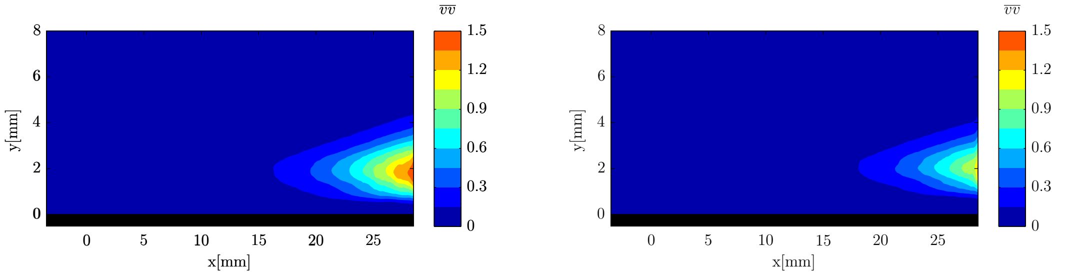

(c) $\overline{vv}$-No control

(d) $\overline{vv}$-Control

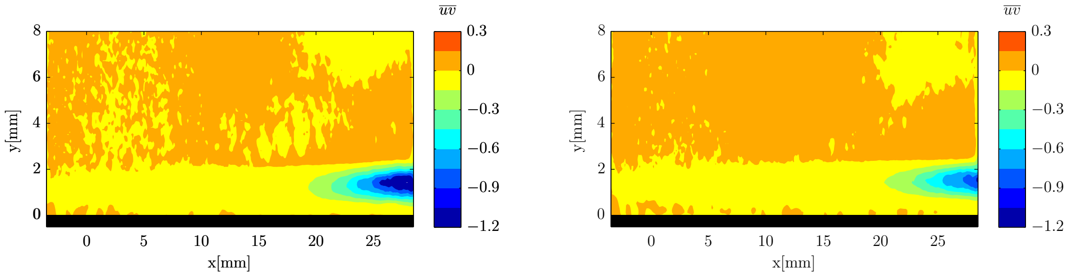

(e) $\overline{uv}$-No control

(f) $\overline{uv}$-Control

Figure D.4: Reynolds stress contours for close loop control at U_∞=20 m/s.

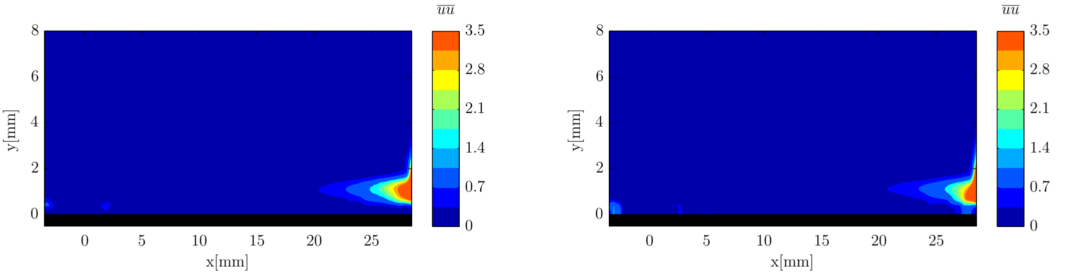

(a) $\overline{uu}$-No control (b) $\overline{uu}$-Control

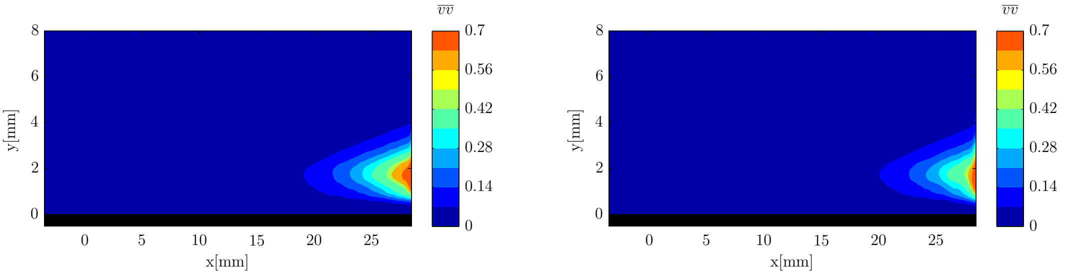

(c) $\overline{vv}$-No control (d) $\overline{vv}$-Control

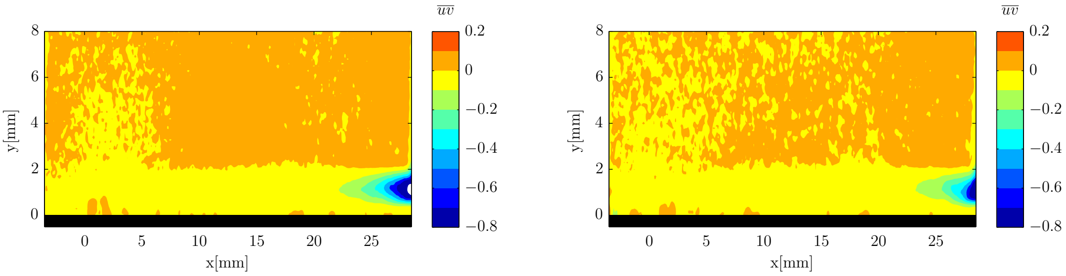

(e) $\overline{uv}$-No control (f) $\overline{uv}$-Control

Figure D.5: Reynolds stress contours for close loop control at U_∞=25 m/s.

D.3 Open loop control

This section gives a description of the normal ($\overline{uu}$, $\overline{vv}$) and shear ($\overline{uv}$) Reynolds stresses contours for open loop case at U_∞=17, 20 and 25 m/s for the sequence of carrier frequencies. Data used in this section has been recorded using the high speed PIV set-up described in Chapter 4. The normal and shear Reynolds stresses contours are plotted from the statistics of the velocity field which has been obtained by averaging 5381 statistically independent vector fields recorded at a sampling rate of 5.4 kHz.

The contours of normal and shear Reynolds stress for U_∞=17 m/s is depicted in Figure **??**, D.7 and D.8 respectively. The stresses values are higher for f_{ac}=700 and 850 Hz as compared to other cases. This is explained by the fact that these frequencies lie in unstable region i.e. close to the T-S wave frequency. Therefore, actuating at these frequencies will amplify the instabilities which can be observed in contours. At f_{ac}=1000 and 1500 Hz, the stresses reduces significantly. This is explained by the fact that 1000 and 1500 Hz lies in a stable region which results in dampening of T-S waves by the dominant blowing effect of the DBD plasma actuator. The reduction is higher for stable frequency of f_{ac}=1500 Hz due to the blowing effect becomes stronger than f_{ac}=1000 Hz. Therefore, f_{ac}=1500 Hz has a more stabilizing effect than 1000 Hz. Similar behaviour is observed for the shear Reynolds stress ($\overline{uv}$) as in case of the normal Reynolds stress contours $\overline{uu}$ and $\overline{vv}$ in terms of amplification and dampening of T-S waves.

The contours of normal and shear Reynolds stress for U_∞=25 m/s is depicted in Figure D.9, D.10 and D.10 respectively. The normal Reynolds stress contours ($\overline{uu}$, $\overline{vv}$) for f_{ac}=1100 Hz are significantly higher as compared to other cases. For f_{ac}=2000 Hz, the stresses reduces significantly as compared to no control cases. In addition, the carrier frequency f_{ac}=2000 Hz lies in a stable region which results in dampening of T-S waves by the dominant blowing effect of the DBD plasma actuator. Similar behaviour is observed for the shear Reynolds stress ($\overline{uv}$) as in case of the normal Reynolds stress contours $\overline{uu}$ and $\overline{vv}$ in terms of amplification and dampening of T-S waves.

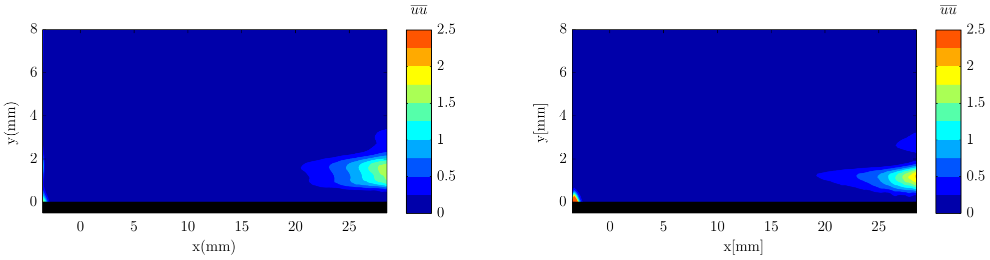

(a) No control

(b) f_{ac}=700Hz

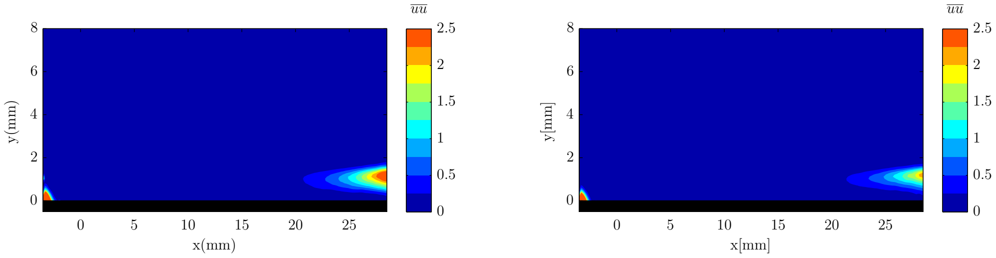

(c) f_{ac}=850Hz

(d) f_{ac}=1000Hz

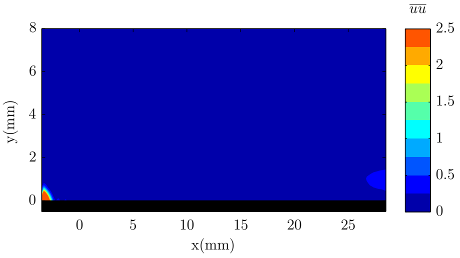

(e) f_{ac}=1500Hz

Figure D.6: Comparison of Reynolds stress $\overline{uu}$ contours for open loop control by varying carrier frequency f_{ac} a) No control; b) 700 Hz; c) 850 Hz; d) 1000 Hz; e) 1500 Hz at U=17 m/s.

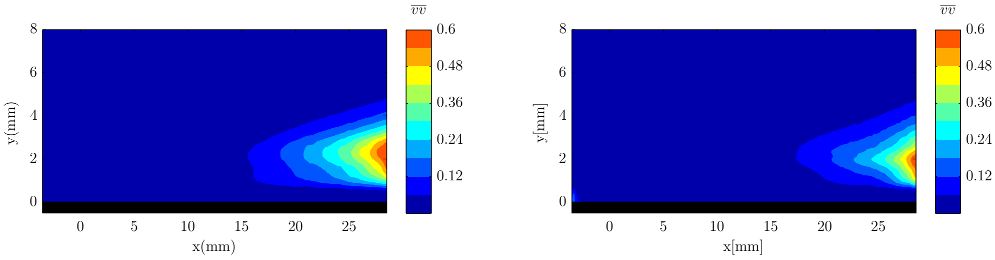

(a) No control

(b) f_{ac}=700Hz

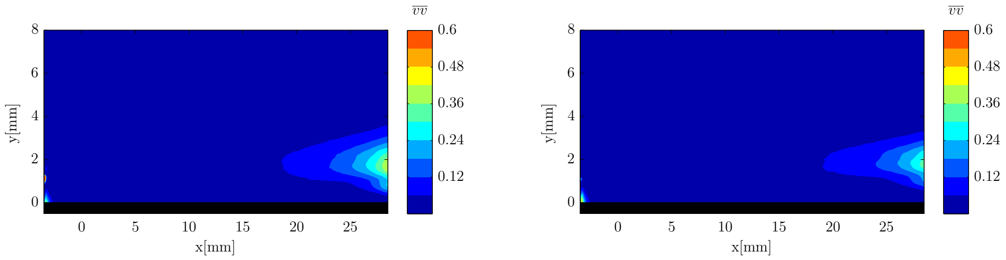

(c) f_{ac}=850Hz

(d) f_{ac}=1100Hz

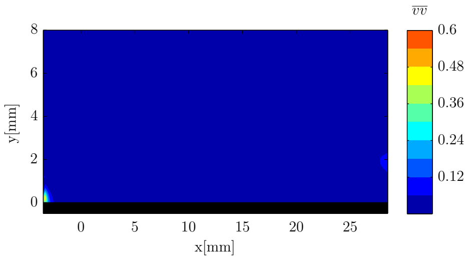

(e) f_{ac}=1500Hz

Figure D.7: Comparison of Reynolds stress $\overline{vv}$ contours for open loop control by varying carrier frequency f_{ac} a) No control; b) 700Hz; c) 850Hz; d) 1000Hz; e) 1500Hz at U_∞=17 m/s.

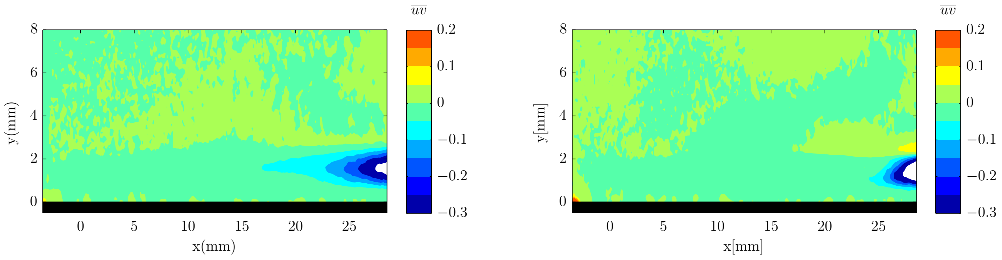

(a) No control

(b) f_{ac}=700Hz

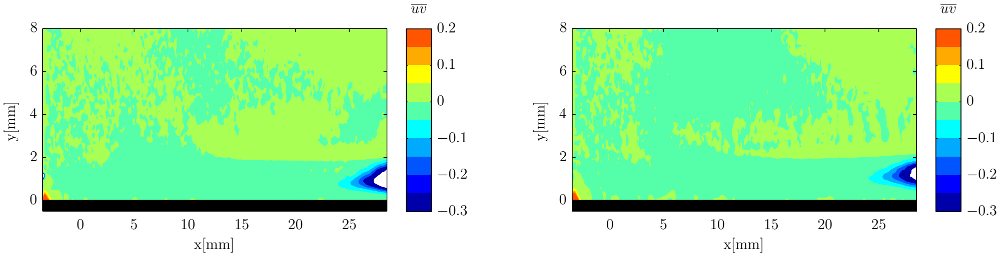

(c) f_{ac}=850Hz

(d) f_{ac}=1000Hz

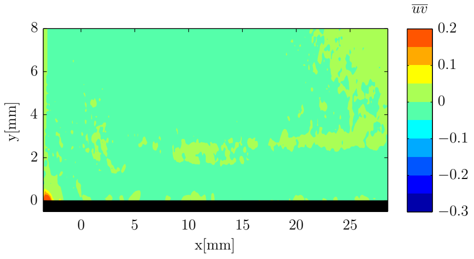

(e) f_{ac}=1500Hz

Figure D.8: Comparison of Reynolds stress $\overline{uv}$ contours for open loop control by varying carrier frequency f_{ac} (a) No control; (b) 700 Hz; (c) 850 Hz; (d) 1000 Hz; (e) 1500 Hz at U_{∞}=17 m/s.

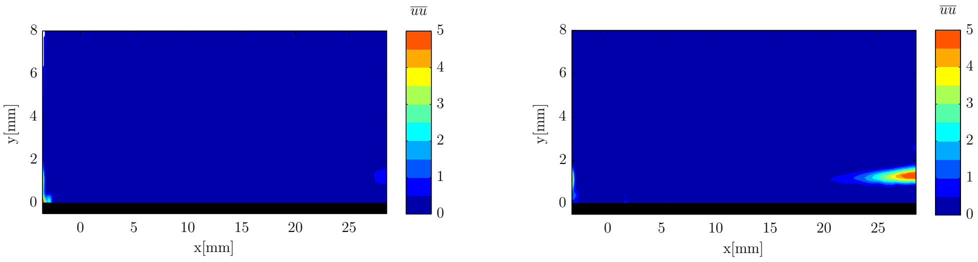

(a) No control

(b) f_{ac}=1100Hz

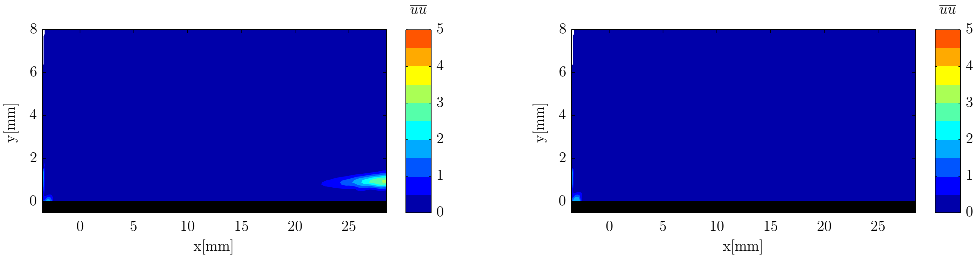

(c) f_{ac}=1500Hz

(d) f_{ac}=2000Hz

Figure D.9: Comparison of Reynolds stress $\overline{uu}$ contours for open loop control by varying carrier frequency f_{ac} (a) No control; (b) 1100 Hz; (c) 1500 Hz; (d) 2000 Hz at U_{∞}=25 m/s.

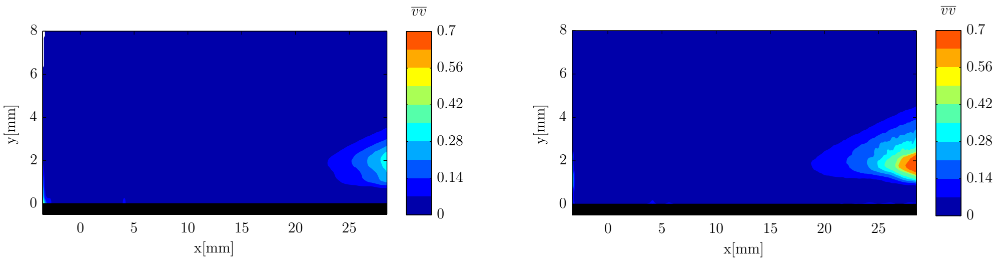

(a) No control

(b) f_{ac}=1100Hz

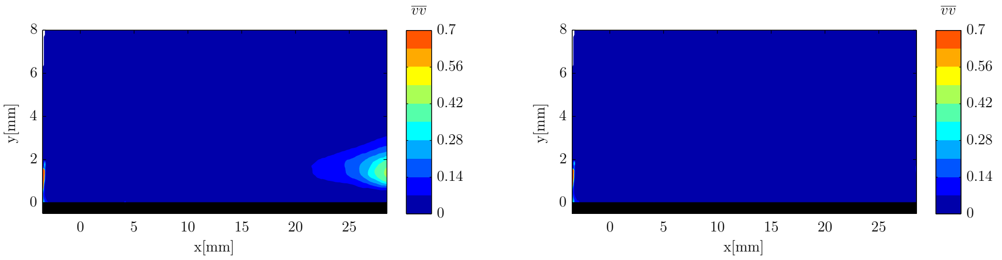

(c) f_{ac}=1500Hz

(d) f_{ac}=2000Hz

Figure D.10: Comparison of Reynolds stress $\overline{vv}$ contours for open loop control by varying carrier frequency f_{ac} (a) No control; (b) 1100 Hz; (c) 1500 Hz; (d) 2000 Hz at U_{∞}=25 m/s.

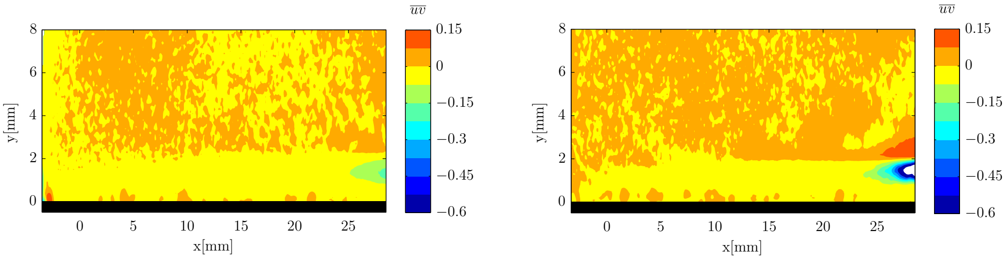

(a) No control

(b) f_{ac}=1100Hz

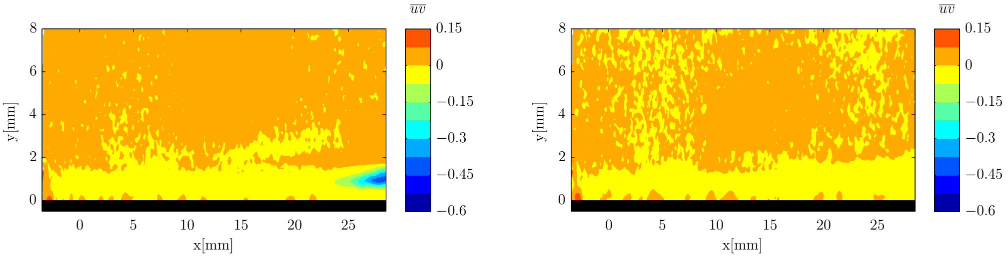

(c) f_{ac}=1500Hz

(d) f_{ac}=2000Hz

Figure D.11: Comparison of Reynolds stress $\overline{vv}$ contours for open loop control by varying carrier frequency f_{ac} (a) No control; (b) 1100 Hz; (c) 1500 Hz; (d) 2000 Hz at U_∞=25 m/s.

Appendix E

Time evolution

Figure E.1 shows the time evolution of velocity fluctuations (u_f and v_f) for positions x=10.10, 17 and 27.80 mm (at y=1.6 mm) respectively. At x=10.10 mm, the fluctuations shows the footprint of the development of T-S waves in its early stage in which amplitudes of these fluctuations are very small. On moving downstream position (x=17 mm), there is a small rise in the amplitudes of the fluctuations which results in the development of typical T-S wave packets. On moving further downstream position (x=27.80 mm), there is a significant rise in the amplitudes of the fluctuations. This results the T-S wave packets which are in intermittent stage.

Figure E.2 shows the time evolution of velocity fluctuations (u_f and v_f) for U_∞=20 m/s. The time traces of velocity fluctuations are plotted for positions x=10.20, 15.70 and 28.90 mm (at y=1.45 mm)respectively. The time traces fluctuations shows the similar behaviour as it is observed for U_∞=10 and 15 m/s. At x=10.20 mm, the fluctuations shows the development of T-S waves in its early stage. The amplitudes of these fluctuations are very small. On moving further downstream (x=15.70 mm), these are developing into T-S waves packets. At x= 28.90 mm, the typical T-S wave packets are apparent. These wave packets are well defined as compared to wave packets formed at the downstream position for U_∞=15 m/s.

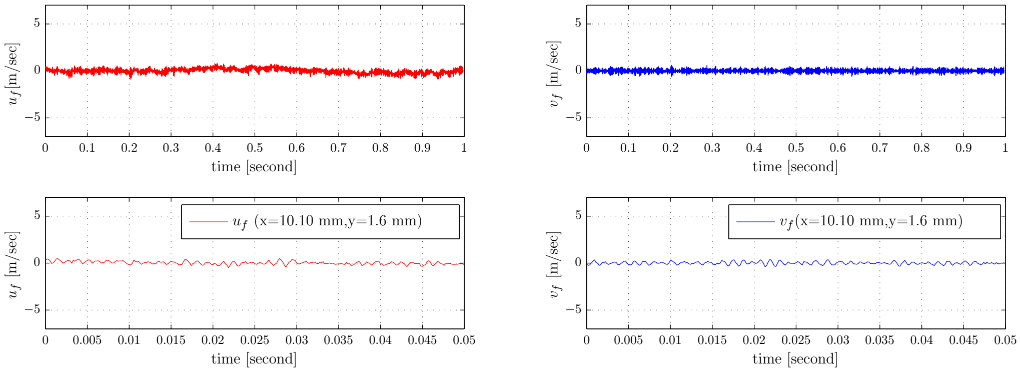

(a) u_f at x=10.10 mm, y =1.6 mm

(b) v_f at x=10.10 mm, y =1.6 mm

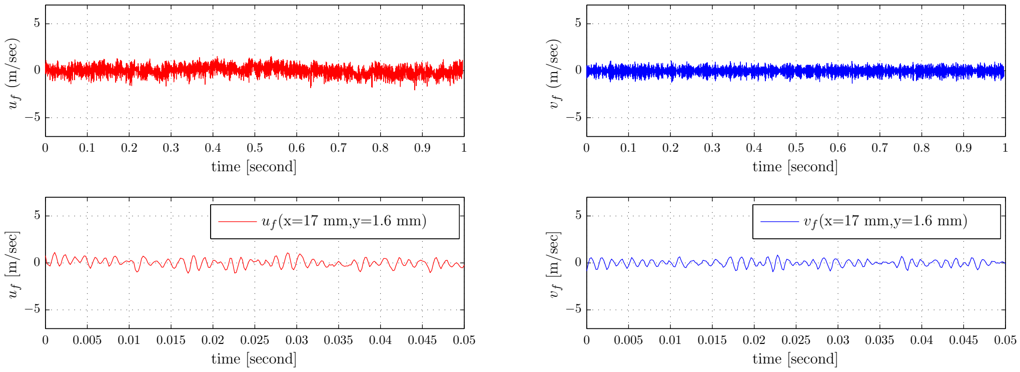

(c) u_f at x=17 mm, y =1.6 mm (Error microphone)

(d) v_f at x=17 mm, y =1.6 mm (Error microphone)

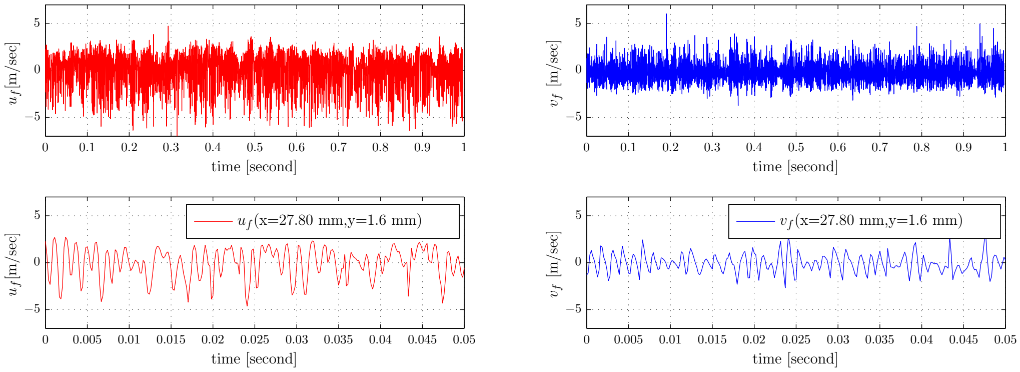

(e) u_f at x=27.80 mm, y =1.6 mm

(f) v_f at x=27.80 mm, y =1.6 mm

Figure E.1: Time evolution of velocity fluctuations (u_f, v_f) at U_∞=15 m/s for clean configuration.

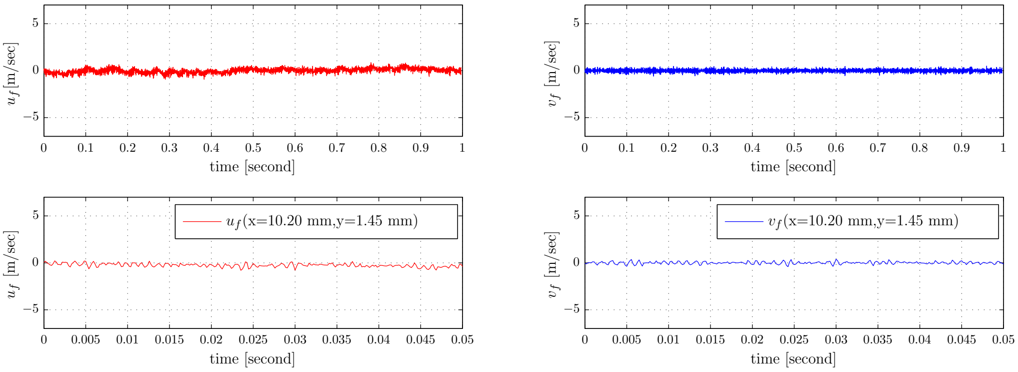

(a) u_f at x=10.20 mm, y=1.45 mm

(b) v_f at x=10.20 mm, y=1.45 mm

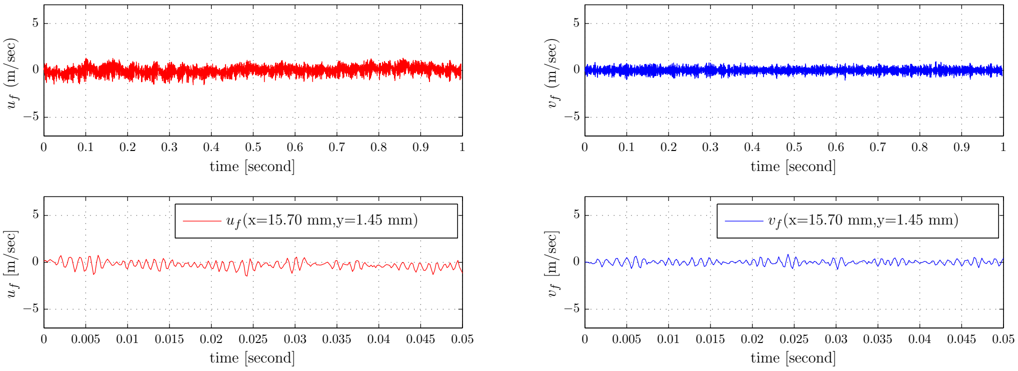

(c) u_f at x=15.70 mm, y=1.45 mm (Error microphone)

(d) v_f at x=15.70 mm, y=1.45 mm (Error microphone)

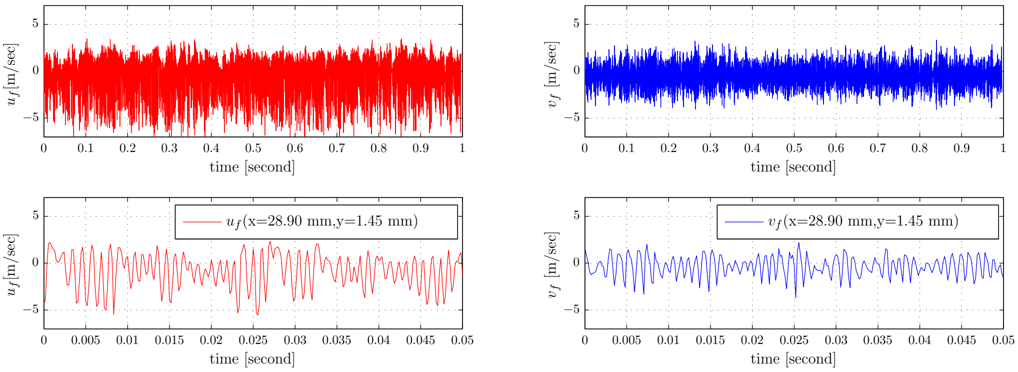

(e) u_f at x=28.90 mm, y=1.45 mm

(f) v_f at x=28.90 mm, y=1.45 mm

Figure E.2: Time evolution of velocity fluctuations (u_f, v_f)at U_∞= 20 m/s for clean configuration.

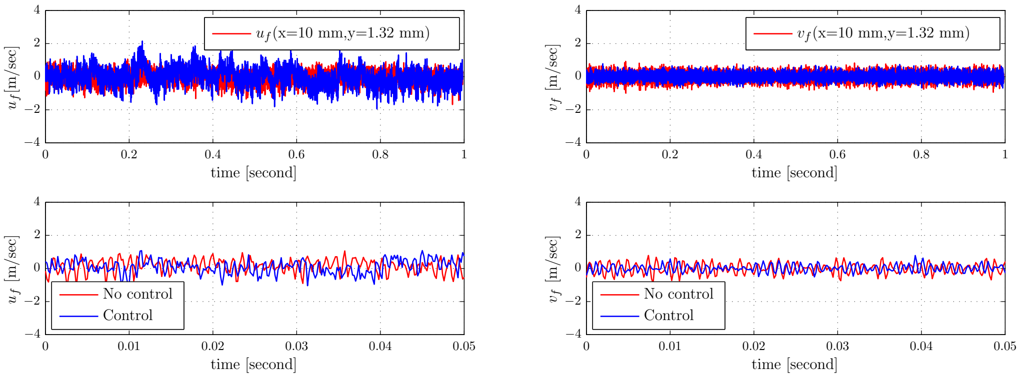

(a) u_f at x=10 mm

(b) v_f at x=10 mm

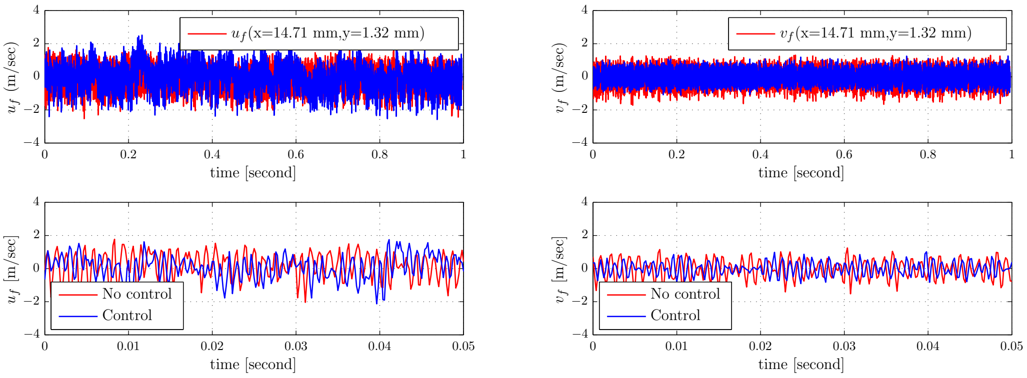

(c) u_f at x=14.71 mm

(d) v_f at x=14.71 mm

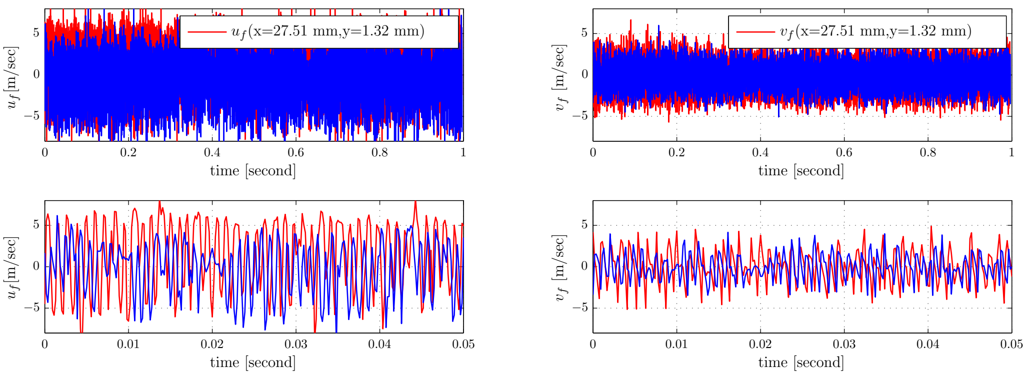

(e) u_f at x=27.51 mm

(f) v_f at x=27.51 mm

Figure E.3: Time evolution of velocity fluctuations (u_f,v_f) for uppermost downstream position at U_∞= 20 m/s for closed loop case.

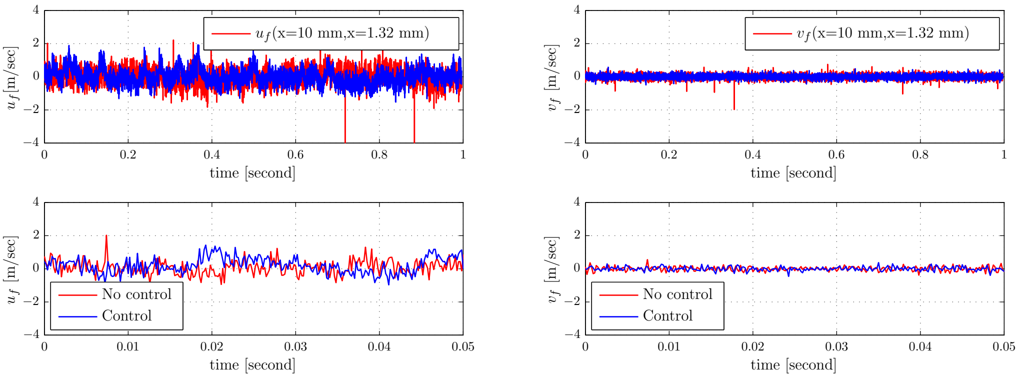

(a) u_f at x=10 mm

(b) v_f at x=10 mm

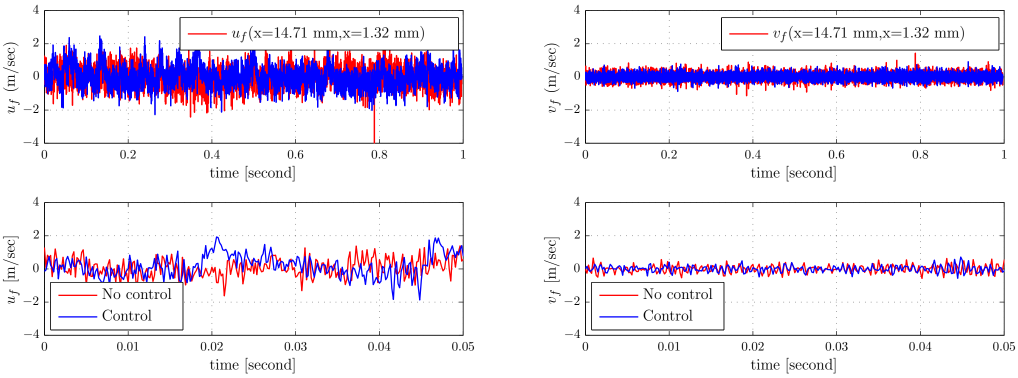

(c) u_f at x=14.71 mm

(d) v_f at x=14.71 mm

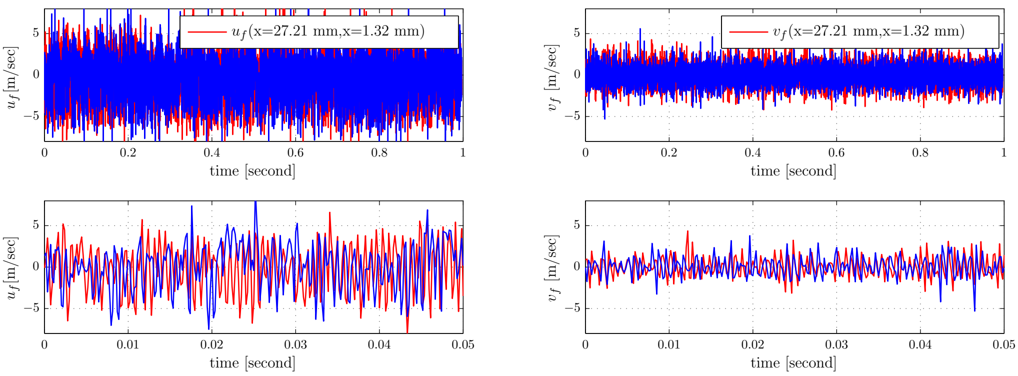

(e) u_f at x=27.21 mm

(f) v_f at x=27.21 mm

Figure E.4: Time evolution of velocity fluctuations (u_f,v_f) for uppermost downstream position at U_∞= 25 m/s for closed loop case.

Appendix F

Cross-correlation

F.1 Correlation studies

Quantitatively, the correlation coefficient between two random variables A and B is defined by eq F.1

$$\rho_{AB} = \frac{Cov(A,B)}{\sqrt{D(A)}\sqrt{D(B)}} \tag{F.1}$$

where Cov(A,B) is the covariance between A and B, and defined as Cov(A,B)=$\overline{(A - \overline{A})(B - \overline{B})}$. Here D(A) denotes the variance of A. The correlation coefficient has two important properties. These are

- $|\rho_{AB}| \leq 1$
- $|\rho_{AB}|=1$

These properties imply that of and only if two time series are linearly dependent, the correlation coefficient will be equal to unity. Near zero $|\rho_{AB}|$ means that the two time series A and B are not linearly related whereas values between 0 and 1 indicate partial linear coupling. The correlation coefficient can be negative, which indicates linear, but out-of-phase, coupling.

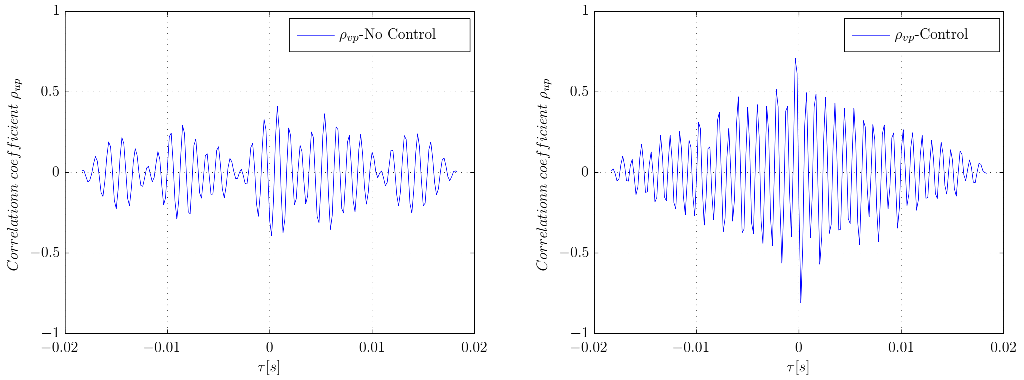

(a) No control

(b) Control

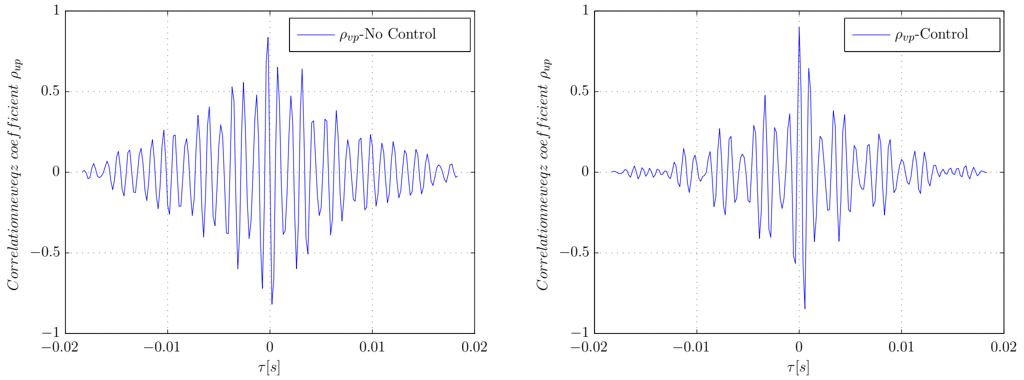

(c) No Control

(d) Control

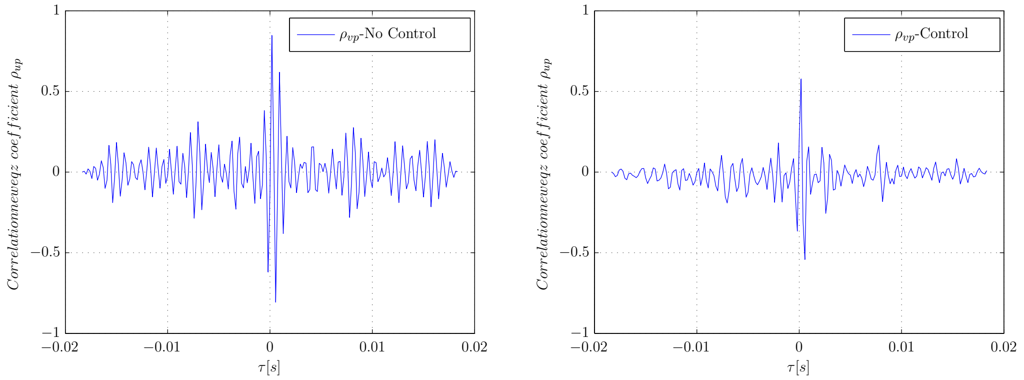

(e) No Control

(f) Control

Figure F.1: Cross correlation of pressure and wall-normal velocity (v_f) signals at U_∞=17, 20 and 25 m/s for closed loop.

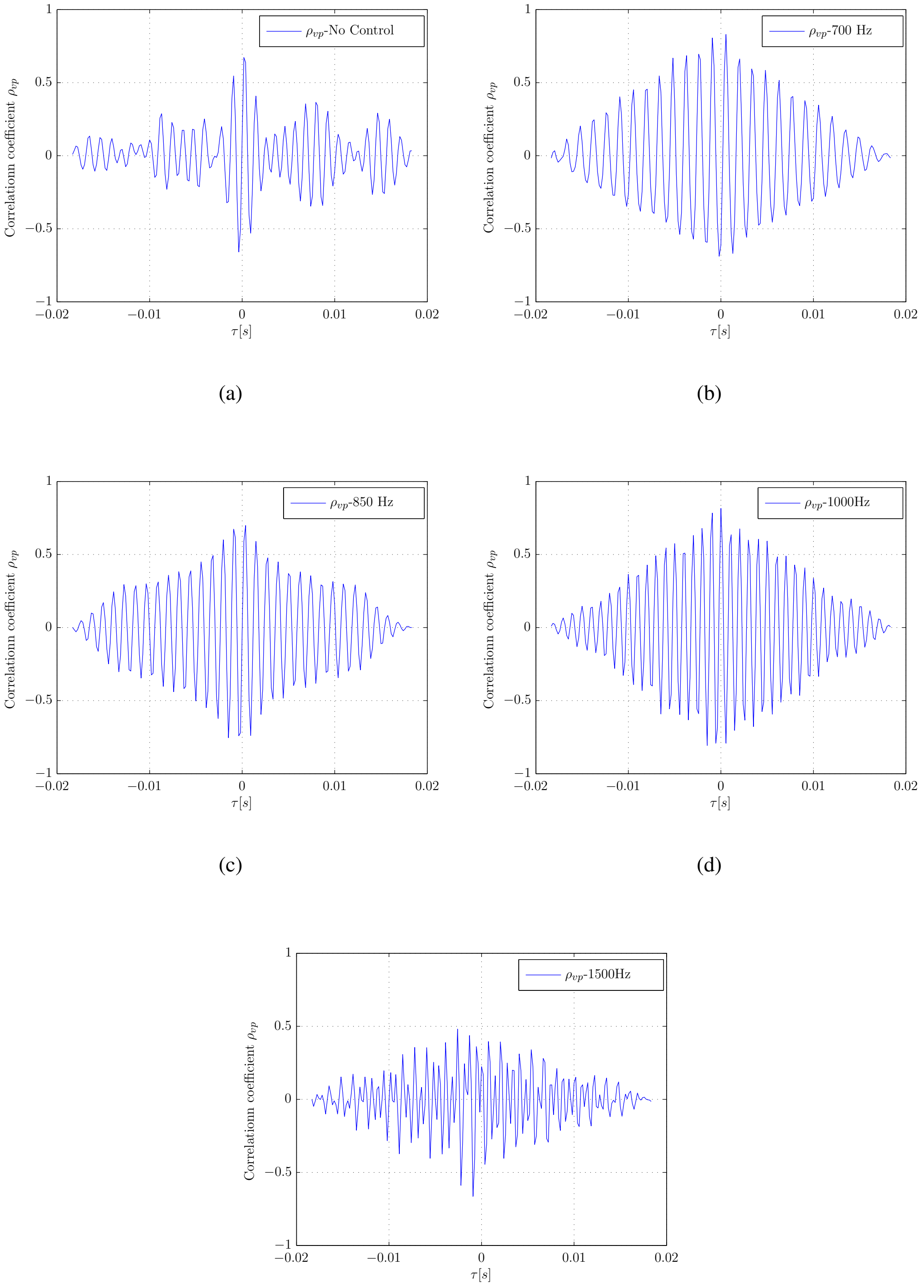

(a)

(b)

(c)

(d)

(e)

Figure F.2: Cross correlation of pressure and wall-normal velocity (v_f) signals at U_∞=17 m/s for open loop.

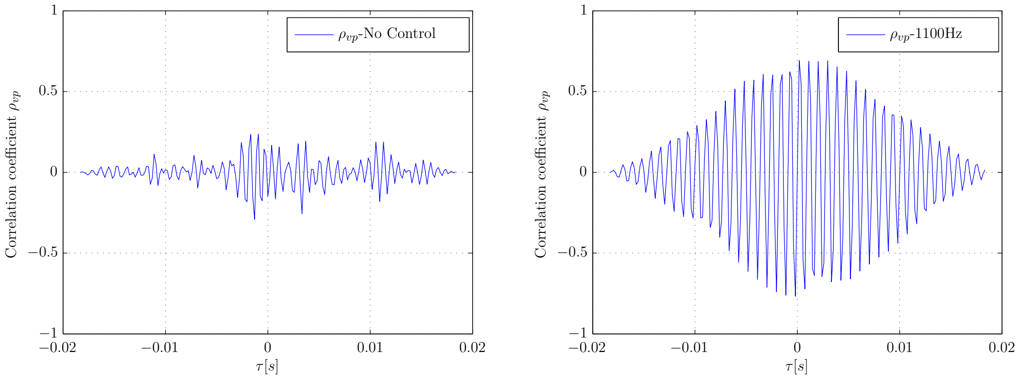

(a) No control (b) f_{ac}=1100 Hz

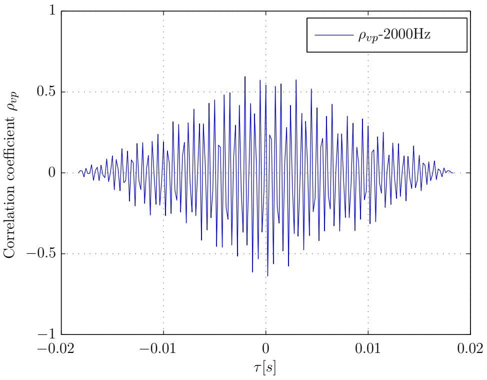

(c) f_{ac}=2000 Hz

Figure F.3: Cross correlation of pressure and wall-normal velocity (v_f)signals at U_∞=25 m/s for open loop case.